

UNIVERSITÀ DEGLI STUDI DI PAVIA

**DOTTORATO IN SCIENZE CHIMICHE E FARMACEUTICHE E
INNOVAZIONE INDUSTRIALE
(XXXIII Ciclo)**

Coordinatore: Chiar.mo Prof. Piersandro Pallavicini

**Photoresponsive Molecular Tools for Targeting Nucleic Acids
Secondary Structures**

Tesi di Dottorato di
Alessandra Benassi

AA 2019/2020

Tutor

Chiar.mo Prof. Mauro Freccero

*“...Per chi viaggia in direzione ostinata e contraria,
col suo marchio speciale di speciale disperazione...”*

(F. De Andrè)

Table of Contents

1. Introduction	7
1.1 The DNA and RNA Quadruple Helix	8
1.1.1 Fundamentals structural elements of G-Quadruplexes	8
1.1.2 Biological Role of DNA and RNA G-Quadruplexes.....	10
1.1.2.1 G-Quadruplexes in Telomeres.....	11
1.1.2.2 G-Quadruplexes in Gene Promoter Regions.....	13
1.1.2.3 G-Quadruplexes in Viruses: the HIV case.....	16
1.1.2.4 G-Quadruplexes in RNA.....	17
1.1.2.5 G-Quadruplexes in parasites	19
1.2 G-Quadruplex ligands: molecular tools for detection and therapy	20
1.2.1 Small Molecules as sensors for Quadruplex Structures	20
1.2.1.1 Light-up Probes	22
1.2.1.2 Aggregation-based probes	23
1.2.1.3 Other Fluorescent Dyes	25
1.2.2 G-Quadruplex Ligands and their therapeutic effects	27
1.2.2.1 Macrocyclic Ligands	28
1.2.2.2. Fused Polycyclic Aromatic Ligands.....	29
1.2.2.3 Modular G-Quadruplex Ligands	31
1.2.2.4 Metal Complexes	32
1.3 Dual-role ligands: the Naphthalenediimides (NDIs) case.....	33
1.4 Towards alternative targeting strategies: photo-activable ligands	40
1.5 Innovative Photo-activation Strategies	43
1.5.1 Quinone Methides (QMs).....	43
1.5.2 Photo-activable 2,5-diaryl tetrazoles	47
2. Aim	54
3. Results and Discussion: Dual Role-Ligands.....	59
3.1 Dual-Role Ligands: NDIs-Carbohydrate conjugates	60
3.1.1 State of the Art and rational design.....	60
3.1.2 Synthesis of Compounds	61
3.1.3 Biological Activity	63
3.1.5 Affinity for Telomeric Quadruplex	67
3.1.6 Spectroscopic Properties	68
3.1.5 Conclusions	70

4. Results and Discussion: Quinone Methides	71
4.1 Towards Alternative Targeting Strategies: Quinone Methides	72
4.1.1 Development of Bi-functionals Photo-Alkylating Ligands	72
4.1.1 State of Art and design of ligands	72
4.1.2 Synthesis of the Compounds	73
4.1.4 Biophysical Assays	78
4.1.5 Photochemical Reactions on G4s	83
4.1.6 Conclusions	86
4.2 Naphthalene-Based Quinone Methide Precursors	87
4.2.1 Design of Naphthalene-based precursors	87
4.2.2 Synthesis of Compounds	88
4.2.3 Spectroscopic Properties in aqueous solution	92
4.2.4 Photoreactivity of QMPs	98
4.2.5 Conclusions	103
5. Results and Discussion:	104
5.1 Photoreactive 2,5-Diaryl Tetrazoles	105
5.1.1 State of art and design of 2,5-Diaryl Tetrazoles	105
5.1.2 Design and Synthesis of Compounds	106
5.1.3 Spectroscopic and Photochemical Properties	109
5.1.4 Fluorescent Properties of Pyrazolines	114
5.1.5 Efficiency of pyrazoline generation vs hydration	117
5.1.6 Biophysical Experiments to analyze G4 binding affinity	119
5.1.7 Looking for biologically active scaffolds	120
5.1.8 Conclusions	130
5.2 Photoresponsive Tetrazoles-Based G4 ligands	131
5.2.1 Design of Tetrazole-based ligands	131
5.2.2 Synthesis of NDI-Tetrazoles conjugates	132
5.2.3 Spectroscopic Properties	135
5.2.4 Photoreactivity	138
5.2.5 Binding Affinity of NDI-Tetrazoles for Quadruplexes	149
5.2.6 Conclusions	155
6. Conclusions	156
7. Experimental Section	160
7.1 Materials and Methods	161
7.1.1. Chemicals, Oligonucleotides and Cells	161
7.1.2 Absorption, Fluorescence and Circular Dichroism Analysis	161

7.1.3 Compounds Characterization	161
7.1.4 Compounds Purification and Analysis	161
7.2 NDI-Carbohydrates conjugates: experimental details	163
7.2.1 Synthesis of Compounds	163
7.2.2 Cell Culture.....	171
7.2.3 Citotoxicity Assays	171
7.2.4 FRET-Melting Assay.....	172
7.3 Quinone Methides	173
7.3.1 Bi-Functional Photo-Alkylating Ligands: Experimental Details	173
7.3.1.1 Synthesis and Characterization of Compounds	173
7.3.1.2 Photochemical Quantum Yields:.....	182
7.3.1.3 FRET-Melting Experiments	182
7.3.1.4 Circular Dichroism Analysis	183
7.3.1.5 Irradiation Experiments with Oligonucleotides.....	183
7.3.1.6 Exonuclease Digestion	184
7.3.2 Naphthalene-based Quinone Methide Precursors.....	185
7.3.2.1 Synthesis of compounds.....	185
7.3.2.2 Spectroscopic and Photochemical Analysis	195
7.4 2,5-Diaryl Tetrazoles	197
7.4.1 Synthesis and Photochemical behaviour of 2,5-diaryl tetrazoles.....	197
7.4.1.1 Synthesis of Compounds	197
7.4.1.2 Spectroscopic and Photochemical Studies	204
7.4.1.3 Fret-Melting Assay.....	204
7.4.1.4 Cells and Parasites Protocols.....	205
7.4.2 NDI-Tetrazole conjugates	206
7.4.2.1 Synthesis of compounds	206
7.4.2.2. Spectroscopic and Photochemical Studies	209
7.4.2.3 CD-Melting Experiments.....	210
References:.....	213

1. Introduction

1.1 The DNA and RNA Quadruple Helix

1.1.1 Fundamentals structural elements of G-Quadruplexes

In 1953, Watson and Crick published the discovery of DNA double helix, now commonly known as B-DNA¹ and, for decades, scientific community considered this as the only relevant DNA structure. However, during the last years, mounting evidence pointed out that nucleic acid sequences can adopt different kind secondary structures, involved in critical physiological processes². Among them, A- and Z-DNA forms, which represent alternative conformations to B-DNA, but also DNA bulges, hairpins, cruciforms, triplexes, quadruplexes and i-motifs are significantly interesting. Their formation has been subject of debate for years, but it has been established that classical biological processes as replication and transcription, involving DNA unwinding, favour their formation. Presence of these secondary structures depends on different factors, as nucleic acid sequence, solution conditions, hydration, ions and proteins. In particular, it has been established that their formation occurs in particular during replication and transcription, which involve DNA unwinding and formation of single strand². Furthermore, DNA secondary structures can regulate gene expression, interactions with proteins and have an impact on genomic stability, DNA repair and damages³.

In this context, G-Quadruplexes (G4s) emerged for their unique structural properties and for their key role in fundamental physiological processes. In details, nucleic acid sequences, including both DNA and RNA, with high guanine contents, may self-assembles to form these supramolecular structures, characterized by two or more guanine tetrads, stacked one on top of each other through π - π interactions (*Figure 1.1*). Guanine quartets are held together by Hoogsteen-type base-pair hydrogen bondings. G4s can be further stabilized by intercalation, into the anionic channel formed by O6 of guanine residues, of different cations⁴, as Na^+ and K^+ , Pb^{2+} and Ba^{2+} ⁵, while, on the contrary, destabilization was observed upon interaction with Li^+ ⁶.

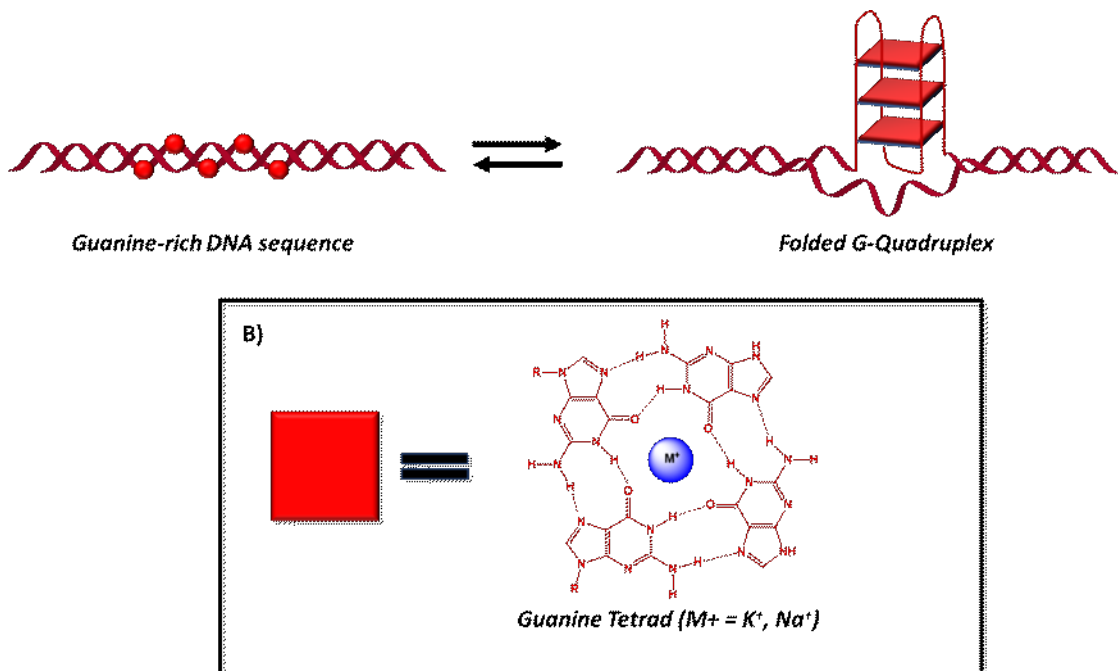


Figure 1.1 – A) Representation of G4 folding from G-rich DNA sequence; **B)** Guanine tetrad.

G4s present high structural variability, depending on folding conditions, including the type of sequence and number of G-tracts, cations, loops length, pH and solution conditions, and finally chemical modifications. Furthermore, G4s can be generated through interaction of only one polynucleotide strand (Monomolecular), two (Bimolecular), three or four (Trimolecular and Tetramolecular)⁷. From a topological point of view, G4s can be classified into three main classes: 1) parallel, with all four strand oriented in the same direction; 2) antiparallel, with two strands pointing in the same direction and other two in the opposite one; 3) hybrid, with two polynucleotide sequences oriented in the same direction⁸. Each topology is characterized by other specific structural features, including loop length and composition, the coordinated cation and the glycosidic angle. Loops can be defined as the nucleotide sequences connecting the different tetrads and can be distinguished into three main classes: propeller, lateral and diagonal (*Figure 1.2*)⁹. Propeller loops connect adjacent parallel strands, lateral antiparallel ones, while diagonal links two sequences across the diagonal of guanine quartet (*Figure 1.2*).

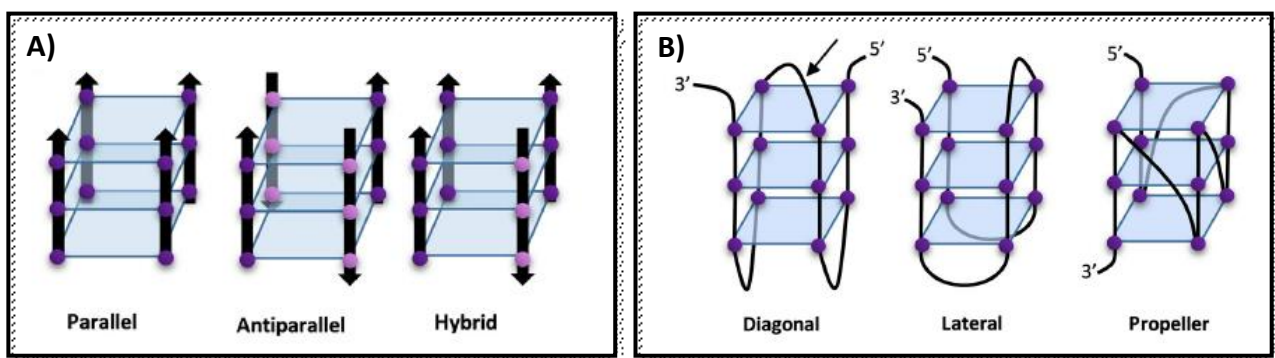


Figure 1.2 – A) Representation of Parallel, Antiparallel and Hybrid G4. **B)** Representation of diagonal, lateral and propeller loops.

Therefore, three propeller loops can be found in parallel topology, while one propeller and two lateral loops are typical of hybrid structures. Antiparallel G4s are more versatile and can be distinguished for the presence of two lateral and one diagonal or three lateral loops. Even loops length can be associated to a certain topology: indeed, long loops are more typical of antiparallel or hybrid topology, while shorter ones are more frequently found in parallel G4s¹⁰. It has been discovered that, in antiparallel G4s, presence of longer loops stabilize the structure, possibly due to the presence of further interactions between the loop and guanine tetrads¹¹. On the contrary, short loops have a positive effect on formation and stability of parallel G4 and, in particular, most of quadruplex present in gene promoter regions are characterized by three one-nucleotide propeller loops¹².

As mentioned before, also cations are important for quadruplex folding and stability¹³ and they can interact with O6 of guanine residues, which create a negatively charged cavity in the centre of the tetrads. Their effect on quadruplex structure depend on several factors, including ionic radii, hydration energy, the type of nucleic acid and on topology¹⁴ but, in general, coordination to K⁺ and Na⁺ are the most common, also because of their abundance in cellular environment, and, in most cases, K⁺ is preferred over Na⁺¹³.

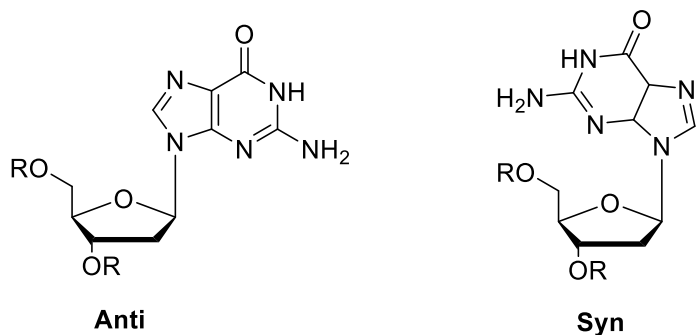


Figure 1.3 – Representation of syn and anti conformation for guanine base.

G4 stability is affected also by another parameter, the glycosidic bond angle (GBA) of guanines, defined as the angle between the sugar moiety, lying on the plane, and the nucleobase, disposed perpendicularly to it. In particular, there are two possible conformation: *syn*, with sugar and the base pointing in the same direction and *anti*, with the opposite orientation (Figure 1.3). When guanines fold into G4, they can face to each other in different configuration: *sin/sin*, *sin/anti*, *anti/sin* and *anti/anti*. Among reported situations, *anti/anti* represents the most favourable, because of the reduced steric hindrance in the resulting structure, while the other cases require higher energy. However, presence of one conformation rather than another is strictly dependent on quadruplex topology: the presence of these different possible combination is strictly dependent on topology: indeed, for example, *anti/sin* disposition is necessary when there is a polarity inversion point, present when strands are oriented in opposite directions. Therefore, these conformations are common in antiparallel and hybrid quadruplexes. On the contrary, in parallel topology, where these inversion points are missing, only *anti/anti* conformation is observed.

Considering all these factors, it seems reasonable that G4s can form many types of different structures and their formation is a complex process, affected by several factors. However, their existence has been recently demonstrated *in vivo*¹⁵, underlining their involvement in several physiological processes, which together with their unique structural features make them an interesting therapeutic target for several pathologies.

1.1.2 Biological Role of DNA and RNA G-Quadruplexes

It has been widely demonstrated that putative quadruplex forming sequences (PQS) are present in several important regions of human genome, including telomeres¹⁶, gene promoters¹⁷ and 5'-Untranslated Region (5'-UTR) of RNA¹⁸. Several computational algorithms predicted the existence of at least 370.000 PQS¹⁹, mainly distributed in the previous mentioned regions: the highest content of PQS has been observed in telomeres, characterized by the TTAGGG repeat. The percentage of PQS is significantly high also in gene promoters, between introns and exons, and in DNA replication origins that are most frequently used²⁰. It has also been discovered that 5'-UTR regions of mRNA are rich in PQS, as well as TERRA sequences, RNA transcripts of telomeres²¹. All these considerations highlight the probable regulatory functions of G4s *in vivo*, despite their physiological role is still subject of investigation and debate²². Another important question that should be addressed in this context, to further clarify G4s biological role, is when they can be formed under physiological environment: DNA is present in a double strand conformation and stabilized by chromatin, however, during processes as replication, transcription and repair, the impairing of complementary strands allows the formation of alternative interactions, including Hoogsteen-hydrogen bonds that lead to the

formation of G4s. Moreover, G4s formation can be induced also by different conditions, as superhelical stress, molecular crowding and specific G4 binding proteins²³.

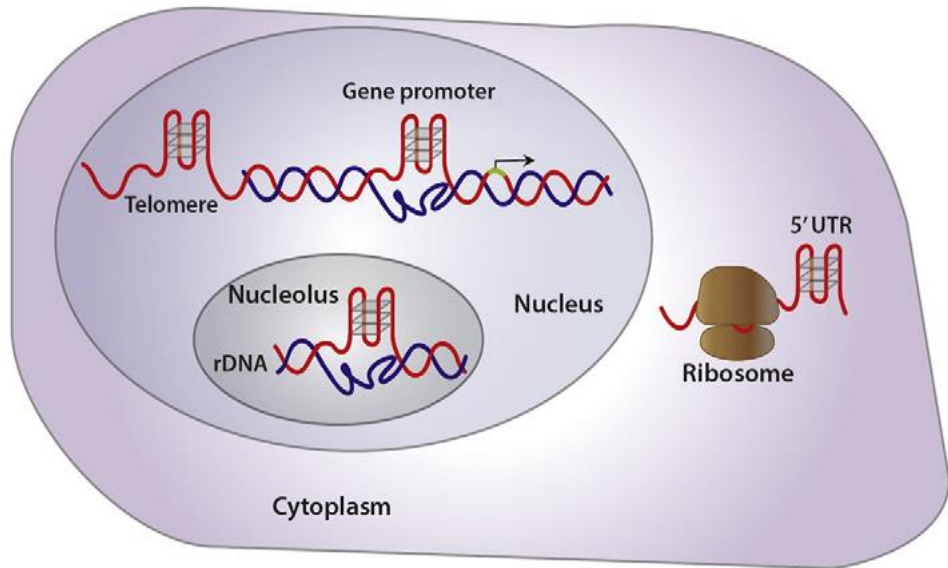


Figure 1.4 – Representation of localization of G4s structures in regions of humane genome¹⁷.

In order to demonstrate and detect quadruplex formation *in vivo*, several tools have been developed during the last years: Balasubramanian and co-workers produced a specific fluorescent antibody, **BG4**, for the specific detection of telomeric quadruplex²⁴. Thanks to this antibody, not only it has been possible to demonstrate presence of G4 in cells, but also that the enzyme telomerase interact with telomeric quadruplex, further corroborating their involvement in physiological processes²⁵. More recently, identification of these secondary structures in the genome has been possible thanks to the development of a next-generation sequencing: a map of G4s in human genomic DNA has been realized using different G4s stabilizing conditions, to individuate DNA-polymerase stalling sites generated by G4 formation²⁶. G4 detection can be accomplished also using small molecules as fluorescent probes, but this approach will be addressed in detail in the next section.

All these achievements had a crucial impact in this research area, not only to prove quadruplex existence, but also to elucidate their biological functions. Here, a brief overview of the G4s physiological roles is provided, classifying the secondary structures for the type of region in which are localized, mentioning also examples of quadruplexes identified in virus and parasites genome.

1.1.2.1 G-Quadruplexes in Telomeres

Telomeres are DNA sequences characterized by repetitive nucleotide sequences with a double strand region and a 3' single-stranded overhang, which have a “capping function”, protecting DNA from degradation and maintaining chromosomal and genomic stability. The double strand portion is composed of several kilobases, while 3'-overhang is constituted by few hundred bases. Moreover, the presence of large loops, called T-loops, are binding sites for different proteins, including TRF1, TRF2, POT1, RAP1, TIN2 and TPP1, which taken together, are part of the shelterin protein complex, protecting telomeres from DNA repair machinery²⁷. Human telomeres are characterized by the presence of the repetitive sequences (TTAGGG)_n, with high

guanine content, that result in the formation of secondary structures. PQS in this region attracted significant attention during the last twenty years and telomeric quadruplex has been deeply studied. In 2002, Neidle et al. reported the crystal structure of a 22-nt human telomeric sequence (wTel22), that presented an intramolecular parallel structure, in presence of K⁺, composed of three guanine tetrads, connected by three chain-reversal loops²⁸. However, ¹H-NMR experiments performed in solution, with Tel26 sequence (5'-AAAGGG(TTAGGG)3AA), indicated that this quadruplex folds into an intramolecular hybrid topology, with three tetrads connected by mixed parallel/antiparallel strands²⁹, which remains the major topology even in presence of increasing concentrations of Na⁺. However, it has been observed that this G4 can form two distinct hybrid-type structure: hybrid-1 and hybrid-2, which depend on the type of flanking regions differing for the loops arrangements, strand orientation, tetrads arrangements and capping structures³⁰.

In details, three TTA loops can adopt chain-reversal lateral, propeller and edgewise conformation in hybrid-1 and lateral-lateral-side conformation in hybrid 2 (*Figure 1.5*). The two topologies differ also for the type of capping structure: hybrid-1 is characterized by a triple-adenine capping at 5'-end, while T:A:T triplet caps the 3'-end of hybrid-2 conformation. Despite the possibility to fold into both topologies, hybrid-2 resulted to be the major conformation of human telomeric sequence, even if they are in equilibrium³¹. These different capping arrangements strongly influence the resulting topology and, moreover, represent a potential binding site for potential drugs.

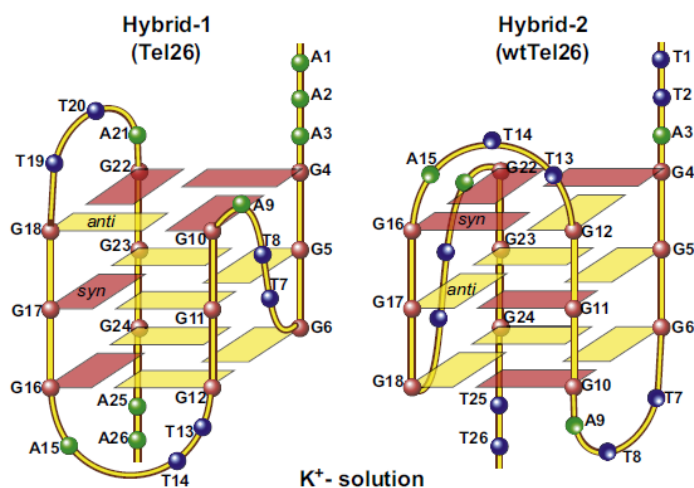


Figure 1.5 – Topologies adopted by human telomeric quadruplex in K⁺ solution²⁸.

More recently, it has also been proposed that highly repetitive telomeric sequences can generate higher-order structures composed by monomeric quadruplex³², which can be distinguished into two different arrangements: 1) “beads on a string”, where single monomers doesn’t interact with each other³³; 2) consecutive G4s exploit stacking interactions on terminal tetrads to assemble into high-order structures³⁴. This second option seems to be the most likely and structures with these features have been determined by different techniques, including electron microscopy and FRET-melting assays. Moreover, use of specific G4-antibodies evidenced the presence of these structures at telomeres tips even *in vivo*³⁵.

Significant effort has been dedicated to the study of G4s in telomeric regions because, from previous considerations, appears evident that their formation can interfere with crucial physiological processes, including replication, causing telomere instability. Indeed, formation of a G4 represents an obstacle for DNA polymerase and, if it cannot be removed, the replication fork can bypass the G4, producing a single-strand gap in position of G4 that results in double strand breaks in subsequent replications³⁶. Presence of G4 can also inhibit telomerase activity, causing telomere shortening³⁷. However, different proteins are able to resolve G4 structures and, in case of telomeres, two in particular: DNA helicase, a class of enzymes involved

in DNA replication with the function to impair DNA double strand, and a single-strand DNA binding protein (ssDNA-binding proteins).

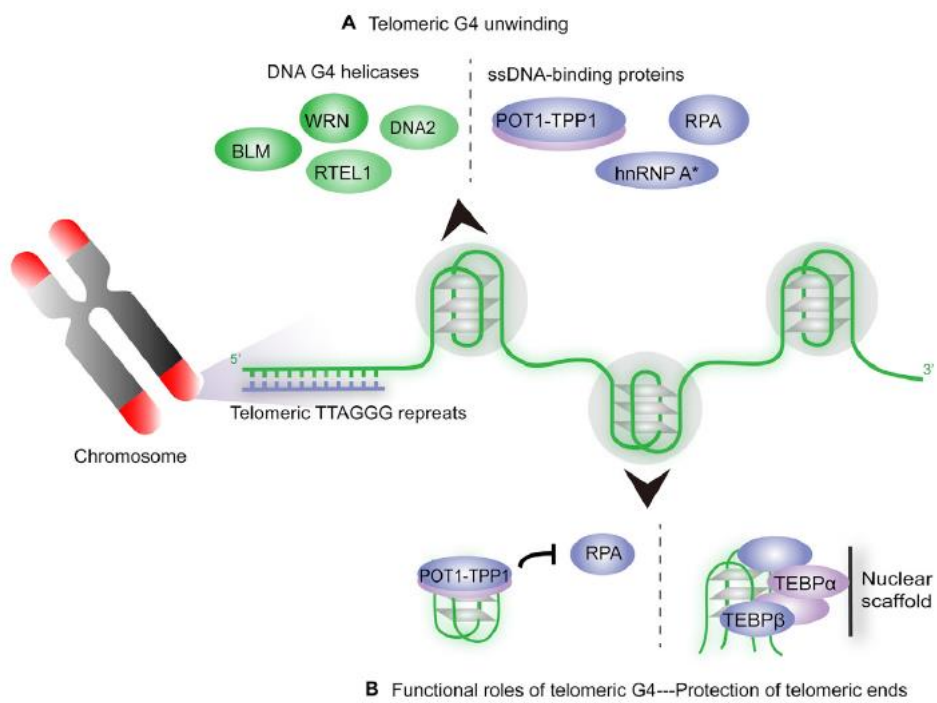


Figure 1.6 – A) Proteins responsible of G4 unfolding. B) Telomere protection by telomeric G4²².

In the class of helicases, it has been reported that BLM, WRN, RTEL1 and DNA2 are able to unwind telomeric G4. Helicases as BLM and WRN act on single strand, necessary for enzyme loading, with 3'-5' polarity. The unwinding of G4 requires different steps: for example, once that enzyme BLM is located on the tail near the quadruplex, it converts the quadruplex into a triplex and, subsequently, into an hairpin, before the complete unfolding³⁸. It has been assumed that BLM and WRN can be recruited by shelterin complex, therefore deficiencies of these enzymes result in higher content of G4s in telomeric regions³⁹. Among ssDNA-binding proteins involved in G4 regulation, POT1 and TPP1 are particularly interesting, because they are responsible of chromosomes protection and length regulation of telomeres. When a G4 structure is formed and interfere with telomere elongation, POT1 or TPP1 unfolds the secondary structure⁴⁰. Interestingly, G4 assembled in telomeric region could act also as down regulators of telomerase, which represents a promising strategy to develop novel anticancer therapies: indeed, this enzyme is overexpressed in several types of tumors and is responsible not only of telomere maintenance but also of “immortality” of tumor cells⁴¹. Therefore, folding and stabilization of telomeric G4 inhibit telomerase activity, leading to damages and death of tumor cells⁴².

1.1.2.2 G-Quadruplexes in Gene Promoter Regions

Bioinformatic analysis evidenced a massive and non-statistical presence of PQS in promoter regions of gene, on sense or antisense strand, in introns or in proximity of Transcription Starting Site (TSS), suggesting that they can act as regulators of gene expression⁴³. In particular, from different experimental results, it emerged that G4s behave as both up-regulator and down-regulators of specific genes, opening even more questions

about their biological functions⁴⁴. PQS in promoters are double-stranded DNA, therefore G4 folding is more complicated: it has been proposed that transition from duplex to tetraplex is favoured by negative chromosomal supercoiling, because G4 can partially neutralize the negative supercoiling,

However, during the last years, a large number of G4 forming sequences have been identified in promoter regions of several oncogenes and, in most cases, it has been demonstrated that their formation reduced the expression of the gene itself, highlighting their role as promising target in anticancer therapy.

In this context, one of the most significant example is represented by c-MYC proto-oncogene, responsible of cellular growth and proliferation, which is overexpressed in several types of tumors. This is one the first reported examples of a G4-containing oncogene. The 5'-extremity of c-MYC is characterized by different DNAase I hypersensitive sites, including the nuclease-hypersensitive element III₁ (NHIII₁), located upstream promoter P₁, which has been deeply studied because represents the preferred transcription starting site and controls 80-90% of the expression of c-MYC. This region includes a pyrimidine-rich coding strand and purine-rich noncoding strand, responsible of polymerase arrest in presence of increasing concentration of KCl and it has been suggested that this result was due to G4 folding on this sequence. Later, this hypothesis has been confirmed and the formation of a parallel intra-molecular tetraplex, composed by three guanine tetrads, stabilized by two AT base-pair terminal capping domains, has been demonstrated⁴⁵. The G4 in this sequence has a potential regulatory function, through interaction with different nucleic acid-binding proteins, such as CNBP and NM23-H2 and play a dual role: binding with mentioned proteins favours the recruitment of transcription factors, inducing the transcription process. On the contrary, extensive folding of G4 structures can down-regulate c-MYC activity, as they hinder interactions with transcription factors leading to suppression of gene expression. This has been confirmed, for examples, by studies reporting the stabilization of the G4 with nucleolin protein, which led to inhibition of c-MYC expression⁴⁶.

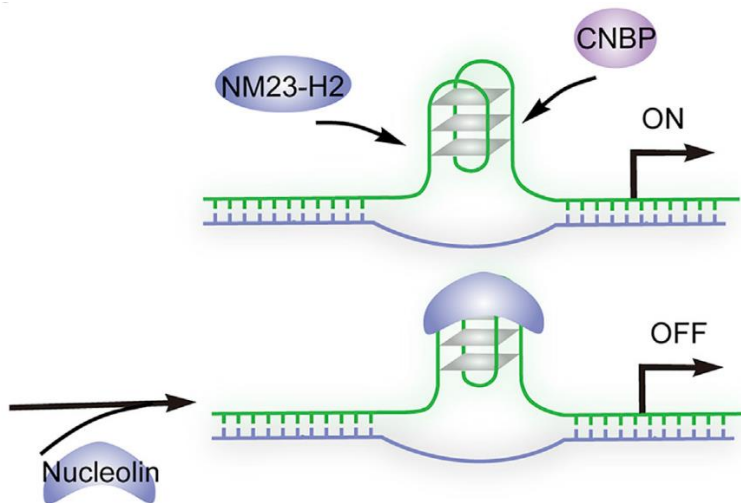


Figure 1.7 – Mechanisms of c-MYC expression regulated by G4 formation: A) binding with NM23-H2 and CNBP induces transcription; B) Interaction with nucleolin protein lead to transcription inhibition²².

The RAS family gene, which includes HRAS, NRAS and KRAS, is considered a critical target in anticancer research and their mutation are involved in different types of tumors⁴⁷. The nuclease hypersensitive element of the KRAS promoter is particularly rich of G-tracts and it has been reported that several transcription factors interact with the G4 in this region⁴⁸. Experiments with oligonucleotides engineered to fold into a more stable

G4, compared to the native sequence, showed that secondary structure was able to interact with several transcription factors, presenting high cytotoxicity against pancreatic cancer cells⁴⁹. Even the oncogene H-RAS, involved in tumorigenesis, contains a G4 structure in its promoter region, which is recognized by zinc finger transcription factor MYC-associated zinc finger protein (MAZ). Unfolding of quadruplex make the sequence readily accessible by the replication machinery, enhancing gene expression⁵⁰. Therefore, stabilization of PQS of RAS genes family can be considered a valid strategy to down regulate their activity.

Another interesting example is represented by Telomerase Reverse Transcriptase (hTert), a catalytic subunit of enzyme telomerase: its corresponding gene promoter region present various PQS and it has been demonstrated that one of these was able to suppress its expression upon interaction with protein factor metastasis suppressor non-metastatic 2 (NME2) and with RE1-silencing transcription factor (REST)-repressor complex. From these studies, it has been discovered that the role of G4s in gene promoter regions is strictly dependent on their interaction with protein binding factor⁵¹.

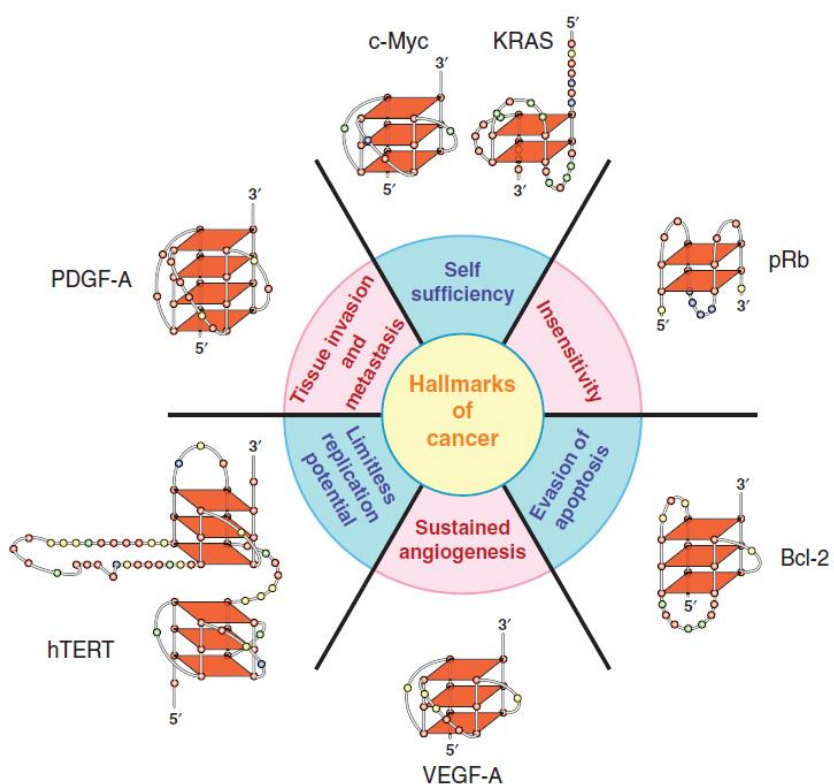


Figure 1.8 – Cancer-related genes containing G4 in their promoter regions⁵².

PQS have been identified also in promoter P1 of BCL-2 proto-oncogene, coding for a protein responsible of cell survival and inhibition of apoptosis, overexpressed in several kind of tumors, including breast, prostate, cervical, colorectal and non-small cell lung carcinoma⁵³. The P1 promoter is located 1386-1423 base-pairs upstream of the translation start site and represents the most important transcriptional promoter of the gene. The 5'-end of the gene includes a GC-rich region, with six guanine tracts, involved in the regulation of the gene expression and it has been demonstrated that this region can fold into three different G4s in potassium solution. Among them, quadruplex formed on the middle of four consecutive guanine tracts is the most stable and NMR resolution revealed that it consists of an intramolecular structure with mixed parallel/antiparallel strands and three guanine tetrads⁵⁴. The regulatory action of these G4s have been demonstrated by different experiments, including luciferase assay: with a mutated sequence, able to form

another G4 located in the upper region of P1 promoter, reduced expression of the gene has been observed⁵⁵. This result highlighted that stabilization of G4 represent a valid strategy to inhibit BCL-2 activity in cancer cells.

Presence of a G4 forming sequence has been established also in c-KIT proto-oncogene, that encodes for a tyrosine kinase receptor, involved in cells proliferation and survival, whose overexpression is associated to different kind of tumors, including gastrointestinal stromal tumors (GIST), mastocytosis, and acute myelogenous leukemia. The region located 200 base-pairs upstream the transcription start site (TSS) is rich in GC base-pairs and is also involved in interactions with different transcription factors, including MAZ in human normal fibroblast and SP1 in hematopoietic cells and carcinomas⁵⁶. The sequence d(AGGGAGGGCGCTGGAGGGAGGG), positioned 87 nucleotides upstream of the transcription start site of the gene, folds into a single G4 structure. The NMR resolution, in potassium solution, revealed the formation of an intramolecular parallel structure, with three guanine tetrads⁵⁷. As in case of BCL-2, it has been demonstrated that stabilization of this quadruplex has a downregulatory effect towards c-KIT gene. In the last years, several molecular tools have been developed to further clarify biological role of c-KIT and BCL-2 gene and to achieve a therapeutic effect, but this aspect will be discussed in detail in the section 1.2.2. More recently, it has been discovered that transcription of Vascular endothelial growth factor (VEGF), a signal protein that stimulates the growth of blood vessels and that is upregulated in carcinoma of the cervix⁵⁸, contains five arrays of more than three consecutive G-tracts in its promoter, which easily fold into G4 structures. This region is also a consensus sequence for different transcriptional factors, as Egr-1 and Sp1, suggesting that the equilibrium from different DNA forms regulate the expression of the gene⁵⁹. Several studies demonstrated that small-molecules, able to interact and stabilize G4 in this region, can suppress the expression of this gene⁶⁰. Moreover, it has been discovered that regulation is also influenced by oxidative stress, which alters the structural balance between G4 and duplex in its promoter region. In VEGF promoter region there are five G-tracts and G4 folding is possible even in unfavourable conditions. In presence of reactive oxygen species (ROS), transcription is enhanced upon oxidation of guanine to 8-oxoguanine (8oxoG): indeed, formation of 8oxoG lead to the formation of an abasic site in the sequence, which favour the folding of the sequence into a G4 structure, which is recognized by transcriptional factors that activate gene expression⁶¹.

1.1.2.3 G-Quadruplexes in Viruses: the HIV case

As mentioned above, G-quadruplexes are widely diffused in human genome and their involvement in regulation of key physiological mechanisms is supported by solid experimental evidence. However, these secondary structures are not exclusive of human genome: indeed, an increasing number of experimental results documented that several PQS are present also in virus genome and they also present regulatory functions. In particular, G4 formation in Epstein-Barr virus-encoded nuclear antigen 1 (EBNA1) mRNA reduces translation of maintenance proteins, influencing antigen presentation⁶². PQS have been identified even in Human Papilloma Viruses (HPV)⁶³ and in Herpes Simplex-1 (HSV-1) genome⁶⁴. An interesting case is represented by G4s in Human Immunodeficiency Virus 1 (HIV-1), responsible of acquired immunodeficiency syndrome (AIDS). This virus is characterized by single-stranded RNA genome, which is integrated, as provirus form, in the chromosomes of the host cell after retro-transcription. At this point, provirus can be involved into two different processes: a productive replicative cycle or a state called “latency”.

The efficient progression of the viral cycle depends on 5'-Long Terminal Repeat (LTR), with 634 base-pairs, containing several sites for different transcription factors. Recently, it has been demonstrated that in this

specific region, formation of multiple G4 structures is possible and they can act as suppressor of viral transcription. In particular, this sequence contains four GGG-tracts, two GGGG-tracts and three additional GG-tracts, which resulted in the identification of three G4s: LTR-I, LTR-II, LTR-III, spontaneously formed in presence of 100 mM K⁺, and LTR-IV, which resulted to be less stable, but its formation and stabilization can be induced by the use of proper G4 ligands⁶⁵.

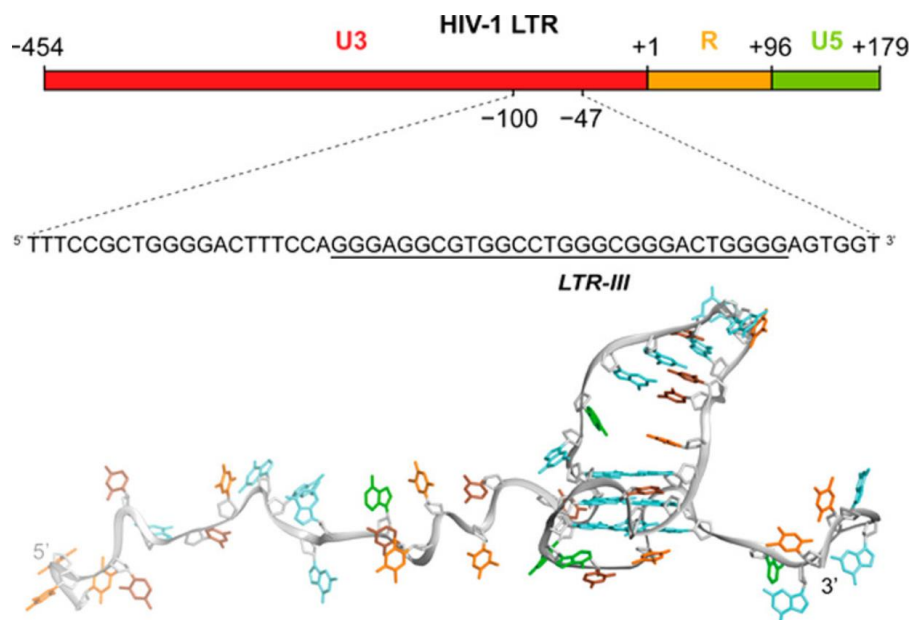


Figure 1.9 – Representation of LTR-III G4⁶⁶.

All three G4s showed structural features comparable to G4 present in oncogenes promoters. Among them, LTR-III showed highest thermal stability, as proved by Circular Dichroism and FRET experiments. Their physiological role has been confirmed by further studies, that demonstrated that several proteins are able to interact with G-rich region of LTR, with different consequences: nucleolin stabilizes the G4 and decrease viral transcription⁶⁷. On the contrary, hnRNP A2/B1 is able to unwind LTR-II and LTR-III, activating transcription process⁶⁸. In presence of mutated sequences, not able to fold LTR-III, mentioned proteins do not affect the activity of the promoter, highlighting the regulatory role of LTR-III. Due to its interesting biological effects, LTR-III has been deeply investigated and its structure has been resolved through ¹H-NMR studies. It has been discovered that LTR-III present a very unique topology: it's characterized by (3+1) hybrid structure, with three guanine tetrads and a long 12-nucleotide loop forming a duplex hairpin⁶⁶. This duplex-quadruplex hybrid structure opened new possibilities to design highly selective molecules, able to interact specifically with the quadruplex-duplex junction, with the potential to inhibit viral transcription, minimizing off-target interactions.

1.1.2.4 G-Quadruplexes in RNA

Due to the massive presence of PQS in fundamental DNA sequences, it is not surprisingly that they can be easily identified in RNAs⁶⁹ and their formation is associated with specific biological functions. Compared to DNA, RNA G4s can be more easily formed *in vivo*, because of the lack of the complementary strand and for their higher stability. In nature, there are several types of biologically active RNAs: messenger RNA (mRNA),

transfer RNA (tRNA), ribosomal ribonucleic acid (rRNA), small nuclear RNA (sRNA) and non-coding RNAs (ncRNA). Initially, the first PQS have been discovered mostly on mRNA, localized on 5'-end of the first intron of pre-mRNA, in both 5'- and 3'-untranslated regions (UTR), and in the coding region of mature RNA, evidencing possible regulatory functions also for these kind of quadruplexes. It has been recently demonstrated that G4s formed in 3'-end of pre-mRNA affects RNA maturation process, as transcription termination and polyadenylation within the nucleus. G4 folding can occur during transcription: indeed, after the hybridization of RNA with complementary DNA sequence, formation of a R-loop structure favour the folding of PQS into G4, which represents an obstacle for the enzyme RNA Polymerase II, unable to continue the process. Indeed, during 3'-end processing all RNA transcripts are cleaved and polyadenylated in the nucleus: polyadenylation, which consists in the addition to multiple adenosine monophosphates (poly(A)tail) to mRNA, is essential to ensure their stability, transport to cytoplasm and translation. In this context, it has been demonstrated that, for example, a G4 is formed in 3'-end of a pre-mRNA encoding for TP53, a tumor suppressor, and interact with the splicing and polyadenylation regulator hnRNP H/F, contributing to p-53 dependent-apoptosis⁷⁰.

G4s can be found also near the splicing junctions and it has been suggested that they can modulate splicing process in association with specific exons and introns splicing enhancers or silencers. This is the case of G4 found in intron 6 of the human telomerase transcript (TERT), able to regulate splicing of TERT acting as a silencer⁷¹. However, G4s are more prevalent in exons, as in case of exon 15 of fragile mental retardation 1 (FMR1) mRNA, which contains two PQS, which act as splicing enhancers. Briefly, experimental results suggested that FMR1 expression is strictly dependent on the interaction of X mental retardation protein (FMRP) with quadruplex sequences in FMR1 mRNA⁷².

RNA G4s are particularly abundant also in 5'-UTR of mRNA and are able to modulate translation process, because 5'-UTR is fundamental for translation initiation and translational control. In this context, it emerged that most of G4s identified in this region behave as translational repressor, as in case of BCL-2 and FMR1. On the contrary, there are reported cases of G4s in 5'-UTR which are necessary to ensure translation: one of the most significant example is represented by VEGF, which contains a 5' PQS on internal ribosome entry site (IRES) domain, responsible of translation initiation in a cap-independent manner⁷³. It has been demonstrated that PQS in IRES directly interact with 40S ribosomal subunit (40S) to induce the translation process. It should be underlined that cap-independent translation is active in only particular physiological conditions, including mitosis, hypoxia, nutritional stress, and cell differentiation: therefore, because of the well-established role of VEGF in angiogenesis and cancer, identification of a G4 that promotes translation of this gene open new possibilities to develop novel anticancer strategies.

In this research context, one of the most remarkable examples of how G4s can misregulate critical physiological processes is represented by PQS identified in hexanucleotide repeat expansions (HRE), in a non-coding region of C9orf72 gene, involved in the development of amyotrophic lateral sclerosis (ALS) and frontotemporal dementia (FTD). Indeed, the expansion of short repetitive sequences (3-6 nucleotides), can induce the expression of proteins through a Repeat Associated Non-AUG translation (RAN translation), that results in accumulation of toxic di-peptides repeat proteins detected in tissues of patients affected by ALS and FTD. The HRE on DNA of this gene can fold into different quadruplex structures, with parallel or antiparallel topology. Formation of this secondary structure represents an obstacle for RNA polymerase transcription, which lead to the production of truncated RNA transcripts. Abortive transcripts generated by HRE region contain other secondary structures, including parallel G4s and hairpins, able to specifically seize fundamental proteins in a conformation-dependent manner, that could explain the occurrence of functional defects in ALS and FTD patients⁷⁴.

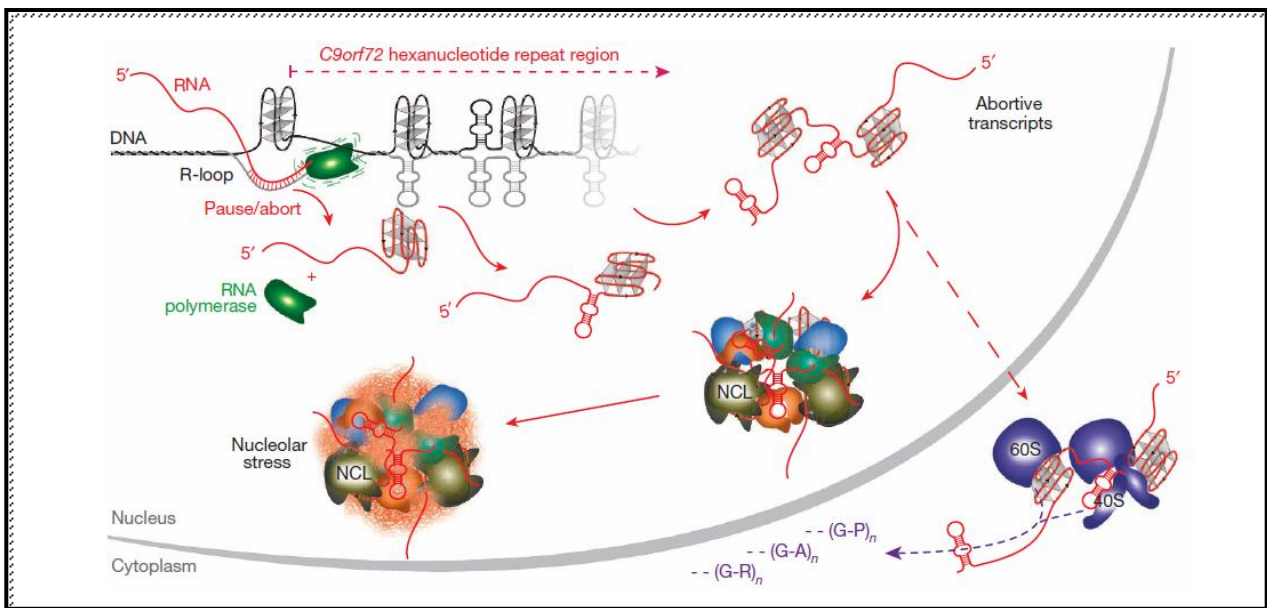


Figure 1.10 – G4s formation on C9orf72 HRE sequence and on RNA transcripts induces the formation of abortive transcripts and recruitments of important proteins⁷⁴.

In physiological environment, there are several types of RNAs that do not encode for any protein, as ribosomal RNA (rRNAs), transfer RNAs (tRNAs), small nuclear RNAs (snRNAs), small nucleolar RNAs (snoRNAs), telomere-associated RNAs (TERRA), long noncoding RNAs (lncRNAs), microRNAs (miRNAs), small interfering RNAs (siRNAs) and PIWI-interacting RNAs (piRNAs). In the last years, PQS have been identified in several of these noncoding RNAs, including tRNAs, lncRNAs and miRNAs⁶⁹. Among them, TERRA lncRNA, generated by transcription of a cytosine-rich sequence of telomeric DNA by RNA Polymerase II, attracted remarkable attention, due to its promising biological role. TERRA lncRNA is characterized by an high content of guanines, which can lead to the production of high-order quadruplex structures or can assemble into a “beads on a string” conformation. This particular RNA can interfere with the activity of telomerase, establishing interaction with telomeric DNA that leads to the generation of hybrid DNA-RNA quadruplex structures. Moreover, it has been demonstrated that TERRA G4 can bind several proteins, including TRF, TRF2 and some proteins of hnRNP family, evidencing that their formation can be implicated in maintenance of chromosomal integrity, upon recognition of corresponding proteins⁷⁵.

All these experimental evidences proved the crucial role of G4 structures also in physiological processes involving several classes of RNA. Although some mechanism needs to be still clarified, their regulatory function seems to be well established and these discoveries represent a solid base to create innovative therapies, using RNA as target, against different pathologies, as cancer and neurodegenerative diseases.

1.1.2.5 G-Quadruplexes in parasites

As previously mentioned, G4s have assumed high relevance in biological context and their formation is not limited to human genome. More recently, PQS have been found also in different organisms, including bacteria, yeasts, viruses and even parasites. This last class of microorganisms attracted significant attention, because G4 can be exploited as a target against several kind of infections. For example, despite the malaria-

causing parasite *Plasmodium Falciparum* is characterized by an elevated content of AT base-pairs, bioinformatic analysis revealed the presence of several PQS in its genome, which could be involved in antigenic variation and diversification. Indeed, it has been discovered that PQS are particularly abundant in *var* gene, encoding for pfEMP1, a family of surface antigens which prevent recognition of infected cells by the immune system of the host, by continuously expressing different PfEMP1 proteins⁷⁶. Formation of G4 in this gene influences *var* gene recombination and switching, therefore it represents a novel interesting target against malaria.

PQS in *Plasmodium Falciparum* has been extensively studied, but, more recently, interesting discoveries have suggested the presence of quadruplexes in the genome of another relevant class of parasites, the *Trypanosomatides*. *Trypanosoma Brucei* and *Leishmania Major* are responsible of two severe infections, the “sleeping sickness” and “leishmaniasis”. Both are transmitted by two different insects, the “tse-tse” fly in the first case and phlebotomus fly in the second one and are responsible of thousands of deaths per year, in Africa, then development of novel therapeutic strategies is urgent. Even in this case, G4s emerged as promising therapeutic target: these parasites are characterized by the presence of telomeric regions rich in guanines, whose variability is fundamental for their survival. However, direct role of G4s in modulation of antigen expression must be still elucidated. Furthermore, it has been reported that 27 PQS have been found in pre-mRNA transcripts of *T. Brucei*, suggesting that G4 formation could influence RNA editing processes in this microorganism⁷⁷. More recently, a deep bioinformatic analysis of the genome of *Leishmania Major* and *T. Brucei* reported that most of PQS, in these parasites, are localized in telomeric sequences. However, in *T. Brucei*, a new non telomeric PQS has been identified, repeated 22 times on chromosome 9, in a gene coding for a purine nucleoside transporter (NT10), a peptidase, an adenylosuccinate lyase, and other proteins with unknown function. The rest of sequences were found on chromosome 11, on a gene encoding for an oxidoreductase. Due to the interesting localization of this new PQS, called “EBR1”, several biophysical experiments have been performed to test its ability to fold into a quadruplex structure: in potassium buffer, the sequence formed a parallel quadruplex, which was partially folded even in absence of metal cations⁷⁸. Despite these evidences, more intensive studies are required to confirm the effective biological role of this new G4s. Nevertheless, these preliminary results suggested that EBR1 could represent a new therapeutic target in the treatment of “sleeping sickness”.

1.2 G-Quadruplex ligands: molecular tools for detection and therapy

1.2.1 Small Molecules as sensors for Quadruplex Structures

As described in detail in the previous section, it appears evident that G4s play a crucial role in several physiological processes, however, despite all experimental evidences reported to date, their specific biological functions in different metabolic pathways need to be clarified. Moreover, algorithms analysis predicted the presence of 370.000 PQS in the human genome and, now, only a small fraction of them has been found and studied. Therefore, in this context, the development of new tools which can help in the identification of quadruplex forming sequences *in vitro* and, above all, in their native environment, is fundamental.

A significant contribution in this research field arrived with the development of fluorescent antibodies, characterized by high specificity for the target. In 2001, Schaffitzel *et al.* individuated selective antibodies for

Oxytricha/Styloynchia parallel telomeric quadruplex, exploiting high throughput screening⁷⁹. Competition experiments in presence of different types of nucleic acid sequences demonstrated their high specificity. In particular, **Sty3** was able to bind parallel conformation with 1000-folds selectivity compared to antiparallel one ($K_d = 126 \text{ pM}$), while **Sty49** recognized both topologies ($K_d = 3\text{-}5 \text{ nM}$). Later, Balasubramanian's group reported the discovery of a new antibody (**BG4**)⁸⁰, with high selectivity for quadruplex structures ($K_d = 0.5\text{-}1.6 \text{ nM}$). Moreover, this antibody allowed visualization of G4s in living cells, exploiting an amplified fluorescence signal, generated by treatment with a secondary and a tertiary, fluorophore-labelled, antibodies. **BG4** showed excellent selectivity and it has been possible to establish formation of G4s in different cellular regions and to determine an increase of G4s amounts during cellular replication.

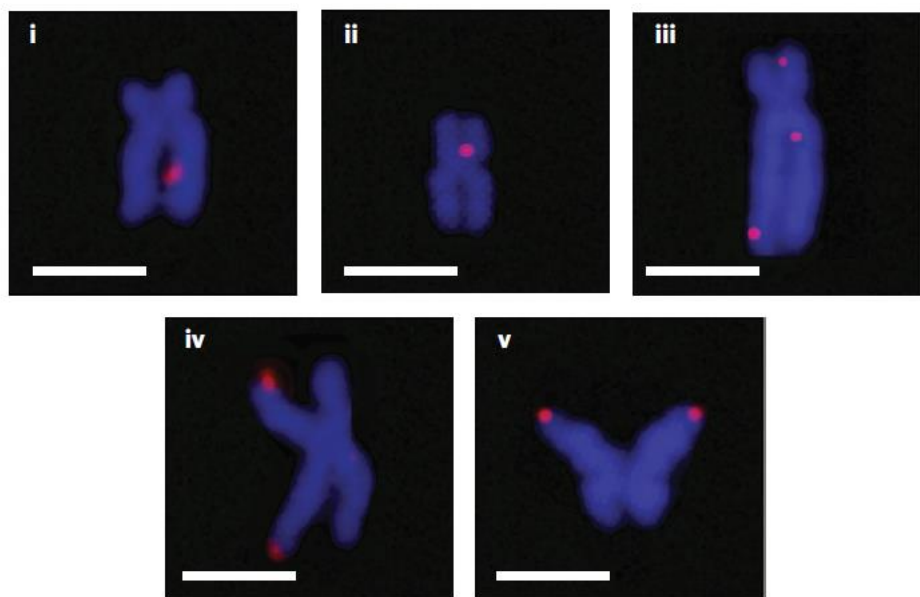


Figure 1.11 – Fluorescence signal of **BG4 on metaphase chromosomes in HeLa cancer cells⁸⁰.**

Although antibodies showed excellent performances in terms of specificity, they present several drawbacks: not only they are highly expensive, but are characterized by poor cellular permeability, they must be conjugated to an additional fluorescent probe to visualize the target and, even with this strategy, selectivity towards specific quadruplex topologies has not been achieved yet.

To overcome these limits, researchers focused their attention to the use of small-molecules as fluorescent probes to identify and investigate the physiological role of quadruplex structures. With this alternative approach, it is possible to rely on the possibility to exploit chemical synthesis to properly modify the structure of the probe, to modulate the fluorescent properties, solubility and affinity for the target.

The ideal fluorescent probe should be able to interact with the target, without altering its conformation or structure. In other words, efficient G4s probes are expected to “take a picture” of the target in its native environment. G-quadruplex structures have some specific structural elements which can be exploited for interactions with ligands, as the guanine tetrads, the loops and the grooves. In more details, three different types of binding modes can be exploited: 1) $\pi\text{-}\pi$ stacking interactions with planar guanine tetrads; 2) selective recognition of loops and grooves, for example through electrostatic interactions or hydrogen-bonds; 3) intercalation between two tetrads⁸¹. With these premises, it is not surprising that compounds able to bind quadruplex structures present some common structural features: presence of an extended, planar, aromatic surface is a necessary requirement to achieve high affinity, because it can establish strong $\pi\text{-}\pi$ stacking interactions with guanine quartet, which are even more stronger in case of an electron-poor aromatic scaffold, because, in this case, strong cation- π -interactions with negatively charged cavity of the G4 ensure

high affinity. Moreover, in order to further improve ligand performances and selectivity, the structure can be modified to achieve also binding of loops and grooves, introducing moieties for exploiting electrostatic attraction to recognize phosphate backbone or hydrogen-bonds with grooves⁸¹.

Therefore, in order to design a fluorescent probe for a G4, all these aspects must be taken into account and, at the same time, the molecules should be selected also for their spectroscopic properties, to guarantee high levels of efficiency in target visualization. Not only they must be able to discriminate the target from other nucleic acid sequences and biomolecules, but they must exhibit strong fluorescence emission under physiological conditions. Additionally, high fluorescence quantum yield is required. Moreover, signal emission must be achieved upon excitation with visible light (possibly among 600-800 nm), because excitation with radiation at lower wavelength do not penetrate efficiently cell tissues.

During the last years, a wide number of molecules have been emerged as promising fluorescent probes for G-quadruplexes and they can be distinguished in different classes on the basis of their chemical structure and on how the target affect the fluorescence reported emission⁸². In this last-mentioned case, three different classes of probes can be identified. The properties of the most recent fluorescent ligands will be reported as following.

1.2.1.1 Light-up Probes

These are compounds which are non-emissive in free solution, because of the conformation freedom guaranteed by rotation or vibration around a single bond, which cause the thermal deactivation of the emitting excited state. Upon interaction with the target, they are forced to adopt a more rigid conformation and rotation is hindered, leading to restoration of fluorescence emission. The most representative category of these kind of probes are cyanine-based dyes, characterized by two heteroaryl moieties connected through a methine or polymethine spacer.

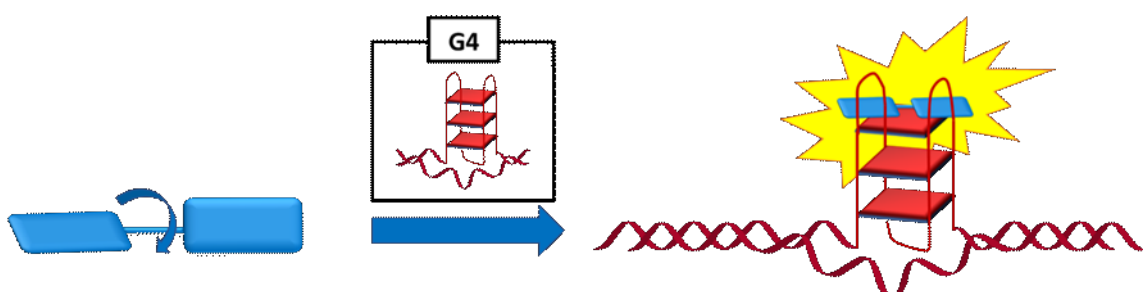


Figure 1.12 – Fluorescence “light-on” mechanism based on rigid conformation of the ligand, forced by G4.

Among them, the most commonly used are **Thiazole Orange** (TO) and **Thioflavin T** (ThT) (Figure 1.12). However, they are unable to distinguish quadruplex from other nucleic acid structures (including ds-DNA), therefore they are not suitable to this purpose⁸³. Despite such a drawback, their unique properties attracted significant attention and, in the last twenty years, researchers extensively modified their structures to both retain their fluorescent properties but, at the same time, achieve higher level of affinity and selectivity. Most common modifications include extension of conjugated system, as in case of **Dir** and **9E-PBIC** (Figure 1.13). The first one, characterized by a modified dimethylindole with anionic propylsulfonate, showed very low fluorescence quantum yield in aqueous solution ($\Phi_f = 0.7\%$) at $\lambda_{exc} = 651$ nm, which was significantly enhanced in the presence of parallel c-MYC ($\Phi_f = 49\%$). Additionally, it demonstrated good selectivity, as other

topologies marginally affected its optical properties⁸⁴. The second one, **9E-PBIC**, a carbazole-based probe, was able to recognize, as in previous case, c-MYC with high selectivity, as testified by 118-folds enhancement in emission intensity at 600 nm⁸⁵. Other chemical scaffolds have been widely employed as light-up probes: for example, several analogues of triphenylamines have been reported. Among them, the most recent example is compound **NBTE** (*Figure 1.13*), which, beside a light-up of the emission at 600 nm in presence of G4 forming sequences, exhibits an emitting excite state with a lifetime remarkably affected by different topologies of G4s. These results allowed the visualization of quadruplexes in living cells by fluorescence lifetime imaging (FLIM), discriminating G4s of different topologies from other nucleic acid sequences⁸⁶. Also other types of heterocyclic-based compounds showed excellent properties as light-up probe, including not only the previous mentioned carbazoles, but even quinazolones⁸⁷, quinoxalines⁸⁸ and quinolines⁸⁹. Very recently, an interesting example of light-up probe with a quinone-based scaffold, **QUMA-1** (*Figure 1.13*), has been reported. It allowed the visualization of the dynamic folding and unfolding of RNA G4s, in living cells¹⁵. This compound showed only weak emission, at 600 nm, in aqueous solution, that significantly increased in presence of different RNA G4s, such as TERRA, FMR1, TB1 and MT3, which forced the ligand in a more rigid conformation. In living HeLa cells, it has been measured how fluorescence intensity of **QUMA-1** foci changed with time, proving the effective formation and unwinding of G4s in physiological environment.

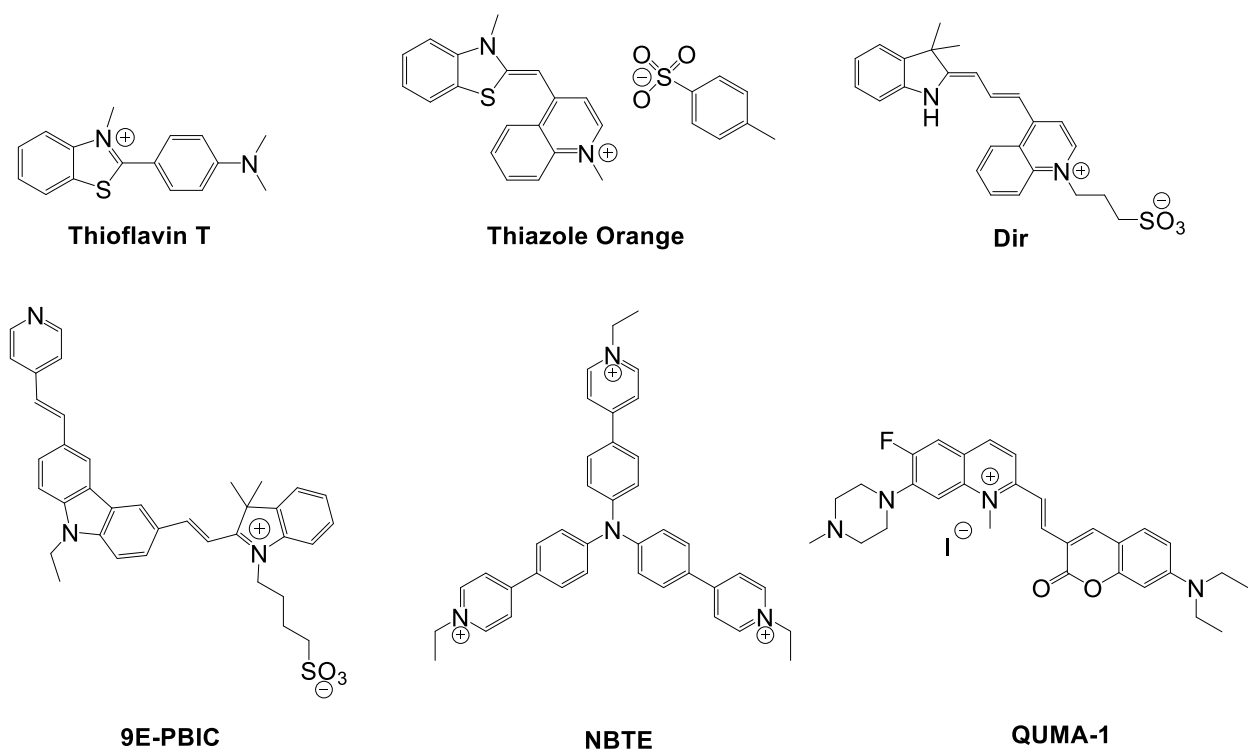


Figure 1.13 – Common examples of fluorescent “light-up” probes.

1.2.1.2 Aggregation-based probes

Many organic compounds, due to their high hydrophobic character, are non-emissive in aqueous solution, because they form different kind of aggregates. This phenomenon has significant impact on their spectroscopic properties and, in most cases, fluorescence emission is quenched as a consequence of

aggregates generation (aggregation-caused quenching, ACQ). However, in other cases, dyes unable to emit in solution, show high fluorescence intensity after aggregates formation, in a process called “aggregation-induced emission” (AIE). There are several models explaining this different behaviour, which includes the formation of a more rigid structure, excimer formation, excited state intramolecular proton transfer (ESIPT) and formation of J-aggregates, which are characterized by stacked monomers in “head-to-tail” conformation, resulting in red-shifted absorption. Alignment of monomers in “head-to-head” disposition, result in the formation of H-aggregates, characterized by fluorescence quenching. This behaviour has been explained taking into account the electronic properties of these aggregates: in particular, J-aggregates show extended surface of coherently coupled molecular transition dipoles, while H-aggregates present a “side-to-side” configuration (*Figure 1.14*)⁹⁰.

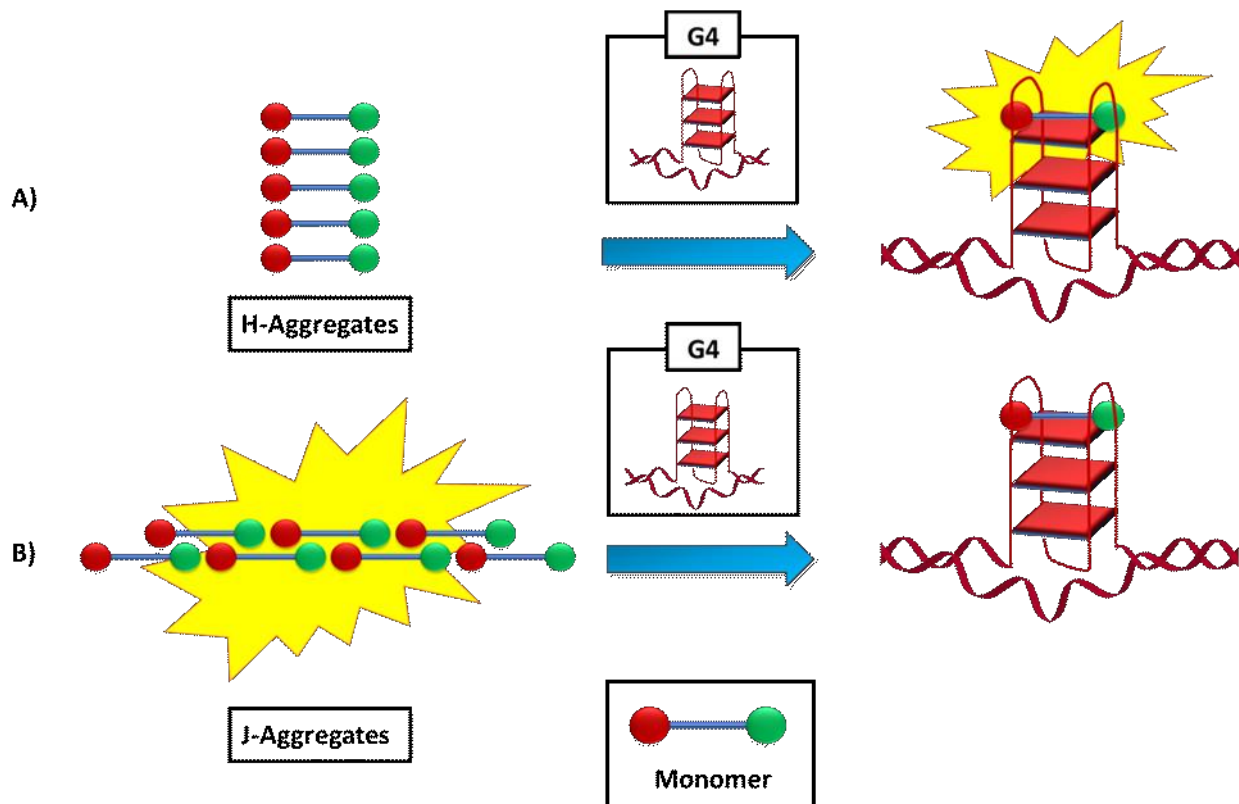


Figure 1.14 – A) Variation of fluorescent properties of H-Aggregates in presence of G4; **B)** Variation of fluorescent properties of J-aggregates in presence of G4.

Both mechanisms have been exploited to detect nucleic acid secondary structures, because interaction with the target lead to the disruption of aggregates, determining a change in fluorescent emission. Among them, H-aggregates are more used in this field: indeed, G4 binding induces a light-up, because it restores the emission of the monomer and this method is more sensitive compared to the measurement of fluorescence quenching, observed with J-aggregates.

During the last years, several types of H-aggregates, able to recognize selectively quadruplex structures, have been described. Among cyanine-based dyes, **CSTS** represents an interesting example: it presents very low fluorescence quantum yield in buffer solution ($\Phi_f = 0.01$), due to the formation of H-aggregates⁹¹. However, its spectroscopic behaviour in presence of different parallel G4s changes significantly and quantum yields increased to $\Phi_f = 0.47$, with maximum emission at 613 nm. More recently, a similar behaviour has been observed with **SQgI** (*Figure 1.15*), a squaraine-based probe with maximum emission intensity at 744 nm, that is completely quenched in aqueous solution, due to self-aggregation process⁹². This probe has been tested

with different quadruplex forming sequences, but best turned-on behaviour was achieved with parallel G4, in particular with Ceb25, that increased the quantum yield up to 0.61. Then, this probe not only displayed excellent fluorescent properties, but was also able to recognize selectively a specific quadruplex topology. Among cyanine dyes, **Dir-Trimer** (*Figure 1.15*), gave interesting results: synthesized with the aim to achieve red-shifted absorption, self-aggregates in aqueous solution and interacts with quadruplexes in its monomeric form⁹³. Upon binding with c-MYC, a significant fluorescence enhancement at 650 nm (138-folds compared to free solution) was observed, while other topologies and single and double-stranded DNA did not affect its spectroscopic properties. This compound has been tested inside HeLa cells where it has been possible to detect formation of quadruplex structure in their physiological context.

Triphenylamine derivative **TPA3PY** (*Figure 1.15*), characterized by introduction of macrocyclic amines, formed H-aggregates at low pH values⁹⁴. In presence of several quadruplex forming-sequences, this ligand showed a fluorescence light-up and red-shifted emission, from 390 to 480 nm. However, despite the good performance, was unable to distinguish among different topologies.

Then, despite remarkable progresses accomplished in this context, aggregation-based probes require further optimization to consolidate their use, because, in general, they present poor selectivity for the target and interact with different nucleic acid structures.

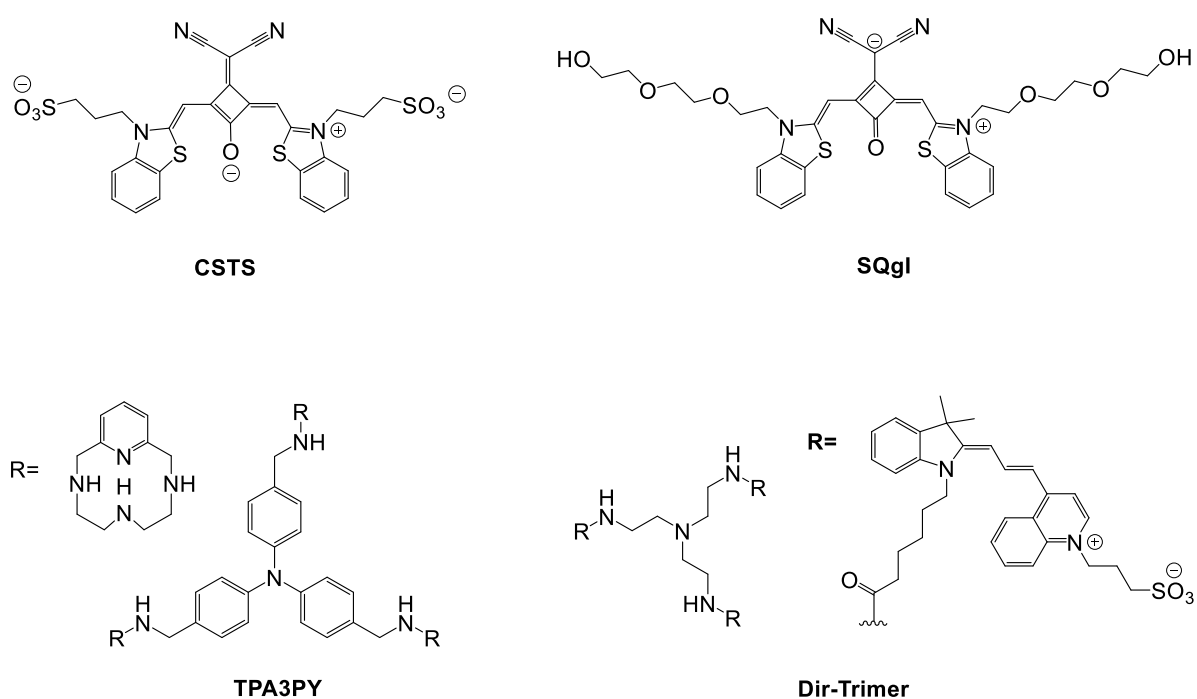


Figure 1.15 – Common aggregation-based probes for G4 structures.

1.2.1.3 Other Fluorescent Dyes

The last class of probes includes all synthesized molecules used to visualize quadruplex structures, but with a different mechanism compared to previous reported categories. In details, we can find three different types of dyes: 1) dimeric and multimeric sensors; 2) metal complexes; 3) fluorescent nucleoside analogues. The first two classes have the same purpose of “light-up” and aggregation-based probes, but, in this case, detection of the target relies on different processes. Dimeric and multimeric sensors are molecules which

can be divided into two major components, according to which is the emitting moiety: the G4 ligand, or the fluorescent reporter. Recently, the probe **IZFL-2** (*Figure 1.16*) showed an interesting mechanism of detection: it is characterized by conjugation of a coumarin moiety to a triphenylbenzimidazole⁹⁵. In buffer solution, fluorescence of this compound was completely quenched but, in this case, suppression of emission signal was attributed to intramolecular photoinduced electron-transfer (PeT) from benzimidazole to the fluorophore. In presence of c-MYC, intense fluorescence was observed: it has been suggested that interaction with the target disrupt the electronic transfer from ligand to coumarin, restoring the emission of the dye. Experiments on 30 different nucleic acid sequences also demonstrated the selectivity of this compound towards c-MYC.

Most of the described compounds are based on organic fluorescent reporters, however, several metal complexes, where the emitting moiety is the coordinated metal, have been employed as fluorescent G4 ligands. An interesting example is **MX2** (*Figure 1.16*), a ruthenium-based complex, coordinated by bipyridines whose aromatic surface has been extended with phenazine, to avoid intercalation into double strand DNA⁹⁶. Fluorescence emission of this derivative was measured in presence of telomeric G4, in both K⁺ and Na⁺ solution and a significant fluorescence enhancement (45-folds) at 600 nm was observed, demonstrating its efficiency to detect quadruplex structure. More recently, the good affinity of the iridium(III)-phenanthroline complex [Ir(phen)₂(2,9-dmphen)]PF₆ (*Figure 1.16*), for G4s have been exploited to develop an aptamer for the detection of prostate specific antigen (PSA), a common marker for the diagnosis of prostate cancer⁹⁷. The aptamer was composed by a sequence able to recognize PSA and a G-rich region, potentially able to fold into G4, but locked by the complementary strand. Upon PSA recognition, G-rich sequence is free and can assemble into a quadruplex, which can be recognized by the metal complex. The dye showed maximum emission a 595 nm, that remarkably increased in presence of various quadruplex forming sequences, including Pu27, C-KIT2 and c-KIT87.

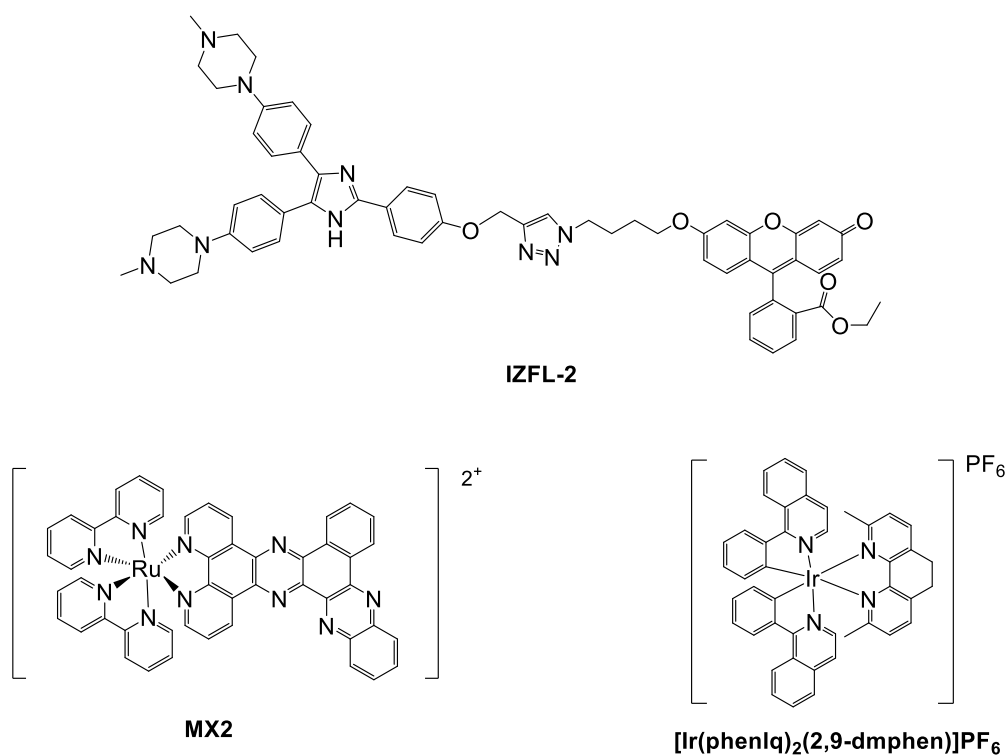


Figure 1.16 – Examples of other common fluorescent dyes for G4s.

The last class of fluorescent probes differs from all previous described because they have been designed for a different purpose: indeed, several fluorescent nucleoside analogues have been developed not to detect quadruplex structure in physiological environment, but to investigate, *in vitro*, quadruplex formation (for example, in case of still unknown G4s) and to elucidate their structure. In this scenario, the most remarkable example is represented by 2-amino purine **2-AP** (*Figure 1.17*), extensively used to study G4 conformation. When incorporated into a quadruplex forming sequence, its fluorescence quantum yield increases significantly, up to 0.68, and this effect is much more pronounced compared to incorporation in double strand DNA. Moreover, its emission intensity was strictly dependent on its position in the sequence, interaction with the cation and stacking with other bases. Therefore, **2-AP** have been employed to study how the bases interact with the cation and their influence on the topology⁹⁸. During the last years, several additional nucleosides analogues have been designed, in order to improve the optical properties, as 8-(2-pyridyl)-2'-deoxyguanosine **2PyG** (*Figure 1.17*) and 8-vinyl-2-deoxyguanosine **VdG**. Among most recent examples, 5-(benzofuran-2-yl)uracil **2X** definitely deserves to be mentioned, as it can be considered a “dual-app” probe, characterized by a fluorophore sensitive to microenvironment and the presence of ¹⁹F⁹⁹. The nucleoside has been incorporated into the loop of telomeric quadruplex, to both investigate its conformation in solution and its potential interactions with new ligands. The incorporated nucleoside showed marked emission at 437 ($\Phi_f = 0.11$), that increased upon quadruplex formation (6-11 folds) with antiparallel topology. Authors associated this variation to reduced stacking interactions among the fluorophore and nucleobases and to an electron-transfer process between the dye and guanine residues. Through addition of G4 ligands, fluorescence was quenched. The measurement of signal decrease is a valid method to determine the binding affinity of added ligand. Another recent “dual-app” probe is **s^edU** (*Figure 1.17*), a uridine derivative containing a selenophene, useful as dispersing agent to perform X-Ray analysis. This compound showed emission at 452 nm and $\Phi_f = 0.012$, in water and, once introduced into telomeric sequence, showed significant increase of emission intensity upon quadruplex formation¹⁰⁰. Selenium was subsequently exploited to perform X-Ray analysis and distinguish the different topologies, confirming its potential use as dual-app probe.

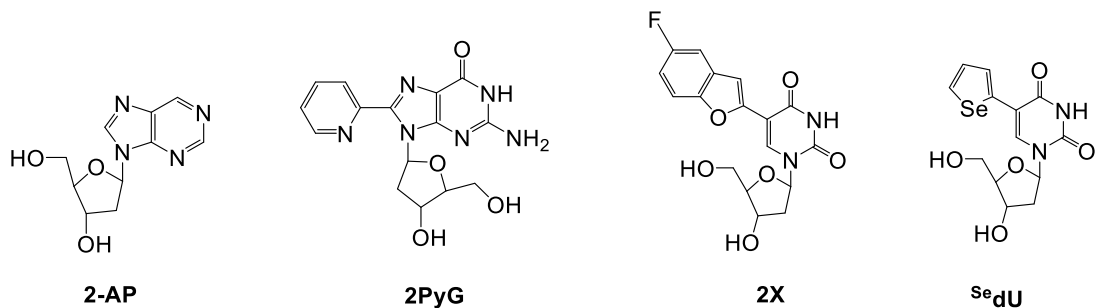


Figure 1.17 – Examples of modified, fluorescent nucleosides used as probes for G4s.

1.2.2 G-Quadruplex Ligands and their therapeutic effects

Small molecules have not only been investigated as G4s sensors, to verify their formation in physiological context, but also as potential drugs. Due to the relevant biological role attributed G4 structures, extensively described in paragraph 1.1.2 , in the last twenty years, an intense “gold-rush” began, to identify novel small-molecules with specific therapeutic effect (in particular against cancer and neurodegenerative diseases), exploiting G4s as a target. In this scenario, several accomplishments have been achieved. In fact, extensive

studies led to the synthesis of hundreds of new molecular entities showing both excellent binding properties towards specific G4s and promising biological effects. Rationalization of the results collected in twenty years of research has been a long and not straightforward process, however, it has been possible to define chemical scaffolds showing remarkable therapeutic effects. Herein, a brief description of principal classes of promising G4s binders is provided, accompanied by the most significant examples. Based on their structural features, quadruplex ligands can be divided in four major classes: macrocycles, fused aromatic rings, modular ligands and metal complexes⁸¹.

1.2.2.1 Macrocyclic Ligands

Macrocyclic ligands are one of the first chemical scaffolds that have been explored: indeed, their extended, flat, surface can establish strong interactions with guanine quartet. Several types of macrocyclic derivatives have been reported, however, most representative are based on Telomestatin derivatives, Porphyrins and phenanthroline-based ligands. Among them, Telomestatin (*Figure 1.18*) represents the most significant example: it is a natural product, extracted from *Streptomyces anulatus* 3533-SV4, constituted by neutral polycyclic structure, with five oxazoles, two methyloxazoles and one thiazoline ring and an overall size that ensure precise overlap with guanine tetrads¹⁰¹. Telomestatin was able not only to bind telomeric quadruplex with high selectivity, compared to duplex DNA, but also to trigger apoptosis in cells, acting as telomerase inhibitor. Despite these excellent results, its low solubility in water and the difficult scale-up synthesis, strongly limited its application. Several porphyrins derivatives have been synthesized in order to improve water solubility and maintain binding and biological properties. In this context, the most studied compound is **TMPyP4** (*Figure 1.18*), that showed good affinity for telomeric quadruplex and not only inhibited telomerase, but downregulated the expression of several oncogenes, including c-MYC, KRAS, RET and c-KIT¹⁰². The major drawback of this ligand was its poor selectivity for G4s compared to double and single-stranded DNA. However, despite this limit, **TMPyP4** is widely employed as a reference to study the affinity of novel ligands with G4s and, in the last years, several modifications of the scaffold have been attained. Interesting results have been achieved also with phenanthroline-based ligand **BOQ1** (*Figure 1.18*), able to selectively recognize GC base-pairs, that showed excellent affinity for telomeric quadruplex and, subsequently, efficient telomerase inhibition¹⁰³.

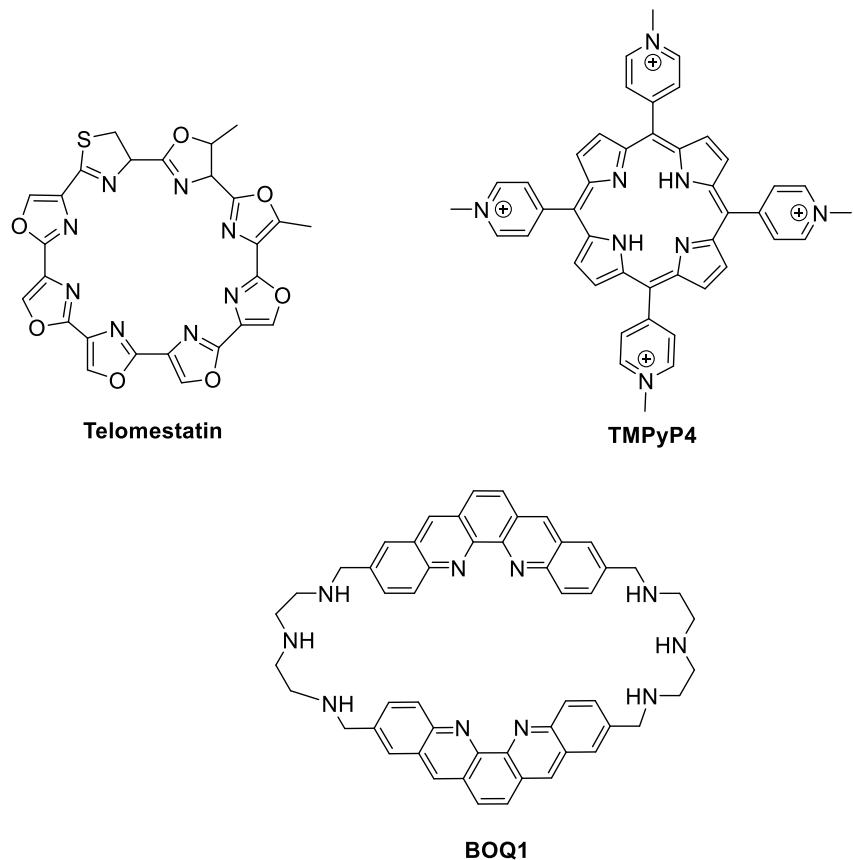


Figure 1.18 – Examples of macrocyclic G4 ligands.

1.2.2.2. Fused Polycyclic Aromatic Ligands

Among the different classes of quadruplex ligands, extended aromatic systems have extensively employed, several types of scaffold have been designed and optimized to further improve their performances. Their principal advantage is given by their extended aromatic system, that guarantee strong π - π interactions with guanine tetrads, which can be properly modified, for example introducing functional groups to increase solubility or interactions with grooves and loops of the quadruplex. To date, the number of this kind of ligands is noteworthy, however, some principal scaffolds can be individuated: 1) acridine derivatives, 2) quindolines, 3) quinazolones, 4) phenanthrolines, 5) naphthalendiimides and perylendiimides (Figure 1.19).

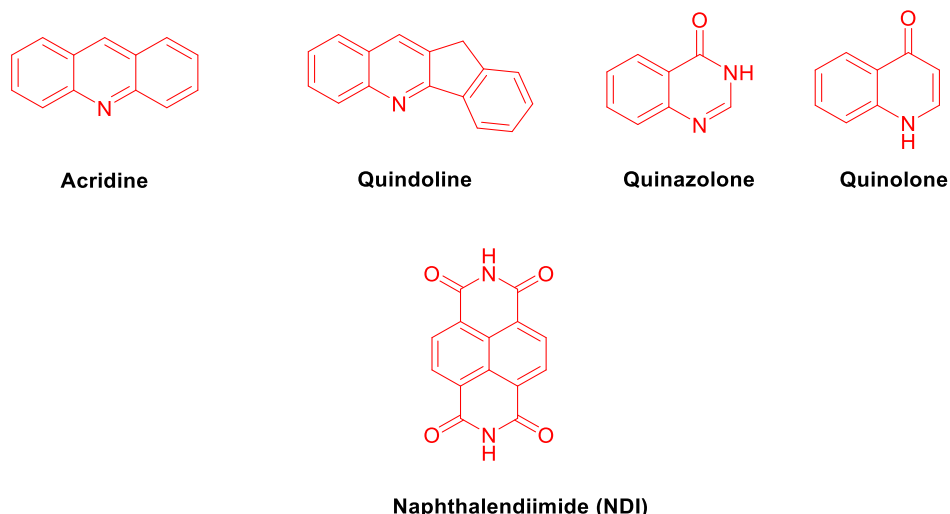


Figure 1.19 – Most significative examples of fused-polycyclic aromatic scaffolds used to synthesize G4 ligands.

Acridines are characterized by three-fused six membered rings, which have been extensively modified with alkyl chains to increase solubility and affinity for the target. In general, 3,6,9-acridines showed higher selectivity for G4 compared to other regiosomers, as testified by **BRACO-19** (Figure 1.20), with excellent affinity for telomeric quadruplex ($K_a = 1.6 \times 10^7 \text{ M}^{-1}$) and efficient telomerase inhibition. However, the most representative example of this class is the ligand **RHSP4** (Figure 1.20), a quinoacridinium salt, with excellent selectivity for the target and for cancer cells (compared to normal ones): its promising activity as anticancer agent has been further demonstrated by its ability to induce DNA damages, at telomeres level, and apoptosis in tumor cells¹⁰⁴. Quindolines are constituted of a quinoline fused to a benzimidazole or a benzofuran and, in this class, **SYUIQ-5** (Figure 1.20) emerged for its good telomeric G4 stabilization and moderate inhibition of telomerase¹⁰⁵. Later, its structure was subsequently modified, for example through methylation of nitrogen atom of quinoline, to introduce a permanent positive charge, that could both improve affinity for the target and stacking interaction with the tetrad. G4s ligands based on quinazolone scaffold are mostly derivatives of Isaindigotone, a natural alkaloid. Among them, the recent case of **RGB1** (Figure 1.20) is particularly significative, because its biological activity relies on the selective interaction with RNA G4s. Treatment of human breast cancer cells MCF-7 with this ligand decreased the expression of the proto-oncogene NRAS, due to the binding of G4 formed in 5'-UTR region of NRAS mRNA¹⁰⁶. Even quinolones led to significant progress in the development of anticancer therapies based on quadruplex ligands: **CX-3543** (Figure 1.20), also commonly known as Quarfloxin, showed potent anticancer effect, because of the binding of ribosomal DNA, preventing its interaction with nucleolin, a nucleolar protein involved in pre-tRNA transcription and ribosome assembly. More recently, it has been demonstrated that another quinolone derivative, **CX-5461**, interacts with C-MYC, c-KIT and hTEL0 and displays high cytotoxicity against BRCA1/2 deficient cells¹⁰⁷. The last-mentioned class of fused polycyclic ligands is represented by naphtalendiimides (**NDIs**), characterized by a unique structure, with planar and electron-poor aromatic core, which ensures high affinity for guanine tetrads and has been exploited to design several bioactive ligands. Naphthalendiimides have been extensively studied in our research group and this thesis also focused on the development of novel NDIs as photoresponsive ligands, therefore, their structure and properties will be discussed more deeply in the following paragraph (1.2.3).

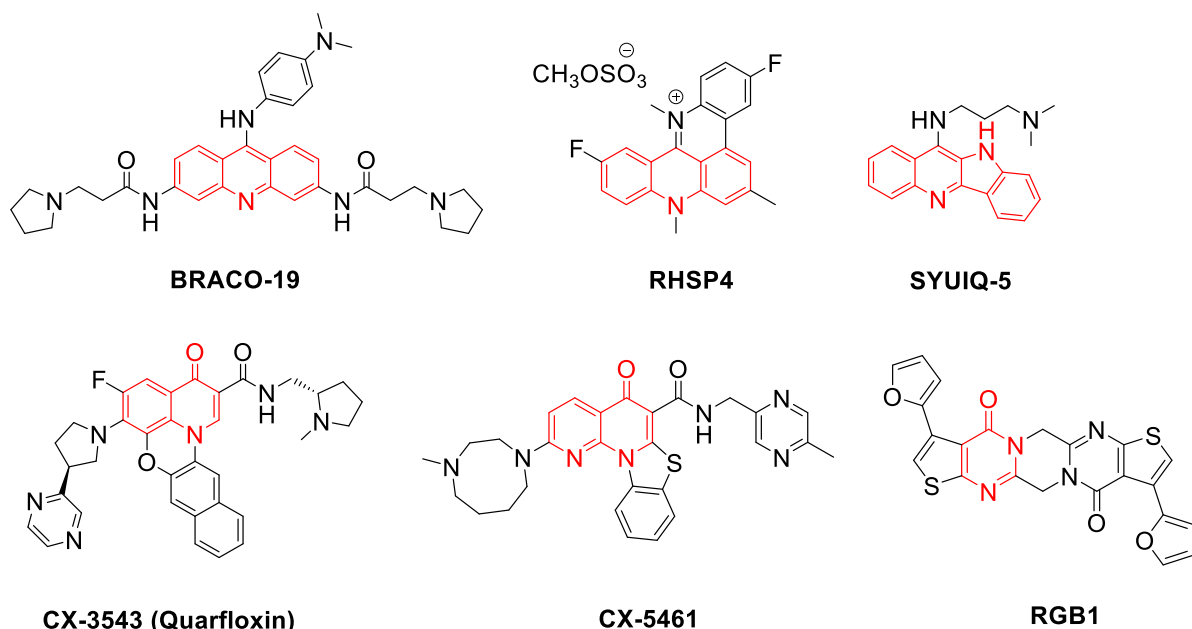


Figure 1.20 – Examples of most efficient fused polycyclic aromatic ligands.

1.2.2.3 Modular G-Quadruplex Ligands

Modular G-quadruplex ligands differ from previous described classes because they have a limited aromatic surface: indeed, they are divided in, at least, two aromatic modules, composed by two fused rings, connected by spacers of different length and nature. In this way, the ability to interact with guanine quartets through π - π stacking interactions is retained, but the structure is more flexible, disfavouring off-target binding. For the development of this class of ligands, several types of covalently connections have been exploited: 1) carbon-carbon bonds, 2) carboxyamides and 3) olefin connections⁸¹. In case of carbon-carbon connection, the most common employed strategy implies the connection of a central core, usually a phenyl or a pyridine ring, to other two aromatic moieties, in 1,3 positions, because experimental results evidenced that this substitution pattern was more effective for quadruplex binding. This kind of structure guarantees rotational freedom, which can be exploited to establish interactions with grooves and loops. Recently, it has been reported that acyclic polyheteroaryl compounds, alternating pyridine and oxazole units, showed remarkable affinity for different quadruplex structures. In particular, the ligand **Iso-TOxabiPy** (Figure 1.21) emerged for its selectivity towards quadruplex c-MYC ($K_a = 16 \times 10^6 \text{ M}^{-1}$) compared to duplex DNA ($K_a = 3 \times 10^6 \text{ M}^{-1}$)¹⁰⁸. Moreover, this compound presented high cytotoxicity against different cancer cell lines, with more pronounced effect on HeLa cells ($\text{IC}_{50} = 134 \pm 30 \text{ nM}$), suggesting its possible use as anticancer agent. The fact that a fused polycyclic system is not mandatory to achieve elevated affinity has been demonstrated also by **IZCZ-3** (Figure 1.21), a tri-substituted imidazole that showed very high selectivity for c-MYC ($K_d = 0.5 \mu\text{M}$)¹⁰⁹. Because of this promising behaviour, further experiments were performed to test its anticancer activity. Obtained results showed significant toxicity against different cancer cell lines, higher on HeLa cells ($\text{IC}_{50} = 2.1 \mu\text{M}$). Moreover, it has been demonstrated that **IZCZ-3** was able to selectively downregulate c-MYC expression, with no effects on other oncogenes. Finally, treatment with this compound induced apoptosis in SiHa cells and inhibited tumor cell growth, demonstrating its remarkable efficiency. The second category of modular ligands are based on the presence of amide as function group, which offers

several advantages, as elevated stability in physiological context, rigid geometry and hydrogen bond donor and acceptor sites. The efficiency of this sub-types of ligands is well represented by *N,N'*-(bisquinoline)pyridine-2,6-carboxiamides ligands. In this case, the binding affinity can be attributed to the formation of strong hydrogen bonds between -NH- group of amide, the nitrogen atom on pyridine and a molecule of water, that locks the molecule in a rigid conformation, able to interact with guanine tetrad. The most famous example is the **Pyridostatine PDS** (*Figure 1.21*), a ligand with unprecedented affinity for telomeric quadruplex and that, upon interaction with the target, activate the DNA-damage response machinery, inducing cell cycle arrest and apoptosis¹¹⁰.

Olefin-based connection has been extensively exploited, as described in the previous section (**1.2.1.1**) to develop fluorescent sensors, in particular on cyanine derivatives and is responsible of the modulable optical properties of these dyes. Recently, photoinduced isomerization of stiff-stilbene ligands **1** (*Figure 1.21*) has been exploited to modulate quadruplex folding or unfolding¹¹¹.

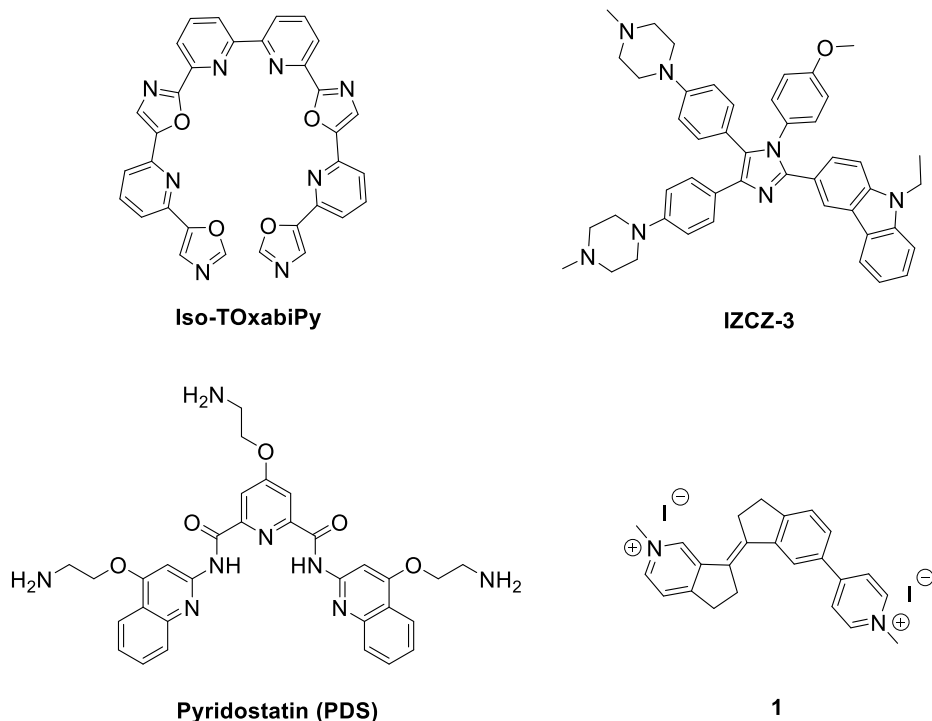


Figure 1.21 – Examples of common modular quadruplex ligands.

1.2.2.4 Metal Complexes

As in the case of fluorescent probes, several types of metal complexes have been designed as G4 ligands for therapeutic applications. After preliminary optimization of their binding properties and cytotoxicity, they have received increased attention during the last years. Due to their particular structures, different binding modes can be observed with these ligands: the metal can coordinates the four guanine residues or, as an alternative, the organic ligands interact with the tetrad, the grooves or the loops⁸¹. To build the complexes, different metals have been employed but, in general, the most used are copper, zinc, nickel, manganese, gold, ruthenium and platinum. Some of these ligands are derivatives of **TMPyP4**, with Zn(II), Cu(II) or Pt(II), as metal centre. However, in most cases, this approach led to lower affinity and poor selectivity, compared

to the original ligand. Recently, it has been reported that compound **Mn(III)-37** (*Figure 1.22*), obtained through modification of **TMPyP4** with four cationic chains, presented an elevated affinity towards G4 compared to duplex DNA (1000 folds higher), accompanied by efficient inhibition of telomerase ($IC_{50} = 580$ nM)¹¹². More recently, also phthalocyanines found consistent application in this context, as both fluorescent probe and therapeutic agents. In particular, a Zn(II) phthalocyanine with tetracationic thiopyridinium arm showed high specificity for G4 structures and interesting anticancer activity¹¹³. The mentioned examples regarded complexes with a macrocyclic structure, which favour the formation of stacking interactions with guanine tetrads. However, in the last few years, also non-macrocyclic complexes have showed interesting results. For example, **Pt(II)-47** (*Figure 1.22*) presented marked selectivity for telomeric quadruplex, c-MYC and BCL2, probably thanks to the presence of hydroxyl group in 6-hydroxyloxoisoaporphine¹¹⁴. Moreover, this complex had higher toxicity on tumor cells, compared to normal ones, and was able to significantly inhibit cancer cells growth, similarly to the common anticancer agent cisplatin.

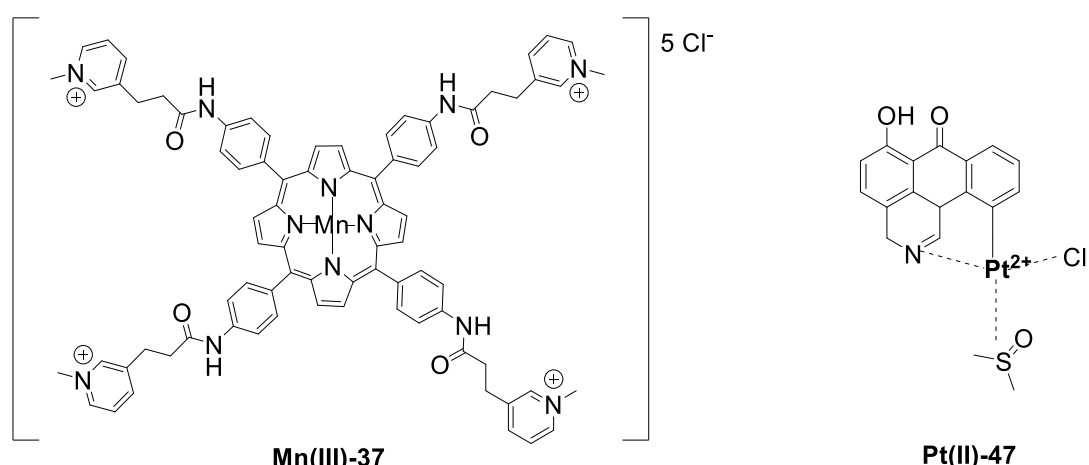
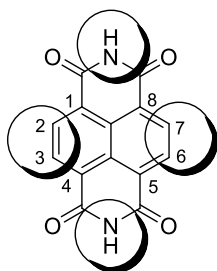


Figure 1.22 – Two recent examples of G4 ligands based on metal complexes.

1.3 Dual-role ligands: the Naphthalenediimides (NDIs) case

Naphthalenediimides (NDIs) or, more precisely, 1,4,5,8-naphthalenediimides (*Figure 1.23*) are organic compounds composed of a naphthalene core, functionalized with two electron-withdrawing imidic groups. The synthesis of these derivatives is straightforward as it can be accomplished in a couple of reaction steps, starting from 1,4,5,8-naphthalenetetracarboxylic dianhydride NDA (*Figure 1.23*). Due to their excellent optical and electrochemical properties, they have been widely employed in organic, biomolecular, optoelectronic and supramolecular science¹¹⁵. Their versatility can be attributed to their unique structural features, which includes a planar surface that can be easily modified, using different types of substituents on aromatic core or on two imidic positions. Moreover, their properties are strictly dependent on the nature of the functional groups and chemical scaffolds introduced and can be easily modulated.

1,4,5,8-Naphthalenediimide (NDI)



○ = Functionalization Site

Figure 1.23 – 1,4,5,8-Naphthalenediimide (NDI) and its principal functionalization sites.

The possibility to induce colour changes and variations of redox properties by simply varying the substituents is their most appealing feature. Presence of electron-withdrawing imides is responsible of low electronic density, generated by a strong π -polarization of the system, and substitution in this position doesn't influence the optical and electrochemical properties of the compound. On the contrary, introduction of electron-donating (ED) heteroatoms on the aromatic core strictly modulate the colour of the substrate: the contemporary presence of electron-rich groups with withdrawing imides creates a push-pull chromophore. The nature of the substituent bound to aromatic core tunes the HOMO-LUMO band gap of the compound, which increases with more electron-rich groups (*Figure 1.24*). Replacement of heteroatom, directly bound to the aromatic core, is sufficient to induce a marked colour-shift of the NDI¹¹⁶.

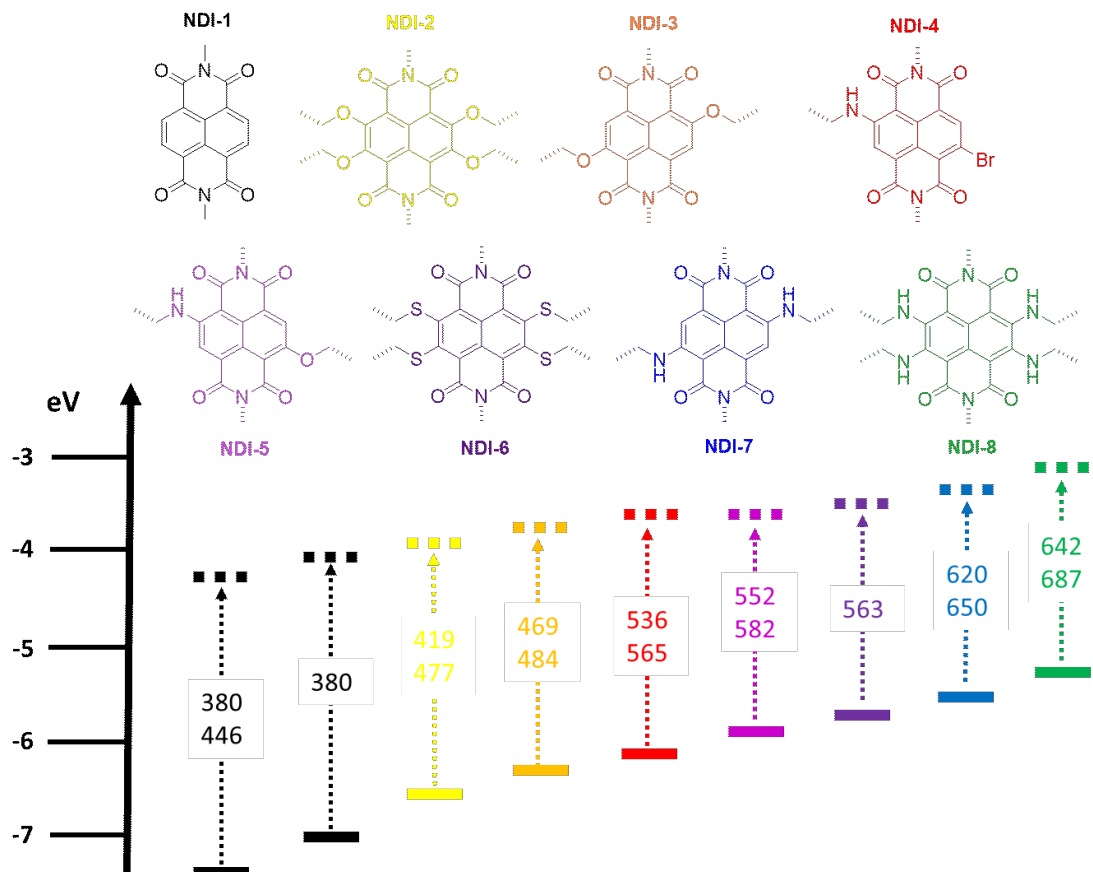
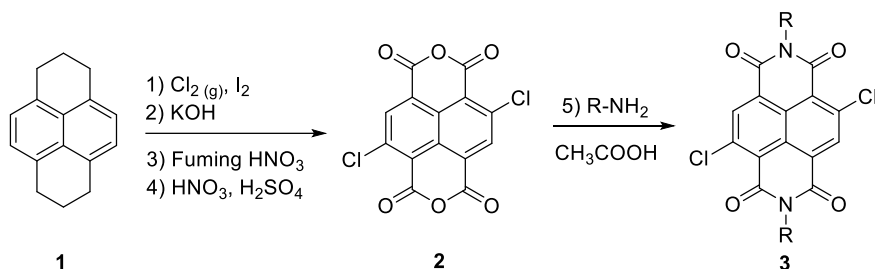


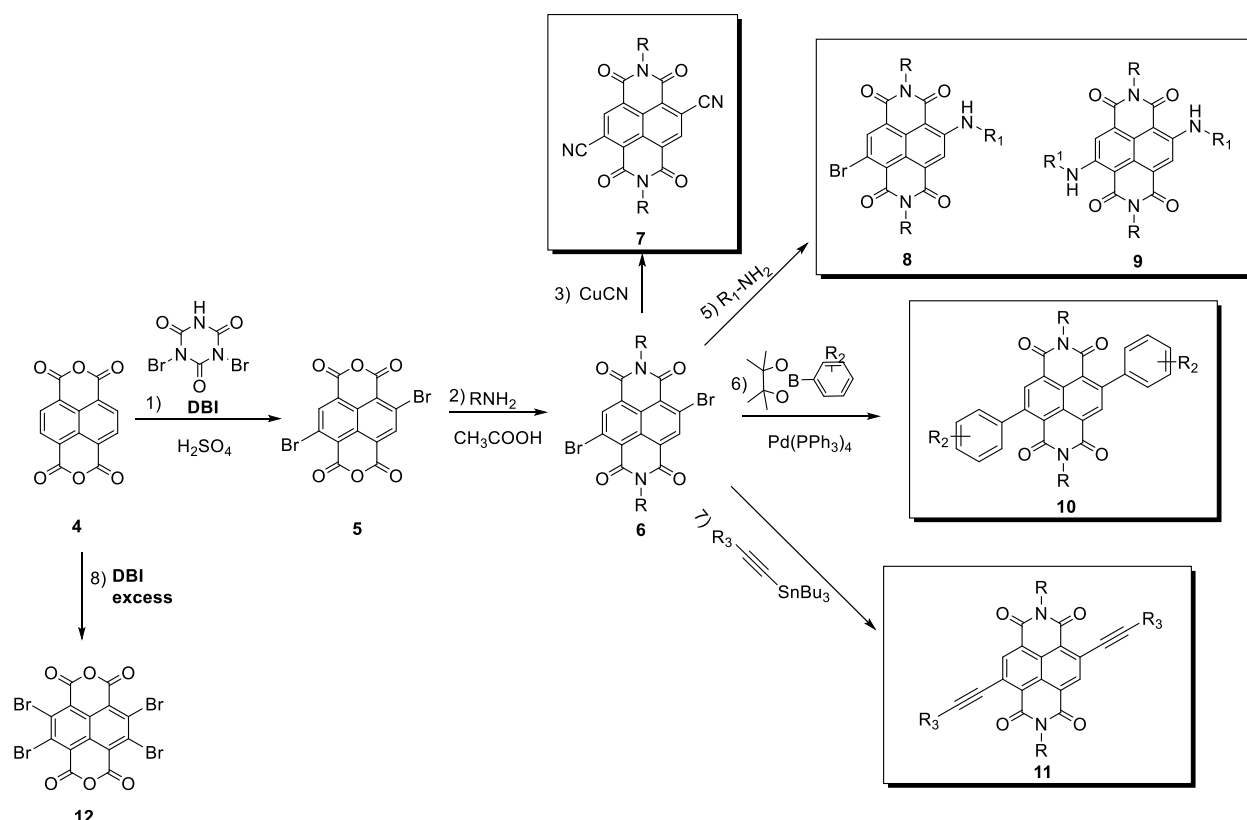
Figure 1.24 – Effects of electron-rich substituents, introduced on NDI aromatic core, on HOMO-LUMO band gap¹¹⁶.

Because of their unique properties, NDIs attracted considerable attention in the last years and several protocols have been optimized to produce a large number of derivatives. In general, synthesis of NDI starts with the oxidation of pyrene and the desired product is obtained with four reaction steps which involve the use of strong acids, strong bases and chlorine gas, to generate the dianhydride **2** (*Scheme 1.1*), which can be transformed in the corresponding NDI through reaction with amines in acetic acid, to avoid substitution on aromatic core. The obtained NDI **3** can undergo a wide number of nucleophilic aromatic substitutions, with amines, alcohols, thiols, cyanides, to produce huge libraries of different derivatives.



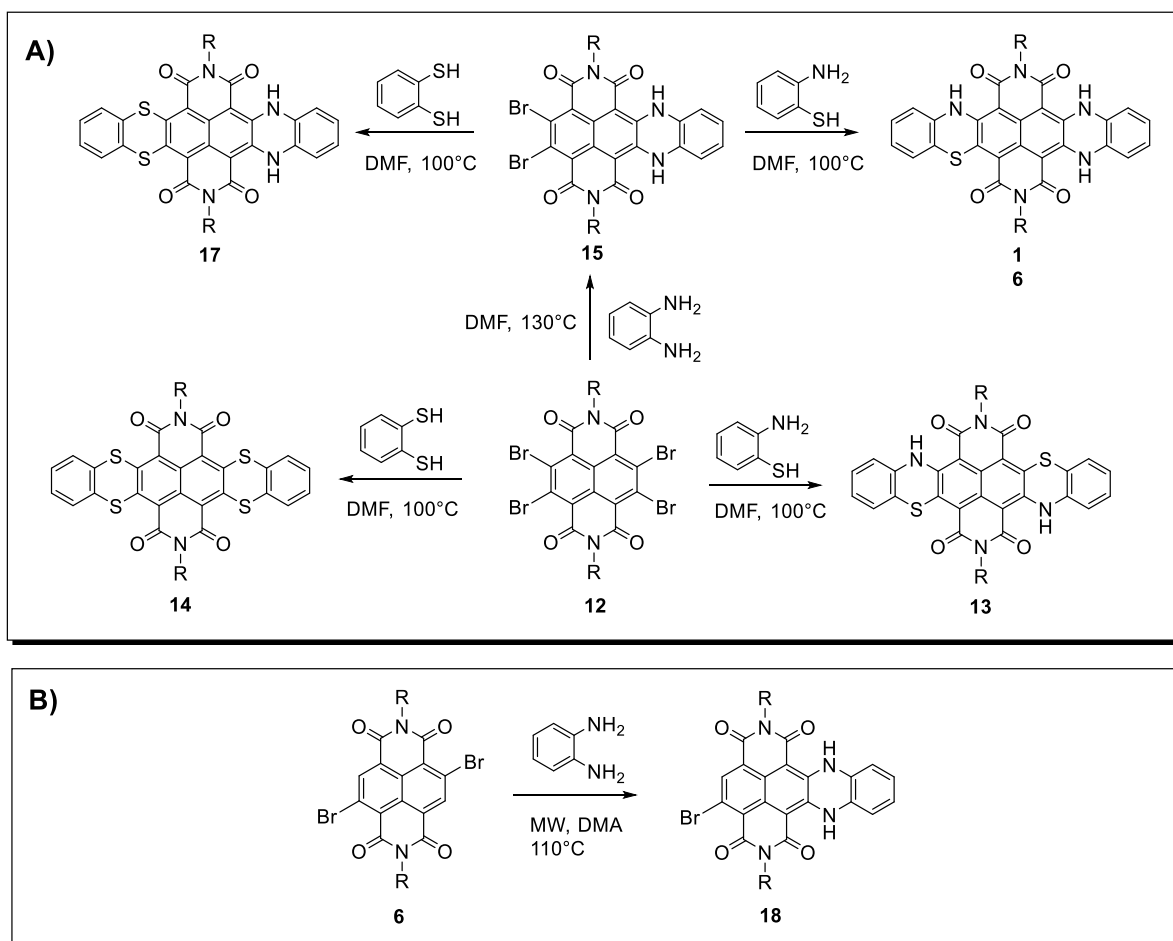
Scheme 1.1 – Synthesis of NDIs.

However, due to the harsh conditions required, the described synthetic pathway is rarely used and, as an alternative, a protocol starting from commercially available anhydride **4** is preferred¹¹⁷: this substrate is treated with dibromoiso-cyanuric acid **DBI**, to generate a mixture of products containing **5**, that, in presence of the preferred amine, lead to the corresponding NDI **6** (*Scheme 1.2*). This last compound is very versatile, because not only can react with previous mentioned nucleophiles, but can be used also for several types of cross-coupling, including Suzuki-Miyaura and Stille reactions, affording a vast plethora of NDI derivatives¹¹⁸. The synthesis of tetra-substituted NDIs is also feasible through tetrabromo dianhydride **12**, prepared with a large excess of brominating reagent¹¹⁹, followed by the same reaction steps applied in the previous case.



Scheme 1.2 – Synthetic routes to different core-substituted NDIs.

The use of compound **6** as key intermediate is a consolidated strategy, exploited by several research groups and, more recently, the same scaffold has been largely exploited to synthesize other types of derivatives, 2,3,6,7-substituted NDIs, characterized by the extension of the aromatic core. Compounds **6** and **12** can undergo through simple condensation reaction with several aromatic nucleophiles, including ortho-phenylenediamine, 1,2-benzenedithiol and 2-aminothiophenol (*Scheme 1.3*) to afford different NDI heterocyclic acene diimides, with an extended aromatic core (**CexNDIs**)¹²⁰. Upon treatment of **12** with 1,2-benzendithiol, in DMF and in presence of potassium carbonate, the corresponding symmetrical acene diimide is produced with almost quantitative yield. The same behaviour has not been observed in presence of ortho-phenylenediamine that, even with longer reaction times, afford only the unsymmetrical NDI **15** (*Scheme 1.3-A*). However, this undesired result led to the development of a large number of hydroazacene derivatives, characterized by red-NIR absorption and with interesting aggregation properties¹²¹. These last mentioned scaffolds can be easily obtained also from substrate **6** (*Scheme 1.3-B*) and an alternative synthetic protocol indicates that the reaction can be performed also under microwave irradiation, at 110°C, for 15 minutes, using dimethylacetamide as solvent. This procedure has been largely used by Freccero's group to synthesize a class of novel quadruplexes ligands. To provide even higher structural diversity, also different metal-catalyzed cross-coupling reactions have been optimized to further extend the aromatic core of NDIs and achieve always more complex structures, which have been found applications in material field, especially in the realization of semiconductors¹¹⁵.



Scheme 1.3 – Common synthetic routes to CexNDIs starting from compound **12 (A) and **6** (B).**

The most appealing feature of NDIs is represented by the possibility to modulate their optoelectronic properties by simply introducing small modifications of the overall structure. Their UV-VIS spectra is characterized by a characteristic band around 380 nm, originated by $\pi-\pi^*$ transition, which is not influenced by core substitution. Their colour can be attributed to the generation of a charge-transfer band (CT band), which depends on the entity of the push-pull character of the system, after the introduction of substituents on the core. Increasing the electronic density on the aromatic system, HOMO and LUMO orbitals increase their energy and the bandgap is reduced (*Figure 1.24*). Bandgap is higher with alkoxy derivatives and decreases with sulfides, reaching minimum values with amines. Tetramine **NDI-8** (*Figure 1.24*), for example, presented absorption band at 629 and 642 nm. Most of these compounds are non-fluorescent, especially the ones carrying primary amino groups, however, recently several NDIs derivatives, including **CexNDIs**, with remarkable emission, have been discovered, further expanding their fields of application.

In fact, NDIs have been employed also in medicinal chemistry and to design innovative G-Quadruplex ligands. Because of their bright colours and the recent discovered fluorescent emission of some specific scaffolds, it is reasonable to think at them as efficient G4 sensors. Because of their planar aromatic system, ideal to establish $\pi-\pi$ interactions, the possibility to act as donor or acceptor of hydrogen bonds (depending on the type of susbsituents introduced) and the presence of π -acidic aromatic system, some of these derivatives presented high affinity for several quadruplex sequences, resulting also in interesting biological activities, suggesting their potential use even as therapeutic agents.

The first example of NDIs employed as G4 ligands have been reported by Neidle's group, in 2009: they synthesized compound **19** (*Figure 1.25*), carrying four pyrrolidine moieties. Its binding properties towards telomeric quadruplex, c-KIT1 and c-KIT2 were compared to reference ligands, **TMPyP4** and **BRACO-19**, and, from FRET-Melting assay, $\Delta T_m = 29^\circ\text{C}$ at 1 μM concentration, was measured with c-KIT2. This value was higher in comparison to reference ligands, proving the excellent affinity of this new scaffold. Moreover, NDI **19** was able to selectively bind the G4 even in presence of duplex DNA. Subsequent biological studies evidenced that **19** could have a dual functional properties, acting on both telomerase enzyme and on the expression of c-KIT gene, involved in the progression of human gastrointestinal stromal tumor¹⁰². Later, in order to drive the selectivity of the substrate towards telomeric quadruplex, novel ligands have been synthesized, characterized by four piperazine moieties, separated from aromatic core of NDIs by alkyl chains of different lengths (3,4 and 5 carbon-atoms)¹²². The choice of a tetrasubstituted naphthalenediimides was not random: presence of four charged piperazines, with spacers of proper lengths, are exploited to establish strong interactions with four grooves and, in particular, with phosphate groups. These compounds showed similar performances, but **20** (*Figure 1.25*) emerged for its high affinity for telomeric quadruplex F21T (with ΔT_m above 23°C) and interesting biological activity: not only high toxicity against a panel of different cell lines but also able to interfere with the binding of fundamental proteins at telomere level and to suppress telomerase activity, with pronounced effect already at 50 nM. Subsequently, the same group investigated the effect of NDIs substituents on G4 binding and selectivity, replacing the piperazine moieties of compound **20** with different types of tertiary amines, including morpholine derivatives¹²³. From these studies emerged that all NDIs showed good affinity and selectivity towards telomeric G4, but the NDIs bearing a 2-morpholinopropylamine presented better performance. Biological studies confirmed these preliminary results and, on the same derivatives, very low IC_{50} values (below 0.6 μM) were measured against different cancer cell lines. Interestingly, these compounds did not show telomerase inhibition, that is in contrast with previous results. However, it has been suggested that anticancer activity of these substrates could arise from other mechanisms: for example, the most efficient NDI **21** (*Figure 1.25*) up-regulated several genes encoding for markers of cellular stress and inhibited the expression of PARP, an enzyme responsible of the repair of DNA strand breaks. The last finding was particularly interesting because several PARP inhibitors are currently in clinical trials for the treatment of different kind of tumours. The success of morpholine derivatives reported

in this work can be explained by the reduced basicity of morpholine, compared to other aliphatic tertiary amines, which prevent its protonation in physiological environment, reducing off-target interactions.

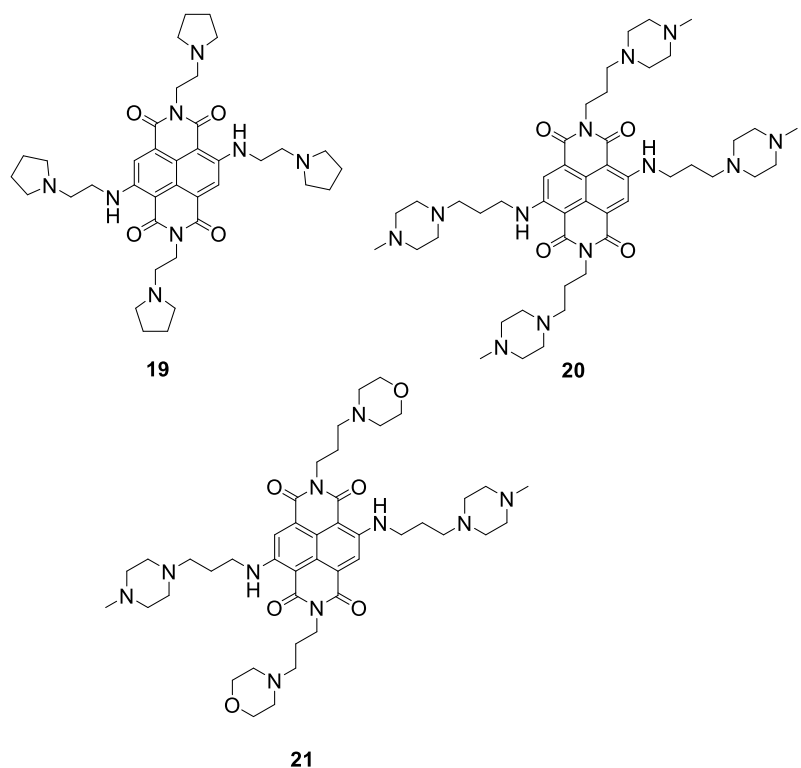


Figure 1.25 – NDIs-based G4 ligands reported by Neidle's group.

NDIs-based G4 ligands have been extensively investigated also by Freccero's group, whose research work led to the identification of molecules with both interesting biological activity and remarkable sensing properties. In 2015, the group reported a library of **CexNDIs** that showed significant antiviral activity against HIV¹²⁴: in particular, compound **22** (Figure 1.26) was characterized by elevated affinity and selectivity for LTR-III quadruplex, even in presence of other G4s and duplex DNA. Moreover, the same ligand displayed high toxicity towards infected cells, which decreased in normal ones (Selectivity Index = 17), representing a solid base for the development of novel anti-HIV drugs.

Conjugation of two distinct NDIs is another strategy that led to novel functional properties. In 2019, the same group synthesized a library of NDIs dimers and investigated both optical and biological properties¹²⁵. Briefly, from this study, compound **23** (Figure 1.26), characterized by two NDIs by a seven-carbon atoms chain, emerged for its noteworthy selectivity towards telomeric quadruplex F21T. Interestingly, its fluorescence emission was modulated by interaction with the target: in free solution, the ligand presented low fluorescence quantum yield ($\Phi_f = 0.002$) that increased in presence of the target ($\Phi_f = 0.044$). Biological studies demonstrated the high toxicity of **23** against different lines of tumor cells ($IC_{50} < 162$ nM), which was reduced in case of normal cells. Furthermore, it was demonstrated that this compound was able to induce DNA-aggregation upon interaction with telomeric sequence, supporting its potential anticancer activity. Concerning the telomeric quadruplex, another ligand, **24** (Figure 1.26), displayed remarkable selectivity towards this specific target, compared to duplex DNA¹²⁶. Its behaviour was particularly interesting because, from ITC and fluorescence analysis, two distinct binding events were detected (with $K_{a1} = 1.6 \times 10^7$ M⁻¹ and K_{a2}

$= 3.3 \times 10^5 \text{ M}^{-1}$). Docking studies suggested that these data could be the result of the interaction of **24** with two adjacent G4s, making this ligand suitable to target more complex structures, as multimeric quadruplexes. The same group engineered several NDIs scaffolds to realize efficient G4 sensors: the dimer **23** (*Figure 1.26*), described previously, was initially designed as a probe. This compound displayed maximum of absorbance at 642 nm and was characterized by low fluorescence quantum yield in solution ($\Phi_f = 0.001$)¹²⁷. The binding affinity was tested against different quadruplex forming sequences and, upon interaction with the targets, significant fluorescence enhancement was measured (40-folds). However, the main disadvantage of this probe was the inability to discriminate among different G4s. Another attempt to build a light-up probe was represented by compound **25** (*Figure 1.26*), obtained through conjugation of NDI to another fluorophore, the coumarin, with a seven-carbon atoms spacer, to realize a novel dye with “push-pull” character¹²⁸. Design of this ligand was based on the idea that, in solution, two fluorophores are free to interact, leading to fluorescence quenching, while the presence of the target disrupt this interaction, restoring the emission. Naphthalendiimide showed absorption in UV region (with maximum at 342 and 360 nm) and in visible one ($\lambda_{\text{max}} = 620 \text{ nm}$), while coumarin presented a maximum peak at 420 nm. The ligand behaviour was analyzed with different G4s and double and single-stranded DNA. Upon excitation at 452 nm, a new emission band centered between 659-666 nm appeared increasing oligonucleotides concentration. The highest light-up has been measured in presence of c-KIT1, indicating a stronger affinity for this particular target (34-folds enhancement, with $K_a = 6.9 \pm 0.2 \times 10^6 \text{ M}^{-1}$), while negligible effect was observed in presence of duplex DNA. In addition to these light-up probes, the group developed even different **CexNDIs** as aggregation-based dyes: substrate **26** (*Figure 1.26*) formed aggregates in aqueous solution and no fluorescence emission¹²⁹. Its spectroscopic behaviour was investigated in presence of three antiparallel (HRAS, HTELL22 in Na^+ and TBA), one hybrid (HTEL22 in K^+), three parallel (c-KIT1, c-KIT2 and c-MYC) G4s and ssDNA and dsDNA. The highest emission enhancement was recorded with telomeric HTEL22 in K^+ solution ($\Phi_f=24\%$, while for **26** in free solution was $\Phi_f=8\%$). Once that interaction with quadruplex was further confirmed through CD analysis and TAQ Polymerase Assay, probe **26** was used to detect G4 in fixed cells, through confocal microscopy. To further improve the specificity of this type of probe, a novel derivative, **27** (*Figure 1.26*), characterized by polyethylene glycol chains, was synthesized¹³⁰. As the previous mentioned ligand, **27** formed aggregates in water solution and displayed low fluorescence quantum yield ($\Phi_f=0.0051 \pm 0.0006$). Its affinity for different quadruplex forming sequences was explored through FRET-melting assay and, despite it showed low affinity for most of the targets, it was highly selective towards G4s compared to duplex DNA. Moreover, in presence of increasing concentration of parallel quadruplexes, its fluorescence emission significantly increased (250 folds, with $\Phi_f=0.09 \pm 0.005$), while other topologies and duplex and single-stranded DNA slightly affected its emission.

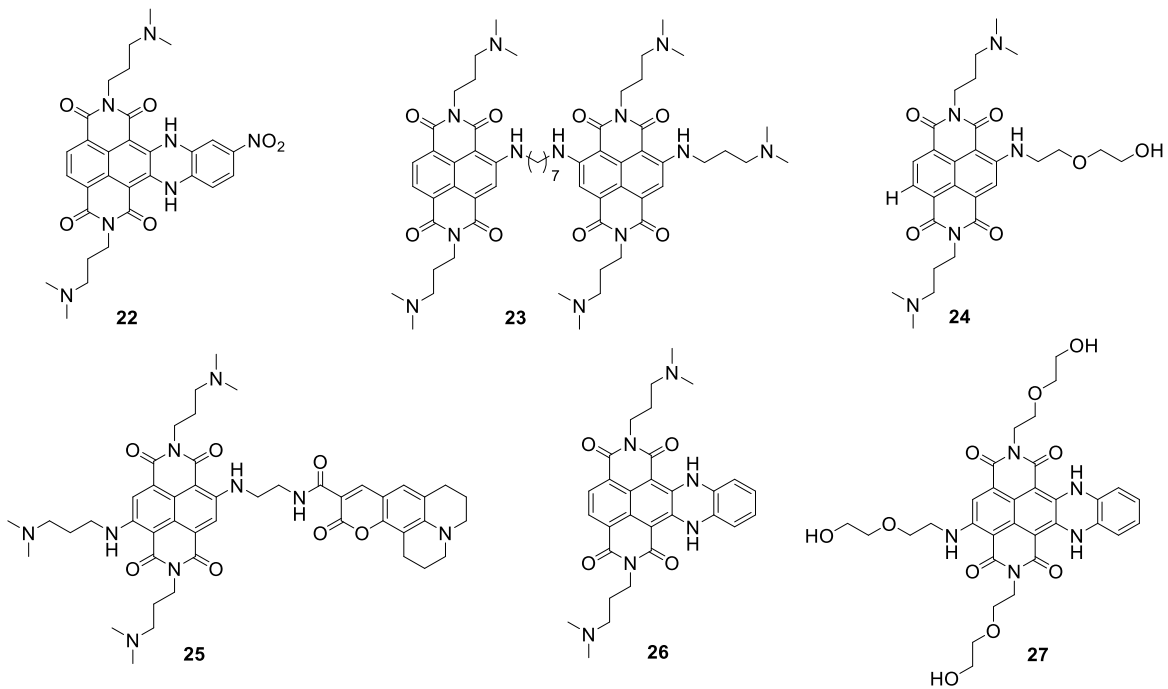


Figure 1.26 – NDIs-based ligands synthesized by Freccero’s group.

1.4 Towards alternative targeting strategies: photo-activable ligands

Quadruplex ligands listed above are non-reactive molecules whose affinity for the target is based on non-covalent reversible interactions, which can be easily disrupted. Although remarkable progresses have been accomplished in this research field, nowadays the low specificity of “classic” G4 ligands still represent a non-negligible issue, which affects both sensors and ligands with potential therapeutic effect. Indeed, in a complex physiological environment, even compounds with highest binding constant, display off-target interactions, resulting in non-specific sensing and undesired side-effects.

To achieve a temporal control of the binding properties in complex contexts, several *stimuli-responsive ligands* are emerging for their applications, based on G4 additional stabilization, DNA-DNA and DNA-proteins crosslinking. The idea that different ligand properties, such as binding affinity, fluorescence and cross-linking, can be easily modulated by a proper “trigger” is particularly appealing.

To reach this goal, several types of stimuli can be exploited, such as redox processes, pH, enzymatic reactions and photochemical activation. In this scenario, light represents one of the most attractive choice. Light-mediated reactions are well consolidated transformations that found applications in different research fields, from organic synthesis to medicinal chemistry, with the recent advent of photo-pharmacology¹³¹. This relatively new research field relies on the design of novel drugs, whose activity can be modulated by light, reducing collateral effects, because activation of the ligand or inhibitor is strictly localized¹³². Indeed, the main advantage of using light is the precise spatiotemporal control of the whole process, in a non-invasive way.

In the last years, photo-activable molecules, in particular azobenzene derivatives¹³³ or compound containing moieties, as alkenes that, upon irradiation, can isomerize or generate a different structure, found application, for example, as regulators of membrane channels, enzyme inhibitors and tubulin binders¹³².

Despite the increasing interest in the development of photo-activable bioactive molecules, a limited number of examples are reported on nucleic acids and, even less on G4 structures. However, recently, different research groups designed and developed novel photo-triggered ligands, to enhance efficacy and specificity towards NA targets.

In this context, light-sensitive molecules designed to target quadruplex forming sequences can be distinguished into two classes, despite the low number of examples: 1) **photo-activable ligands based on non-covalent interactions** and 2) **photo-activable ligands that establish covalent interactions with the target**.

The first class of compounds has been used for different purposes, from the development of pro-drugs to the synthesis of binders that change their affinity for the target upon irradiation. One of the first interesting example has been reported by Balasubramanian's group, that designed a so-called "photocaged" quadruplex ligand, in order to enhance the selectivity of the previous described ligand, **PDS**, for diseased tissues¹³⁴. In fact, introducing a photolabile moiety, that can be removed under photoirradiation, the ligand can be selectively released only in the selected area, limiting its potential toxic effect. To this aim, PDS has been covalently conjugated to 4,5-dimethoxy-2-nitrobenzyl bromide, to obtain compound **28** (Figure 1.27). Binding properties of this substrate have been analyzed on different G4s, including SRC (a gene involved in proliferation of malignant cells), c-MYC and telomeric G4. It has been demonstrated that, in dark condition, the photocaged ligand displays no affinity for selected oligonucleotides. Upon irradiation, the affinity increased significantly, proving the release of the ligand worked properly. Subsequently, it has been observed that irradiation of MRC5-SV40, incubated with 2 µM of ligand, resulted in downregulation of the expression of c-MYC, SRC and RET genes, with more pronounced effect on SRC, whose mRNA levels decreased up to 80% after 30 minutes of irradiation. These results demonstrated the efficiency of this approach, which represents a solid starting point to make new photocaged quadruplex ligands, that can be activated only in presence of the desired target.

More recently, other example of photo-activable ligands have been reported, such as stiff stilbene ligand **1** (Figure 1.27) which has been used to photo-induce the folding and unfolding of a quadruplex structure. In details, the molecule, characterized by the presence of a double bond, isomerizes under irradiation and the two isomers present different affinity for the same telomeric sequence: in particular, *E* isomer showed stronger interactions with the target. Irradiation experiments, monitored through Circular Dichroism (CD) analysis, confirmed that **1** can act as a "fuel", inducing a conformational change of the topology, which was completely reversible. This interesting work evidenced that photo-responsive ligands could be used to regulate quadruplex folding or unfolding even in their native environment, to selectively interfere with specific biological processes or understand they physiological role.

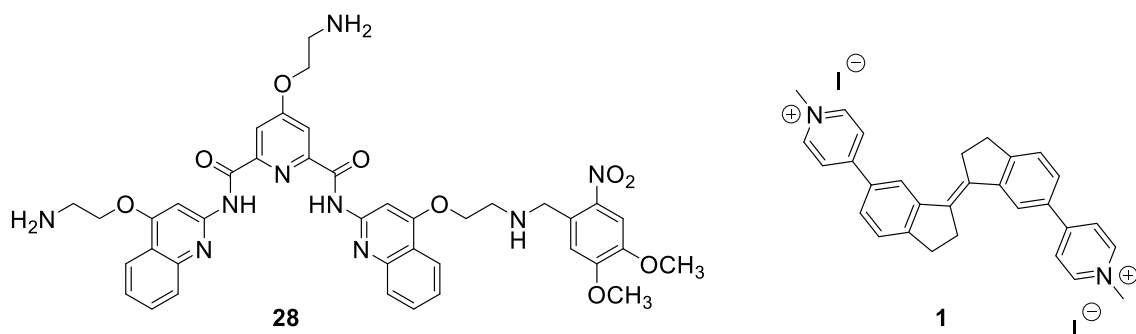


Figure 1.27 – Examples of reversible photo-activable G4 ligands.

More recently, the same authors reported another compound characterized by the presence of pyridinium modified with dithienylethene, **30** (Figure 1.28) that, under irradiation at 450 nm, generate the corresponding cyclic derivative **30c** (Figure 1.28), which can return to the original state upon excitation at 635 nm¹³⁵. It has been observed that, in presence of telomeric quadruplex in potassium solution (hybrid topology), the cyclic isomer **30c** showed high affinity, due to stacking interactions with guanine tetrad. On the contrary, open conformation resulted in disruption of the structure, probably due to a possible intercalative mode. Then, two ligands showed similar affinities, but induced significant variation of the G4 structure. Moreover, cytotoxicity analysis evidenced lower toxicity for compound **30c** ($IC_{50} = 23 \mu M$), compared to open conformation ($IC_{50} = 10 \mu M$). The possibility to modulate not only the binding mode to the target, but also toxicity, suggested future application of these compound as photo-triggerable prodrugs.

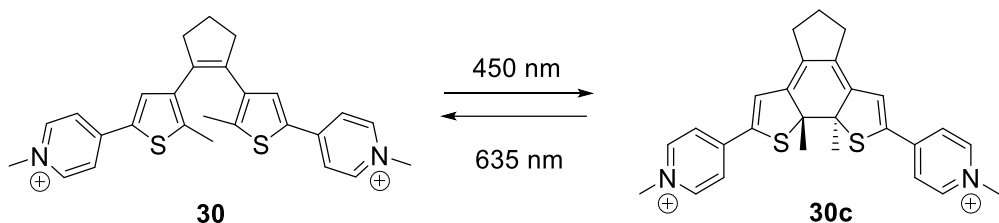


Figure 1.28 – Photo-induced ring-closure on compound **30.**

As an alternative to classic non-covalent ligands, several photo-activatable ligands, able to establish covalent interactions with the target, have been reported. The advantage of this second approach is that both the ligand and the target result covalently tethered, further stabilising the G4 folding. This damage may result into important biological effects, which could not be easily repairable by the DNA repairing systems. Covalent modification is a concept that has been widely employed with enzymes. Covalent inhibitors known as mechanism based inhibitors (MBIs), consist of a “warhead”, a molecule with high affinity for the catalytic site of the enzyme and a reactive moiety able to form the covalent bond with a functional group present in the site of interest¹³⁶. During the last years, several example of enzyme covalent inhibitors have been reported, for protein kinases, caspases, EGFR, RAS family and Acetylcholinesterase. The same concept could be translated to design novel G4 ligands, however, covalent targeting of specific nucleic acid sequences has been much less explored. However, already known-quadruplex ligands have been modified with photoreactive units, in order to achieve the formation of a covalent bond with nucleobases of the target.

For example, piridodicarboxyamide (**PDC**) have been modified with two different photo-reactive moieties, benzophenone and 4-azido-2,3,5,6-tetrafluorobenzoic acid, separated by spacers of different length and nature, to achieve selective alkylation of G4s. Both these moieties, upon irradiation in UVA region, can generate reactive intermediate that can ultimately generate G4 covalent binding. Benzophenone, from its excited triplet state, can react through [2+2] cycloaddition with alkenes to generate an oxetane or, as an alternative, can extract hydrogen from accessible donors, creating a new covalent bond with alkyl radical¹³⁷. Conversely, aromatic azides can evolve into nitrenes, which can give addition reaction to double bond, insertion into C-H and N-H bonds. These photo-reactive units were introduced on the central pyridine ring because experimental results evidenced that modification in this position do not alter **PDC** binding properties. The obtained ligands have been analyzed with two sequences, the telomeric quadruplex and c-MYC, and irradiated at 360 nm. All compounds were able to form covalent adducts, as tested by gel-electrophoresis analysis, however compound **31** (Figure 1.29) showed the highest alkylation efficiency, that was marginally affected by the presence of duplex DNA. Moreover, sequencing methods have been applied to individuate alkylation sites and, for **31**, only two sites were found, in the thymine-loop of telomeric 22AG, supporting the stacking interaction of the ligand with external quartets. Interestingly, in presence of c-MYC,

low or negligible alkylation was observed, showing the specificity of this approach. In the end, biological MTT assay pointed out that toxicity of the ligand towards cancer cells MCF-7 and A459 was marked only upon irradiation, suggesting that possible toxic effects were due to G4 alkylation. In the context of photo-induced G4 alkylation, Freccero's group contributed significantly: to mention the most recent example, the group reported the development of a naphthalenediimide conjugated to a Mannich base: the ligand **32** (*Figure 1.29*) upon irradiation at 532 nm, generate a reactive phenoxy radical capable of thymine covalent targeting¹³⁸. Indeed, it has been demonstrated that, upon irradiation, selective alkylation of G4s was accomplished, with incredibly high efficiency (64%), with low effect on duplex and single-stranded DNA.

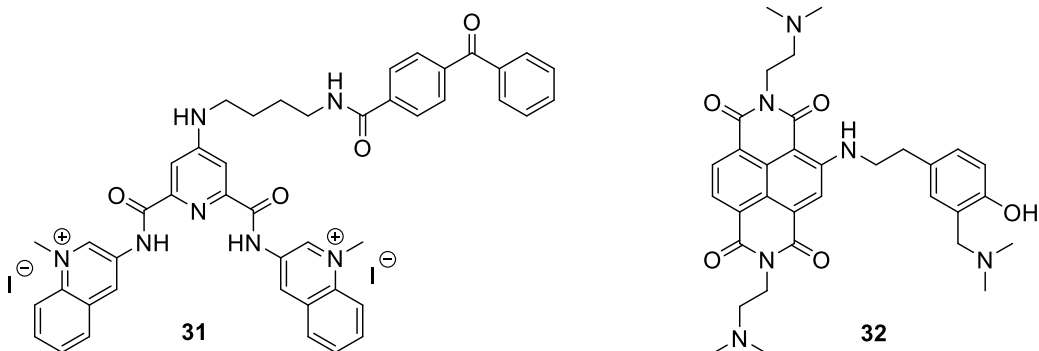


Figure 1.29 – Examples of photo-activable ligands that form covalent bond with G4.

1.5 Innovative Photo-activation Strategies

Potential advantages of using light-activable ligands attracted the attention of an increasing number of scientists, however well-suited photochemical processes for the development of quadruplex ligands are still limited. Identification of innovative photoreactive units, with biocompatible reactivity, easily modulable properties and versatile structures represents the rate-determining step in this research area.

In this scenario, this thesis has been focused on the development of innovative, light-responsive quadruplex ligands, with the attempt to optimize both their specificity for the target and the photochemical properties. To this aim, we concentrated our efforts on two types of photogenerated reactive intermediate, Quinone Methides (QMs) and Nitrile Imines (NI), whose properties will be briefly discussed in the next paragraph.

1.5.1 Quinone Methides (QMs)

Quinone Methides (QMs) (*Figure 1.30*) represent an interesting class of electrophiles, which have been employed for several types of applications, in organic synthesis¹³⁹ and in medicinal chemistry, for bioconjugation reactions¹⁴⁰ and as cross-linking agents¹⁴¹, thanks to their versatile nature. From a structural point of view, they are quinone analogues, in which a methylene group is replaced by a carbonyl function. We can distinguish ortho-quinones (o-QM) and para-quinone methides (p-QM) (*Figure 1.30*). In particular, o-QMs can undergo through different reaction pathways: they can react with different types of nucleophiles

(including water, amines, alcohols, thiols)¹⁴² or be involved in hetero Diels-Alder with electron-rich dienophiles¹⁴³. The reactivity of generated o-QMs resembles that of α, β -unsaturated ketones, however they are much more electrophilic, because of the high charge separation character of the resonance form, further stabilized by aromatic conjugation.

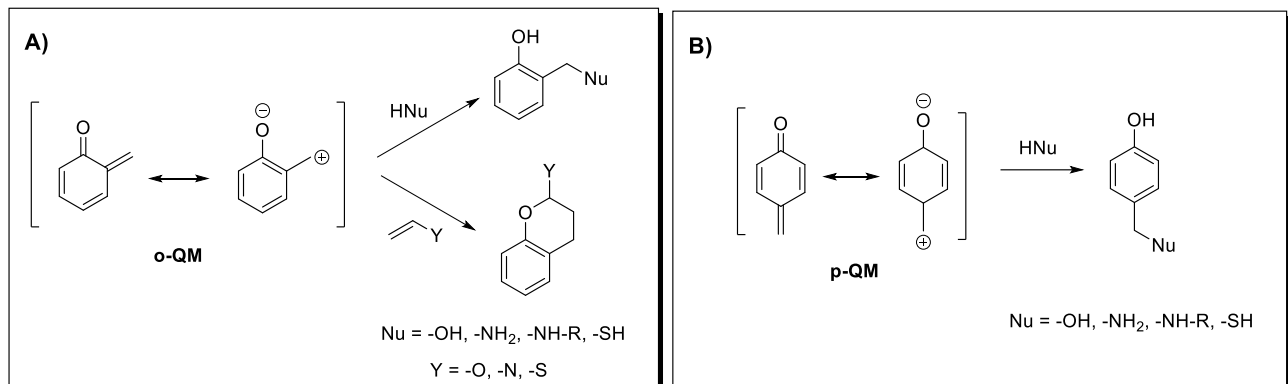


Figure 1.30 – Common reaction pathways with nucleophiles and dienophiles for A) o-QM and B) p-QM.

Furthermore, the specific case of o-QM is particularly interesting, not only for their high versatility, but also because they display interesting biological activity, as proved by the potent antitumor agents Mitomycin C and anthracycline. o-QMs can be generated exploiting different activation processes: oxidation of phenols, dehydration from hydroxybenzylalcohols, elimination of nitriles from 1,2-benzoxazines, use of strong bases and acids and fluoride-mediated desilylation¹⁴⁴. All these methods rely on the use of harsh reaction conditions or, in alternative, require other reagents or catalysts, therefore, among the available protocols, photochemical generation represents the most interesting alternative. Light-mediated generation of QMs can be achieved with different types of substrates, through acid elimination, hydration or tautomerization of phenols or naphthols¹⁴⁵, photohydration of alkenes¹⁴⁶ and deamination of Mannich salt¹⁴⁷.

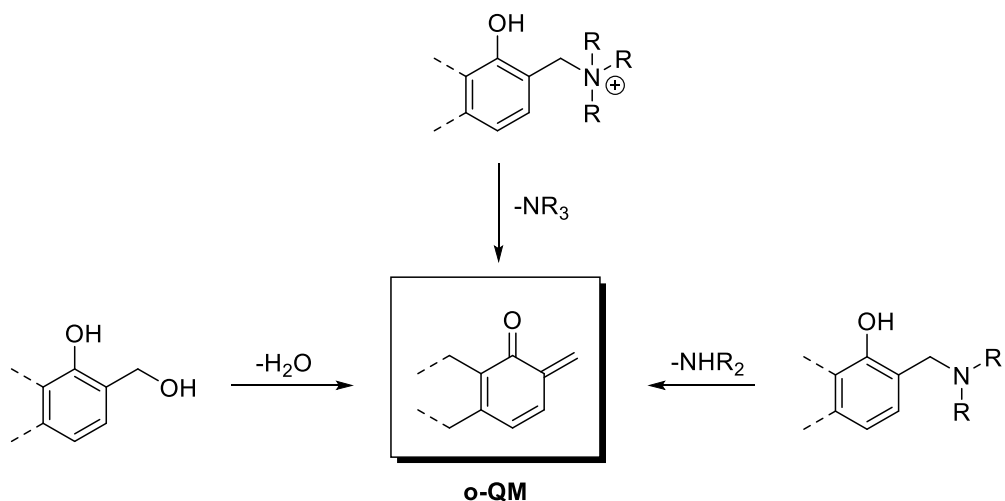


Figure 1.31 – Photogeneration of o-QM from different aromatic phenols.

The generation is triggered by the acidity of phenols and naphthols in the first singlet excited state, followed by intramolecular proton transfer (ESIPT), which causes the transfer of phenolic proton to oxygen atom at the benzylic position. Further experimental evidences of this kind of mechanisms has been obtained by different studies on aminomethyl p-Cresol derivatives: it has been established that QM generation efficiency is a function of the pH which affect the protonation of amine and it is favoured when the Mannich base is protonated or in its zwitterionic form¹⁴⁷. As an alternative, it has been suggested that also solvent could play

a crucial role in the generation of QM, acting as proton-acceptor (ESPT mechanism) and favouring the expulsion of the leaving group¹⁴⁸. The C-L bond heterolysis (*Figure 1.31*) can occur in a concerted step, but femto second laser flash photolysis studies pointed out that the expulsion of the living group occurs after the proton transfer¹⁴⁹.

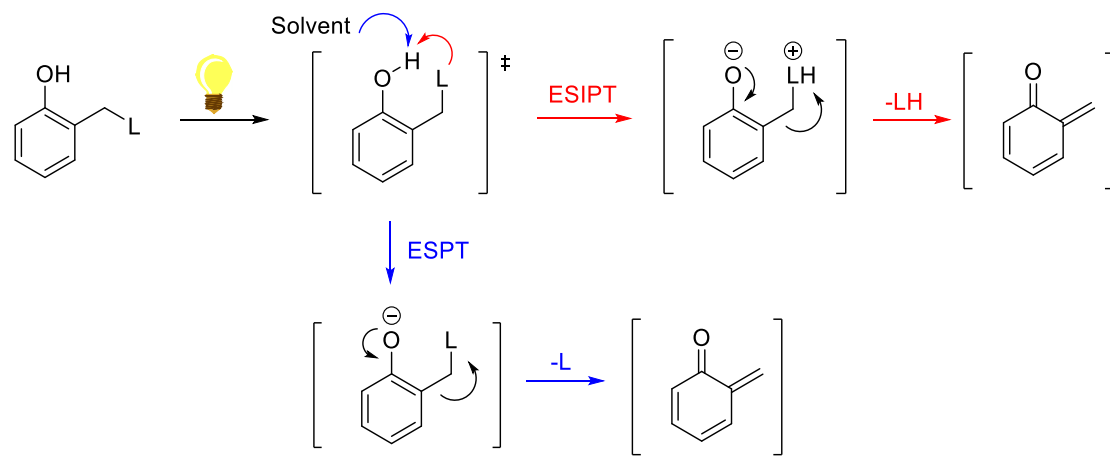


Figure 1.32 – Mechanisms for the photogeneration of o-QM.

The o-QM is a highly reactive intermediate, with lifetime of milliseconds in water solution, therefore its isolation is impossible but can be effectively detected by Laser Flash Photolysis. Moreover, it has been observed that also thermal generation and reactivity of QM can be modulated by choice of proper substituents on the aromatic system. In particular, the electronic effects of the groups introduced on the system strongly influence the generation rate of the intermediate and its stability and decomposition. Electron-donating substituents accelerate the formation of QM, because they favour the expulsion of the leaving group, stabilizing the electron-poor intermediate and reducing its electrophilicity. To the same extent, electron-rich derivatives decomposed rapidly. Conversely, electron-withdrawing substituents decreases the QM generation rate, generating a highly reactive QM but, at the same time, they suppress its regeneration and formed products are characterized by high thermal stability¹⁵⁰.

Due to their wide versatility and interesting properties, quinone methides found a wide application in medicinal chemistry, in particular for functionalization of biomolecules. Recently, Liu *et. al.* engineered a quinone methide precursor that could be genetically encoded into living system and could be activated by light. To incorporate this derivative into *E. coli* and mammalian cells, as unnatural amino acid, a tyrosine has been properly modified to obtain compound **33** (*Figure 1.33*). Upon irradiation, this compound was able to rapidly react with nucleophiles on adjacent aminoacids¹⁵¹. This approach represents a unique opportunity to spatiotemporal control the reactivity of the intermediate in a living system, which could be very useful for different purposes, for example to study interactions of protein with other biological targets or to regulate specific metabolic pathways. The same group reported also a heterobifunctional cross-linker, **34** (*Figure 1.33*) that, under irradiation, eliminated a fluorine atom, leading to quinone methide formation¹⁵². The cross-linker was conjugated to N-hydroxysuccinimidyl (NHS) group that, in physiological environment, reacts readily with lysine residues of proteins. Then, the photocaged QM could form two covalent bonds with proteins and authors demonstrated its ability to alkylate different amino acid residues, including glutamine, arginine and asparagine, which are inaccessible with existing cross-linking agents. Moreover, the same

molecule was able to efficiently alkylate the DNA sequence interacting with the protein of interest, making it useful to study complex protein-nucleic acid interactions.

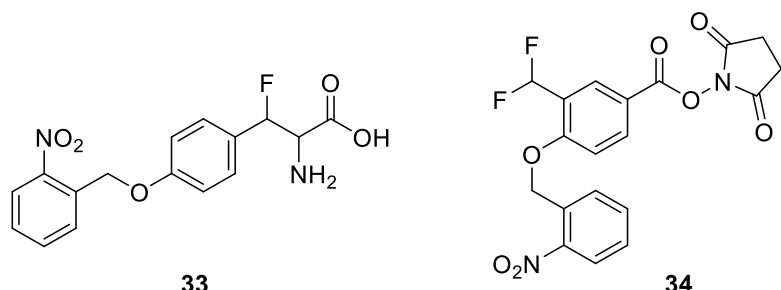


Figure 1.33 – Photocaged Quinone used as cross-linking agents on proteins.

In order to point out the relevance of using QM for targeting nucleic acids, examples described by Rokita's group deserve to be mentioned, even if, in this case, activation of the quinone methide was not light but fluoride mediated. In 2014, authors developed a conjugated system, composed of a bis-quinone methide precursor conjugated to acridine **35** (Figure 1.34-A), with the function to guarantee the interaction with DNA, with the aim to induce migration of the cross-linkers through the DNA sequence¹⁵³. Upon activation, the compound generated the QM, which could form intra and inter-strand cross-links. However, the formed covalent adduct could be reverted into the QM, then this process was exploited to promote QM shift along the strand, forming and disrupting its covalent interactions with nucleobases. The position change of QM was monitored through sequencing experiments, based on gel electrophoresis analysis, and it has been demonstrated that this continuous regeneration of the intermediate could last for several days. Despite this method resulted to be sensitive to different parameters, as nucleic acid sequence and to electronic properties of QM, this remarkable result showed that is possible to control covalent modification on DNA, *in situ*, using the chemistry of QMs.

In 2016, the same group reported a similar work, developing a system composed of a QMP conjugated to an oligonucleotide sequence or a peptide nucleic acid (PNA) that ensured high selectivity for a selected nucleic acid sequence: under a specific trigger, the QM was generated, which gave a reversible self-adduct: this modified product, delivered to the DNA sequence of interest, regenerated the QM, affording selective alkylation of the target¹⁵⁴. More recently, a further investigation demonstrated that migration process could be even more efficient using an electron-rich mono-alkylating ligand, based on the structure of the conjugate QMP-acridine reported previously, that accelerate both alkylation process and regeneration of the intermediate¹⁵⁵.

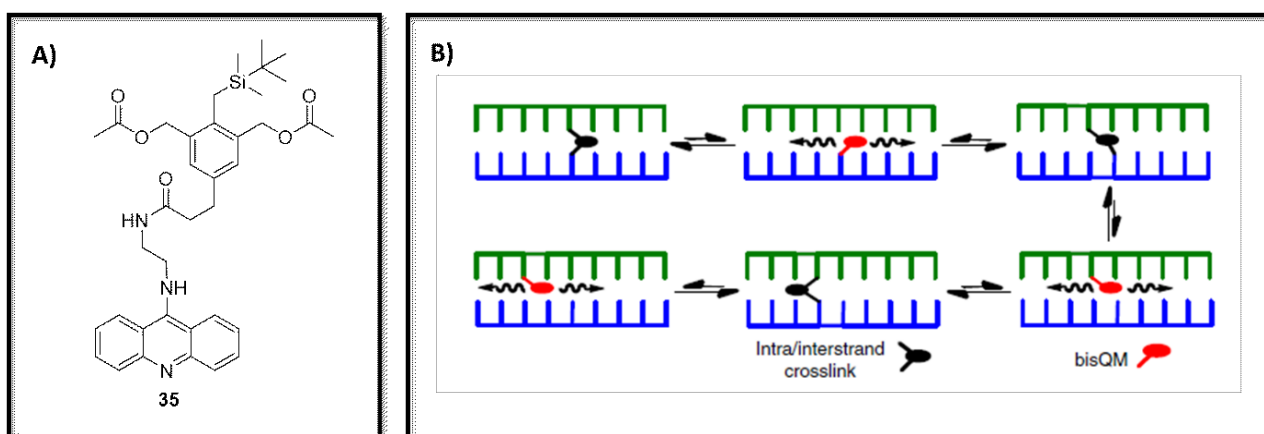


Figure 1.34 – A) Structure of migrating bis-QMP 35; B) Migration mechanism along DNA sequence described for 35¹⁵³.

Some interesting examples of QMs designed as potential DNA alkylating agents have been reported by Freccero's group, that, in the last decade, developed different QMPs, mostly employed to selectively alkylate nucleic acids, including G4s. In 2004, they developed a series of BINOL, which were expected to efficiently generate the quinone methide, thanks to the proximity of 2,2'-hydroxy groups, that could favour the intramolecular proton transfer in the excited state¹⁵⁶. Among them, compound **36** (Figure 1.35) showed excellent results: not only was able to rapidly generate the desired intermediate, but, upon irradiation at 360 nm, in presence of DNA, displayed 90% of cross-linking efficiency at 50 μM. More recently, the group developed novel conjugates NDIs-QMP, based on hydroxybenzyl alcohols as quinone methide precursors¹⁵⁷. Among them, derivative **37** (Figure 1.35), incubated with telomeric G4, upon thermal activation, showed efficient alkylation, with 16.8% yield after 24 hours. In a subsequent work, similar analogues, bearing trimethyl ammonium salts as QMPs, were synthesized¹⁵⁸. Compounds were tested again on telomeric quadruplex hTel and, upon activation, emerged that substrate **38** (Figure 1.35) showed efficient alkylation of the target (12% of alkylation at 50 μM).

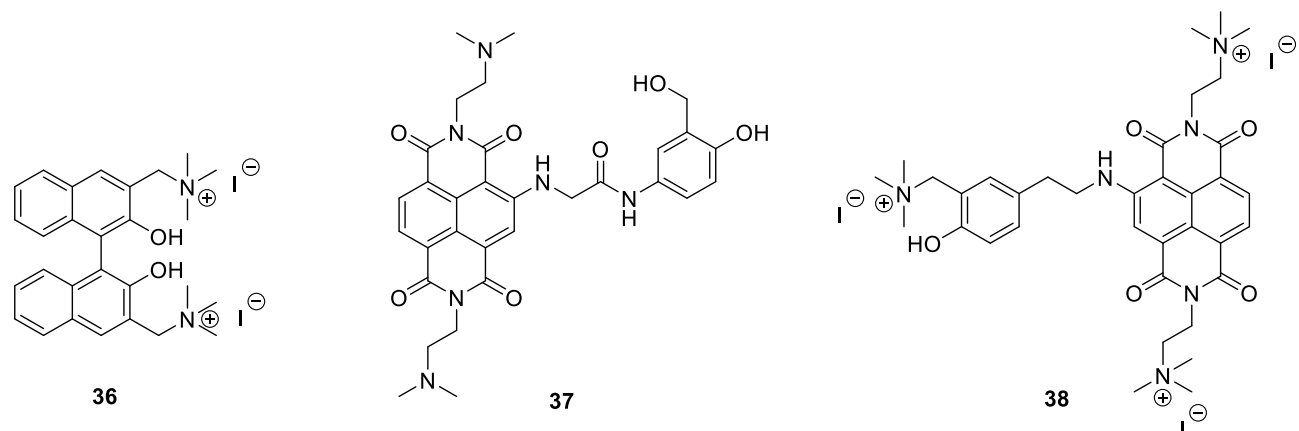


Figure 1.35 – Quinone Methide precursors used for DNA alkylation.

This remarkable reactivity made QMs appealing reactive intermediates for applications in medicinal chemistry, to covalently label specific biological targets. However, their use in G4s research field is limited, due to the difficulty to find the proper balance between photoreactivity and selectivity for the target. Part of this thesis work has been focused on these two critical aspects, with the aim to partly contribute to fill this gap.

1.5.2 Photo-activable 2,5-diaryl tetrazoles

As previously mentioned, to find applications in biological context, photo-induced reactions have to satisfy specific features. In particular, the process must be fast and selective, in order to avoid secondary transformation, reagents and products must be stable in physiological environment and non-toxic, and, finally, the wavelength used must be biocompatible. In the pool of light-mediated reaction, one in particular attracted significant attention, for its interesting properties, which is the light-induced cycloaddition of 2,5-

diaryl tetrazoles with alkenes, that generate optically-active pyrazolines. Tetrazoles are five-membered aromatic heterocyclic compounds, that don't exist in nature and they can be mono-, di- or tri-substituted: functionalization in position 5, on the carbon atom (*Figure 1.36*), is the most frequent and its derivative found application in biochemistry, medicine, pharmacology, materials, photography and even military field¹⁵⁹. However, their principal use regards medicinal chemistry: indeed, at the moment there are 43 drugs containing tetrazoles and 23 of them have been FDA-approved, for example, as antimicrobial, antiviral, antiallergic and anticancer agents¹⁶⁰.

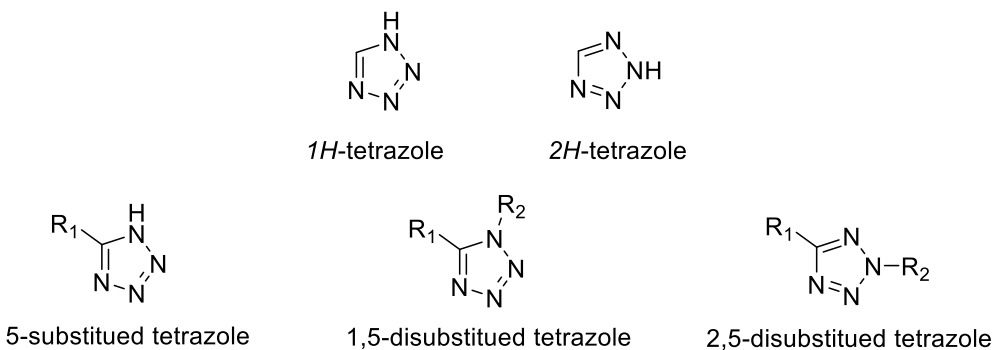


Figure 1.36 – General examples of different tetrazole structures.

One of the keys of their success in this context is that 5-substituted tetrazoles can be considered as isosteres of carboxylic acids, because of the presence of a hydrogen, with a similar pK_a (4.5-4.9 for tetrazoles) and for the analogue electrostatic potential. However, tetrazoles are characterized by higher stability, better cell membrane permeation and the presence of the pentacyclic aromatic ring can provide also π -stacking interactions¹⁶¹. In solution, 5-substituted tetrazoles exist in two tautomeric forms, *1H* and *2H* (*Figure 1.36*) and, despite the higher stability of *1H* tautomer¹⁶², basic conditions alter the tautomeric equilibrium, providing the opportunity to introduce, through simple nucleophilic substitution, a wide pool of substituents on both positions.

One of the most interesting properties of tetrazoles is their photoreactivity: upon irradiation, cleavage of the tetrazole ring occurs, affording a wide pool of photoproducts. The reaction pathway, and, subsequently, the nature of the generated intermediates and products, strictly depends on substituents present on the substrate and on the wavelength of irradiation¹⁶³.

Although their remarkable versatility, the attention of researchers has been focused on specific type of scaffold, that showed the most interesting properties for potential biological application, 2,5-diaryl tetrazoles. These compounds can be activated under irradiation at $\lambda_{\text{exc}} = 300 \text{ nm}$ and, through the expulsion of a nitrogen molecule, they generate a reactive intermediate, a nitrile imine dipole (NI) (*Figure 1.37*).

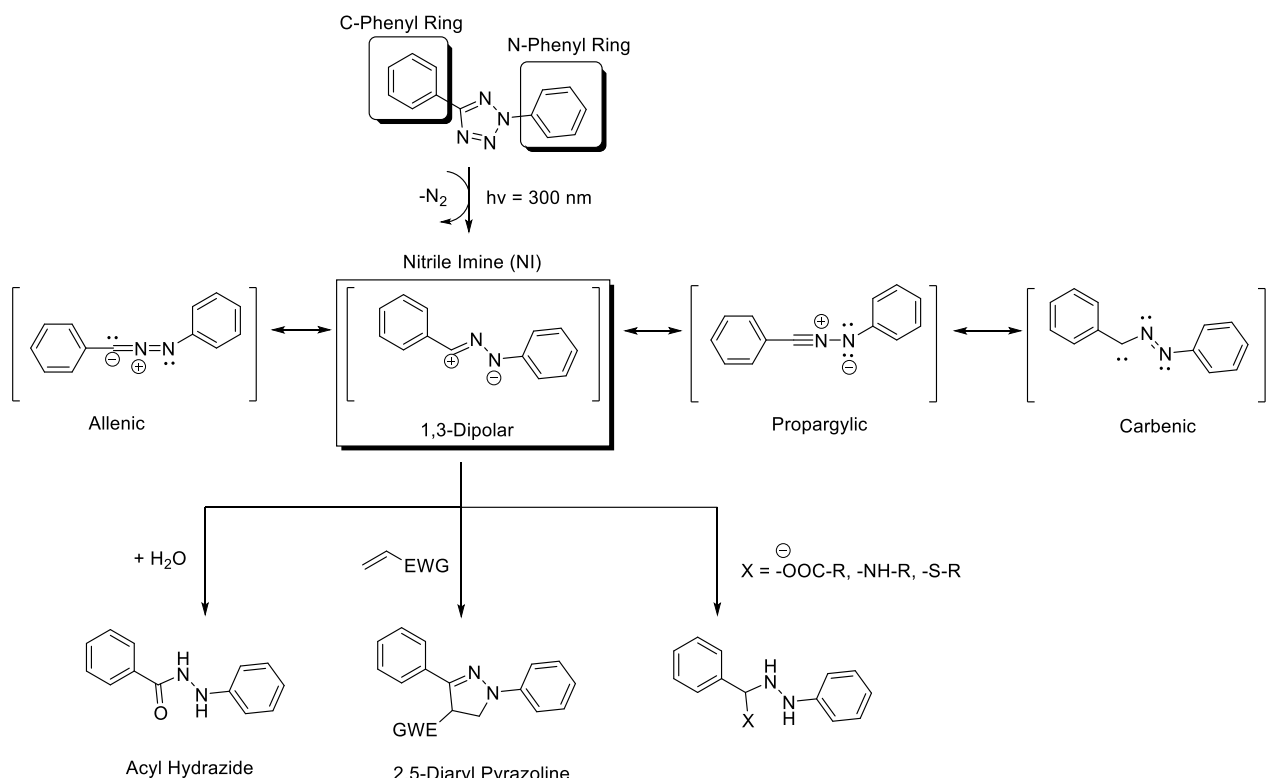


Figure 1.37 – Photogeneration of Nitrile Imine (NI) from 2,5-diaryl tetrazoles and some of its possible reaction pathways.

The reaction pathway has been deeply investigated and, recently, it has been demonstrated that, upon irradiation with laser, at 266 nm, the tetrazole is excited to its triplet state, then the intermediate lose nitrogen to produce the nitrile imine¹⁶⁴. This reactive, non-stabilized, specie cannot be isolated and has been observed only as intermediate, with transient spectroscopic techniques¹⁶⁵. Concerning the structure of NI, four different structures have been suggested for this intermediate: propargylic, allenic, 1,3-dipolar and carbenic (Figure 1.37). Different studies provided contrasting results: a computational study reported in 1993, indicated that NI has a non-planar, allenic structure¹⁶⁶, while a more recent work evidenced that carbene character should be dominant, despite all four resonance forms are necessary to describe the NI¹⁶⁷. However, an interesting X-Ray analysis of 2-(4'-methoxyphenyl)-5-(2"-isopropoxy-4"-methoxyphenyl)tetrazole coordinated by zinc, showed that 1,3-dipolar form represents the major electronic structure¹⁶⁸. Once that it's formed, NI can undergo different types of reaction, depending on the reaction conditions, as the solvent, wavelength of irradiation and the presence of eventual trapping agents. In particular, the NI can react through nucleophilic additions (especially with water), cycloadditions with electron-poor alkenes or can give rise to ring-closure, to afford a diazirine. Among these different pathways, cycloaddition with alkenes attracted significant interest for its potential use as bioorthogonal ligation, a powerful tool to visualize and track biomolecules *in vitro* and *in vivo* and to elucidate their biological functions¹⁶⁹. Bioorthogonal reactions must satisfy specific requirements: the process must be fast, to perform the reaction at low concentrations of reagents, compounds used must be stable in physiological environment and non-toxic, side-reactions must be avoided and formation of the product should be detected easily¹⁷⁰. The light-induced cycloaddition of tetrazoles with alkenes meets most of these features, therefore different research groups developed several 2,5-diaryl tetrazoles which could be employed for bioorthogonal ligation. In this context, contribute of Lin's group has been decisive: in 2008, they reported a novel tetrazole, **39** (Figure 1.38) to selectively modify Lysozyme¹⁷¹. Upon irradiation at 300 nm, the compound rapidly reacted with acrylamide, to generate the corresponding cycloadduct. Pyrazolines obtained by this reaction presented

also another interesting feature: they are fluorescent, while tetrazole is not. This represents a great advantage, because fluorogenicity of the reaction allows an easy detection of the product, especially in cellular environment. In the same work, the efficiency of the reaction has been tested *in vitro*: after conjugation of **39** to Lysozyme, the solution has been irradiated and, through gel-electrophoresis and LC-MS analysis, the formation of desired product has been confirmed. Later, the same group worked to optimize the reactivity of the tetrazole, in order to obtain an even more rapid and selective process and avoid side-reactions of NI with nucleophiles, as water: they found that presence of electron-donating substituents on *N*-phenyl ring has a strong impact on the reaction outcome, accelerating the cycloaddition step and affording the corresponding pyrazoline with high yield¹⁷². A smart alternative to avoid the formation of undesired products, which decreases the efficiency of bioorthogonal labeling, is to exploit an intramolecular process: Yu *et. al* designed a small library of tetrazoles containing an *o*-allyloxy group on *N*-phenyl ring, conjugated to 7-β-alanyltaxol, a microtubule binding agent, in order to develop a fluorogenic probe for microtubule¹⁷³. Among the synthesized derivatives, compound **40** (*Figure 1.38*), showed best performances: upon irradiation at 365 nm, was completely converted into pyrazoline in 320 seconds, as further confirmed by strong increase in fluorescence emission. To prove its utility, CHO cells have been incubated with 10 μM of **40** and briefly irradiated at 405 nm with a diode-laser and the irradiated region displayed a 7-folds enhancement in fluorescence emission, proving the efficiency of this approach. Another issue that has been faced by Lin's group during the last years is the wavelength of irradiation: 2,5-diaryl tetrazoles present absorption in UV range, up to 300 nm, that is not compatible with biological conditions. In order to solve this problem, the group reported, in 2013, oligothiophene-based tetrazoles, characterized by absorption at 400 nm¹⁷⁴. Compound **41** (*Figure 1.38*), designed to be also completely water-soluble, showed fast generation of the pyrazoline (with second order kinetic constant of $1299 \pm 110 \text{ M}^{-1} \text{ s}^{-1}$) upon irradiation at 405 nm. To prove its efficiency *in vivo*, authors developed a docetaxel (a microtubule binding agent) modified with mono-isopropyl fumarate, an electron-poor alkene: CHO cells were pre-treated with this conjugate, then 40 μM of tetrazole **41** was added. Irradiation with laser, at 405 nm, led to remarkable fluorescence enhancement at 458 nm (typical maximum absorption of pyrazoline) after only 30 seconds of irradiation. As an alternative, naphthalene-tetrazoles conjugated have been developed by the same research group, to red-shifted the activation wavelength of photoreactive unit¹⁷⁵. In particular, naphthalene unit has been exploited as two-photon absorption probes, which means that these derivatives can be activated to the double of their classic wavelength: instead of using 300 nm for the activation, wavelengths in the NIR region (700nm) can be exploited. They synthesized various compounds, differing for the type of substituents introduced on two naphthalene rings¹⁷⁵: in general, all molecules showed rapid photolysis, but **42** was chosen to label proteins modified with *N*^ε-acryloyl-L-lysine. Irradiation of protein with 700 nm femtosecond pulsed laser, in presence of an excess of tetrazole, led to the formation of the expected pyrazoline. Similar to the previous described work, in order to evaluate the efficiency *in vivo*, CHO cells were treated with tetrazole and fumarate-modified docetaxel, then have been irradiated with 700 nm femtosecond-pulsed laser and, after only 43 seconds, a strong fluorescence enhancement, attributed to pyrazoline formation, has been recorded. Based on these results, in 2016, Zhou *et. al* exploited a pyrazoline modified with two naphthalene moieties as fluorescent two-photon probe, used to track the activity of caspase (an enzyme involved in the programmed cell death), in mice tumor¹⁷⁶.

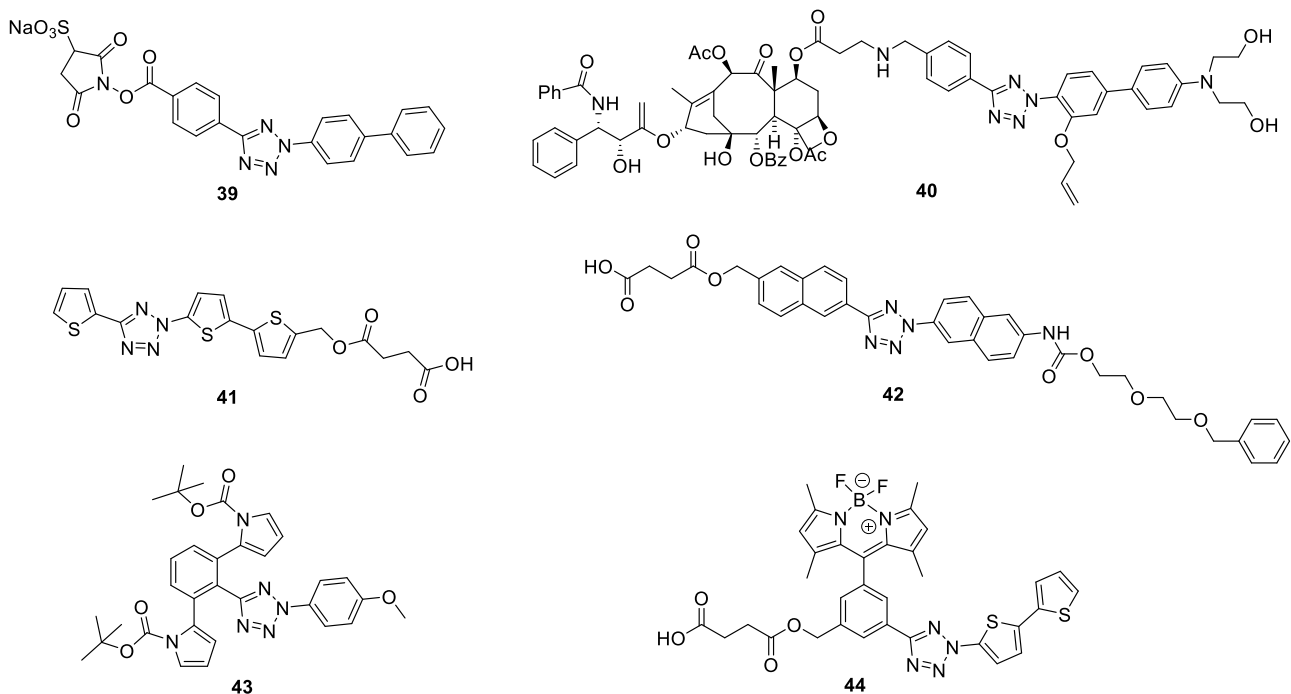


Figure 1.38 – Examples of Tetrazoles used for bioorthogonal ligation on proteins.

Despite the promising results achieved and the interesting application found for photoinduced click reactions, the progress in this research field has been slowed down by different studies that underlined different issues: the main one is represented by collateral reactions of nitrile imine dipole with nucleophiles, especially water, carboxylate groups and thiols, naturally abundant in proteins¹⁷⁷. This serious drawback limits the applicability of this approach, leading to lower efficiency and important side-effects. In order to overcome this problem, Lin *et al.* developed tetrazole **43** (Figure 1.38), modified with *o*-2-N-Boc-pyrroles, in order to increase the steric hindrance around nitrile imine to stabilize it and, subsequently, decrease its reactivity against nucleophile, favouring the desired cycloaddition¹⁷⁸. Preliminary irradiation of **43** in presence of different alkenes, glutathione and a mixture of amino acids, led to the selective formation of pyrazoline. Further experiments demonstrated that the generated intermediate presented a half-life of 102s, significantly longer compared to a non-stabilized NI, which was around 7.2 seconds. To verify the applicability of this approach, compound **43** has been used to label a glucagon receptor, (GCR), which is a common target for the treatment of diabetes, modified with a reactive cyclopropene. Then, HEK 293 cells expressing the modified GCR were incubated with 500 nM of **43** and were irradiated at 302 nm. After only 1 minute, fluorescence emission, that colocalized with the target receptor, increased significantly and pyrazoline was formed with 89% labeling efficiency, demonstrating the success of this strategy.

Another issue affecting the photoinduced cycloaddition of tetrazoles with alkenes is the low fluorescence quantum yields of the corresponding pyrazolines, resulting in difficult detection of the biological target. However, several strategies can be employed to improve emission properties of the product, as the modification of structure of the pyrazoline, to enhance the emission, or the conjugation to another fluorescent chromophore. An *et. al* followed this second strategy and synthesized a small library of bithiophene tetrazoles conjugated to BODIPY, a boron-based fluorescent probe, popular for its excellent quantum yield and stability in physiological conditions¹⁷⁹. Authors speculated that photo-click reaction could be exploited to modulate fluorescent properties of the BODIPY, through photoinduced electron transfer. Indeed, tetrazole-BODIPY conjugates showed excellent quantum yields (from 14 to 50%), that dropped significantly in the corresponding pyrazoline (0,1%), confirming the existence of an interaction between these two chromophores. However, decrease of fluorescence emission cannot be exploited for detection of specific target, however, authors observed that, in oxidative environment, with hydrogen peroxide, pyrazoline can

be easily oxidized to generate the corresponding pyrazole, unable to interact with BODIPY through electron transfer. To evaluate the efficacy of this method, authors synthesized compound **44** (*Figure 1.38*): this derivative, after oxidation to pyrazole, was unable to interact with BODIPY, whose emission was regenerated. This interesting property was exploited to detect oxidative stress in HeLa cancer cells, previously treated with fumarate-docetaxel, another microtubule binding agent.

As described above, photoinduced cycloaddition of tetrazoles with alkenes have been widely exploited for bioconjugation of proteins but, more recently, application on nucleic acids start to emerge. In 2017, Huang *et al.* developed a tetrazole modified with *o*-allyloxynaphthalene to detect specific microRNA sequences, in cellular environment. Compound **45** (*Figure 1.39*) was covalently conjugated to miR-122 through a hexanedioic acid linker. Irradiation, with UV light, of this oligonucleotide-tetrazole derivative, afforded rapidly the corresponding pyrazoline, characterized by intense emission at 520 nm. To verify the absence of undesired biological processes, due the specific recognition of the target miRNA, HepG2 cells were treated with this compound and, through luciferase assay, it has been demonstrated that suppressed the expression of miR-122 and of other important genes, such as BCL-2. Moreover, confocal microscopy recorded strong emission intensity, from cell cytoplasm, between 450-550 nm, after irradiation at 302 nm, further confirming the formation of the pyrazoline. To demonstrate that this photoclick reaction can be exploited also to label nucleic acid sequences, 2-deoxyuridine has been modified with tetrazole scaffold, to induce the reaction with cyanine, a common fluorescent probe, covalently bound to maleimide¹⁸⁰. Irradiation of compound **46** (*Figure 1.39*) at 300 and 365 nm afforded the corresponding pyrazoline, in 15 minutes, with 74% yield. Cyanine dye was selected to exploit energy transfer with pyrazoline: indeed, emission spectra of pyrazoline perfectly overlayed with absorption of cyanine then excitation of pyrazoline resulted in increased fluorescence emission of the probe. Despite the interesting results, this approach presents some limitations, because require incorporation of bulky tetrazole moiety into natural nucleobases. Conversely, alkene can be more easily incorporate in natural nucleic acid sequences: 5-vinyl-2-deoxyuridine (VdU), a thymidine analogue containing an alkene moiety, which is recognized as substrate by DNA polymerase, can be introduced in genome of living cells. On these basis, Wu *et al* designed a library of tetrazoles, conjugated to coumarin, to label, *in vivo*, DNA modified with VdU. Coumarins were chosen both for their fluorescent properties and for the possibility to red-shift the absorption of tetrazole unit. Preliminarily, efficiency of the reaction was tested irradiating synthesized tetrazoles in presence of an oligonucleotide containing acrylamide and, after 30 minutes, product was formed in 62.9% yield, accompanied by increased fluorescence emission at 395 nm. Once that the efficiency of the reaction was verified, water-soluble compound **47** (*Figure 1.39*) was synthesized. A549 cells were incubated with VdU and, subsequently, with **47** (10 μM). Emission enhancement, attributed to pyrazoline formation, was observed only upon irradiation with a 365 nm LED, confirming the positive outcome of the cycloaddition. The efficiency of this reaction was tested also *in vivo*: zebrafish embryos have been treated with VdU and, subsequently, with **47**. Irradiation, at 365 nm, led to dose-dependent fluorescence increase, which was limited to the irradiated area, ensuring an excellent spatial-temporal control of the reaction. In the end, authors demonstrated that the whole process did not exhibited cytotoxic effects towards zebrafish, which displayed a survival rate of 80% for 40 days.

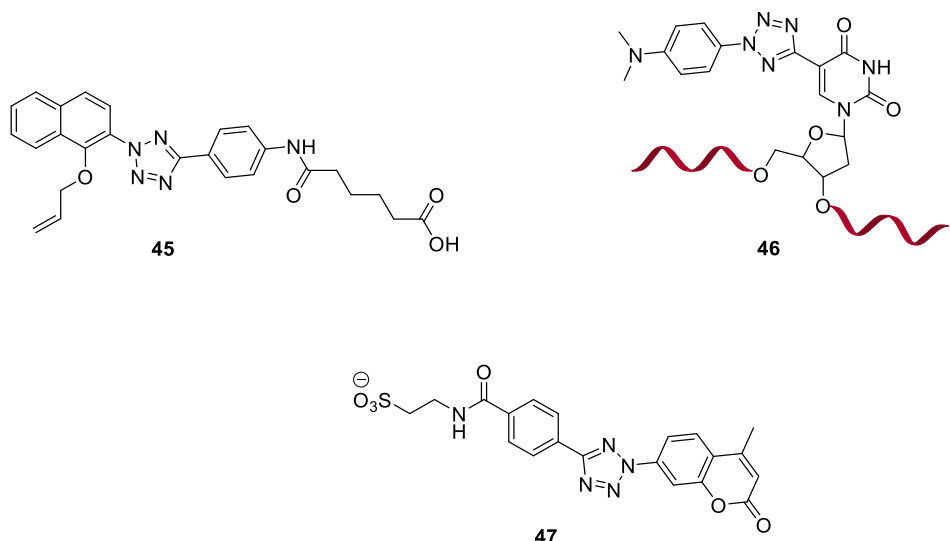


Figure 1.39 – Representation of tetrazoles used for bioorthogonal ligation on nucleic acids.

These are only few examples of applications of 2,5-diaryl tetrazoles in medicinal chemistry fields and, during the last years, the unique properties of these compounds attracted increasing attention and they have been used not only to label biomolecules, but also to build photo-degradable hydrogels, for the controlled released of drugs¹⁸¹, and to design novel, photoresponsive, polymers¹⁸². Although remarkable progresses have been accomplished in this research context, this reaction still suffers of different issues, as the activation wavelength, the formation of side-products and low fluorescence quantum yield of pyrazoline. Then, further optimization of their structures and photoreactivity are still necessary to improve their performances and also to expand their application fields to NA.

2. Aim

Nowadays, it has been widely demonstrated that G4 formation can occur both *in vitro* and *in vivo*, and experimental results evidenced their ability to regulate specific metabolic processes and their utility as potential therapeutic target for several pathologies, including cancer and neurodegenerative diseases.

In this scenario, small molecules emerged as powerful tool both as therapeutic agents, that are able to regulate specific physiological processes interacting with G4s, and fluorescent sensors, capable to detect G4 formation *in vitro* and *in vivo* by fluorescence signalling upon binding.

Although remarkable progresses have been accomplished in the development of efficient quadruplex ligands, several issues are still to be addressed: hundreds of small-molecules have been synthesized in the last years, however, most of them suffer of poor selectivity for a specific G4.

In this context, the aim of this work is to develop functional molecular tools, targeting nucleic acid secondary structures, engineered to achieve: 1) dual-role ligands, with a naphthalenediimide core, combining excellent binding properties towards G4s with intense fluorescence emission, to achieve both target detection and biological effects; 2) innovative targeting strategies, based on photoreactive or light-responsive ligands.

The first part of this thesis is aimed at the optimization of NDI structures to obtain dual-role ligands, able to bind selectively the target and, at the same time, detect its presence in cells, monitoring the distribution and compartmentalization. To reach this goal, a library of novel NDIs derivatives has been synthesized and their structure has been modified introducing a carbohydrate moiety. This choice was dictated by two reasons, being: 1) sugar moieties maintain higher affinity for G4 structures but, at the same time, with higher selectivity, upon formation of strong hydrogen bonds with phosphate backbone and grooves of the target¹⁸³ and 2) the possibility to enhance cellular uptake in cancer cells, exploiting the overexpression of GLUT receptor, typical of tumor cells , to achieve therapeutic effects with negligible side-effects.

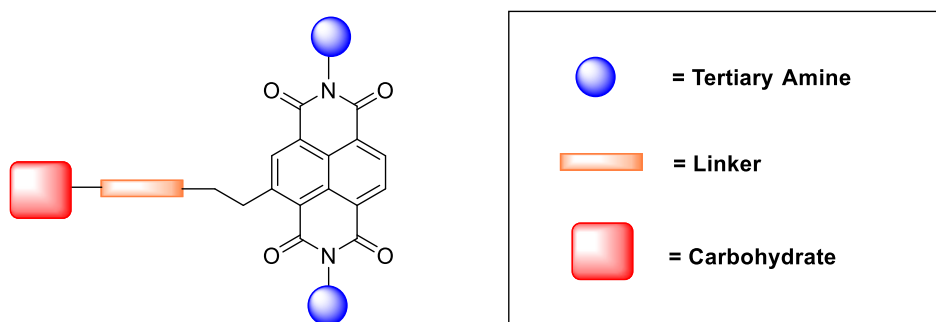


Figure 2.1 – General structure of NDI-carbohydrate conjugate.

Moreover, for each compound of the library, an analogue containing the corresponding thio-modified sugar has been synthesized, in order to increase the stability, under physiological conditions. Additionally, the imide positions of the NDI core have both been modified with aminoethyl morpholine and compared with NDIs bearing 3-(dimethylamino)-1-propylamine, to verify if the reduced basicity could guarantee higher selectivity for G4, respect to duplex DNA.

The binding affinity of these new ligands have been tested on a specific target, the human telomeric quadruplex, to assess their potential as anticancer agents.

The second part of this thesis work has been focused on alternative targeting strategies, as we concentrated on the design and development of novel, photoreactive ligands, able to react upon light activation. To our purpose, we explored the usefulness of two different photoreactive units: functionalized **Mannich bases** as

precursors (QMPs) of **Quinone Methides (QMs)** and **2,5-diaryl tetrazoles**, generating the reactive 1,3 dipole **nitrilimine**. The choice of adopting two different strategies depends on the possibility to exploit different types of reactivity and, subsequently, different interactions with the target, which can be exploited to achieve both biological effect and sensing.

Quinone Methides have been selected for their electrophilic properties and, subsequently, for their ability to form covalent bond with nucleotides of G4, ensuring a stronger interaction, as the ligand is literally “anchored” to its target. To further strengthen this effect, we have introduced two photoreactive units. The design of the ligands bearing the light-activable moieties followed a precise ratio: our molecules present a so-called “V-shaped” structure, which is typical of common, already described, quadruplex ligands, and ensure high affinity for guanine tetrads. In details, they are composed of three distinct aromatic units (*Figure 2.2*), connected through two alkyne moieties. This disposition has a double purpose: to ensure an extended planar surface, critical to establish π - π stacking interactions with G4, and to provide a highly conjugated chromophore, to red-shift the photoactivation of QMP in the visible light window, therefore improving the biocompatibility.

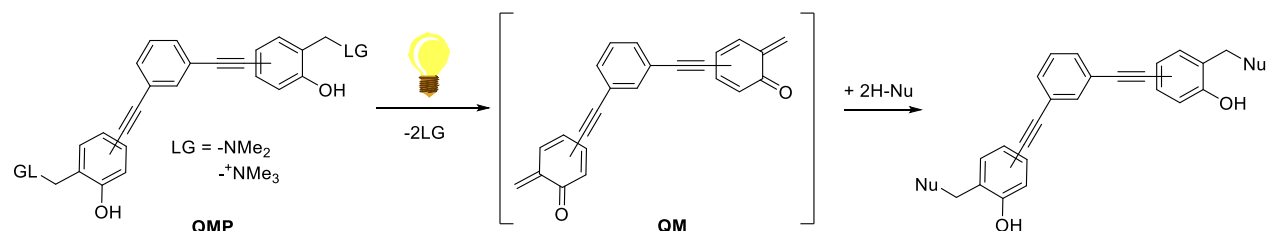


Figure 2.2 – General structure and mechanism of synthesized QMPs.

Of each synthesized compound, we have investigated the binding affinity toward G4s and the photoreactivity, generating quinone methide, which is capable to alkylate specific G4 structures. In the attempt to further red-shift the activation wavelength, two naphthalene moieties have been used as QMPs, and have been conjugated to phenyl ring through alkyne-based spacer. However, the poor results observed with these last compounds, in terms of generation of corresponding QM and binding properties, prompted us to further investigate the photoreactivity of a series of 6-substituted naphthols, in order to evaluate how electronic effects of groups introduced on the scaffold can tune the absorption properties, the acidity (which is a key parameter) and the intermediate generation efficiency.

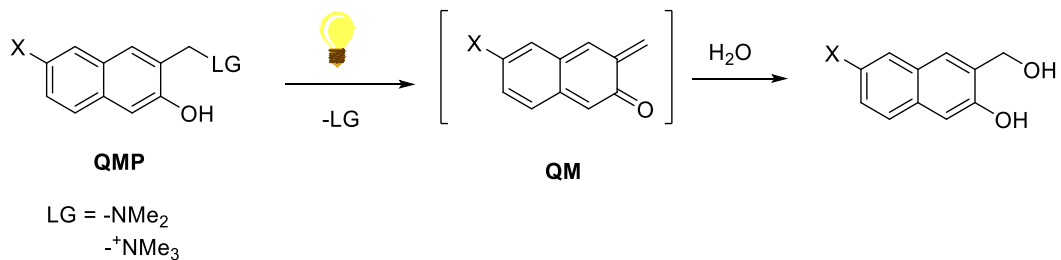


Figure 2.3 – General structure and reactivity of synthesized 6-substituted naphthols.

The third strategy explored in this work is represented by the photoinduced cycloaddition of 2,5-diaryl tetrazoles: to the best of our knowledge, this reaction has never been reported for application on nucleic

acids secondary structures, neither to develop photo-responsive ligands. Therefore, due to its interesting features namely efficiency and reactivity of the resulting nitrile imines, we decided to start investigating how to exploit this process for applications in G4s context.

The unique versatility of the light-generated intermediate, the 1,3-nitrile imine dipole (NI), opened a range of possibilities to detect and interact with quadruplexes. In principle, three different scenarios emerged:

- 1) photogeneration, *in situ*, of the fluorescent probe, in presence of the G4, to exploit the excellent emission properties of pyrazolines resulting from the cycloaddition;
- 2) the reaction could produce a ligand with different binding properties compared to the substrate, therefore, light could act as switch of the affinity;
- 3) photogenerated nitrile imine, which is electrophilic at the C atom, could establish a covalent bond with the target.

The first and the second targeting approach rely on non-covalent interactions with the target and allow the spatio-temporal control of the fluorescence emission of the ligand, reducing the signal generated from off-target interactions and increasing specificity. Conversely, in the third scenario, as in the case quinone methides, is the formation of a covalent bond with the target that could be used to stabilize and lock the G4 and interfere with its physiological role.

Due to the lack of data in the current literature, the investigation on 2,5-diaryl tetrazoles has been further divided into two parts: in the first one, in order to understand the photochemical behaviour of 2,5-diaryl tetrazoles in aqueous solution and identify suitable candidates for applications on G4, we have synthesized a small library of compounds and analysed their photochemical behaviour. Briefly, we have examined their reactivity in water, in absence and in presence of alkenes as trapping agents. Subsequently, we have synthesized the corresponding 2,5-diaryl pyrazolines and investigated their fluorescent properties, to identify novel and efficient fluorescent probes.

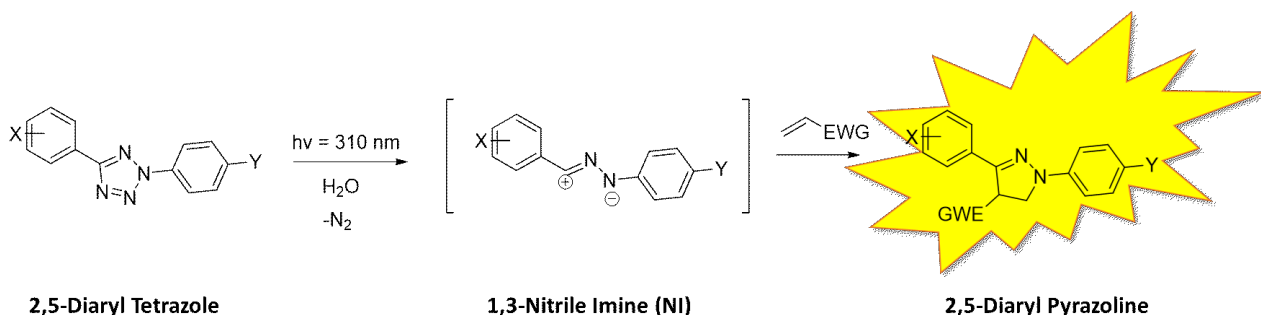


Figure 2.4 – Photoinduced cycloaddition of 2,5-diaryl tetrazoles with alkene.

In the second part of this project, we moved towards the targeting of quadruplex structures. We have measured the binding affinities of several tetrazoles towards different G4s. Then, to address the photoreactivity of our compounds to selected targets, we synthesized a library of novel quadruplex ligands, with 2,5-diaryl tetrazole tethered to NDI through spacers of different lengths. As in the case of quinone methide precursors, this choice was made not only to increase affinity for guanine tetrad, but also to red-shift the activation wavelength of the tetrazole.

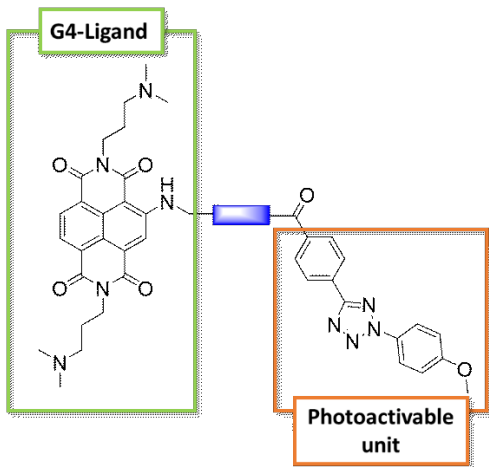


Figure 2.5 – General representation of NDI-Tetrazole conjugate synthesized in this work.

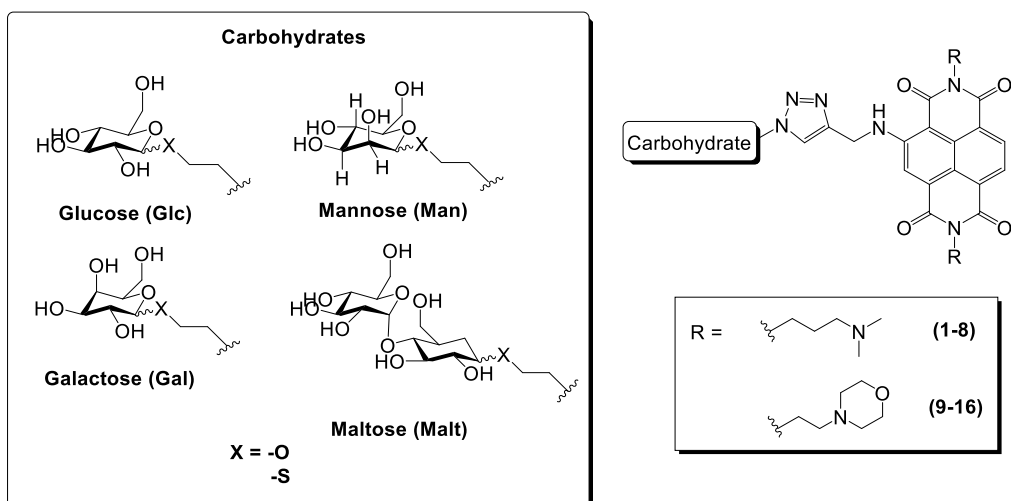
As in the previous case, we have investigated the photochemical behaviour of NDI-tetrazoles conjugates, in aqueous solution, at different wavelengths, to verify if activation could be triggered also in the visible region. In the end, we have explored their binding properties towards different types of G4s, to ensure that the photochemical process could effectively occur in presence the ligand bound to the target.

3. Results and Discussion: Dual Role-Ligands

3.1 Dual-Role Ligands: NDIs-Carbohydrate conjugates

3.1.1 State of the Art and rational design

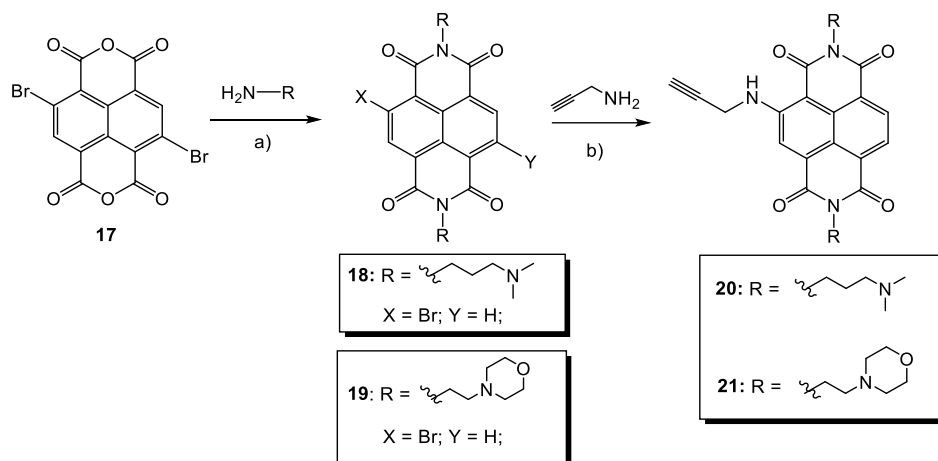
The first part of the work has been dedicated to the design and the synthesis of novel dual-role ligands, based on naphthalene diimide scaffold and on the evaluation of their biological activity, in particular as potential anticancer and antiparasitic agents. Different libraries of conjugates NDI-carbohydrates have already been reported by Freccero's group and interesting results have been obtained¹⁸³: introduction of carbohydrate derivatives, in particular monosaccharide and disaccharides, provide additional hydrogen-bonds interactions with phosphate backbone and grooves, as reported in literature, improving the affinity for G4 structures¹⁸⁴. At the same time, the presence of this derivative reduces the overall positive charge of the molecule, but maintain its solubility and fluorescent properties¹⁸³. In particular, the choice to introduce a carbohydrate was prompted by the necessity to increase the cellular uptake in cancer cells, compared to normal ones. Indeed, it is well-known that tumor cells, in order to satisfy the high requirement of glucose, overexpress GLUT receptor on membranes¹⁸⁵. Libraries of NDI-carbohydrates conjugates have been already reported by Freccero's group¹⁸⁶, however, this new set of compounds has been designed to improve their stability and cellular uptake. One of the major novelties of this work is represented by the introduction of thio-modified sugars, with a sulphur atom that replaces oxygen on the anomeric carbon. This strategy aims to increase the resistance of these derivatives in physiological environment. Indeed, previously synthesized compounds, they hydrolyse rapidly in water and in cell culture media. Another interesting structural modification that has been introduced is aminoethyl morpholine, replacing 3-(dimethylamino)-1-propylamine, at the imide positions. In fact, lower basicity of morpholine, could be exploited to reduce the population of the ammonium salt lessening electrostatic interactions with duplex DNA and improving the overall affinity of the ligand for G4s. Conjugation of NDI to carbohydrates has been accomplished exploiting a copper-catalyzed 1,3-dipolar cycloaddition between an azide, on the sugar derivative, and an alkyne, introduced on NDI scaffold. The opposite combination of reactive unit has been previously described, however, in that case, it has been observed that significant steric hindrance between triazole and NDI was generated. For all synthesized compounds, the conjugation relies on ethylene glycole spacer, because previous investigations pointed out that this was the optimal length to achieve higher cellular uptake. In the end, it should be underlined that we have explored different types of carbohydrates, in particular Glucose (**Glc**), Galactose (**Gal**), Mannose (**Man**) and Maltose (**Malt**) and, for each of them, the corresponding thio-analogue has been synthesized (*Scheme 3.1*).



Scheme 3.1 – Library of synthesized conjugates NDIs-Carbohydrates.

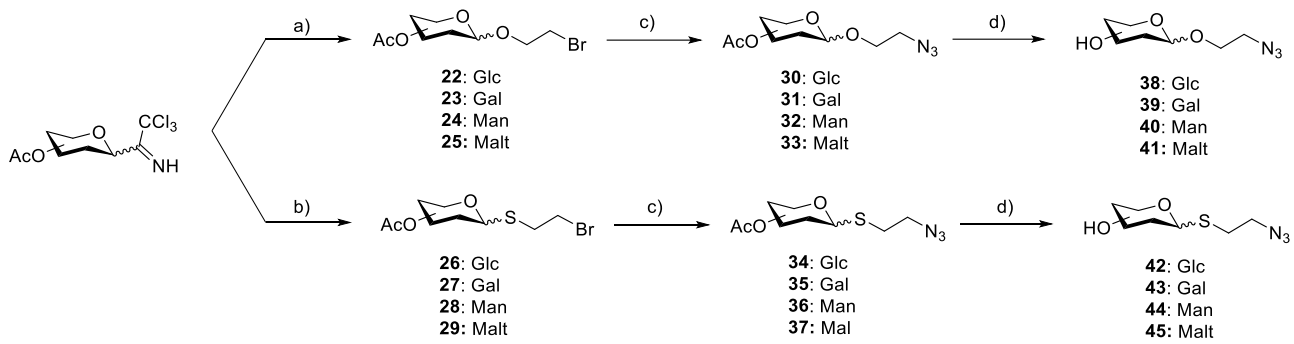
3.1.2 Synthesis of Compounds

The key step in the synthesis of final conjugates was the copper-catalyzed azide-alkyne cycloaddition, which involved NDI bearing an alkyne and azide-modified sugar. Naphthalene diimides have been obtained exploiting a previously published protocol¹⁸³, based on three reaction-steps (*Scheme 3.2*): di-bromo-substituted naphthalenetetracarboxylic dianhydride **17** (*Scheme 3.2*) underwent to imidation reaction with 3-(Dimethylamino)-1-propylamine and aminoethyl morpholine, in acetic acid, under reflux, to afford **18** and **19**. Both compounds were obtained as mixture, depending on the number of bromine atoms remained on the aromatic core, but they have been used for the subsequent step without no further purification. In the end, we have carried out a nucleophilic aromatic substitution on NDI core, with an excess of propargylamine, in acetonitrile, to obtain the corresponding NDI **20** and **21** (*Scheme 3.1*). In this case, due to their excellent water-solubility, they have been purified through reverse phase column chromatography.



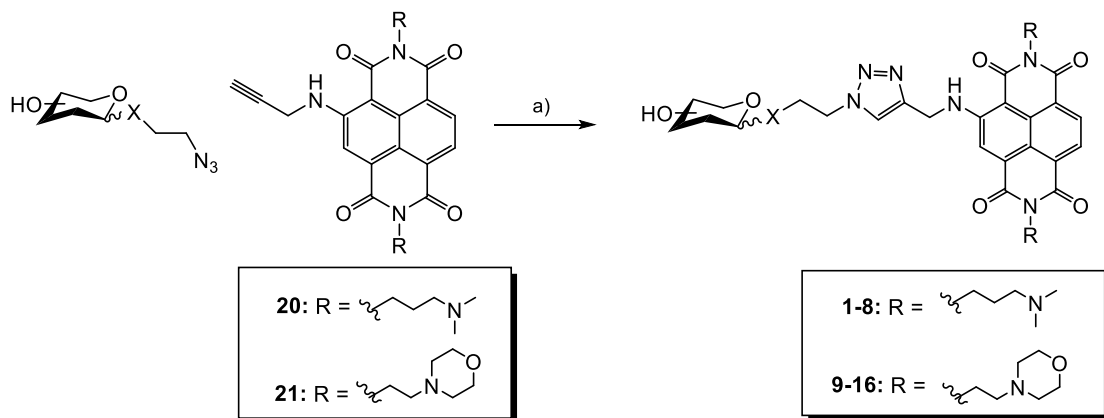
Scheme 3.2 - Synthesis of alkyne-modified NDIs **20 and **21**:** a) amine (3 eq.), acetic acid, reflux, 30 min.; b) propargylamine (3 eq.), acetonitrile, reflux, 16 hours.

Even carbohydrates derivatives have been obtained exploiting a previously reported synthetic route¹⁸⁷: briefly, starting from peracetylated trichloroacetimidate, reaction with 2-bromo-ethan-1-ol afforded compounds **22-25** (*Step a-Scheme 3.3*). Azide has been introduced through simple nucleophilic substitution reaction, performed with sodium azide, using DMF as solvent (*Step c – Scheme 3.3*). The final removal of acetate-protecting groups, in sodium methoxide, afforded the expected carbohydrates **38-41** (*Step d-Scheme 3.3*). Analogues thio-sugars have been synthesized exploiting the same synthetic procedures with the difference that the first step was performed in presence of 1-bromo-2-chloroethane and thiourea, to replace oxygen with sulphur (*Step b – Scheme 3.3*).



Scheme 3.3 - Synthesis of azido-sugars 38-45: a) 2-bromo-ethanol (1.1 eq.), $\text{BF}_3\text{*OEt}_2$ (1 eq.), anhydrous DCM, r.t., 30 min; b) thiourea (1.1 eq.), $\text{BF}_3\text{*OEt}_2$ (2 eq.), acetonitrile, 1-bromo-2-chloroethane (2.5 eq.), Et_3N (4 eq.), reflux-r.t., 15 hours; c) NaN_3 (10 eq.), DMF, r.t., 24-96 hours; d) sodium methoxide (2 ml/ 1 mmol of protected sugar), MeOH , r.t.

All synthesized carbohydrates **38-45**, were conjugated to NDIs **20** and **21** through copper-catalyzed cycloaddition (*Scheme 3.4*): reaction was carried out with catalytic amount of copper sulphate $\text{CuSO}_4\text{*5H}_2\text{O}$ and sodium ascorbate, in 1:1 H_2O : $t\text{BuOH}$ mixture. In one hour, the reaction was completed, then the corresponding triazole products **1-16** were purified and isolated through reverse-phase column chromatography.



Scheme 3.4 – General Synthesis of conjugates 1-16: a) sodium ascorbate (1 eq.), $\text{CuSO}_4\text{*5H}_2\text{O}$ (0.1 eq.), H_2O : $t\text{BuOH}$ 1:1, r.t., 1 hour.

In the end we have obtained sixteen new molecules, eight of them characterized by the presence of 3-(dimethylamino)-1-propylamine and the others with morpholine amine. Moreover, the synthesized NDI-thiosugar conjugates, with the description of their structural features, are summarized in *Table 3.1*.

Entry	-X	Sugar	NDI
1	O	Glucose	20
2	S	Glucose	20
3	O	Mannose	20
4	S	Mannose	20
5	O	Galactose	20
6	S	Galactose	20
7	O	Maltose	20
8	S	Maltose	20
9	O	Glucose	21
10	S	Glucose	21
11	O	Mannose	21
12	S	Mannose	21
13	O	Galactose	21
14	S	Galactose	21
15	O	Maltose	21
16	S	Maltose	21

Table 3.1 – General Structure of NDI-carbohydrate conjugates 1-16

3.1.3 Biological Activity

NDI-Carbohydrates **1-16** have been designed as novel, fluorescent, G4 ligands but, in particular, to further improve the biological properties of previous synthesized compounds¹⁸³, in terms of anticancer activity and cellular uptake. Then, we focused our attention mostly on the analysis of cytotoxicity of these compounds and, due to the recent discovery of G4 in the genome of some parasites, even on their antiparasitic activity. To this aim, we have performed a preliminary screening to evaluate their activity against two different cell lines, MRC5 (normal human lung fibroblast) and HT29 (colorectal adenocarcinoma), and cells were incubated with increasing amounts of ligands **1-16**, at 37°C, for 3 days, then IC₅₀ values (i.e. the concentration of ligand at which only 50% of cells survived) were determined through MTT assay and results are summarized in *Table 3.2*.

	MRC5	HT29	
Entry	IC ₅₀ (µM)	IC ₅₀ (µM)	Selectivity Index (S.I.)
1	0.92 ± 0.04	0.46 ± 0.09	2
2	3 ± 2	0.7 ± 0.1	3.7
3	0.9 ± 0.4	0.43 ± 0.01	2.2
4	3 ± 2	0.9 ± 0.2	3.1
5	1.9 ± 0.6	0.5 ± 0.2	3.9
6	1.5 ± 0.2	0.3 ± 0.1	4.4
7	1.8 ± 0.5	0.5 ± 0.3	3.8
8	2.9 ± 0.4	0.3 ± 0.1	9.9
9	7.9 ± 0.5	1.7 ± 0.5	4.4
10	35 ± 12	28.9 ± 0.8	1.2
11	30 ± 15	8 ± 4	7.2
12	23 ± 2	3.3 ± 0.6	6.6
13	10 ± 3	4 ± 2	2.9
14	23 ± 6	26 ± 2	0.9
15	52 ± 4	13 ± 5	4.0
16	71 ± 10	14 ± 1	5.2

Table 3.2 – Cytotoxicity of compounds **1-16 towards MRC5 and HT29 cells.** ^a Standard Deviation. ^b Selectivity Index was measured as the ratio between IC₅₀ on HT29 cells and IC₅₀ on MRC5.

In general, derivatives **1-8**, bearing 3-(dimethylamino)-1-propylamine, displayed higher toxicity compared to morpholino-substituted NDIs, with IC₅₀ values that, on HT29 cells, are below 1 µM. Moreover, compounds **5,6** and **7** showed good selectivity towards cancer cells, evidencing thatthese compounds offer a therapeutic window to avoid damages on healthy cells. The most remarkable outcome was observed with NDI **8**, characterized by excellent selectivity (10-folds higher) towards tumor cells. On the contrary, morpholino-substituted NDIs **9-16** resulted to be less toxic, as demonstrated by their significantly higher IC₅₀ values, on both MRC5 and HT29 cells. However, almost of them showed better specificity, compared to propylamino derivatives, towards HT29: in particular, **9, 11, 12** and **16** gave the best performances. Concerning the effects of thio-sugars, it does not seem that replacement of one oxygen atom influenced the toxicity or the selectivity in a significative manner, but, in case of compounds **1-8**, presence of thio-analogues slightly increased the selectivity index, for each compound. From these experiments, compound **8** emerged for its elevated toxicity against tumor cells and the excellent selectivity index, suggesting that the presence of thio-maltose could be crucial to this purpose. Indeed, despite the less pronounced effect observed in this case, derivative **16**, among all morpholino derivatives, displayed one of the highest selectivity.

In order to further confirm these biological data, cellular uptake of compounds **1-16** was evaluated on HT29 cells by flow citometry analysis. Cells have been incubated for 2 hours in presence of 10 µM of NDI, then their permeation into cells was measured, exploiting fluorescence emission of NDIs (λ_{em} = 485 nm and 550 nm). Results, summarized in *Figure 3.1*, clearly evidenced a noteworthy difference in uptake of 3-(dimethylamino)-1-propylamine derivatives and morpholines: in fact, compounds **9-16** poorly penetrate into HT29 cells and

the highest uptake was observed with **14**, that achieved 10%. This outcome suggests that the lower toxicity obtained through MTT assay, could be attributed to the fact that only a small fraction of compound can effectively permeate into the target cell. NDIs **1-8** displayed better permeation, with percentage above 20% with almost all compounds. Furthermore, it should be noticed that NDIs that showed higher toxicity penetrate more efficiently into HT29 cells. In more details, **5** and **6**, characterized by the presence of Galactose, gave highest uptake percentages (30% and 26%, respectively), as **8** (27% of uptake), conjugated to thio-modified to disaccharide maltose, which resulted to be also the most toxic and selective compound.

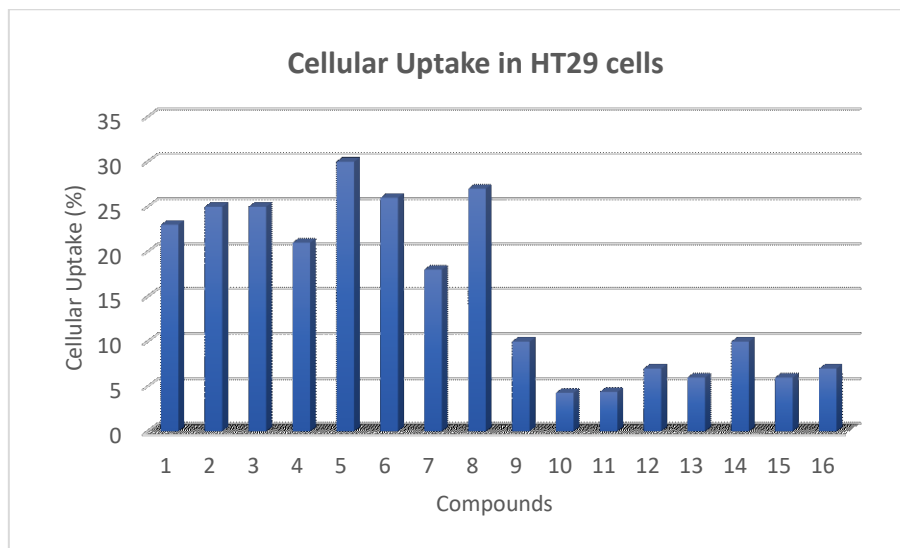


Figure 3.1 – Cellular Uptake percentages measured for compounds **1-16 on HT29 cells.**

Taken together, these results suggest that **8** is the most promising compound for potential therapeutic applications, because of its very high toxicity ($IC_{50} = 296$ nM on HT29 cells) and good selectivity (S.I. = 9.9) towards tumor cells.

Biological activity of conjugates NDI-sugars is not limited to their anticancer activity and as previously anticipated, we have evaluated the toxicity of ligands **1-16** against *T. Brucei* and *Leishmania Major* and results are reported in *Table 3.3*.

The obtained trend resembles the case of cells, with morpholine derivatives that display significantly lower cytotoxicity compared to NDIs modified with 3-(dimethylamino)-1-propylamine. Once again, no significant differences are observed between sugars and their thio-analogues. Conversely, compounds **1-8** gave outstanding results, displaying very elevated toxicity against *T. Brucei*: most of measured IC_{50} values are below 100 nM. A particular interesting case is represented by the couple of compounds **5** and **6**, bearing a Galactose and Thio-Galactose, respectively. Despite the only difference among them is the presence of sulfur atom on sugar moiety, they presented significantly different toxicity: in particular, **5** is the less toxic compound of the series ($IC_{50} = 151$ μ M), while **6** is the one with more potent antiparasitic activity ($IC_{50} = 37$ μ M). Then, this outcome suggests that, in this specific case, the replacement of oxygen with sulfur in the sugar moiety, could be responsible of specific interactions that determine different biological activity.

	Trypanosoma Brucei	Leishmania Promastigote
Entry	IC ₅₀ (μM)	IC ₅₀ (μM)
1	0.08 ± 0.06	0.8 ± 0.1
2	0.05 ± 0.02	1.4 ± 0.6
3	0.05 ± 0.02	0.3 ± 0.03
4	0.08 ± 0.06	1.5 ± 0.5
5	0.15 ± 0.02	1.4 ± 0.1
6	0.04 ± 0.01	0.74 ± 0.01
7	0.06 ± 0.03	0.78 ± 0.05
8	0.06 ± 0.04	0.5 ± 0.1
9	0.31 ± 0.06	10 ± 1
10	1.18 ± 0.07	30 ± 2
11	2.1 ± 0.2	> 50
12	0.7 ± 0.2	21 ± 1
13	0.8 ± 0.3	7.7 ± 3.5
14	0.8 ± 0.3	> 50
15	3 ± 2	> 50
16	3 ± 0.1	> 50

Table 3.3 – Antiparasitic activity of compounds **1-16 against *T. Brucei* and *Leishmania Major*.**

Concerning the results on *Leishmania M.*, the first thing that is possible to notice is that, in general, these compounds present significantly lower effects against this parasite and, in particular, morpholine derivatives can be considered almost non-toxic, with most of their IC₅₀ values above 50000 nM. Again, NDIs **1-8** are definitely more toxic, and, in this case, it should be noticed that thio-sugars affect the biological activity of the compounds. In details, the most remarkable example is represented by **3** and **4**: indeed, introduction of thio-mannose seems to dramatically decrease the toxicity of this scaffold (IC₅₀ = 299 nM with **3** and 1525 nM with **4**). Conversely, **5** and **6** showed the opposite behaviour: thio-maltose analogue resulted to be more toxic, with IC₅₀ = 738 nM. For compounds **14** and **16**, IC₅₀ values have not been measured because they did not display any effect on parasite survival.

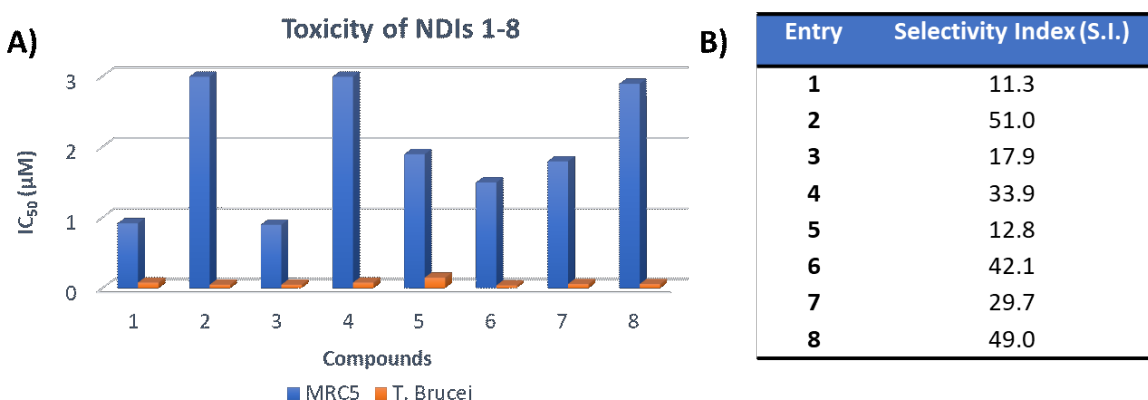


Figure 3.2 – A) Cytotoxicity of NDIs **1-8** against MRC5 and *T. Brucei*; **B)** Selectivity Indexes between MRC5 and *T. Brucei* for compounds **1-8**.

The case of NDIs **1-8** is even more remarkable if a comparison between their toxicity on *T. Brucei* and normal human fibroblast MRC5 is performed: in fact, all compounds display potent toxic effect at very low concentrations, with only negligible effect on MRC5 survival. Selectivity indexes have been measured and, as it's possible to observe, excellent specificity has been accomplished with basically each NDI. Once again, **8** showed the most effective result, with S.I. = 49, together with the thio-glucose derivative **2**, whose S.I. reached the maximum value (S.I. = 51). These observations are fundamentals, because not only evidenced that NDIs **1-8** display potent antiparasitic effects, but also that they can selectively act on parasites at low concentrations, with only low to null-side effects on human cells.

From these experimental results emerged that, as expected, conjugates **1-16** showed interesting biological activity. In particular, dimethylamino derivatives **1-8** are characterized by higher toxicity against cancer cells and, among them, **8** displayed excellent selectivity, suggesting its potential use for therapeutic applications.

3.1.5 Affinity for Telomeric Quadruplex

Because of the relevant biological activity showed by compounds **1-16**, against cancerous cells, we have also explored their binding properties towards specific quadruplex forming sequences, in particular with telomeric G4, F21T, whose stabilization induce significant anticancer activity. To evaluate the affinity of our ligands for the target, we have exploited Fluorescence Resonance Energy Transfer assay (FRET Melting assay). In this kind of experiments, oligonucleotide sequences modified with two fluorophores, is unfolded increasing the temperature (usually up to 95°C) and modification of the structure induces variation of the fluorescence signal intensity. Plotting the emission (at fixed wavelength) versus the temperature, the melting temperature of the oligonucleotide, in presence or in absence of a ligand, can be measured.

Each ligand has been tested against F21T at two concentrations, 1 and 2 μM , and results reported here are the average of three different measurements. Data are summarized in *Figure 3.3* and the first thing that it's possible to notice is that binding affinities are in perfect accordance with biological data: indeed, NDIs **1-8**, characterized by the presence of (dimethylamino)-propylamine, displayed significantly higher stabilization compared to morpholine derivatives, with values ranging from 13 to 24 °C. On the contrary, compounds **9-16** displayed low affinity for the target, with melting temperatures that are never above 12°C, even at higher concentrations. Then, it should be underlined that the affinity for the target depends mostly on the amine introduced at the imide position of NDI, rather than the type of sugar introduced: indeed, from reported data, it appears evident that the nature of the sugar does not influence the stabilization property of the ligand. Similarly, replacement of oxygen with sulphur did not induce any significant variation of the affinity for the target.

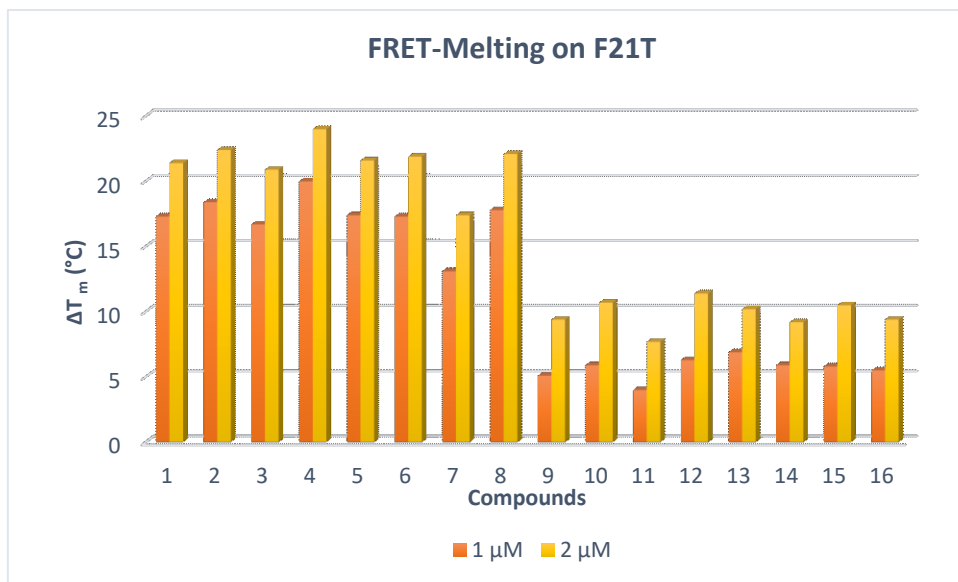


Figure 3.3 – Results of FRET-Melting assay, performed on NDIs **1-16, at 1 and 2 μM, in presence of 0.2 μM of F21T, LiCaco 10 mM, KCl 10 mM and LiCl 90 mM.**

Only in the case of NDIs **7** and **8**, containing maltose and thio-maltose, respectively, a little variation of induced stabilization is observed: at 1 μM concentration, **7** displayed ΔT_m = 13°C, which increased significantly with **8** (ΔT_m = 17,8°C). However, the highest stabilization was afforded by compounds **4** (ΔT_m = 20°C), followed by **2** (ΔT_m = 18,4°C), even if their toxicity was slightly lower compared to other scaffolds of the same series.

The most interesting fact emerged from these experiments is the clear correlation between the quadruplex binding affinity and the toxicity against tumor cells, HT29: indeed, morpholine derivatives **9-16**, that presented lower activity against cancer cells, induced also poor stabilization of the target. Conversely, NDIs **1-8** are responsible of both elevated toxicity and higher stabilization of telomeric quadruplex, suggesting that their biological properties could be determined by interactions with the target also in the cellular environment.

These interesting outcomes represents a good preliminary evaluation of the biological behaviour of synthesized ligands, but further experiments are mandatory to reinforce these data, as the evaluation of binding affinity of ligands for other common G4s and their selectivity in presence of double and single-stranded DNA.

3.1.6 Spectroscopic Properties

To effectively determine if synthesized NDI-carbohydrate conjugates **1-16** could be exploited also as G4 sensors, we have analyzed spectroscopic and fluorescence properties of one representative compounds, **8**. The choice to analyze only one derivatives is reasonable justified by the fact the nature of amines in imidic positions and of the sugar, connected through an alkyl chain to the aromatic core of NDI, don't affect absorption and emission properties of NDI scaffold. Indeed, what is really decisive is the presence of two electron-withdrawing imidic groups and the presence of electron-rich amine directly attached on naphthalene. Therefore, here we have reported the UV-VIS and fluorescence analysis of compound **8**, bearing 3-(Dimethylamino)-1-propylamine and thio-maltose.

Initially, we have measured molar absorbivity of the substrate in both DMSO and water solution: in details, increasing amount of a stock solution of **8** ($C = 2.7 \text{ mM}$) have been added to 3 ml of solvent, up to $35 \mu\text{M}$ concentration, and analyzed with UV-VIS spectrophotometer. As reported in *Figure 3.4*, molar absorptivities were not significantly different in water and DMSO solution and they displayed similar values. In the spectra, it is possible to observe the typical $\pi-\pi^*$ absorption band of NDI core, with double peak at 354 and 375 nm, and the charge-transfer band (CT), with maximum at 514 nm, originated by presence of electron-rich amine on aromatic core of NDI.

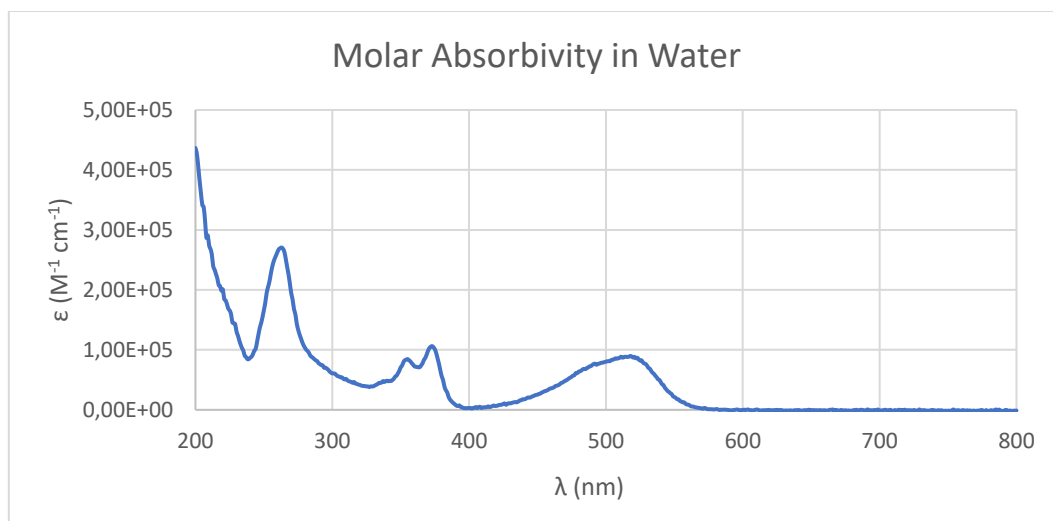


Figure 3.4 – UV-VIS Aborption of compound **8 in Water.**

At this point, we have investigated its fluorescence properties, again in water and in DMSO solution. Their emission has been compared at $27 \mu\text{M}$ concentration, upon excitation at $\lambda = 350 \text{ nm}$ in water and $\lambda = 310 \text{ nm}$ in DMSO. As it is possible to observe in *Figure 3.5*, fluorescence intensity was significantly higher in water and moreover, in this case the maximum emission was recorded at 580 nm, while in DMSO was at 568 nm.

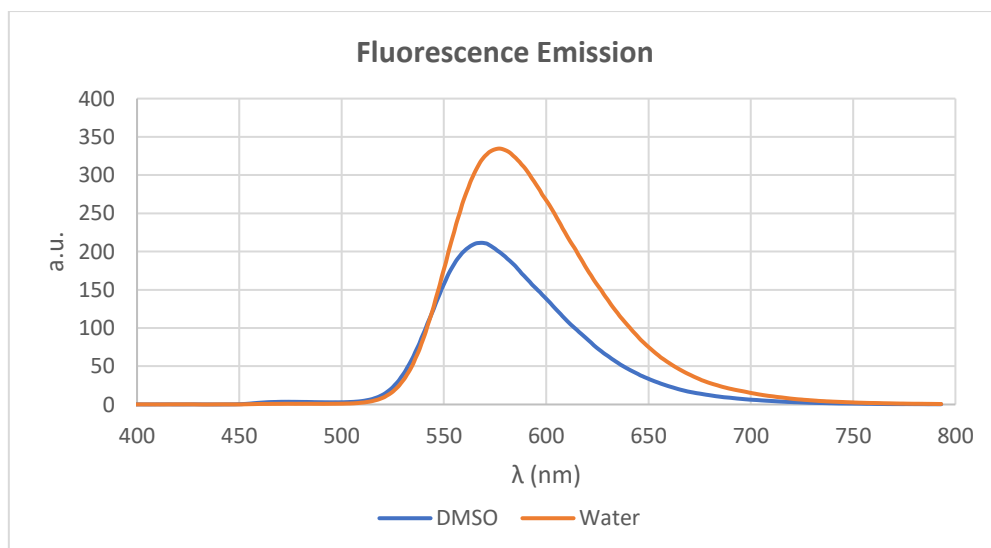


Figure 3.5 – Fluorescence emision of **8 ($C = 27 \mu\text{M}$) in water and DMSO.**

To confirm these qualitative observations, we have measured fluorescence quantum yields (Φ_f) in both solvents, using DAPI (4',6-diamidino-2-phenylindole) as standard reference. The experiment was performed adding increasing volumes of stock solution of **8**, in 3 ml of solvent, up to 30 μM concentration. Each value, reported in *Table 3.4*, is the result of three different measurements. As expected, quantum yield in water was almost one order of magnitude higher compared to DMSO and was equal to 0.15 ± 0.04 , an excellent outcome, that confirmed that NDI-carbohydrate can efficiently employed as sensor in physiological environment.

Φ_f (H ₂ O)	Φ_f (DMSO)
15 ± 4	2 ± 1

Table 3.4 – Fluorescence Quantum Yield of compound **8 in water and DMSO.**

3.1.5 Conclusions

This first part of the work has been focused on the design and the synthesis of novel conjugates NDI-carbohydrates, to explore the effect of monosaccharides or disaccharides on the biological activity of these well-known quadruplex ligands, in particular as both anticancer and antiparasitic agents. The presence of NDI scaffold offers the possibility to exploit these derivatives also as a fluorescent probes: spectroscopic analysis of compound **8** confirmed this possibility. Indeed, not only they present absorption in the visible region, centred at 500 nm, but they display the highest emission intensity in water solution, at 580 nm, with a fluorescence quantum yield which is competitive with some of the most common employed fluorescent dyes, such as cyanines.

Biological assays demonstrated that introduction of carbohydrates was a successful strategy: NDIs **1-16** affected in a significant manner the survival of cancer cells and, in particular, 3-(dimethylamino)propylamino derivatives displayed a more pronounced effect. In this context, compound **8** emerged not only for its effect towards tumour cells, but in particular for its excellent selectivity, which could offer a potential therapeutic window.

Additionally, NDIs-sugars showed also interesting antiparasitic activity, with more marked effects on *T. Brucei*. IC₅₀ determined against this parasite were significantly lower, compared to values obtained with cells, and highest toxicity was observed with Thio-Galactose derivative **6**. Furthermore, IC₅₀ values measured against *T. Brucei* are significantly lower than values recorded on normal human fibroblasts, evidencing that these NDIs could be exploited as selective antiparasitic drugs, with low side effects on normal human cells. The last interesting observation that could be highlighted is that, from these studies, most remarkable results have been accomplished with thio-carbohydrates, especially in the case of the NDIs **8**, and **6**, the most toxic on *T. Brucei*, and **2**, that emerged for its unprecedented selectivity towards the parasite.

FRET-Melting analysis clearly highlighted the excellent affinity of the ligands **1-8**, for telomeric quadruplex, evidencing that their promising antitumor activity could be determined by their interaction with the target in physiological environment. Obviously, additional experiments are required to effectively confirm this hypothesis, analysing their affinity for other quadruplex sequences and double and single-stranded DNA. These encouraging preliminary results represent a solid base for further investigations of the behaviour of these conjugates: in particular, the elucidation of their mechanism of action is necessary, to understand if they could effectively be used as anticancer and antiparasitic agents at therapeutic levels.

4. Results and Discussion: Quinone Methides

4.1 Towards Alternative Targeting Strategies: Quinone Methides

4.1 Development of Bi-functionals Photo-Alkylating Ligands

4.1.1 State of Art and design of ligands

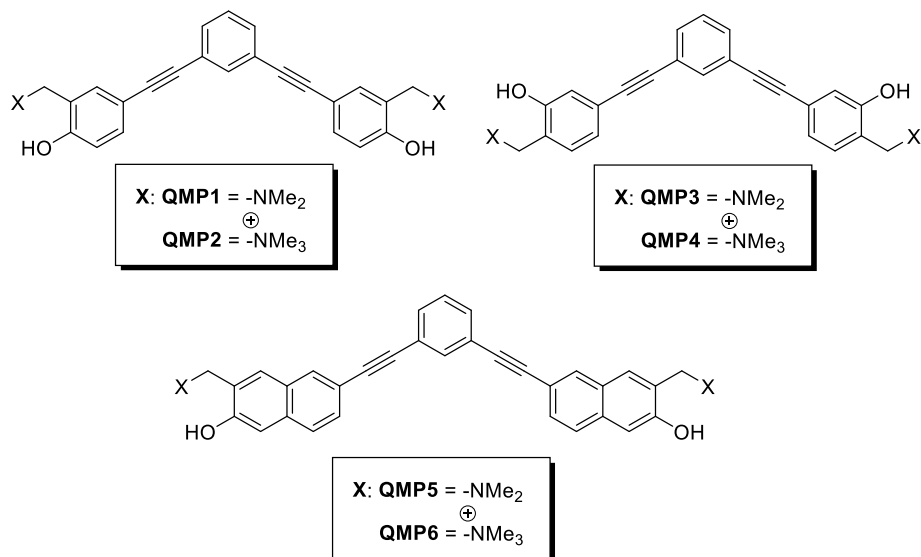
In the quadruplex research field, photo-activatable molecules are attracting significant attention, as described in the Introduction.

An approach that resulted to be particularly promising, but it is still little explored, is the formation of a covalent bond with the target. The advantage of this approach relies on the possibility to “lock” the ligand on its specific target, reducing off-target interactions and possible collateral and undesired process.

Quinone Methides (QMs) are particularly suitable to this purpose: they can be easily photogenerated by different types of precursors and have already been employed to target both proteins¹⁵² and nucleic acids¹³⁸. Photogeneration of quinone methides have been extensively studied by Freccero’s group¹⁸⁸ and it has been demonstrated that it is highly efficient using Mannich bases and their corresponding ammonium salts, as light-responsive precursors.

However, in order to achieve selective targeting of quadruplex structures, in cellular environment, quinone methide precursors should satisfy two requirements: 1) high affinity for the target, to ensure selective alkylation of the target, avoiding side-processes; 2) biocompatible activation wavelength, to prevent DNA damages.

Then, this part of the project has been focused on the design and the synthesis of novel quadruplex ligands, bearing not one, but two quinone methide precursors, to induce cross-alkylation of the DNA sequence, that reinforce the bond with the target and avoid possible off-target migration¹⁵⁵. Moreover, the simultaneous presence of two precursors, should increase the cross-section, without affecting the photoreactivity, leading improved efficiency of the overall process.



Scheme 4.1 – V-Shaped Ligands synthesized as novel Quinone-Methide Precursors.

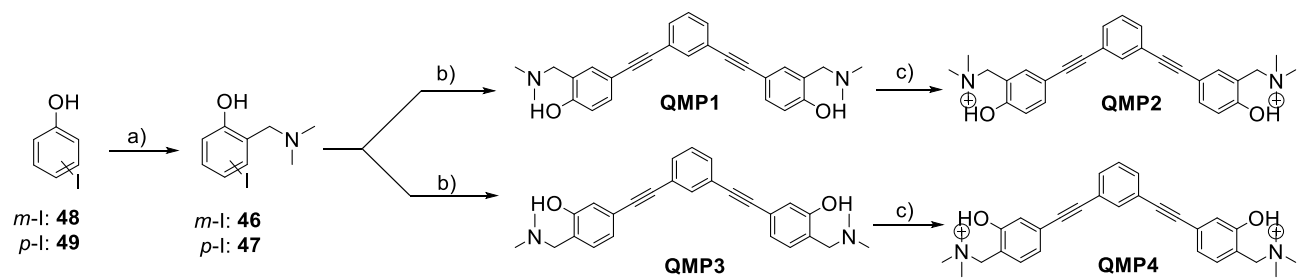
For what concern the structure of the compounds, we designed novel “V-shaped” ligands (*Scheme 4.1*): this choice was driven by the recent discovery that non cyclic structure with this particular structural shape, constituted by non-fused aromatic rings, presented high affinity for several quadruplex forming sequences¹⁰⁸. On this basis, we have developed six novel compounds, **QMP1-QMP6** (*Scheme 4.1*), characterized by three aromatic phenyl rings and, in the case of **QMP5** and **QMP6**, by one phenyl ring and two naphthalene moieties, connected through two alkyne spacers: this particular disposition has been driven by the necessity to realize a fully conjugated system, in order to red-shift the wavelength of activation of these compounds.

For each ligand, we have investigated their photochemical behaviour, evaluating the efficiency of the generation of corresponding quinone methides, and the products formed by this photochemical transformation. In a second moment, we have analyzed their affinity for several quadruplex forming sequences through FRET-Melting assay and Circular Dichroism analysis and, in the end, their ability to alkylate specific quadruplex has been determined.

4.1.2 Synthesis of the Compounds

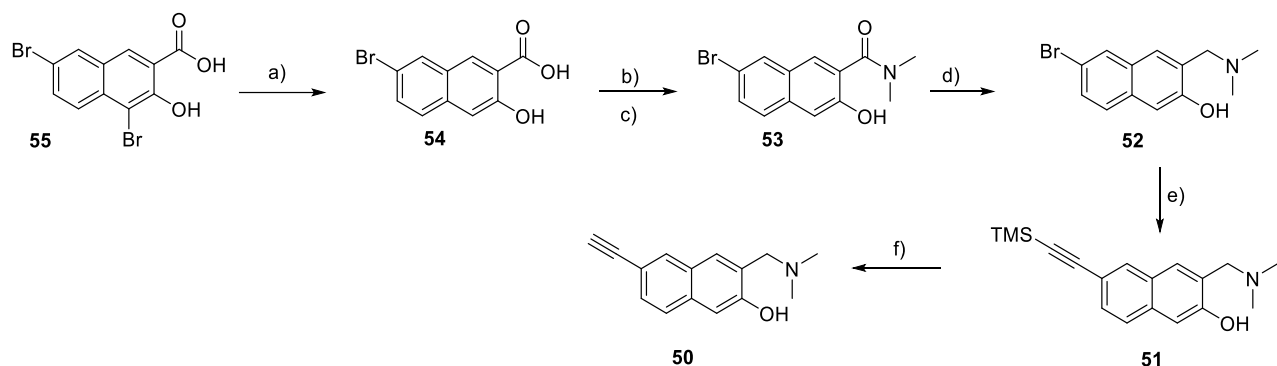
For the synthesis of compounds **QMP1-QMP6**, two different synthetic strategies have been adopted, one for **QMP1-QMP4** and the second one to produce the two naphthalenic-based derivatives **QMP5** and **QMP6**.

The key steps of the adopted protocols are Sonogashira cross-coupling exploited to conjugate the different aromatic moieties. In details, synthesis of precursors **QMP1-QMP4** started from commercially available *m*-iodophenol (**48**) and *p*-Iodophenol (**49**). The first step was based on a Mannich reaction, to introduce the dimethylamino group in orhto-position, respect to hydroxy group, fundamental for the subsequent generation of quinone methide (*Step a in Scheme 4.2*). These reactions were carried out in presence of paraformaldehyde and dimethylamine and were refluxed in ethanol for two hours, to afford the desired product in moderate yield (33%). After purification through column chromatography, **46** and **47** have been employed for the subsequent Sonogashira cross-coupling with 1,3-diethynylbenzene (*Step b in Scheme 4.2*). High amount of catalyst (10% of Bis(triphenylphosphine)palladium chloride [$Pd(PPh_3)_2Cl_2$] and copper iodide (10%) afforded the desired products, **QMP1** and **QMP3**, in 39% and 20% yield, respectively, even after 16 hours at 60°C, evidencing the poor reactivity of this scaffold. Quantitative methylation of these two products was achieved upon treatment with an excess of iodomethane, in presence of sodium acetate, for two days, at room temperature (*Step c in Scheme 4.2*).



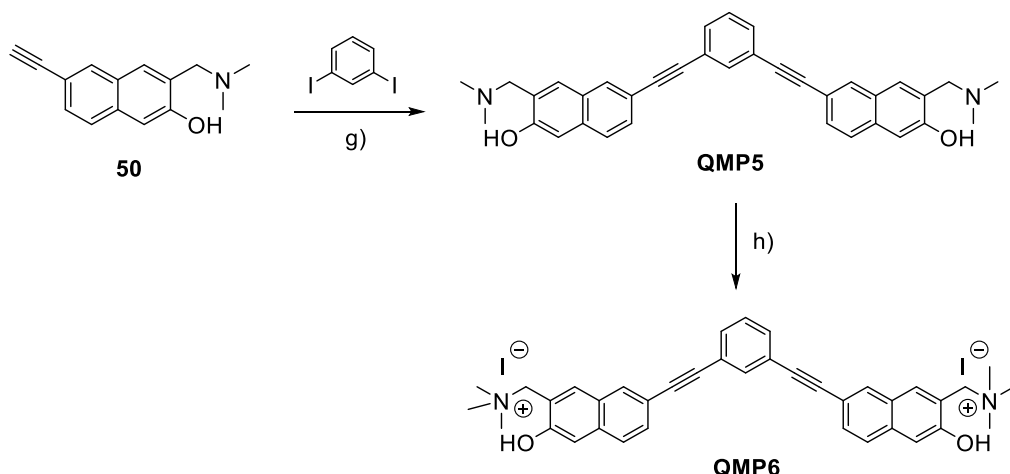
Scheme 4.2. – Procedure for the synthesis of **QMP1-QMP4**: a) Paraformaldehyde (18 eq.), HNMe₂ (33% solution in ethanol), EtOH, reflux, 2h; b) [Pd(PPh₃)₂]Cl₂ (10%), Cul (10%), 1,3-diethynylbenzene (1 eq.), THF:TEA 2:1, 60°C, 16h ; c) CH₃I (5 eq.), NaOAc (1 eq.), ACN, r.t., 2d.

Synthesis of two-naphthalene based precursors required more synthetic steps, starting from compound **55**: reductive dehalogenation with tin, in refluxed acetic acid, led to carboxylic acid **54** (*Step a* in Scheme 4.3) with quantitative yield. The corresponding amide **53** was obtained in 93% yields in two-steps: treatment of **54** with thionyl chloride generated the intermediate acyl chloride, reacted with dimethylamine solution in Schotten-Baumann conditions, in presence of sodium hydroxide (*Step b* and *c* in Scheme 4.3). To obtain Mannich-base **52**, we have performed a reduction with lithium aluminium hydride. Finally, in this case we have exploited Sonogashira cross-coupling to conjugate the alkyne to naphthalene unit: in this case, reaction was performed with lower amount of palladium complex (4%) and copper iodide (4%), in pure triethylamine and, after only two hours under reflux, product formation was completed. Deprotection of trimethylsilyl with potassium carbonate, in methanol solution, afforded the final precursor **50**, used for the synthesis of **QMP5** and **QMP6**.



Scheme 4.3 – a) Sn (1.3 eq.), HCl 37% : CH_3COOH (1:3), reflux, 12h; **b)** SOCl_2 , reflux, 4h; **c)** HNMe_2 (11% in EtOH), NaOH (1.2 eq.), DMC , 0°C, 1h; **d)** LiAlH_4 (2.5 eq.), THF , 0°C-reflux, 2h; **e)** ethynyltrimethylsilane (4 eq.), $[\text{Pd}(\text{PPh}_3)_2]\text{Cl}_2$ (4%), Cul (4%), TEA , 80°C, 1h; **f)** K_2CO_3 (4 eq.), MeOH , r.t., 2h.

Finally, the synthesis of two final products, **QMP5** and **QMP6**, have been accomplished in two-reaction steps: **50** was used for a second Sonogashira cross-coupling with commercially available 1,3-diiodobenzene, using the same procedure described previously, with 4% of palladium catalyst, in pure triethylamine. After only two hours at 80°C, **QMP5** was obtained in 86% yield (*Step g* in Scheme 4.4). Subsequent methylation, with iodomethane (*Step h* in Scheme 4.4), afforded the final product, **QMP6**, in quantitative yield.



Scheme 4.4 – Synthesis of QMP5-QMP6: **g)** 1,3-diiodobenzene (0.5 eq.), $[\text{Pd}(\text{PPh}_3)_2]\text{Cl}_2$ (4%), Cul (4%), TEA , 80°C, 2h; **h)** CH_3I (5 eq.), NaOAc (1 eq.), ACN , r.t., 2d.

4.1.3 Spectroscopic Properties and Photochemical Behaviour

In a first moment, we have analyzed absorption profile of compounds **QMP1-QMP6**, to identify the most suitable wavelengths for photoactivation. Spectra have been recorded in pure water and in buffered solution at pH 7.2 (KCl 100 mM, LiCaco 10 mM) and they are reported in *Figure 4.1*. Phenyl derivatives **QMP1-QMP4** presented maximum absorption among 290 and 299 nm in water, that is red-shifted up to 320 nm in buffered solution. Conversely, replacement of two phenyl ring with two naphthalene units had a strong impact on UV-VIS profile: the highest peak is centered at 325 nm and showed a very large band, whose tail is extended to 400 nm, suggesting that activation of precursors could be performed almost in the visible region.

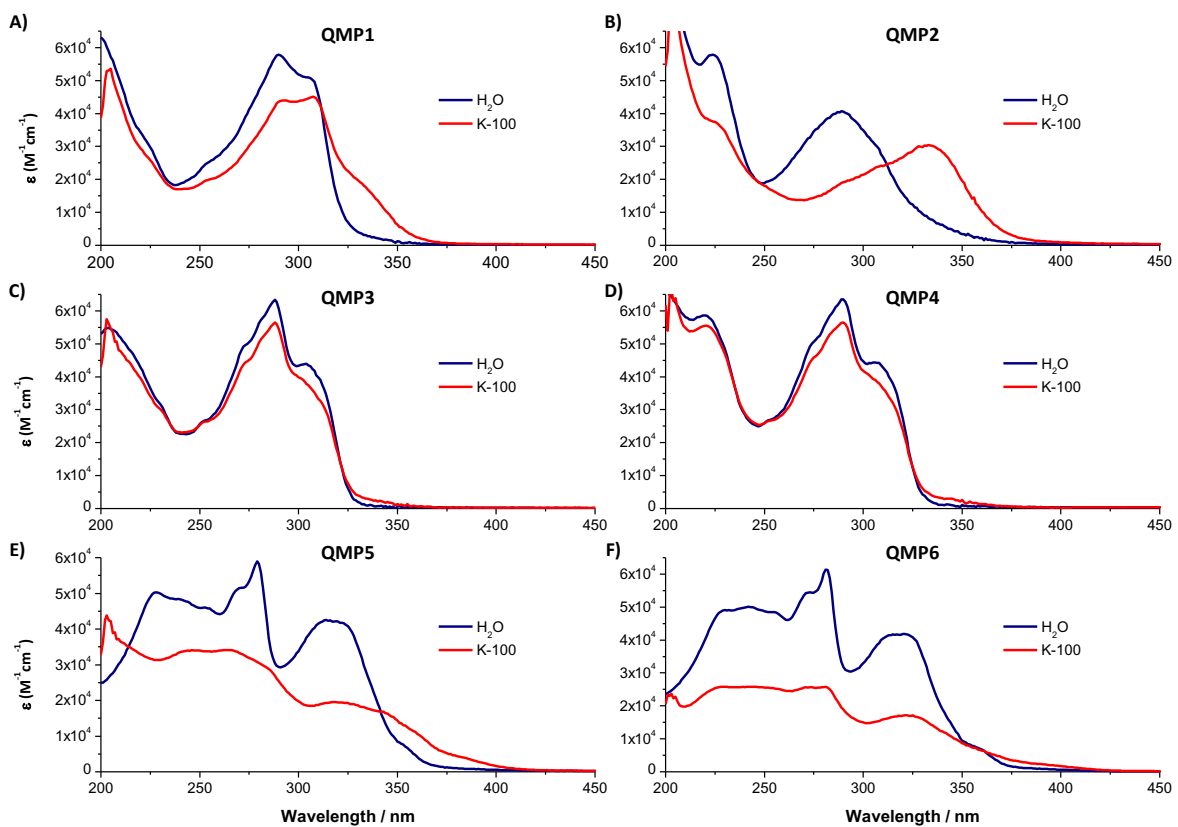


Figure 4.1 - Ligand molar absorptivity in water and in 10 mM lithium cacodylate buffer (pH 7.2), 100 mM KCl.

Moreover, as it's possible to observe in *Figure 4.1*, pH has a significant impact on the absorption properties of the compounds, in particular on **QMP1**, **QMP2**, **QMP5** and **QMP6**: at pH 7.2, the hydroxy group is partially deprotonated and the present of a negative charge induces a red-shift of maximum peaks of the spectra. These data are summarized in *Table 4.1* and, as it's possible to observe, molar absorptivity is rather similar for all derivatives. Furthermore, these data evidenced that activation of these compounds can be performed at more compatible wavelengths, as 365 nm and, for some of them, even at 400 nm.

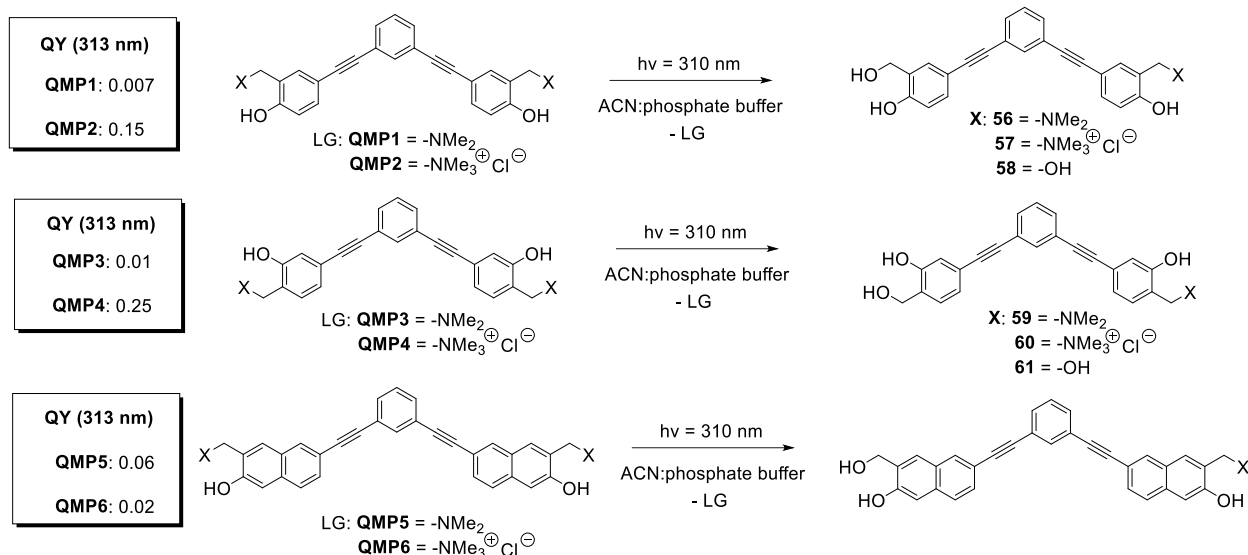
Ligand	Solvent	λ_{max} (nm)	$\epsilon_{\text{max}} (\text{M}^{-1} \text{cm}^{-1})$	$\lambda_{\text{Abs tail}}$ (nm)
QMP1	Water	299	$5.24 \cdot 10^4$	340
	Buffer	320		380
QMP2	Water	291	$6.28 \cdot 10^4$	340
	Buffer	320		380
QMP3	Water	291	$5.80 \cdot 10^4$	327
	Buffer	291		327
QMP4	Water	291	$6.28 \cdot 10^4$	327
	Buffer	291		327
QMP5	Water	325	$4.08 \cdot 10^4$	380
	Buffer	325		410
QMP6	Water	325	$4.08 \cdot 10^4$	380
	Buffer	325		410

Table 4.1 – Absorption properties of compounds QMP1-QMP6 in water and in buffer (KCl 100 mM, LiCaco 10 mM, pH 7.2).

In a second moment, we began the evaluation of their photoreactivity, to verify their ability to undergo to photolysis and generate the corresponding intermediate quinone methide. To this aim, we have measured, for each derivative, photolysis quantum yields (Φ) of substrate consumption, a photochemical parameter to indicate the rate of precursor photolysis and intermediate generation, taking into account the photon absorbed by the substrate. Then, we have irradiated compounds **QMP1-QMP6** at 313 nm, in 1:1 ACN: buffered solution at pH 7.4 (phosphate buffer 50mM), with a high-pressure mercury lamp, previously calibrated by ferrioxalate actinometry. Quantum yields have been determined applying the following equation:

$$\Phi (313 \text{ nm}) = (\text{mol of tetrazoles reacted}) / \text{mole of absorbed photons}$$

and monitoring substrate consumption through HPLC analysis. Irradiation of precursors **QMP1**, **QMP3** and **QMP5** resulted in very low quantum yields values, as reported in *Scheme 4.5*, and, even after 30 minutes of irradiation, only low substrate conversions were accomplished (never above 30%). On the contrary, ammonium salts **QMP2** and **QMP4** showed efficient photolysis ($\Phi = 0.15$ and $\Phi = 0.25$, respectively) and almost complete substrate conversion (90%) was achieved only in 9 minutes of irradiation. This marked difference in photoreactivity depends on the fact that ammonium salts are better leaving groups, compared to neutral dimethylamino derivatives. Interestingly, **QMP6**, displayed only low conversion in these experiments, despite the presence of two ammonium salts.



Scheme 4.5 – Photolysis Quantum Yields and photoproducts observed for QMP1-QMP6.

Quinone methides are reactive intermediate, not stable in solutions, whose lifetime is in the order of milliseconds, therefore their formation can be proved only in two ways: 1) through laser-flash photolysis (which allow the analysis of short-living intermediates) and 2) through isolation of products originated by the reaction of quinone methide with species present in solution. In our case, to evidence QM generation, we decided to adopt the second strategy and we have irradiated our compounds on a preparative scale, to isolate and characterize photoproducts derived by addition to water (*Scheme 4.5*). To this purpose, we have irradiated our compounds with multi-lamps photoreactor (Rayonet), with two lamps (32W) at 310 nm, and different outcomes have been observed, depending of the type of substrate. In details, Mannich-bases **QMP1** and **QMP3** showed not only low reactivity but, even with long irradiation times (up to 90 minutes) the major products formed were not the expected **56** and **59** (*Scheme 4.5*), but **62** and **63** (*Scheme 4.6*), derived from the photohydration of one of alkyne moiety. Further experiments demonstrated that this byproduct was formed exclusively upon photoirradiation and it was not the result of a ground state reactivity. The expected quinone methide derivatives, **56** and **59** are produced only in traces (<1%) and their formation has been detected only through LC-MS analysis.

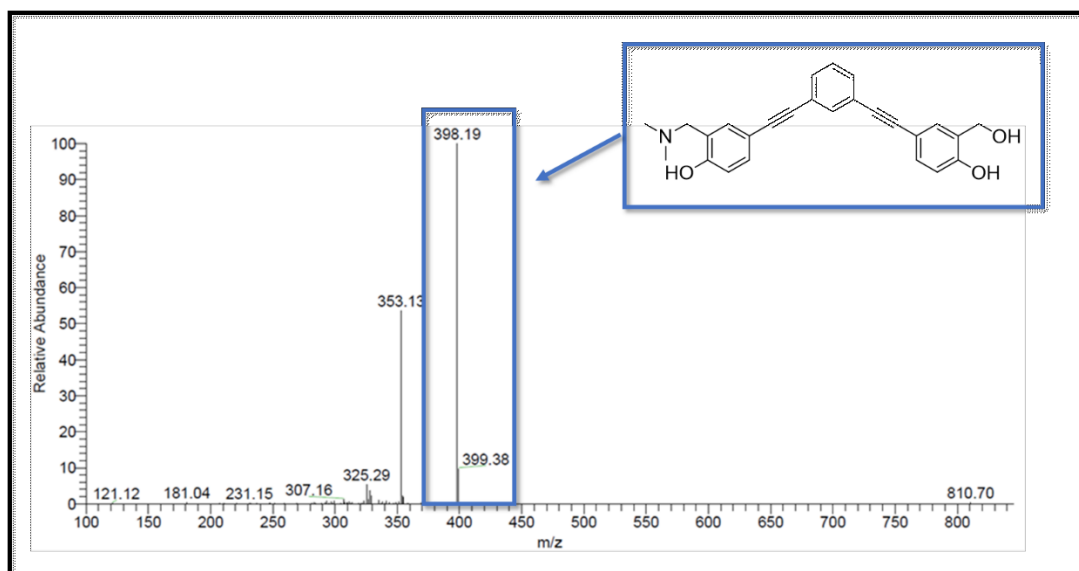
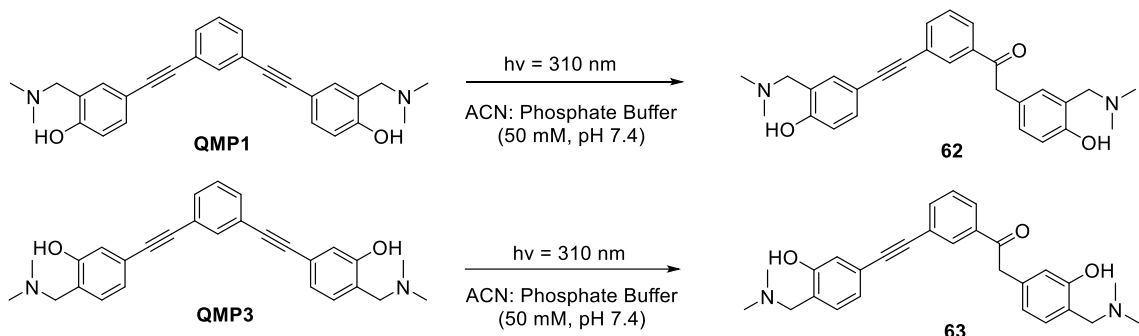


Figure 4.2 – ESI-MS analysis of hydration product **62.**

On the contrary, ammonium salts **QMP2** and **QMP4**, in accordance with quantum yields measurements, displayed elevated photoreactivity and, only after 30 minutes in the photoreactor, substrate was completely consumed (conversions above 90%). Moreover, in this case we have demonstrated the formation not only of the expected adducts **57** and **60**, but even of bis-hydration products, **58** and **61**. It should be highlighted that, with these compounds, hydration of alkyne moiety has not been observed, even in trace.



Scheme 4.6 – Photogeneration of hydrated alkynes **62 and **63**.**

These experiments evidenced the different reactivity of synthesized precursors, strongly affected by the nature of the leaving group, which could consequently lead to different alkylation efficiency of quadruplexes. However, isolation of hydration products **57**, **58**, **60** and **61** represents a solid proof of quinone methide photogeneration and formation of mono- and bis-adducts could result in corresponding mono- and bis-alkylation of DNA, as assumed during design of the molecules.

4.1.4 Biophysical Assays

To evaluate the binding affinity and selectivity of **QMP1-QMP6** for quadruplex structures, different biophysical assays have been performed, including FRET-Melting and Circular Dichroism Analysis. Stabilization properties of our ligands have been evaluated towards a small pool of quadruplex forming-sequences, differing for the type of topology: the telomeric F21T, two variants of parallel c-MYC (FMyct and F(Pu24T)T), differing for the size of central loop, c-KIT2, the human minisatellite repeat native sequence FCEB25wtT, a sequence from BCL2 (FBcl2T) and antiparallel telomeric F21CTAT. Experiments were performed with 0.2 μ M of oligonucleotide in presence of 2 μ M ligand and, in general, no one of the tested compounds showed remarkable stabilization properties. The best outcomes have been observed with **QMP2** ($\Delta T_{mF21T} = 7.9^\circ\text{C}$ and $\Delta T_{mFMyct} = 8.1^\circ\text{C}$)- and **QMP6** ($\Delta T_{mF21T} = 7.1^\circ\text{C}$ and $\Delta T_{mFMyct} = 8.1^\circ\text{C}$ - in the presence of F21T and FMyct, respectively).

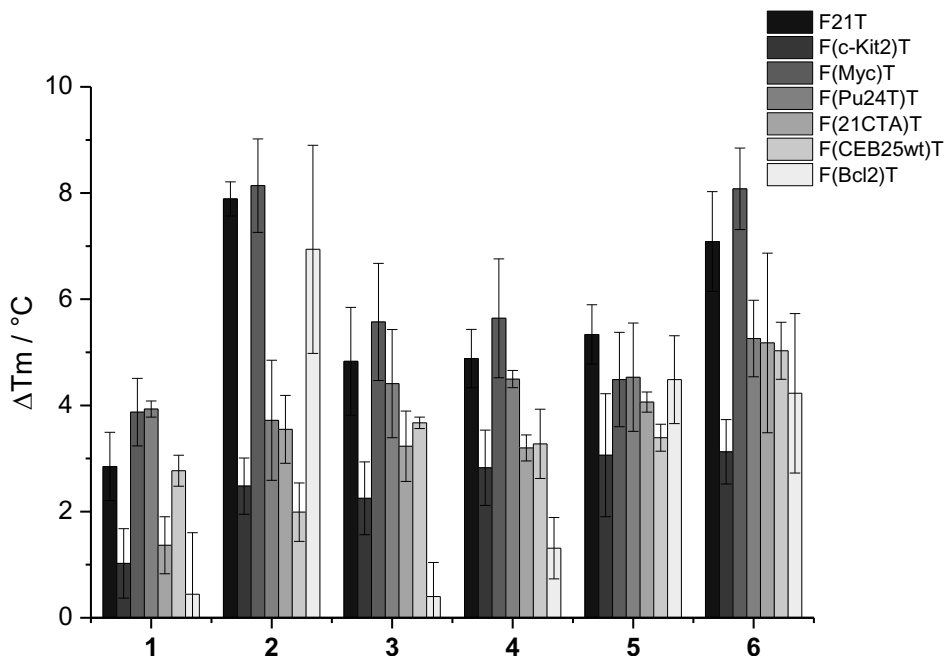


Figure 4.3. - FRET-melting experiments in the presence of F21T, F(c-KIT2)T, F(Myc)T, F(Pu24T)T, F(21CTA)T, F(CEB25wt)T, and F(BCL2)T (0.2 μ M). Experiments were performed with LiCaco 10 mM (pH 7.2), LiCl 99 mM and KCl 1 mM (LiCl 90 mM and KCl 10 mM for F21T and F(21CTA)T), in presence of **QMP1-QMP6** (2 μ M). Standard deviation is the result of three different measurements.

Despite a marked selectivity towards a specific topology has not been individuated, further experiments have been performed on telomeric F21T and on F(Pu24T)T, to demonstrate their effective ability to interact with the target. FRET-melting experiment on these two oligonucleotide sequences has been repeated in presence of increasing concentrations of ligands **QMP1-QMP6**, up to 20 μ M (corresponding to 100 eq.), and with **PhenDC3**, as a reference: in *Figure 4.4*, ΔT_m values are reported as a function of compound concentration and, as it is possible to observe, at only 2 μ M, there's no significant difference in the stabilization induced by different compounds. Gradually increasing the concentration, a specific trend can be observed, which is basically the same with both oligonucleotides: in details, **QMP6** showed highest stabilization properties, with $\Delta T_m = 33^\circ\text{C}$ and 29°C for F21T and F(Pu24T)T, respectively, at 20 μ M. It was followed by its corresponding Mannich-base, **QMP5**, while phenyl derivatives showed significantly lower stabilization, even at elevated ligand concentration, with **QMP3** and **QMP4** presenting slightly better efficiency. It seems that the interactions with the target are more influenced by the substituents disposition (*meta* or *para*) rather than the nature of the leaving group.

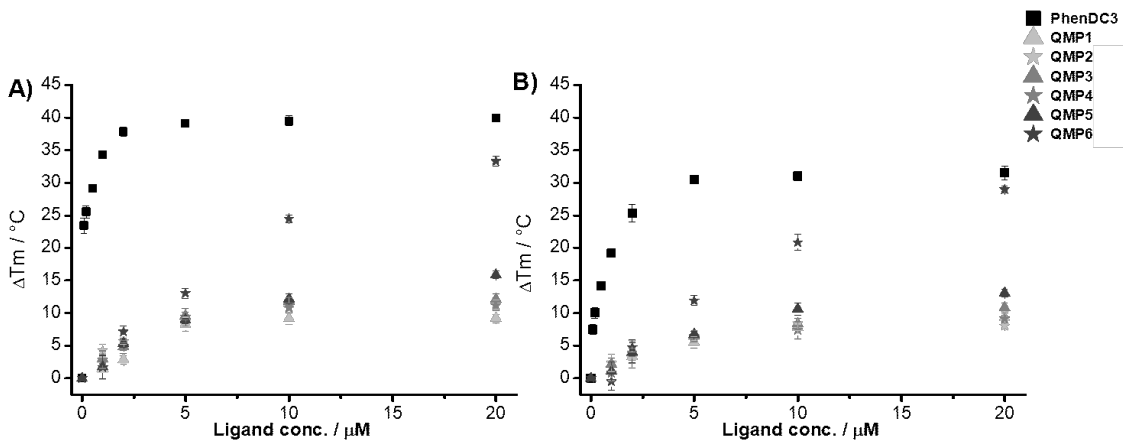


Figure 4.4 - ΔT_m dependence of (A) F21T and (B) F(Pu24T)T as a function of ligand concentration. (A) Experiments performed with DNA 0.2 μ M, LiCaco 10 mM (pH 7.2), LiCl 90 mM and KCl 10 mM; (B) Experiments performed with DNA 0.2 μ M, LiCaco 10 mM (pH 7.2), LiCl 99 mM and KCl 1 mM. **QMP1-QMP6** were used in concentration from 0 μ M up to 20 μ M. **PhenDC3** was used as a reference compound.

Once their ability to interact with G4s has been assessed, the selectivity of ligands **QMP1-QMP6** have been tested in presence of increasing concentrations of non-fluorescently labelled, double-stranded DNA (ds26), again through FRET-Melting assay. With F(Pu24T)T, due to the lower stabilization observed previously, the experiments have been carried out in presence of 100 eq. of compounds. Measures were recorded at 0, 3 and 10 μ M of double-stranded DNA and, as reported in *Figure 4.5*, all compounds displayed good selectivity and the ΔT_m , for each compound, remained basically unaffected in presence of the competitor. This result evidenced that, despite the poor stabilization properties of quinone methide precursors, they are able to interact selectively with the desired target, even in a more complex environment.

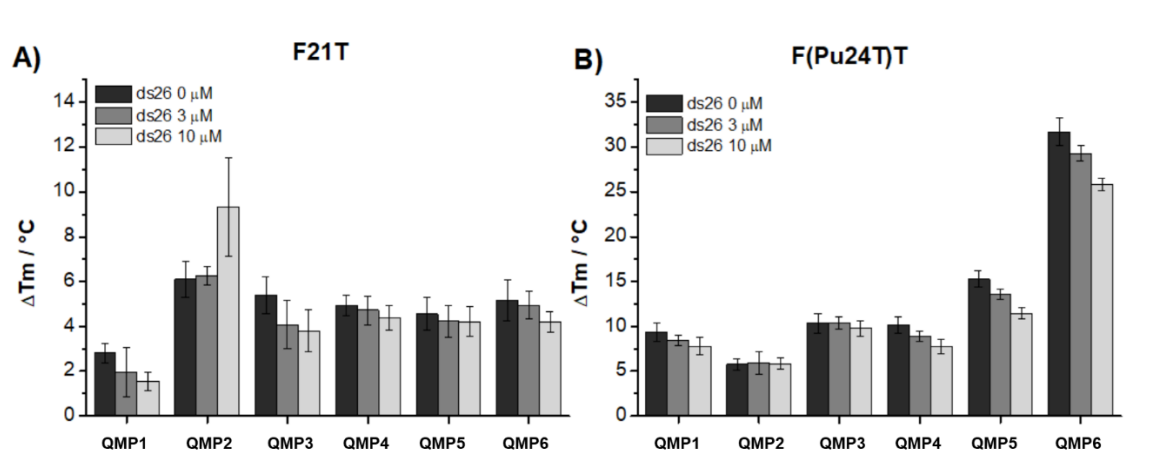


Figure 4.5 - FRET-melting competition assay with (A) F21T and (B) F(Pu24T)T in the absence and in the presence of double-stranded DNA competitor (ds26). (A) Experiments performed with F21T 0.2 μ M, compounds 1 μ M, ds26 0, 3, or 10 μ M (black, dark gray, and gray bars respectively), LiCaco 10 mM (pH 7.2), LiCl 90 mM and KCl 10 mM; (B) Experiments performed with F(Pu24T)T 0.2 μ M, compounds 20 μ M, ds26 0, 3, or 10 μ M (black, dark gray, and gray bars respectively), LiCaco 10 mM (pH 7.2), LiCl 99 mM and KCl 1 mM.

To obtain more details about the interactions of quinone methide precursors with telomeric quadruplex (22AG sequence), we have performed CD titrations to measure the binding affinity constants. Experiments have been performed on pre-folded oligonucleotide in K⁺ and in Na⁺-rich buffer, to examine their behaviour with two distinct topologies (hybrid 3+1 and antiparallel, respectively). In potassium-rich buffer, dichroic signal of 22AG showed a peak at 293 nm, a shoulder at 265 nm and a trough at 240 nm, coherently with description reported in literature¹⁸⁹. Upon addition of increasing concentrations of ligands, variation of the intensities of different bands are observed: in general, an increase of the intensity of the band at 293 nm was observed, together with hypsochromic shift of 3 nm, except in case of **QMP4**, for which no one of these effects was observed. As reported in *Figure 4.6*, the presence of isodichroic points, wavelengths at which the signal intensity remains stable, evidenced a “two-state model”, an equilibrium based on the formation of single DNA-bound species from free oligonucleotide, with no formation of other intermediates. This behaviour has been observed for ligands **QMP1-QMP4**, indeed, all of them presented a clear isodichroic point at 240 nm. Conversely, naphthalene derivatives **QMP5** and **QMP6** did not show any clear isoelliptic point, suggesting that, in presence of these compounds, more bound structures contribute to the equilibrium. Another interesting fact that should be underlined is the increasing band above 300 nm, found in the spectra of **QMP3**, **QMP4**, **QMP5** and **QMP6**: since DNA does not absorb at that wavelength, it has been reasonably attributed to the induced CD spectra of the ligands, due to the chiral environment.

The same titrations were performed in Na⁺-rich buffer, condition that determine the folding of 22AG into an antiparallel quadruplex: indeed, the spectra of oligonucleotide alone, is characterized by a positive band at 295 nm and a negative one at 245 nm. Upon addition of increasing concentrations of ligands, except **QMP5**, a significant increase of the ellipticity at 260 nm was observed, accompanied by a 2nm bathochromic shift. Moreover, as in the previous experiment, isoelliptic points have been identified, confirming, also in the case, a two-states equilibrium between the bound and free DNA. **QMP5** showed a completely different behaviour from other compounds: band at 293 significantly increased, together with hypsochromic shift of 5 nm. The induced CD signal is clearly visible in the spectra of **QMP3**, **QMP4**, **QMP5** and **QMP6**, but no with other two ligands. From these experiments, it has been possible to calculate binding affinity for all compounds except **QMP5**, due to its unusual behaviour. Data are reported in *Table 4.2* and, as it's possible to observe, we have obtained dissociation constants in the micromolar range for all quinone methide precursors, in either K⁺ and Na⁺ rich solution, therefore they present only moderate affinity.

Despite both FRET-Melting analysis and Circular Dichroism evidenced a low affinity of these compounds for G4s, they also indicated good selectivity and, moreover, we should not forget that the aim of this ligand is to alkylate DNA upon photoactivation, therefore, stronger interactions could be achieved after exposure to light.

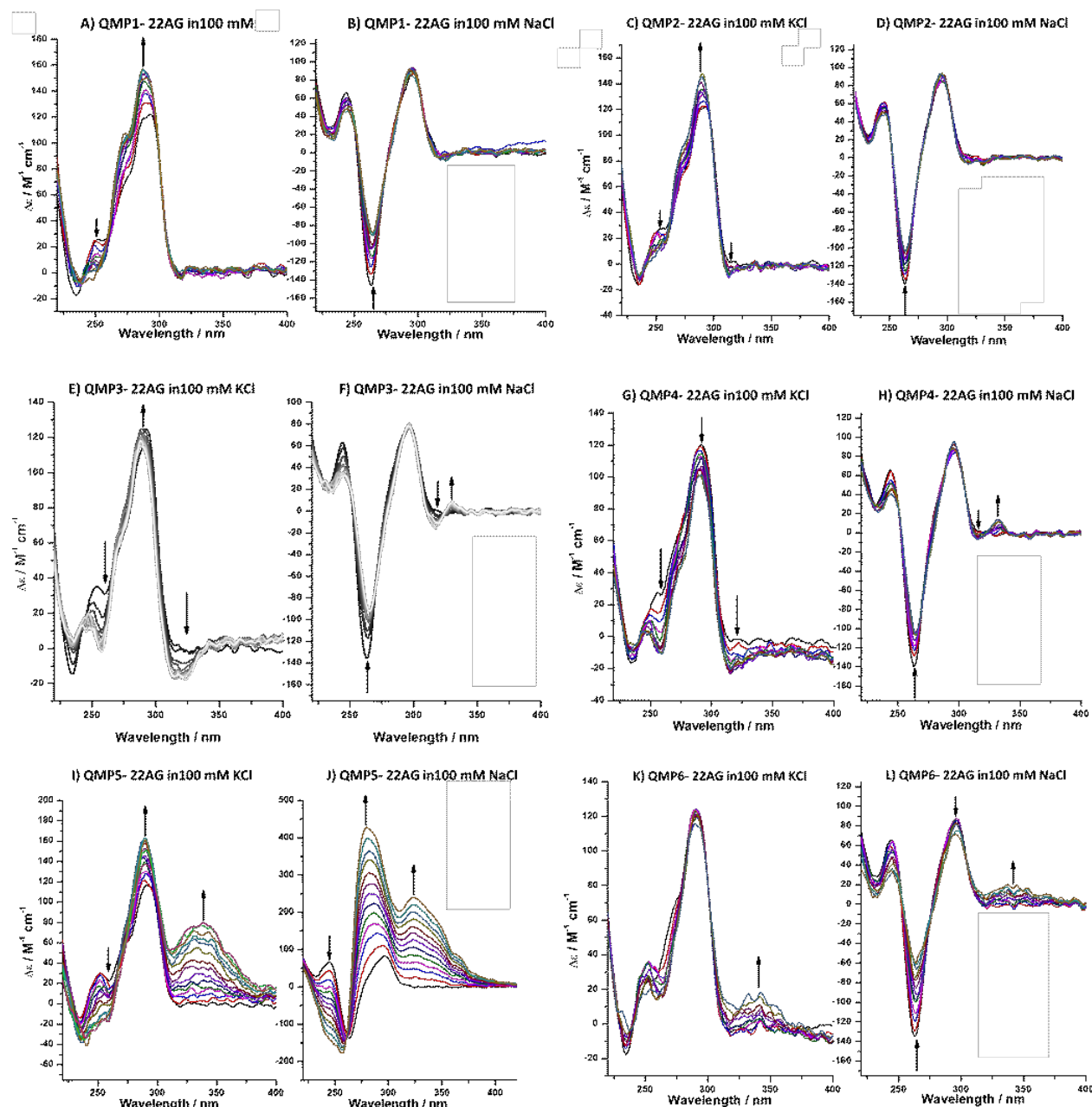


Figure 4.6 – CD Titrations of QMP1-6 with 3 μ M 22AG in K^+ - and Na^+ rich buffer. Conditions for A,C,E,G,I,K): 10 mM lithium cacodylate buffer (pH 7.2), 100 mM KCl. Conditions for B,D,F,H,J,L): 10 mM lithium cacodylate buffer (pH 7.2), 100 mM NaCl.

Ligand	$K_d \cdot K^+ (M)$	$K_a \cdot K^+ (M^{-1})$	$K_d \cdot Na^+ (M)$	$K_a \cdot Na^+ (M^{-1})$
1	$9.6(\pm 0.6) \cdot 10^{-6} (\lambda_{250})$	$1.0(\pm 0.3) \cdot 10^5 (\lambda_{250})$	$13.3(\pm 0.3) \cdot 10^{-6} (\lambda_{263})$	$0.75(\pm 0.01) \cdot 10^5 (\lambda_{263})$
	$5.9(\pm 0.7) \cdot 10^{-6} (\lambda_{290})$	$1.7(\pm 0.2) \cdot 10^5 (\lambda_{290})$		
2	$23.3(\pm 15.3) \cdot 10^{-6} (\lambda_{290})$	$0.43(\pm 0.8) \cdot 10^5 (\lambda_{290})$	$18.1(\pm 3.5) \cdot 10^{-6} (\lambda_{261})$	$0.55(\pm 0.7) \cdot 10^5 (\lambda_{261})$
3	$5.0(\pm 2.8) \cdot 10^{-6} (\lambda_{255})$	$2.0(\pm 0.7) \cdot 10^5 (\lambda_{255})$	$5.6(\pm 2.2) \cdot 10^{-6} (\lambda_{263})$	$1.8(\pm 0.5) \cdot 10^5 (\lambda_{263})$
4	$6.5(\pm 1.0) \cdot 10^{-6} (\lambda_{255})$	$1.5(\pm 0.3) \cdot 10^5 (\lambda_{255})$	$7.1(\pm 3.6) \cdot 10^{-6} (\lambda_{263})$	$1.4(\pm 0.9) \cdot 10^5 (\lambda_{263})$
5	$31.9(\pm 21.8) \cdot 10^{-6} (\lambda_{250})$	$0.31(\pm 0.7) \cdot 10^5 (\lambda_{250})$	-	-
	$14.2(\pm 3.2) \cdot 10^{-6} (\lambda_{290})$	$0.70(\pm 0.2) \cdot 10^5 (\lambda_{290})$	-	-
^a 6	$4.6(\pm 1.0) \cdot 10^{-6} (\lambda_{267})$	$2.2(\pm 0.4) \cdot 10^5 (\lambda_{267})$	$58.8(\pm 1.6) \cdot 10^{-6} (\lambda_{263})$	$0.17(\pm 0.01) \cdot 10^5 (\lambda_{263})$

Table 4.2 - Binding constants measured using a non-linear regression with the Hill equation, at proper wavelength (maximum of the ICD spectrum of **QMP1-QMP6**).

4.1.5 Photochemical Reactions on G4s

In the end, we have evaluated the ability of quinone methide precursors to effectively form a covalent bond with G4, with 22AG and Pu24T, upon activation with light. In details, we decided to exploit the extended absorption tail of the ligands and perform experiments through irradiation at 365 nm, reducing possible DNA damages. To explore the reactivity of the ligands, we have irradiated 22AG in presence of different concentrations of **QMP1-QMP6**, for various times, and formation of covalent adducts has been evidenced through denaturing gel electrophoresis analysis. In the first tests, it emerged that **QMP1**, **QMP2** and **QMP4** are able to alkylate DNA (*Figure 4.7*), while in presence of other three ligands, no product has been detected. These results are in accordance with the photochemical studies: indeed, higher alkylation efficiency has been observed with **QMP2** and **QMP4**, which displayed not only highest quantum yields, but also formed the corresponding bis- and mono-adduct with water, in significant amount. For Mannich base **QMP1**, low quantum yield was measured, and the hydrated QM was found only in trace, but its generation is confirmed also by these experiments, due to its ability to alkylate the DNA. The absence of alkylation observed with **QMP3** could be attributed to both the absence of absorption at the activation wavelength and to the low photolysis efficiency. Concerning naphthalene derivatives, their complete absence of reactivity could be attributed to their insufficient photoreactivity.

Best performances were achieved with **QMP2**: indeed, different ligand concentrations (from 1 to 10 equivalents compared to 22AG), in 60 minutes of irradiation, afforded from 6.7 to 27.9% of DNA alkylation efficiency. Good outcomes have been obtained also with the other ammonium salt, **QMP4**, that induced good alkylation yields (11.3-22.0%). It has been noticed that, at highest concentration, quinone methide precursors display also significant thermal activation, therefore it has been determined that the ligand/G4 DNA 2:1 ratio represented the optimal condition to achieve both good yields and low thermal activation.

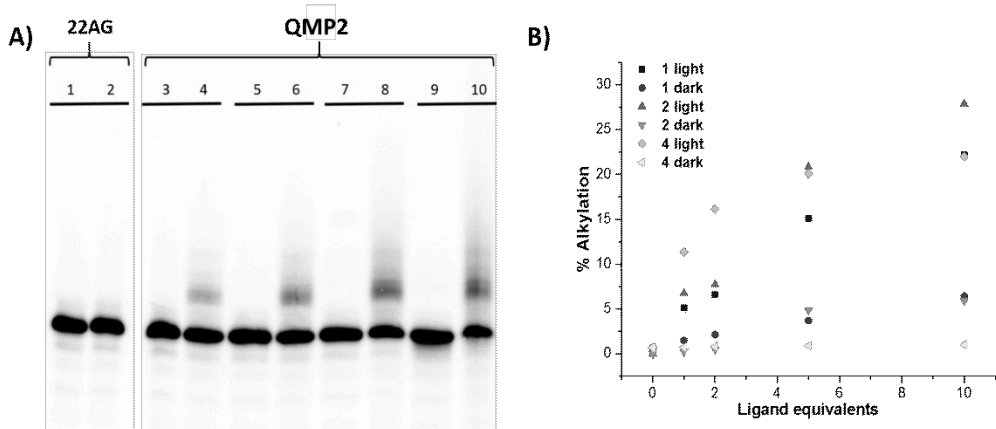


Figure 4.7 - A) Denaturing gel electrophoresis (15% acrylamide) of the adducts formed with 22AG (10 μ M) in K^+ buffer (100 mM) with **QMP2** (10, 20, 50, and 100 μ M). **B)** Analysis of alkylation yield of the telomeric sequence 22AG (10 μ M, 100 mM K-rich buffer) obtained upon irradiation in presence of **QMP1**, **QMP2**, and **QMP4** (10, 20, 50, and 100 μ M). Yields of alkylation were reported also for dark experiment.

Therefore, the experiments were repeated, in these conditions, with both 22AG and Pu24T, at 10 μ M, in 100 mM K-rich buffer, in presence and in absence of 20 μ M of **QMP1**, **QMP2** and **QMP4**. Moreover, the corresponding dark reactions were performed, to verify the absence of thermal activation. After 8 hours of irradiation, **QMP2** and **QMP4** afforded highest alkylation yields (26-19 % with 22AG, 21.4-13.2% with Pu24T), while **QMP1**, characterized by low reactivity, displayed only low yields on both targets (8.6 % with 22AG, 8.1 % with Pu24T).

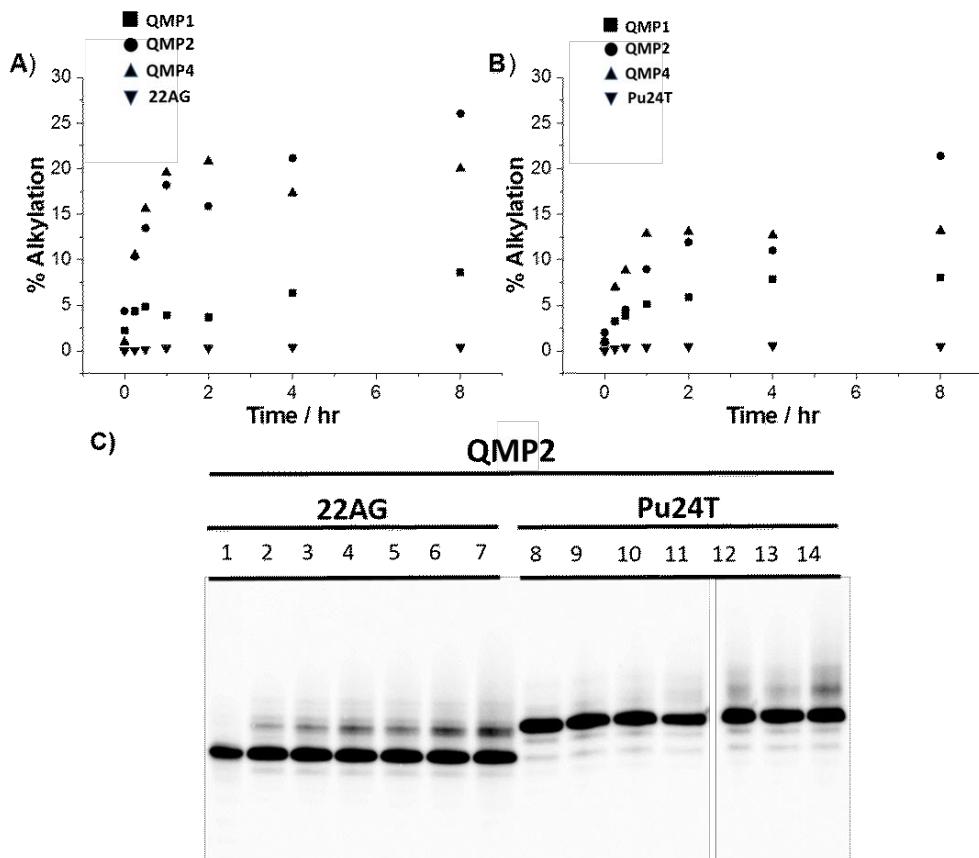


Figure 4.8 – Alkylation yields of A) 22AG and B) Pu24T (10 μ M, 100 mM K-rich buffer) at different irradiation times (0, 0.25, 0.5, 1, 2, 4, and 8 hours) in the presence of **QMP1**, **QMP2**, and **QMP4** (20 μ M) or in the absence of ligand. C) Denaturing gel electrophoresis (15% acrylamide) of the alkylation adducts generated in presence of 22AG and Pu24T (10 μ M) in K⁺ buffer (100 mM) with **QMP2** (20 μ M). Experiments 1 and 8 are performed in dark condition.

Then, the selectivity of the process was investigated, and irradiation has been repeated on 22AG (that resulted to be the preferred target), with increasing concentrations of duplex DNA (ds26), up to 10 equivalents. As it's possible to notice in *Figure 4.9*, **QMP4** was only slightly affected by the presence of DNA, while efficiency of **QMP1** and **QMP2** decreased significantly (up to 50%), evidencing that substituents disposition strongly influence the interaction with the target and, in meta-derivatives, quinone methide is placed in a more favorable position for the alkylation.

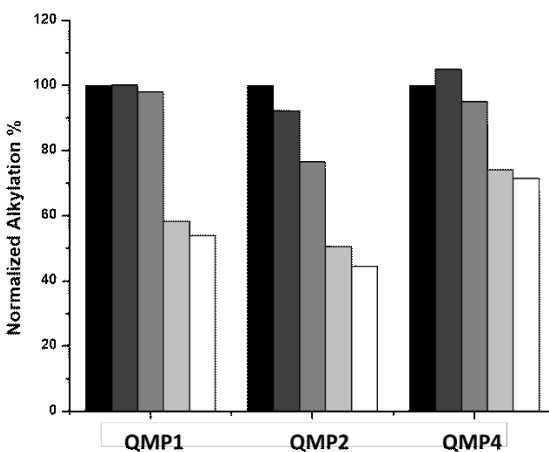


Figure 4.9 – Alkylation yields obtained with human telomeric sequence 22AG (10 μ M, 100 mM K-rich buffer) in presence of **QMP1**, **QMP2**, and **QMP4** (20 μ M) in the absence (black bars) or in the presence of ds 26 competitor (10, 20, 50, and 100 μ M).

To individuate the alkylation sites of these three ligands, further MALDI-TOF MS spectrometry has been carried out on the reaction mixture produced by irradiation of 20 μ M of **QMP1**, **QMP2** and **QMP4**, in presence of 10 μ M 22AG. Analysis of compound **QMP1** evidenced that this ligand did not produce any alkylated product. The situation was remarkably different in presence of two ammonium salts: with **QMP2**, two mono-charged product peaks were observed, one main product at $[M+H]^+ = 7358.2$ Da, corresponding to the mono-alkylated 22AG, and the other one with molecular mass $[M+H]^+ = 7299.7$ Da, associated to the cross-linked product generated by bis-alkylation of 22AG, in accordance with preliminary photochemical studies, where formation of both mono and bis-hydrated QMs were detected. A similar behavior was observed with **QMP4**, that showed not only the formation of the mono- and bis-alkylated products, but even a third mono-charged peak with mass $[M+H]^+ = 7319.0$ Da, attributed to the mono-alkylated 22AG where the second activable moiety of **QMP4** reacted with water instead of the nucleobase.

Finally, digestion experiments with *snake venom phosphodiesterase I* (digestion from 3'-end) and *calf spleen phosphodiesterase II* (digestion from 5'-end), followed by MALDI-TOF analysis, have been exploited to determine the alkylation sites of quinone methides, in particular of **QMP2**, which afforded highest alkylation yields: after 30 minutes, enzymes phosphodiesterase I wasn't even able to start the digestion of the sequence, which is the time employed by the same enzyme to completely hydrolyze the unmodified

sequence. After overnight treatment, only the first guanine at 3'-end was partially digested while, on 5'-end, phosphodiesterase II displayed a remarkably slower DNA fragmentation. Taken together, these data pointed out that ligand was placed in proximity of 3'-end and, in this position, completely blocked the activity of phosphodiesterase I and slowed down the digestion in the opposite direction.

4.1.6 Conclusions

The design of novel photoactivable quinone methide precursors led to the development of six novel ligands, bearing two photoreactive units, introduced as neutral Mannich bases or ammonium salts. Analysis of their photochemical behaviour demonstrated the high reactivity of the second type of derivatives. **QMP2** and **QMP4**, able to effectively generate the corresponding quinone methide. On the contrary, the other compounds reacted very slowly upon irradiation and we have observed that, even at high substrate conversion, the principal product obtained from these processes was not the expected adduct with water, but the product arising from the hydration of the alkyne. FRET-Melting assays and CD analysis highlighted that these types of compounds have moderate affinity (in comparison to potent G4 ligands) for quadruplex structures, as it can be deduced from their low melting temperature values. However, the most positive evidence was their good selectivity: indeed, increasing concentrations of duplex DNA only slightly affected the stabilization properties of quinone methide precursors. A similar behaviour was observed during alkylation experiments, particularly with **QMP4**. Results of photochemical experiments in presence of G4s reflected the reactivity free solution and ammonium salts **QMP2** and **QMP4** showed highest alkylation efficiency, especially on telomeric 22AG sequence, and formation of the expected adducts with DNA have been further confirmed by MALDI-TOF analysis.

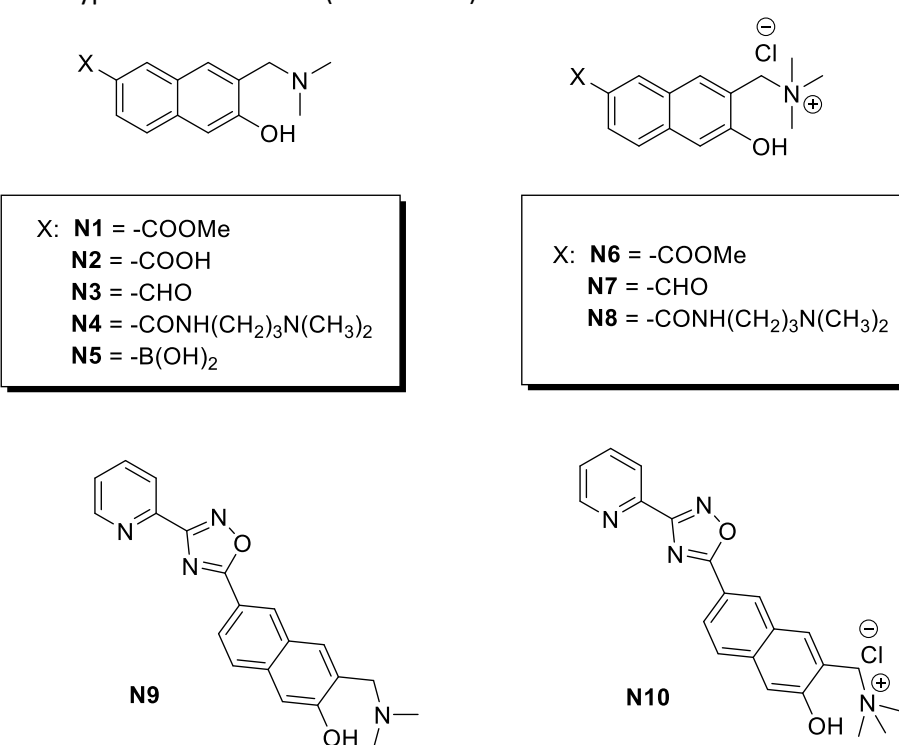
Then, we managed to obtain two efficient photo-alkylating ligands for telomeric quadruplex, however, despite our initial hypothesis, we have observed low reactivity and efficiency with two naphthalene-based ligands, **QMP5** and **QMP6**: indeed, although they presented a more extended conjugated system and absorption almost in the visible region (tails up to 400 nm), they showed very low reactivity and products derived from quinone methide were not even observed. Another fact that should be underlined is that these precursors displayed also good affinity and selectivity for the target, compared to phenyl derivatives, indicating that introduction of a larger aromatic surface was a useful strategy. Therefore, a deeper analysis to clarify the reason of their low efficiency and optimize their structure and reactivity should be conducted, to develop even more efficient and biocompatible quadruplex ligands.

4.2 Naphthalene-Based Quinone Methide Precursors

4.2.1 Design of Naphthalene-based precursors

Naphthalene derivatives represent a promising scaffold for the development of efficient quadruplex ligands: the main advantage is their extended and planar aromatic surface, which can stack on guanine tetrads, establishing strong π - π stacking interactions. However, despite their promising absorption properties, with ligands **QMP5** and **QMP6** quinone methide formation was negligible in presence and in absence of DNA. Therefore, we decided to further investigate the photochemical behaviour of this scaffold, in order to understand the origin of the low reactivity and how to improve their performances.

To this aim, we have synthesized a small library of 6-substituted- 3-((dimethylamino)methyl)naphthalen-2-ols, bearing different types of substituents (*Scheme 4.7*).



Scheme 4.7 – Structures of Naphthalene-based Quinone Methide Precursors N1-N10.

In details, we have functionalized naphthalene scaffold with different types of electron-withdrawing substituents: this choice has been prompted by the need to generate stable products, that don't regenerate the starting substrate. For three compounds, **N1**, **N3** and **N4**, we have also synthesized the corresponding ammonium salts, to verify if, even in this case, alkylation of nitrogen ensured higher reactivity. In the end, we have produced other two derivatives, **N9** and **N10**, as new photoalkylating quadruplex ligands. The structure resembles the “V-shaped ligands” but, because this represents a preliminary investigation, we have introduced only one photoreactive unit, to verify if it's possible, at least, achieve good reactivity with only one quinone methide precursor. Moreover, the structure is significantly different from previous reported compounds: the central phenyl ring has been replaced by pyridine unit and the alkyne by an 1,2,4-oxadiazole. Heterocyclic aromatic scaffolds have been introduced to increase the affinity for the target: indeed, different

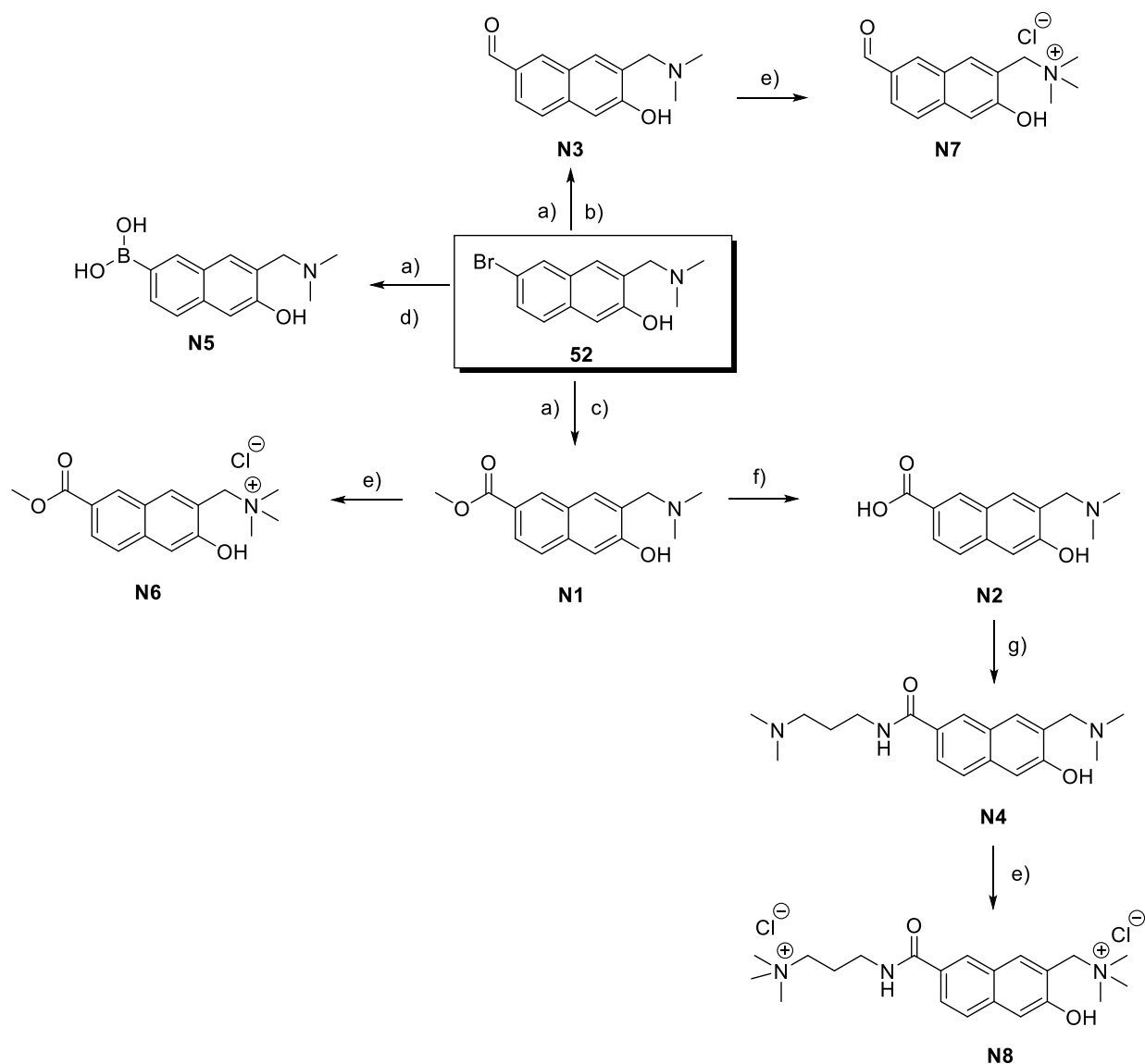
heteroatoms could establish multiple hydrogen bond interactions with the target, increasing the affinity of the ligand.

Then, in this part of the work, we have optimized the synthetic procedure to obtain compounds **N1-N10** and, subsequently, we have investigated their spectroscopic and photochemical properties, in aqueous solution.

4.2.2 Synthesis of Compounds

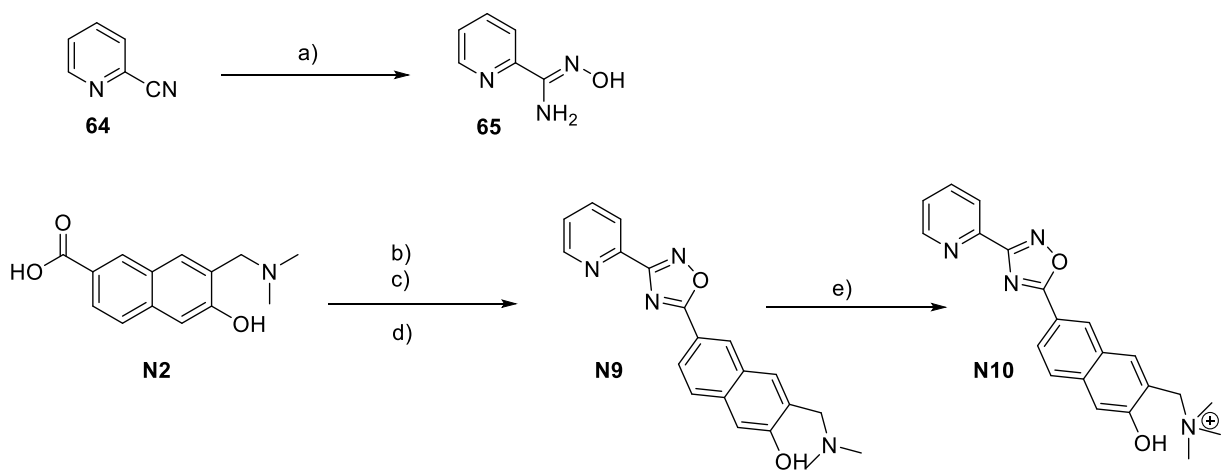
Synthesis of compounds **N1-N8** rely on the same key intermediate, which is the 6-bromo-3-((dimethylamino)methyl)naphthalen-2-ol **52**, reported in the previous section (4.1.2) and we have optimized three different synthetic pathway to obtain all desired products from this substrate (*Scheme 4.8*).

Boronic acid derivative **N5** was obtained in a single reaction-step: treatment of **52** with Butyllithium, at -78°C in THF, in presence of trimethylborate, produced the intermediate boronate, which was hydrolyzed at the end of the reaction, dissolving the reaction mixture in HCl 10% solution. The final product was isolated through reverse-phase column chromatography. A similar protocol was applied to synthesize also **N1** and **N3**, generated in good yields from the reaction between **52** and organolithium reagent, performed in presence of dimethyl carbonate and DMF, respectively (*Step a and b in Scheme 4.8*). Subsequently, **N1** was used to produce the corresponding ammonium salt, **N6**, with quantitative yield, through methylation with an excess of trimethyl iodide, in acetonitrile. Hydrolysis of methyl ester on **N1**, conducted in H₂O:THF 3:1 with potassium carbonate, led to elevated yields of carboxylate **N2**. The final product was obtained upon acidification of the solution with HCl 10% and purification of the crude through reverse phase column chromatography. The resulting carboxylic acid derivative **N2** was employed for the synthesis of amide **N4**: we have carried out a coupling reaction with 3-(dimethylamino)propylamine, using PyBOP as activating agent, in DMF. The reaction mixture was stirred at room temperature for one hour and the expected amide **N4** was obtained in high yields (79%). Finally, quantitative alkylation with trimethyliodide afforded the corresponding ammonium salt. The last two derivatives, **N3** and **N7**, have been synthesized with an analogue protocol: transmetallation reaction of **55** with butyllithium, followed by addition of DMF at -50°C, afforded the Mannich base **N3** in good yields (71%). After purification, this product underwent to classic methylation reaction to obtain the corresponding ammonium salt **N7**.



Scheme 4.8 – Synthetic Procedure used to obtain compounds **N1-N8:** a) BuLi (2.5 eq.), THF, -78°C , 1h, under Ar; b) DMF (10 eq.), -50°C , 2h; c) dimethyl carbonate (10 eq.), -50°C , 2h; d) $\text{B}(\text{OMe})_3$ (10 eq.), -50°C , 2h; e) CH_3I (5 eq.), NaOAc (1.5 eq.), r.t., 2d; f) K_2CO_3 (2.2. eq.), $\text{H}_2\text{O}: \text{THF}$ 3:1, reflux, 16h; (g) 3-(dimethylamino)-propylamine (3 eq.), PyBOP (1 eq.), DMF, r.t., 1h;

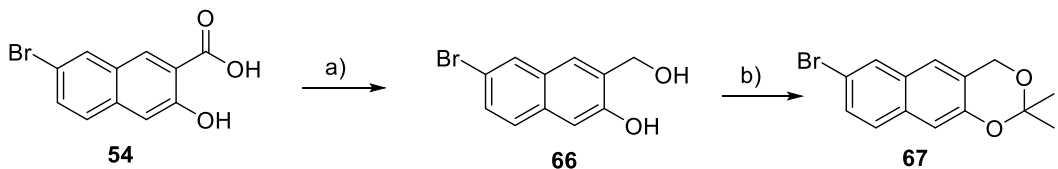
Even the synthesis of heterocyclic derivatives **N9** and **N10** required only few reaction steps, whose key precursors were carboxylic acid **N2** and 2-cyanopyridine **64** (Scheme 4.9). In details, commercially available **64** was reacted with hydroxylammonium chloride in presence of potassium carbonate, in $\text{EtOH:H}_2\text{O}$ 1:1, for 3 days at room temperature, to produce the corresponding **65** in 77% yield. Subsequently, a three-steps procedure was used to combine this product with carboxylic acid of **N2** and generate the corresponding oxadiazole: in details, a coupling reaction between **N2** and **65** have been performed, using PyBOP as activating agent, to generate the intermediate hydroxyimino-amide, which has been used for the final step without purification. In the end, *tert*-butylammonium fluoride (TBAF) have been used to induce ring-closure, which occurred in 2 hours, at room temperature, using THF as solvent, and the final oxadiazole derivative **N9** has been isolated in high yield. Finally, exhaustive methylation led to its corresponding ammonium salt, **N10**.



Scheme 4.9 – Synthetic Procedure to obtain **N9 and **N10**:** a) K_2CO_3 (1.5 eq.), $NH_3OH^*\text{Cl}$ (1.5 eq.), $EtOH:H_2O$ 1:1, r.t., 3 d; b) PyBOP (1 eq.), DIPEA (2 eq.), DMF, r.t., 30 min; c) **65** (1 eq.), DMF, r.t., 6 d; d) TBAF (2 eq.), THF, r.t., 2 h.

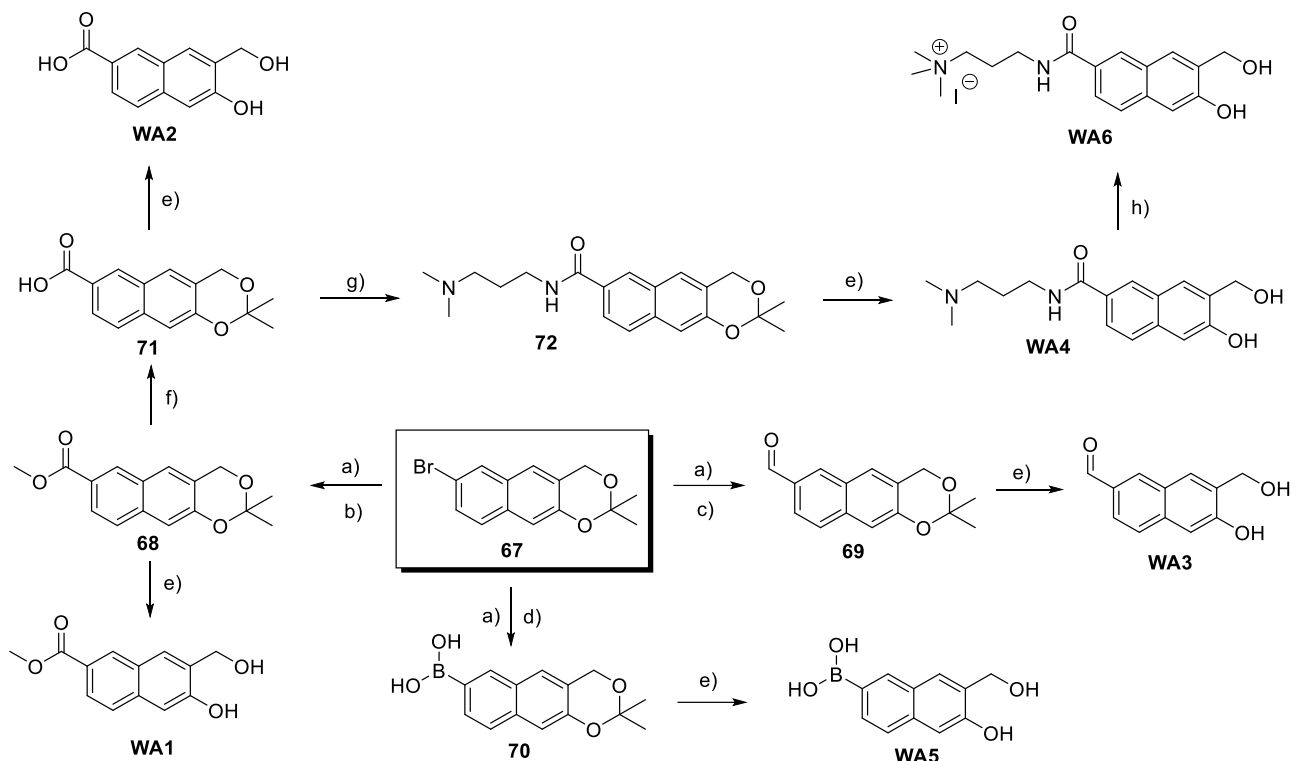
As mentioned in the introduction, photochemical behaviour of all these substrates have been investigated to examine quinone methide generation and the formation of corresponding adducts with water. However, these experiments were performed on analytical scale, then, to correctly identify the expected water-adducts generated by the photochemical process, we have synthesized, for each derivative, the corresponding 6-substituted-3-(hydroxymethyl)naphthalen-2-ols **W1-W7**.

In this case, the key intermediate to obtain different compounds was **67** (*Scheme 4.10*) which was not commercially available and has been produced in three reaction steps: reduction with borane-dimethylsulfide complex afforded the desired alcohol in quantitative yield, while protection of two hydroxy groups with acetone, in presence of a large excess of dimethoxypropane, afforded **67** with excellent yield (*Scheme 4.10*).



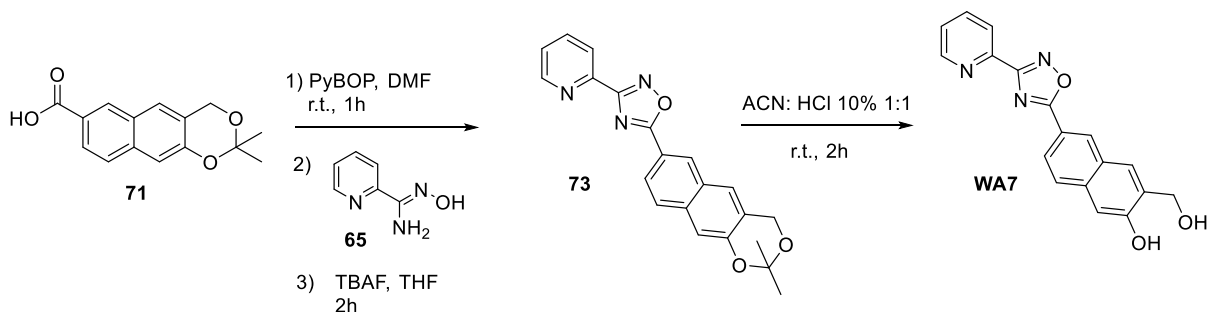
Scheme 4.10 – Synthetic procedure to obtain precursor **67:** a) $BH_3^*\text{SMe}_2$ (2.5 eq.), THF, 0°C -reflux, 1h; b) $Me_2C(OMe)_2$, PTSA (0.5 eq.), Acetone, r.t., 16h.

Compound **67** was then used to produce water-adducts **WA1-WA5**, which are expected to be generated upon irradiation of compounds **N1-N8**. Briefly, as in the previous described procedure, **67** underwent three distinct reaction with butyllithium, in presence of dimethyl carbonate, DMF and trimethyl borate, to afford, respectively, **68**, **69** and **70**, in excellent yields (*Step a,b,c and d in Scheme 4.11*). Then, the methyl ester **68** was hydrolyzed with potassium carbonate, to produce the corresponding carboxylic acid **71**, that was employed in the subsequent coupling reaction with 3-(dimethylamino)-propylamine, using PyBOP as activating agent, to afford the desired amide **72** (*Step f and g in Scheme 4.11*). The final derivatives **WA1-WA5**, with free hydroxy groups, have been obtained with same reaction protocol: acetal was removed upon treatment with diluted hydrochloridric acid (10% solution) in $ACN:H_2O$ 1:1, at room temperature, for 3 hours (*Step e in Scheme 4.11*).



Scheme 4.11 – Synthetic procedures for the synthesis of water adducts WA1-WA5: a) *Bu*₃*Li* (2.5 eq.), THF, -78°C, 1h; b) dimethyl carbonate (10 eq.), THF, -50°C, 2h; c) DMF (10 eq.), THF, -50°C, 2h; d) *B(OMe)*₃ (10 eq.), THF, -50°C, 2h; e) HCl 10%:ACN 1:1, r.t., 3h; f) *K*₂*CO*₃, *H*₂*O*:THF 3:1, reflux, 16h; g) 3-(dimethylamino)-propylamine (1 eq.), DIPEA (2 eq.) PyBOP (1 eq.), DMF, r.t., 1,30h; h) *CH*₃*I* (5 eq.), ACN, r.t., 2d.

Concerning the oxadiazole derivatives **N9** and **N10**, we have also synthesized their corresponding water adduct, **WA7** (*Scheme 4.11*): the used synthetic protocol is basically the same exploited to obtain the Mannich bases: indeed, carboxylic acid **71** underwent to a coupling reaction with **65**, using PyBOP as activating agent, in DMF. After 6 days, the final cyclization step was performed with tert-butylammonium fluoride to generate the desired oxadiazole **73**, which was used for the final hydrolysis without purification. Treatment with diluted solution of hydrochloric acid (10%) afforded, in only two hours, the desired benzylic alcohols **WA7**.



Scheme 4.12 – Synthetic procedure used to obtain water-adduct WA7.

4.2.3 Spectroscopic Properties in aqueous solution

To evaluate the photoreactivity of these new naphthalene-quinone methide precursors, we have started with the analysis of their absorption properties, to verify their molar absorptivity in water and to evaluate the irradiation wavelengths.

We have prepared solutions of compounds **N1-N10** in ACN:H₂O 1:1, with C= 1*10⁻⁵ M, and measured molar extinction coefficients. Recorded spectra, reported in *Figure 4.10*, showed different behaviours but, in general, for each derivative, we can observe an intense absorption band at 250 nm and another one extended among 265 and 400 nm. However, it should be underlined that the position of this band strictly depends on the type of compound: for example, in case of **N1**, **N6**, **N2** and **N5**, the band starts around 265 nm and decays at 350 nm. In case of **N3** and **N7**, peak intensity increases at 280 nm and is extended up to 400 nm. This behaviour can be observed also on **N4**, **N8** and **N9** and **N10** but the absorption drops rapidly before 370 nm. Furthermore, even the intensity of this band is strongly affected by the nature of the substrate: in details, **N2** and **N5** showed the lowest absorption in this wavelength range, while aldehydes derivatives, **N3** and **N7**, oxadiazole-based precursors, **N9** and **N10**, displayed elevated molar absorptivity in this region. Transformation of Mannich base into ammonium salt does not influence significantly the absorption spectra, in particular neither molar absorptivity nor the position of maximum peaks. Only in case of aldehydes-based substrate, an interesting variation is observed: ammonium salt, **N7**, is characterized by a more intense and broader band between 285 and 400 nm, suggesting that this specific compound could be activated in the visible region. Ammonium salts **N8** and **N10**, bearing the amide function and the oxadiazole, respectively, showed the same absorption profile of their Mannich bases but with higher molar absorptivity, but this could be due to their higher solubility in aqueous solution.

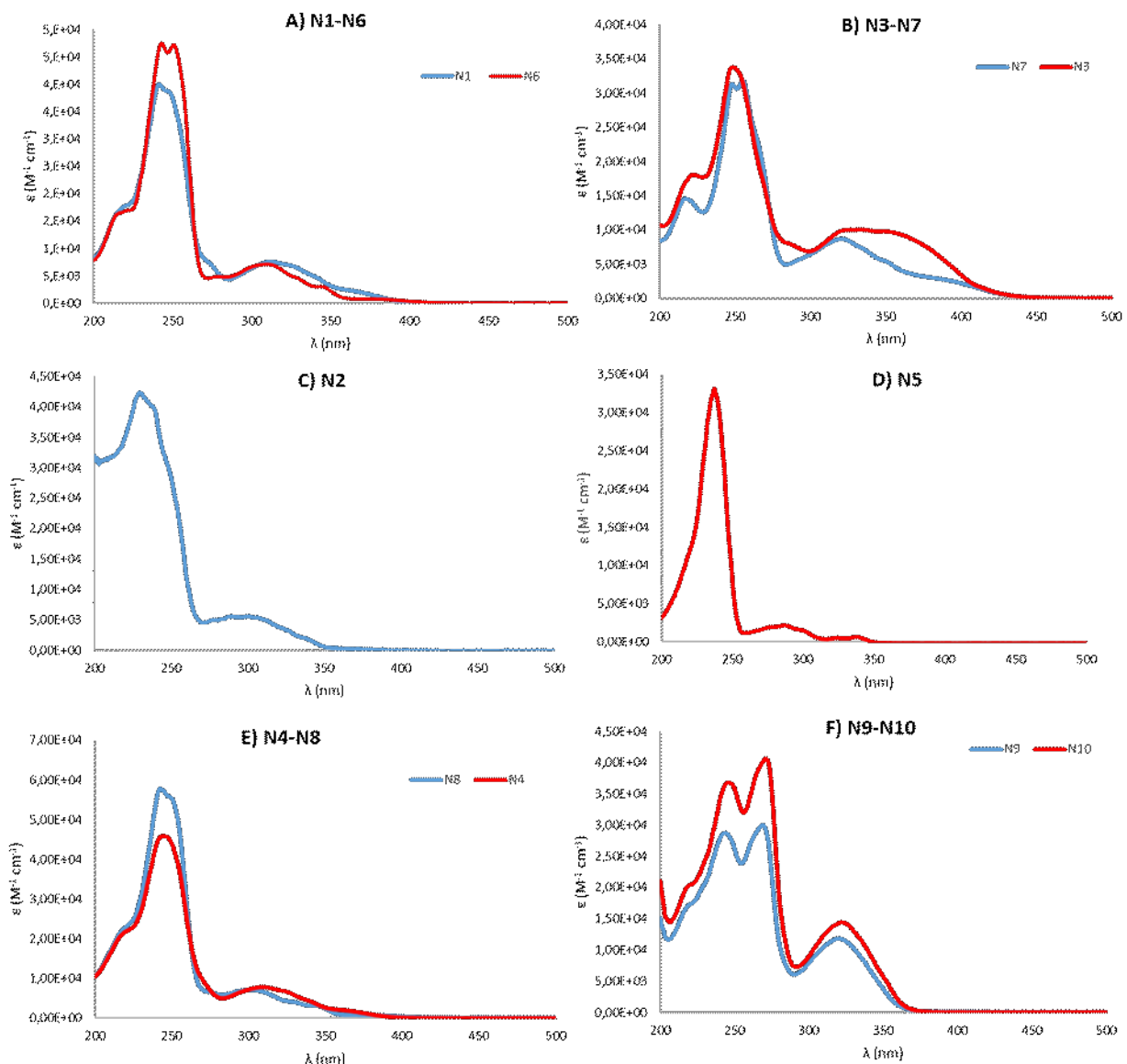


Figure 4.10 – Absorption spectra of compounds **N1-N10, recorded in 1:1 ACN:H₂O solution.**

From these spectra clearly emerged that, thanks to their absorption properties, activation of quinone methide precursors could be achieved not only in the UV-region, at 310 nm, but at more red-shifted wavelengths, as 365 nm, more compatible with biological environment. To this aim, in *Table 4.2*, we have summarized molar extinction coefficients at these two wavelengths: at 310 nm, higher values are displayed by aldehydes **N3** and **N7**, and oxadiazoles-based precursors, **N9** and **N10**, followed by the ester derivatives **N1** and **N6**, and the amides **N4** and **N8**. At 365 nm, most intense absorption is observed again in presence of aldehyde as substituent, followed by Mannich bases **N1** and **N4**, that, in this case, showed a more pronounced difference in molar absorptivity compared to their corresponding ammonium salts. Interestingly, **N5**, the boronic acid, displayed no absorption at 365 nm, therefore we hypothesized low to null reactivity for this compound, at 365 nm.

Compound	Λ_{\max} (nm)	$\epsilon_{310\text{nm}}$ ($M^{-1} \text{cm}^{-1}$)	$\epsilon_{365\text{nm}}$ ($M^{-1} \text{cm}^{-1}$)
N1	311	7617	2276
N6	311	7096	804
N2	242, 297	5122	346
N3	253, 354	8288	8919
N7	257, 373	7798	3710
N4	253, 337	7925	1974
N8	246, 305	6511	769
N5	239, 293	551	0
N9	248, 265, 323	10479	557
N10	247, 273, 326	12432	989

Table 4.2 – Molar extinction coefficients of compounds N1-N10 at 310 nm and 365 nm, in ACN:H₂O 1:1 solution.

A key parameter that strictly influences quinone methide generation is the acidity of proton of the phenolic group: indeed, as previously described, formation of the intermediate occurs through an intermolecular proton transfer (ESIPT) between the hydroxy group and the adjacent dimethyl amino or ammonium group. Therefore, higher is the acidity of this proton, more rapidly photolysis occurs. Substituents introduced in position 6 of naphthalene derivatives, with their electronic effects, could influence the overall acidity of the scaffold, determining lower or increased photoreactivity. Furthermore, it should be taken into account that irradiation experiments will be performed also at physiological pH (7.4) and, in this condition, naphthol derivatives **N1-N10** are in equilibrium with their deprotonated forms, characterized by different UV-VIS spectra. In details, quinone methide precursors can generate two different species upon deprotonation, the zwitterionic derivative **NZ** (*Figure 4.13*) and the corresponding anionic form (**NA**), completely deprotonated (*Figure 4.13*).

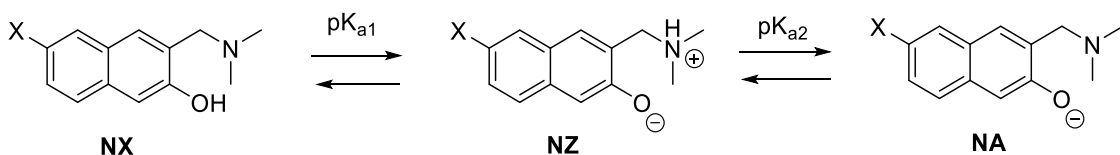


Figure 4.13 – Deprotonation equilibrium of generic naphthalene quinone methide precursor.

Then, in order to evaluate absorption properties of the species effectively irradiated in physiological conditions, and to verify how substituents affect pK_a values of these quinone methide precursors, we have performed, for each of them, spectrophotometric titrations.

Compounds **N1-N10** were dissolved in water (to achieve concentration in the order of 10^{-5}) and pH was gradually increased adding small volumes of diluted NaOH solutions until $pH = 11/12$ (experiments were stopped when no significant variations of absorption spectra were detected) and, for each addition, UV-VIS spectra was recorded.

As it's possible to observe in *Figure 4.11*, a similar behaviour can be individuated for different precursors: the absorption band centred around 250 nm decreased significantly, while a new peak, extended between 300 and 450 nm, depending on the type of substituents introduced, appeared. Intensity of this new absorption maxima is not the same for all compounds: indeed, for carboxylic acid **N2** and boronic acid **N5**, molar extinction coefficient, in this spectral region, remained very low, evidencing that photoactivation performed in these conditions could result in poor reactivity of these two derivatives, despite the generation of phenolate. On the contrary, aldehydes **N3** and **N7** not only generated a new, intense peak, upon deprotonation, but their absorption tails achieved 450 nm, in the visible region. A similar, but less pronounced, effect was observed with oxadiazole derivatives **N9** and **N10**.

Moreover, in each spectrum, several isosbestic points can be clearly located, indicating an equilibrium between two different species in solution. Only **N2** and **N5** showed a different type of spectra, where no defined isosbestic points can be individuated: this unusual results could be attributed to the fact that both derivatives present more deprotonation sites, therefore an higher number of species can be generated, determining a more complex equilibrium.

Subsequently, we have determined, for each compound, the corresponding pK_a values, reported in *Table 4.3*. In details, we have plotted molar absorptivity at a fixed wavelength, as a function of the pH and the resulting curve was fitted to calculate the desired parameter.

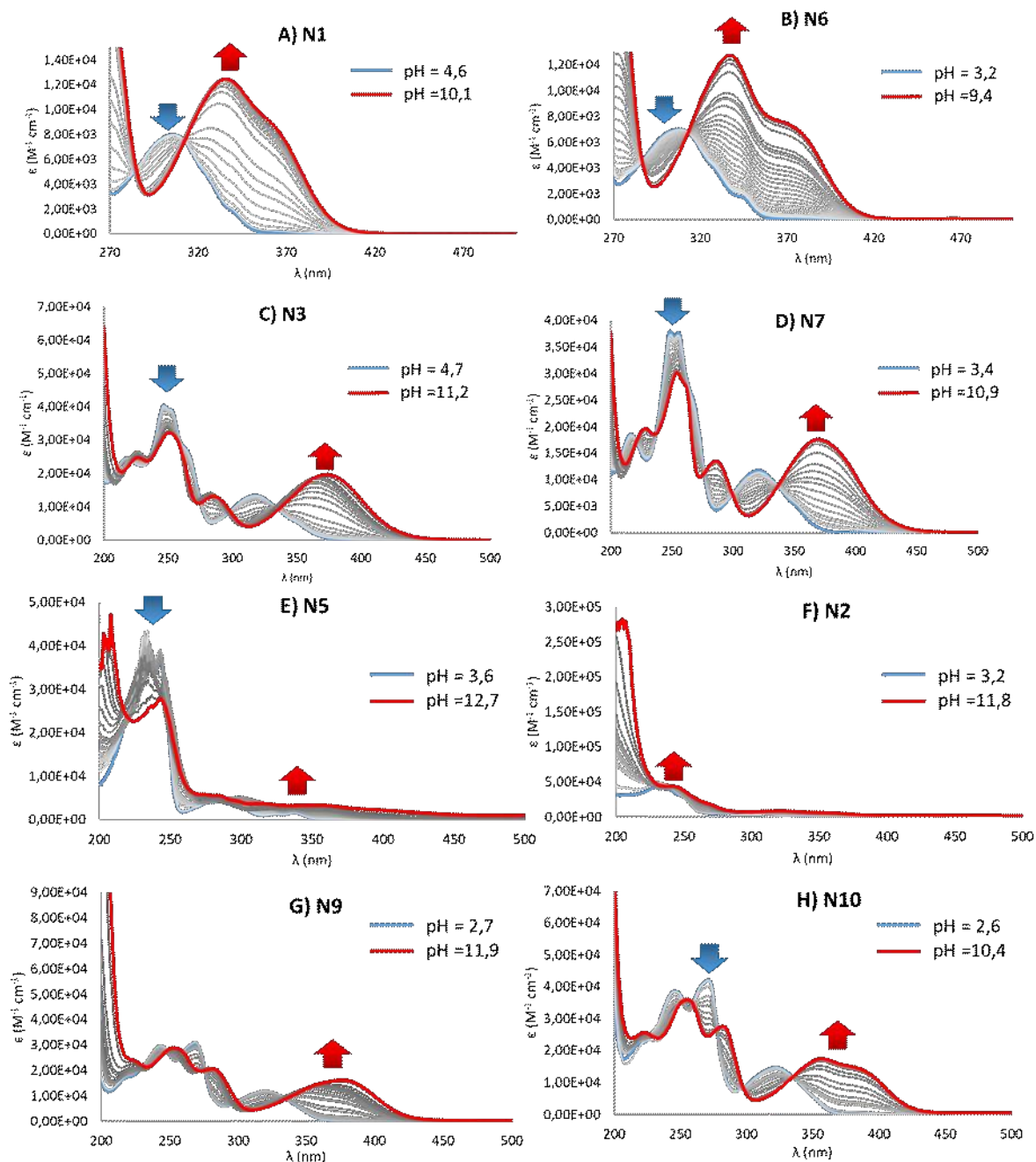


Figure 4.11 – Spectrophotometric titrations of compounds N1-N10. Analysis of compounds have been performed in 3 ml of water ($C = 10^{-5}$ M), in presence of 10^{-3} M NaCl, adding little amounts of NaOH 0.01 M or 0.1 M to gradually increase pH solution. At each addition, spectra of the solution were recorded.

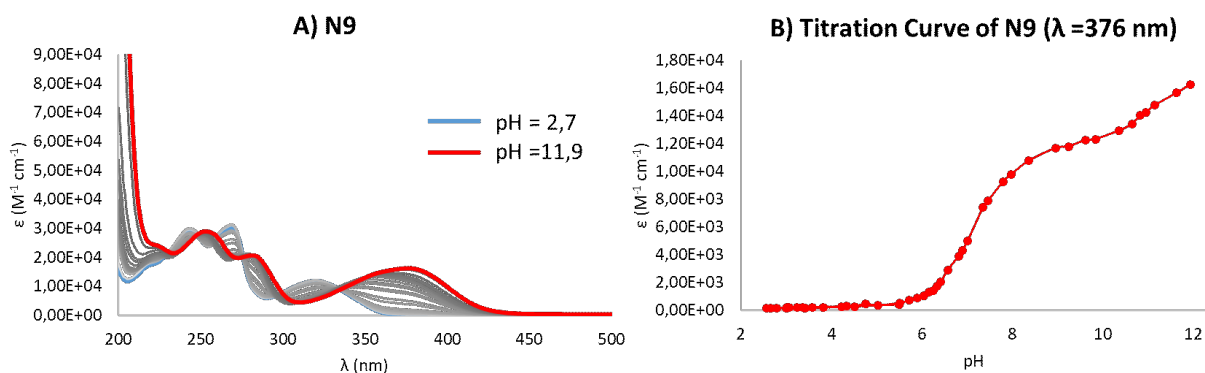


Figure 4.12 – A) Spectrophotometric titration of compound **N9** and **B)** its titration curve, obtained plotting molar absorptivity at 376 nm as a function of pH.

As reported in *Table 4.3*, pK_a values of compounds **N1-N10** are among 7.14 and 8.29, therefore, as previously stated, at physiological pH, we have the contemporary presence of precursor and its zwitterionic form, characterized, in general, by red-shifted absorption. This experimental outcome evidences that activation of these derivatives at higher wavelengths should be even more feasible, because of the intense band generated between 350 and 400 nm, due to deprotonation of hydroxy group. As expected, it should be also noticed that the nature of substituents influences the acidity: in particular, electron-withdrawing groups, as -COOMe, -CHO and pyridine-oxadiazole moiety, determined lower pK_a values. On the contrary, reducing the electron-withdrawing ability of the substituent, pK_a values increased, as in case of carboxylic acid **N2**, achieving the highest value with boronic acid **N5** (pK_a = 8.29). For some derivatives, in particular for Mannich bases, it has been possible to calculate also the second pK_a (as it's possible to observe, for example, in *Figure 4.12-B-B*), associated to the formation of the fully deprotonated species **NA** (*Figure 4.12*), which happens only at elevated pH values, above 10.5.

Finally, spectroscopic analysis of compounds **N1-N10** highlighted their interesting properties: in particular, the use of naphthalene scaffold as quinone methide precursor ensures maximum bands centered between 300 and 400 nm, even in aqueous solution. Moreover, these outcomes pointed out that spectroscopic properties strictly depend on the electronic effects of substituents: indeed, groups with strong electron-withdrawing character displayed higher and red-shifted absorption. Spectrophotometric titrations confirmed that, in physiological conditions, all substrates are in equilibrium with their zwitterionic forms, that displayed intense absorption around 350 nm. Therefore, irradiation experiments could be performed in aqueous solution, irradiating not only at 310 nm, but also at 365 nm.

Compounds	pKa ₁	pKa ₂
N1	7.41 ± 0.01	10.72 ± 0,01
N6	7.77 ± 0.01	
N2	7.85 ± 0.07	10. 8 ± 0,1
N3	7.120 ± 0.007	
N7	7.5 ± 0.01	
N4	7.41 ± 0.05	11.32 ± 0.09
N8	8.9 ± 0.2	
N5	8.29 ± 0.06	12.29 ± 0.1
N9	7.14 ± 0.01	10.9 ± 0.05
N10	7.45 ± 0.01	

Table 4.3 – pK_a values determined for compounds N1-N10.

4.2.4 Photoreactivity of QMPs

After the analysis of their spectroscopic properties, we started the evaluation of photoreactivity of compounds **N1-N10** and, in particular, the quinone methide generation efficiency, through determination of photolysis quantum yields. As previously described, this parameter has been measured with an optical desk, equipped with a high-pressure mercury lamp, previously calibrated by ferrioxalate actinometry. Quantum yield values have been determined applying the following equation:

$$\Phi \text{ (313 nm)} = (\text{mol of tetrazoles reacted}) / \text{Moles of absorbed Photons}$$

Solution of compounds **N1-N10** ($C \approx 10^{-4}$ M), dissolved in 3 ml of 1:1 ACN: phosphate buffer (50 mM, pH 7.4), were irradiated at 313 nm, for variable times, depending on the rate of photolysis. The amount of consumed substrate has been detected through HPLC analysis and the formation of corresponding benzyl alcohols **WA1-WA7** has been demonstrated using previously synthesized compounds as references. The results are reported in *Table 4.4* and, as it's possible to observe, even in this case, the behaviour is significantly different, depending on the type of substituents present. Indeed, higher quinone methide generation efficiency has been observed with boronic acid **N5** ($\Phi = 2.6 \cdot 10^{-1}$), followed by carboxylic acid **N2** ($\Phi = 1.9 \cdot 10^{-1}$), despite their lower molar absorptivity at the irradiation wavelength, compared to other derivatives. Amide **N4** and its corresponding ammonium salt displayed basically the same, good, reactivity, as well as methyl ester **N1** and **N6**, despite their slightly lower values. Surprisingly, aldehydes **N3** and **N7** and oxadiazole derivatives **N9** and **N10**, showed no reactivity at this wavelength, despite their excellent absorption properties. Even after 6 hours of irradiation, no trace of any kind of product has been observed, neither a decrease of substrate concentration. Even the ammonium salts, that usually react rapidly to afford the expected intermediate,

were characterized by complete absence of reactivity. This unusual and unexpected behaviour could be attributed to alternative deactivation mechanism of the excite state, not involving quinone methide generation.

Compounds	Φ (313 nm)	C (M)
N1	$1.0 \cdot 10^{-1}$	$3.0 \cdot 10^{-4}$
N6	$1.4 \cdot 10^{-1}$	$3.2 \cdot 10^{-4}$
N2	$1.9 \cdot 10^{-1}$	$3.4 \cdot 10^{-4}$
N3	$7.0 \cdot 10^{-4}$	$1.8 \cdot 10^{-4}$
N7	^a N.D.	$6.0 \cdot 10^{-4}$
N4	$1.8 \cdot 10^{-1}$	$2.8 \cdot 10^{-4}$
N8	$1.7 \cdot 10^{-1}$	$4.0 \cdot 10^{-4}$
N5	$2.6 \cdot 10^{-1}$	$6.0 \cdot 10^{-4}$
N9	^a N.D.	$1.0 \cdot 10^{-4}$
N10	^a N.D.	$8.0 \cdot 10^{-5}$

Table 4.4 – Quantum Yield values measured for compounds N1-N10, in 3 ml of 1:1 ACN:phosphate buffer (50 mM, pH 7.4), with the optical desk, with lamp filter centered at 313 nm.

To further validate the results obtained by spectrophotometric titration experiments, we decided to measure quantum yield values at different pH, to further demonstrate that efficiency of the process is strongly influenced by pH of the solution. We performed this analysis only on compound, **N1**, selected as a model: indeed, is characterized by discrete but not excellent efficiency, a good compromise to evidence differences in reactivity among various pH. As previously mentioned, for this quinone methide precursor, three different species can be generated upon deprotonation (*Figure 4.14*): in acidic solution, the fully protonated methyl ester **N1-H** is the only product. Increasing pH values, the zwitterionic **N1-Z** is formed until, in highly basic conditions (pH > 10), the anionic specie **N1-A** becomes the major product.

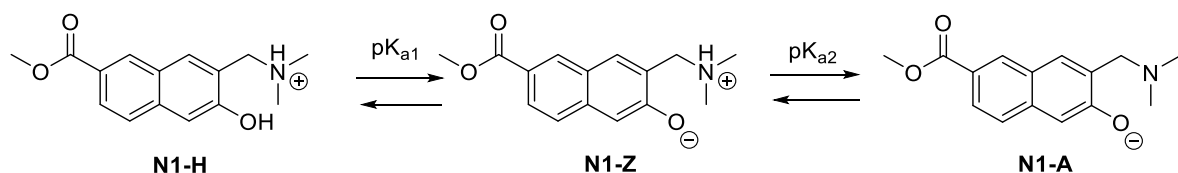


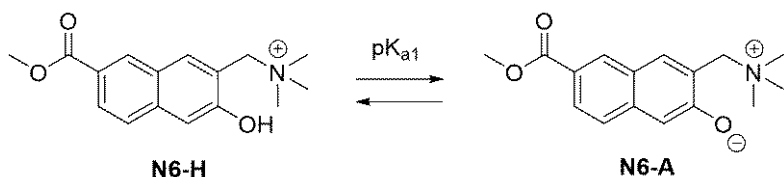
Figure 4.14 – Protonation equilibrium for compound N1.

Therefore, to verify how protonation equilibrium influence quinone methide generation, we have irradiated a 3×10^{-4} M solution of **N1** in pure phosphate buffer (50 mM), at different pH values: 5, 7.4, 8 and 12 and measured the photolysis quantum yield, irradiating at 313 nm with the optical desk. Results, reported in *Table 4.5*, confirmed what expected: irradiation at pH = 5, 7.4 and 8, respectively, afforded similar good quantum yield values. In fact, in this pH range the two principal forms are **N1-H** and **N1-Z**, which can rely on the intramolecular proton transfer thanks to the protonation of amino group, which is also an excellent leaving group in these conditions, favouring quinone methide formation. On the contrary, photoactivation performed at pH = 12 didn't lead to the formation of the desired water adduct **WA1**, not even in trace. However, irradiation produced a new product, the corresponding carboxylate, derived from ester hydrolysis, induced by strong basic conditions and that was not light-mediated.

pH	Φ (313 nm)
5	$8.0 \cdot 10^{-2}$
7.4	$1.0 \cdot 10^{-1}$
8	$1.0 \cdot 10^{-1}$
12	*N.D.

Table 4.5 – Photolysis quantum yields of N1 at different pH. Experiments were performed irradiating 3×10^{-4} M solutions of **N1**, in 3 ml of phosphate buffer, at 313 nm, with optical desk. Reactions were monitored through HPLC analysis.

As further proof of pH-mediated generation of quinone methide, we have measured also the photolysis quantum yield of the corresponding ammonium salt of ester, **N6**, at pH = 5.3 and pH = 10.3, which are the conditions to obtain quantitatively the protonated form **N6-H** and the anionic **N6-A** (*Figure 4.13*). In this case, no significant differences in photolysis efficiency have been observed: this is due to the presence of ammonium group that, even in basic conditions, represent an excellent leaving group and, upon excitation, can be expelled to generate the corresponding quinone methide.



pH	Φ (313 nm)
5.3	$1.5 \cdot 10^{-1}$
10.3	$1.5 \cdot 10^{-1}$

Figure 4.13 – Protonation equilibrium of N6 and photolysis quantum yields measured at pH = 5.3 and pH = 10.3. A 3.2×10^{-4} M solution of **N6** has been irradiated for 5 minutes with the optical desk, at 313 nm. Reaction was monitored through HPLC analysis.

Subsequently, we have investigated products formed upon irradiation in aqueous solution. In particular, comparing HPLC profiles of irradiated solution with references adducts **WA1-WA7**, we have established that all reactive substrates were able to generate the expected product. In some cases, reaction was very clean, as with boronic acid **N5**, amide **N4**, and led to exclusively formation of water adducts (*Figure 4.14*).

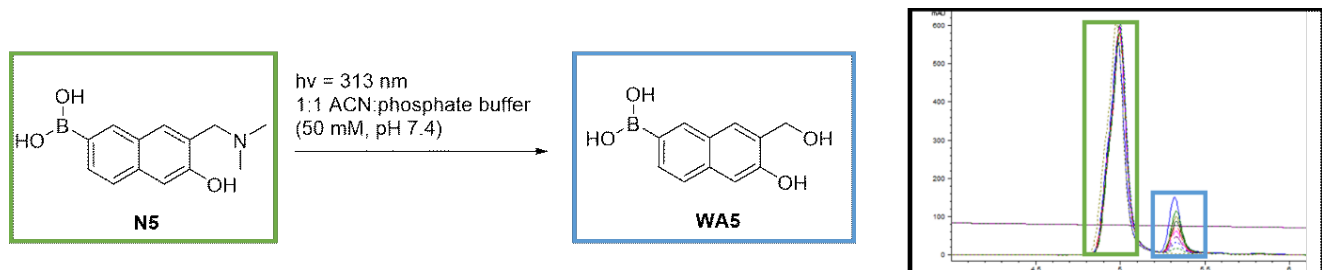


Figure 4.14 – HPLC profile of photogeneration of **WA5 from **N5**.**

However, again not all substrates showed the same behaviour: irradiation of **N1**, performed at $C = 3 \times 10^{-4} \text{ M}$, led to the formation of water adduct **WA1** only as minor product and the generated quinone methide reacted preferentially with another QMP, inducing the formation of C-Alkylated product **N1-CAlk** (*Figure 4.14*).

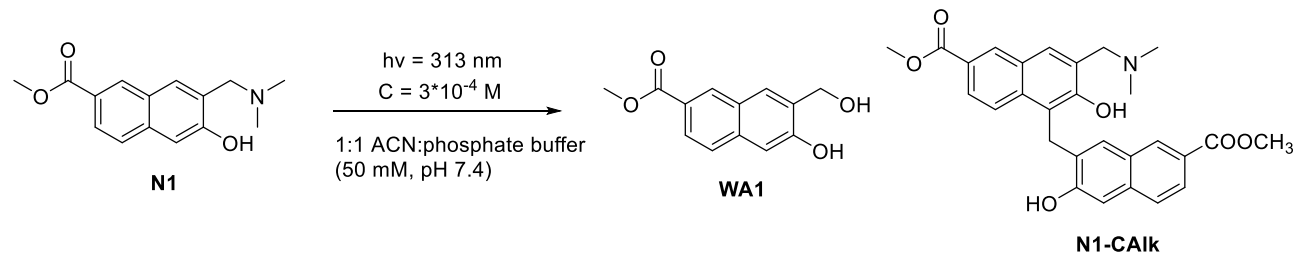


Figure 4.14 – Photogeneration of water-adduct **WA1 and C-alkylation product **N1-CAlk** from **N1**.**

Self-alkylation of quinone methide represents a side-process, that should be avoided, especially for biological applications: indeed, with aim to optimize this scaffold to achieve efficient DNA alkylation, formation of these type of adducts should be avoided, because could limit the reaction on the desired target. To this aim, we have conducted irradiation of **N1** at different concentrations, to individuate optimal conditions to prevent self-alkylation. Quinone methide precursors was irradiated in 1:1 ACN: phosphate buffer solution (pH 7.4, 50 mM), for 60 seconds, and the ration between concentration of **N1-CAlk** and **WA1** was determined through HPLC analysis, at substrate conversion of 20%. As reported in *Figure 4.15*, formation of self-adduct becomes predominantly at high substrate concentration (C above $1 \times 10^{-4} \text{ M}$). On the contrary, water adduct **WA1** was produced in high yields in diluted solution, with concentration $< 1 \times 10^{-4} \text{ M}$, pointing out that this is the limit to take into account to avoid secondary and undesired processes.

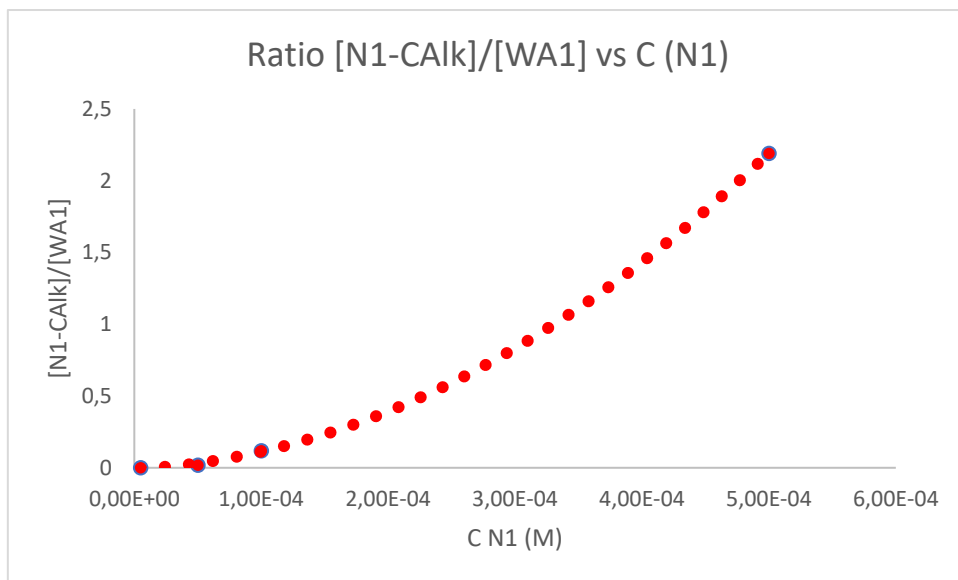


Figure 4.15 – Plot of $[N1-CAIk]/[WA1]$ vs **N1 concentration. Experiments were performed irradiating 3 ml of **N1** solution at different concentrations, with optical desk, at 313 nm, for 60 seconds. Reaction was monitored through HPLC Analysis.**

In order to confirm that this secondary product was effectively the self-alkylated quinone methide, we have carried out its preparative synthesis, irradiating 10 mg of **N1** in 1:1 ACN:phosphate buffer solution (50 mM, pH 7.4), with multi-lamps photoreactor, Rayonet, for 20 minutes. The product was isolated through purification on reverse phase column chromatography and was identified through NMR analysis.

In the end, in order to evaluate the photoreactivity of these precursors in more biocompatible conditions, we have measured their photolysis quantum yields at 366 nm, in pure phosphate buffer (pH 7.4, 50 mM), to verify their potential for biological applications. Experiments were performed with the same procedure described for 313 nm but, in this case, the optical desk was equipped with a 366 nm filter. Moreover, in this case we were forced to use higher concentrations of substrates **N1-N10**, because of lower molar extinction coefficients at this wavelength. Results are summarized in *Table 4.6* and there are significant differences compared to what observed at 310 nm: in particular aldehyde **N7** and oxadiazole derivatives **N9** and **N10**, that at 310 nm showed completely absence of photoreactivity, in these conditions are able to react and generate the corresponding quinone methide, despite the slow photolysis rate. On the contrary, aldehyde **N3** displayed again no reactivity. Methyl esters **N1** and **N6** and amides **N4** and **N8**, reacted with the same efficiency reported for 313 nm. Surprisingly, even carboxylic acid **N2** and boronic acid **N5**, despite their very low absorption at 366 nm, maintained the same photolysis efficiency, confirming their excellent reactivity.

Compounds	Φ (360nm)	C (M)	Time (min)
N1	$1.0 \cdot 10^{-1}$	$5.7 \cdot 10^{-4}$	2
N6	$1.4 \cdot 10^{-1}$	$5.0 \cdot 10^{-4}$	3
N2	$9.0 \cdot 10^{-2}$	$5.0 \cdot 10^{-4}$	5
N3	/	$7.5 \cdot 10^{-5}$	180
N7	$1.0 \cdot 10^{-3}$	$1.0 \cdot 10^{-4}$	50
N4	$1.3 \cdot 10^{-1}$	$5.5 \cdot 10^{-4}$	3
N8	$8.0 \cdot 10^{-2}$	$5.0 \cdot 10^{-4}$	6
N5	$2.4 \cdot 10^{-1}$	$1.4 \cdot 10^{-3}$	5
N9	$2.0 \cdot 10^{-2}$	$2.4 \cdot 10^{-4}$	20
N10	$1.2 \cdot 10^{-2}$	$1.2 \cdot 10^{-4}$	140

Table 4.6 – Photolysis Quantum Yields of compounds N1-N10 measured at 366 nm, in pure phosphate buffer solution (50 mM, pH 7.4).

4.2.5 Conclusions

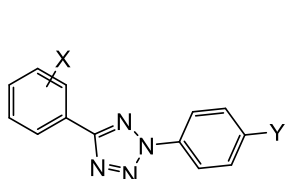
In this part of the project, we have investigated photoreactivity of naphthalene-based quinone methide precursors, to gain more details about their photochemical behaviour, due to poor efficiency that we have observed with V-shaped ligands **QMP5** and **QMP6**. Then, here we have synthesized a small library of 6-substituted 3-(dimethylamino)methyl)naphthalen-2-ols, **N1-N10**, characterized by the presence of electron-withdrawing groups, and their corresponding water adducts, **WA1-WA7**. Spectroscopic analysis underlined that presence of naphthalene unit is effectively responsible of red-shifted absorption, between 300 and 400 nm, which is crucial to achieve photoactivation in more biocompatible conditions. Moreover, we have performed spectrophotometric titrations on each compound, to gain further details about their behaviour in solutions. Irradiation performed at 310 nm proved that almost all compounds are able to generate the corresponding quinone methide with good efficiency, except aldehydes **N3** and **N7** and oxadiazoles derivatives **N9** and **N10**. We have also optimized irradiation conditions in order to avoid formation of undesired products, as self-alkylation adduct. In the end, we have demonstrated that photolysis of these precursors presented high efficiency even upon irradiation at 366 nm, in pure phosphate buffer, evidencing their potential use for biological applications. Furthermore, it should be underlined, that, at these wavelengths, even compounds that displayed no reactivity at 313 nm, were able to generate the desired water adduct, despite the slow photolysis rate.

5. Results and Discussion: 2,5 – Diaryl Tetrazoles

5.1 Photoreactive 2,5-Diaryl Tetrazoles

5.1.1 State of art and design of 2,5-Diaryl Tetrazoles

As described previously, we decided to explore different targeting strategies based on the development of photoactivable quadruplex ligands. The second approach we adopted is based on the use 2,5-diaryl tetrazoles, heterocyclic aromatic compounds that, upon irradiation at 300 nm, generate a reactive intermediate, a nitrile-imine dipole (NI), that can react with different species. These compounds have never been employed to target DNA secondary structures. Therefore, due to the lack of data in the current literature, preliminarily we thoroughly investigated the photochemical behaviour of 2,5-diaryl tetrazoles to further exploit them as efficient and innovative ligands.



T1: D-D	X = -pOH; Y= -pOCH ₃
T2: D-D	X = -mOCH ₃ ; Y= -pOCH ₃
T3: A-A	X = -pNO ₂ ; Y= -pCOOCH ₃
T4: A-D	X = -pNO ₂ ; Y= -pOCH ₃
T5: D-A	X = -pOCH ₃ ; Y= -pCOOH
T6: A-D	X = -pCOOH; Y= -pOCH ₃
T7: D-A	X = -p(O(CH ₂) ₂) ₃ OH; Y= -pCONH(CH ₂) ₂ N(CH ₃) ₂
T8: A-A	X = -pCONH(CH ₂) ₂ N(CH ₃) ₂ ; Y= -pCONH(CH ₂) ₂ N(CH ₃) ₂
T9: A-D	X = -pCONH(CH ₂) ₂ N(CH ₃) ₂ ; Y= -p(O(CH ₂) ₂) ₃ OH;

D = Electron-Donating Substituent
A = Electron-Withdrawing Substituent

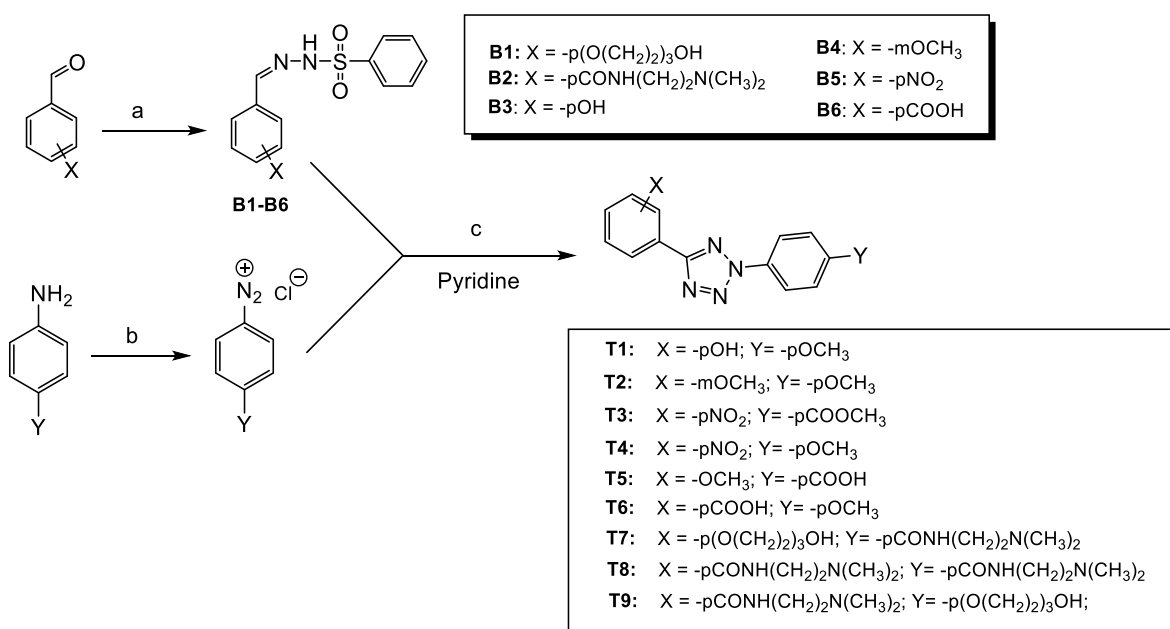
Scheme 5.1 – Library of synthesized substituted 2,5-diaryl tetrazoles.

To this aim, we have synthesized a small library of compounds (*Scheme 5.1*), modified on two aromatic rings with electron-donating and electron-withdrawing substituents. In details, we have investigated how different electronic effects of substituents could influence their photochemical properties, in particular the generation of the nitrile imine, and the reactivity towards alkenes and nucleophiles. Indeed, it has been reported that, in physiological conditions, the nucleophilic addition of water and carboxylates becomes competitive with the desired cycloaddition, reducing the overall process efficiency. However, the presence of electron-donating substituents on N-phenyl ring accelerate the cycloaddition step. Then, in order to individuate the most reactive and selective scaffold, for each compound we have measured the rate of the generation of the nitrile imine dipole (Photochemical Quantum Yield, Φ) and analyzed the selectivity of the cycloaddition step towards a specific alkene, acrylamide, in water solution. Moreover, because of our interest in the development of also fluorescent sensor, we determined the fluorogenicity of the reaction, to establish if tetrazoles could be effectively considered as “light-up” probes: in particular, we have synthesized the corresponding pyrazolines and measured their fluorescence quantum yields, in water.

In the end, to prove their utility as quadruplex ligands, we have analysed the affinity of water-soluble compounds (**T7**, **T8** and **T9**) against different types of quadruplexes, through FRET Melting assay.

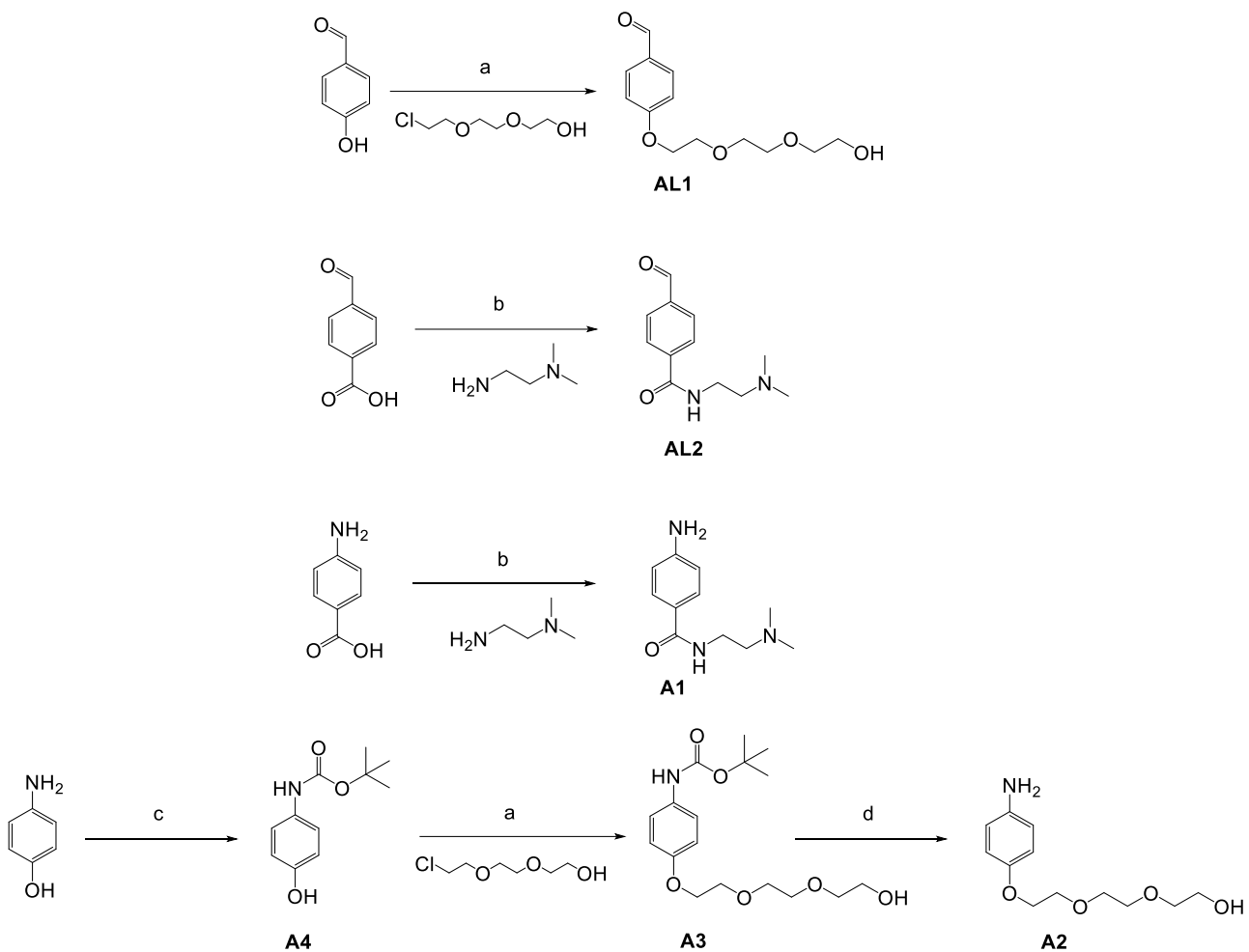
5.1.2 Design and Synthesis of Compounds

2,5-diaryl tetrazoles synthetic procedure is relatively simple and involves only a couple of steps. These scaffolds can be obtained through a coupling reaction, under basic conditions, between a benzensulphonyl hydrazone and an arene diazonium salt (*Scheme 5.2*). Hydrazones can be prepared from corresponding benzaldehydes, upon condensation with commercially available benzensulphonyl hydrazide, while diazonium salt is generated through oxidation of corresponding aniline with sodium nitrite.



Scheme 5.2 – Synthetic Scheme of tetrazoles T1-T9. a) benzensulphonyl hydrazone (1 eq.), EtOH, r.t.; b) NaNO₂ (1 eq.), HCl 37%, EtOH 50%, 0°C, 30 min; c) DIPEA (2.5 eq.), 0°C, 4 hours.

Benzaldehydes **AL1** and **AL2** and aniline derivatives **A1** and **A2** required to synthesize compounds **T7-T8** were non commercially available, then they have been synthesized according to the procedure reported in *Scheme 5.3*. **AL1** has been obtained through alkylation on 4-hydroxybenzaldehyde in presence of potassium carbonate and (2-(2-chloroethoxy)ethoxy) methanol, in acetonitrile (*step a, Scheme 5.3*)¹⁹⁰. After 12 hours under reflux, purification of the crude through column chromatography afforded the product in 64% yield. Amide **AL2** has been synthesised with a coupling between 4-formylbenzoic acid and *N,N*-dimethylethylendiamine, in presence of PyBOP as activating agent (*step b, Scheme 5.3*) and DIPEA. Reaction was stirred for 2 hours at 0°C acetonitrile and **AL2** has been isolated in 70% yield, after purification on column chromatography. Anilines **A1** and **A2** have been generated with similar reaction protocols: condensation between p-aminobenzoic acid and *N,N*-dimethylethylendiamine (*Step b in Scheme 5.3*) afforded the substituted aniline **A1**. On the contrary, synthesis of **A2** required more reaction steps: amino group of p-aminophenol was quantitatively protected with di-tert-butylcarbonate¹⁹¹, then substitution reaction with (2-(2-chloroethoxy)ethoxy)methanol, in basic acetonitrile solution, led to the formation of **A3**, which was finally deprotected in 1:3 trifluoroacetic acid: DCM solution (*Step d in Scheme 5.3*) to afford the desired **A2**.



Scheme 5.3 – Synthetic procedure for the synthesis of **B1, **B2**, **A1** and **A2**:** a) K_2CO_3 (2.5 eq.), ACN, reflux, overnight; b) PyBOP (1 eq.), DIPEA (2 eq.), ACN, r.t., overnight; c) di-*t*-butyl-di-carbonate (1 eq.), THF, r.t., 16 hours.; d) 20 eq. of TFA, DCM, 0°C, 5 hours.

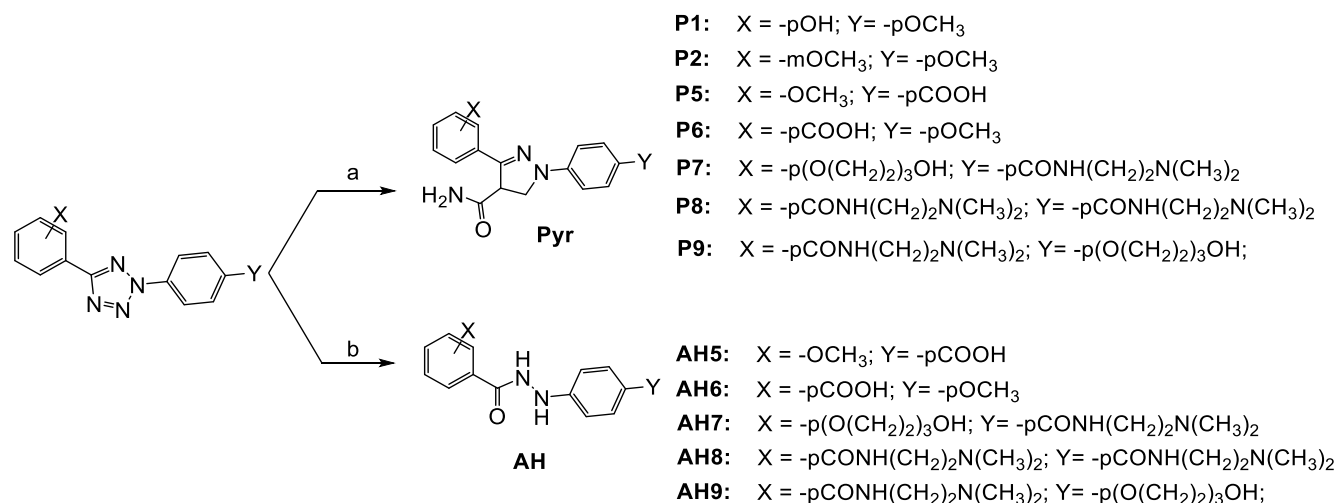
Concerning the synthesis of benzensulfonyl hydrazones, they have been synthesized with a very straightforward protocol, which relies on the condensation between benzaldehyde and benzenesulphonyl hydrazide, which occurs in ethanol, at room temperature. For all compounds, the generation was fast and clean: indeed, quantitative yield of product formation has been obtained after only few hours. Moreover, no purification was needed for this step. Arene diazonium salts were generated with a classic method: oxidation of anilines with sodium nitrite in presence of concentrated HCl (*Step b* in Scheme 5.2), at 0°C, afforded the corresponding product after only one hour, which was not isolated.

Then, 2,5-Diaryl tetrazoles have been synthesized following Kakehi's method (*step c* in Scheme 5.2)¹⁹²: solution of arendiazonium salt was added dropwise to a cooled solution of benzenesulphonyl hydrazone, dissolved in pyridine. Desired products were isolated, after column chromatography, with different reaction yields, depending on type of derivatives considered, but, in general, they never exceed 65%, which is consistent with data previously reported in literature.

The nine synthesized compounds contain all the possible combinations of the electronic effects of substituents: donor-donor (D-D), donor-acceptor (D-A), acceptor-donor (A-D) and acceptor-acceptor (A-A). In general, we have introduced a methoxy group as representative donor moiety. To decrease the electronic-density on the tetrazole, we have explored two different substituents: carboxylic acid and nitro group. In the end, to increase the water solubility of these compounds, we have synthesized tetrazole **T7-T9**, which

represents three most interesting combination of substituents, and in which the methoxy substituent has been replaced by polyethylene glycole chain and the carboxylic acid by an amide function, with a terminal dimethylamino group.

As discussed in the introduction, we have also synthesized, on a preparative scale, the products obtained from photoactivation of tetrazoles, pyrazolines (**P1, P2 and P5-P9**) and acyl hydrazides (**AH5-AH9**), deriving from water addition to nitrile imine. Acyl hydrazides have been isolated only for derivatives that efficiently reacted in water solution. These compounds have been used as references for photochemical analytical experiments and, in case of pyrazolines, we have investigated their fluorescence properties.



Scheme 5.4 - Preparative synthesis of Pyrazolines (Pyr) and Acyl Hydrazides (AH); a) acrylamide (20 eq.), irradiation performed with Rayonet, at 310 nm, with two 15W lamps; b) Irradiation performed in water solution, with Rayonet, at 310 nm, with two 15W lamps.

Synthesis of pyrazolines and acyl hydrazides have been accomplished exploiting the photochemical route: in details, solution of tetrazole **T1-T9** (10^{-3} M) in 1:1 ACN:H₂O or pure water (depending on substrate's solubility) were irradiated at 310 nm to obtain acyl hydrazides. On the contrary, to induce the formation of pyrazolines, 20 eq. of acrylamide were added to the reaction mixture. Reaction times depends on photolysis quantum yields of tetrazole but, in general, no more than two hours of irradiation were necessary. Furthermore, to isolate desired adducts, reactions were stopped at low conversions (30-40%), to avoid formation of possible secondary photoproducts. Conditions exploited for each derivative are summarized in *Table 5.1*.

Compound	Solvent	Concentration (10^{-3} M)	Time (min)
P1	ACN:H ₂ O 1:1	5	80
P2	ACN	5	60
P6	ACN	9	60
P5	ACN	9	60
P7	H ₂ O	2	30
P8	H ₂ O	5	80
P9	H ₂ O	3	30
AH5	ACN:H ₂ O 1:1	5	60
AH6	ACN:H ₂ O 1:1	5	120
AH7	H ₂ O	7	45
AH8	H ₂ O	5	60
AH9	H ₂ O	7	120

Table 5.1 - Summary of synthesised and characterised photoproducts and reaction conditions used.

5.1.3 Spectroscopic and Photochemical Properties

The first step to evaluate the photochemical properties of these compounds was the recording of the UV-VIS spectra, to measure their molar absorption and molar extinction coefficients (*Figure 5.1*). Experiments were performed in 1:1 acetonitrile: phosphate buffer (50 mM, pH 7.4) solution and, for the water soluble tetrazoles **T6**, **T7**, **T8** and **T9** also in phosphate buffer (PBS) alone.

Spectra of tetrazoles are reported in *Figure 5.1*, divided according to the electronic properties of the aryl substituents: electron donor (D) or electron acceptor (A) at 2 and 5 position tetrazole atoms. The electronic effects influence the position of the maximum absorption peak: In particular, the more pronounced shift was observed in presence of the nitro group: indeed, **T3** and **T4** (*Figure 5.1*) show their highest absorption slightly above 300 nm, in a red-shifted position respect to the other tetrazoles. However, this effect is not observed replacing the nitro group with another electron withdrawing substituent in the same position such as **T6**, **T8** and **T9** (*Figure 5.1*). In general, almost all compounds showed a maximum absorption at 290 nm, with tails extended up to 340 nm. This evidence suggests that photoactivation could be efficiently achieved in this spectral region, where nucleic acids exhibit negligible absorption.

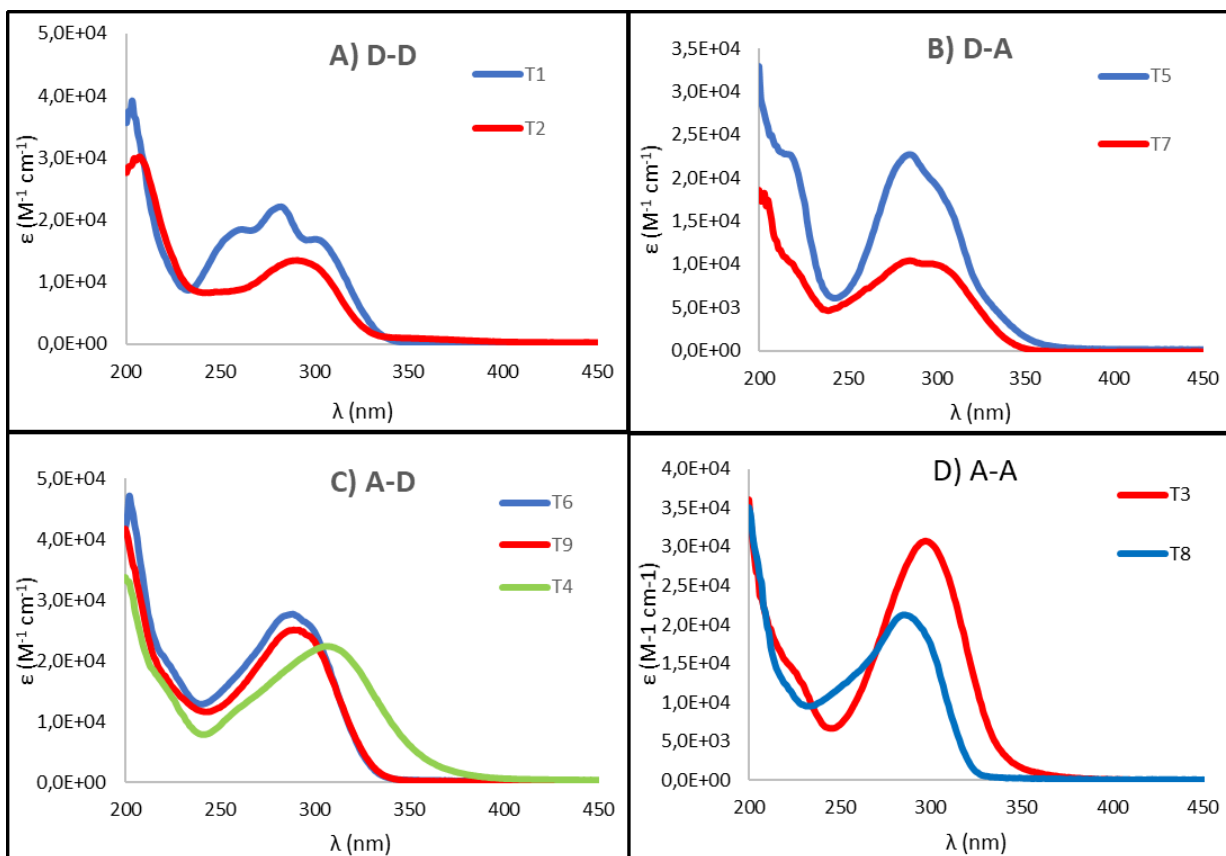
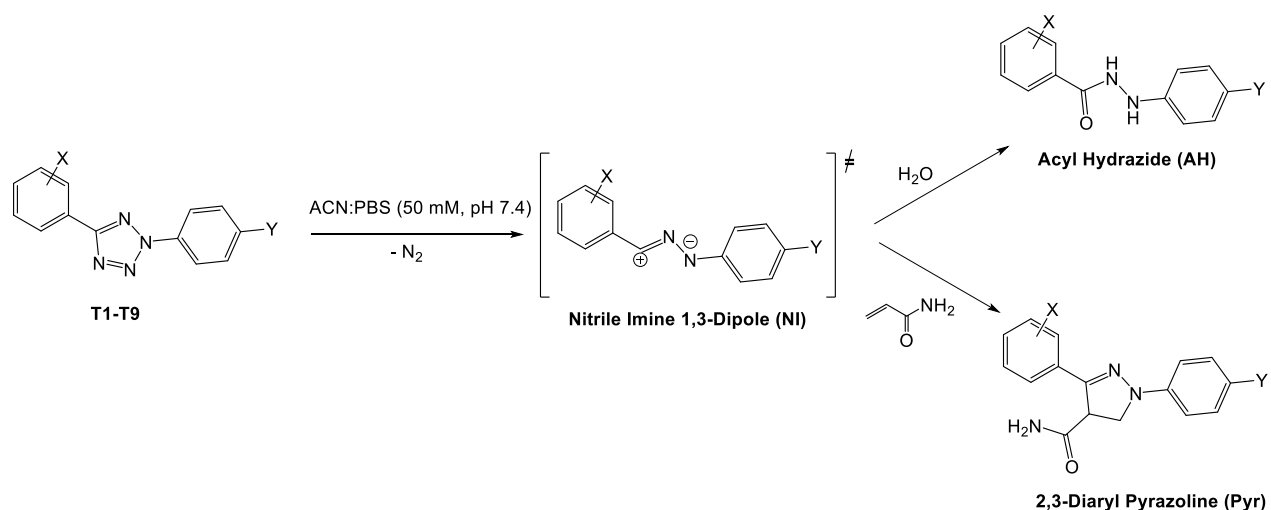


Figure 5.1 - UV-VIS spectra of 2,5-diaryl tetrazoles (2×10^{-5} M) recorded in 1:1 ACN:PBS (50 mM, pH 7.4) solution.

The analysis of absorption properties was followed by photochemical studies, to evaluate the influence of substituents on nitrile imine generation efficiency, therefore we have measured, for each compound, the photochemical quantum yield (Φ). Experiments have been performed in aqueous solution, to estimate the efficiency in conditions mimicking the physiological environment.



Scheme 5.5 – Photolysis reaction of 2,5-diaryl tetrazoles and generation of corresponding acyl hydrazides and pyrazolines.

Photochemical quantum yields have been determined irradiating tetrazoles **T1-T9** at 313 nm, with an optical desk, using ferrioxalate as standard reference. Photolysis reactions were monitored through UV-VIS and HPLC analysis, to both observe substrate consumption and the formation of the corresponding acyl hydrazide **AH**, the result of addition of water to nitrile imine intermediate. Experiments were performed in ACN:phosphate buffer 1:1 and, for water soluble **T7-T9**, also in pure phosphate buffer solution, at pH = 7.4. Quantum yields values have been measured applying the following equation described in section 4.2.4. Quantum yield values listed in *Table 5.2* suggest that, as expected, electronic effects of substituents influence the photolysis efficiency of tetrazoles. In general, it should be underlined that all compounds present efficient generation of the intermediate **N1**, with QY values ranging from 0.1 to 0.65, except in case of **T3** and **T4**: despite these were the tetrazoles with highest molar absorptivity at the wavelength of irradiation, they showed negligible reactivity and formation of the corresponding acyl hydrazides have not been detected.

Entry	Substituent Effect	Φ 310 nm	Solvent
T1	D-D	0.1150 ± 0.0002	ACN:PBS
T2	D-D	0.2 ± 0.1	ACN:PBS
T3	A-A	0.0044 ± 0.0003	ACN:PBS
T4	A-D	0.002 ± 0.002	ACN:PBS
T5	D-A	0.14 ± 0.07	ACN:PBS
T6	A-D	0.25 ± 0.09	ACN:PBS
T7	D-A	0.13 ± 0.02	ACN:PBS
T8	A-A	0.569 ± 0.004	ACN:PBS
T9	A-D	0.65 ± 0.07	ACN:PBS
T6	A-D	0.24 ± 0.08	PBS
T7	D-A	0.03 ± 0.01	PBS
T8	A-A	0.22 ± 0.05	PBS
T9	A-D	0.4 ± 0.1	PBS

Table 5.2 - Photolysis Quantum Yields of 2,5-Diaryl Tetrazoles were obtained through irradiation with an optical desk of 3 ml of 10^{-5} M solution in 1:1 ACN:PBS or PBS, at 310 nm. Values reported are the results of three different measurements.

Such low values are measured only in presence of nitro-group, suggesting that this substituent has a detrimental effect on tetrazole photolysis, probably because it favours different deactivation pathways. Simultaneous presence of two electron-donating substituents on the phenyl rings (combination defined D-D) afforded good reactivity, as in case of **T1** ($\Phi = 0.1150$). Replacement of hydroxy with methoxy group had a positive impact on quantum yield ($\Phi = 0.2$ for **T2**). Introduction of electron-withdrawing moieties on N-phenyl ring decreased photolysis rate, as in case of **T5** and **T7**, but this effect is less pronounced compared to the case of nitro-derivatives and the reactivity remains measurable. Most remarkable results were achieved with an acceptor at the phenyl ring on tetrazole C5 and an electron-donating group on the phenyl ring on N2, as shown by the efficient reactivity displayed by compounds **T6** and **T9**, even in pure phosphate buffer solution

(Φ = 0.2 and 0.65 respectively). Interestingly, tetrazole **T8**, despite the presence of two acylamino groups, showed efficient photolysis in both tested conditions, suggesting that high electron density on the 2,5-phenyl substituents of the tetrazole ring is not mandatory to achieve efficient photolysis. Then, from these outcomes, we can speculate that ring opening of 2,5-diaryl tetrazoles is only slightly influenced by the electronic nature of substituents introduced on two aromatic rings, except when a nitro-group is present. Moreover, the solvent affects the photolysis efficiency, especially in the case of **T7**, whose Φ in pure buffer is almost one order of magnitude lower.

Another aspect that should be underlined is that all these reactions are exceptionally clean and, in each case, formation of a single product, the acyl hydrazide, has been detected, even at high conversion of substrate (above 70%). This could be observed in UV-VIS profile of the reaction or in HPLC analysis: in *Figure 5.2*, HPLC profile of compound **T9** has been reported, as example, but for all compounds we observed the same outcome, with the quantitative formation of acyl hydrazide. Moreover, the absorption spectra of the tetrazoles **T1-T9** (*Figure 5.3*) during the irradiation exhibit isosbestic points, indicating the clear formation of a new, single product for each reaction.

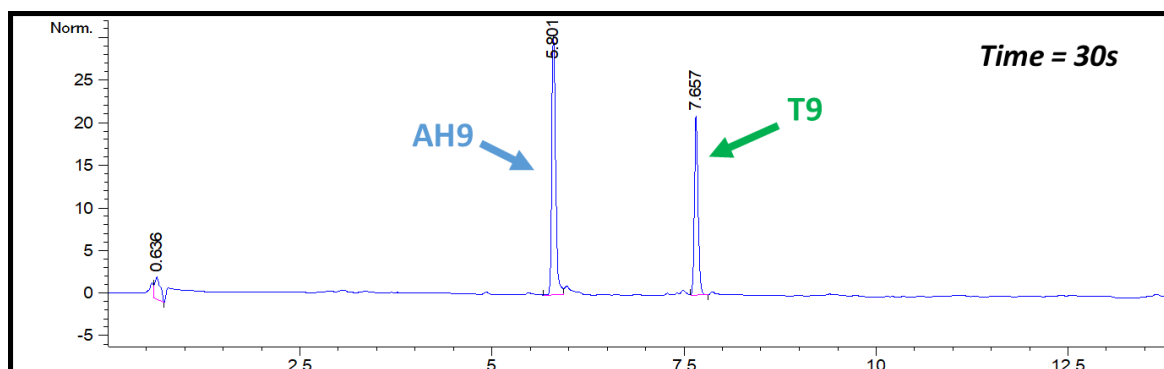


Figure 5.2 – HPLC profile of compound **T9, after 30 seconds of irradiation (310 nm, two 15-W lamps) in phosphate buffer solution (pH 7.4, 50 mM), at $C = 6 \times 10^{-5}$ M.**

In general, during irradiation, tetrazoles displayed similar absorption properties: the maximum band centred at 290, associated to $n-\pi^*$ transition of tetrazole, decreased significantly, indicating the ring rupture of tetrazole. At the same time, another peak, extended from 350 to 540 nm, depending on the type of substituents present, increased, although its intensity is significantly compared to the peak at 290 nm. Moreover, with most of analysed substrates, only few minutes of irradiation are sufficient to achieve almost complete substrate consumption, proving the high efficiency of this photochemical process.

To summarize, from these experiments emerged that compound **T9** seems to be the most efficient substrate, because of its excellent photolysis rate in water solution, followed by **T8** and **T6**.

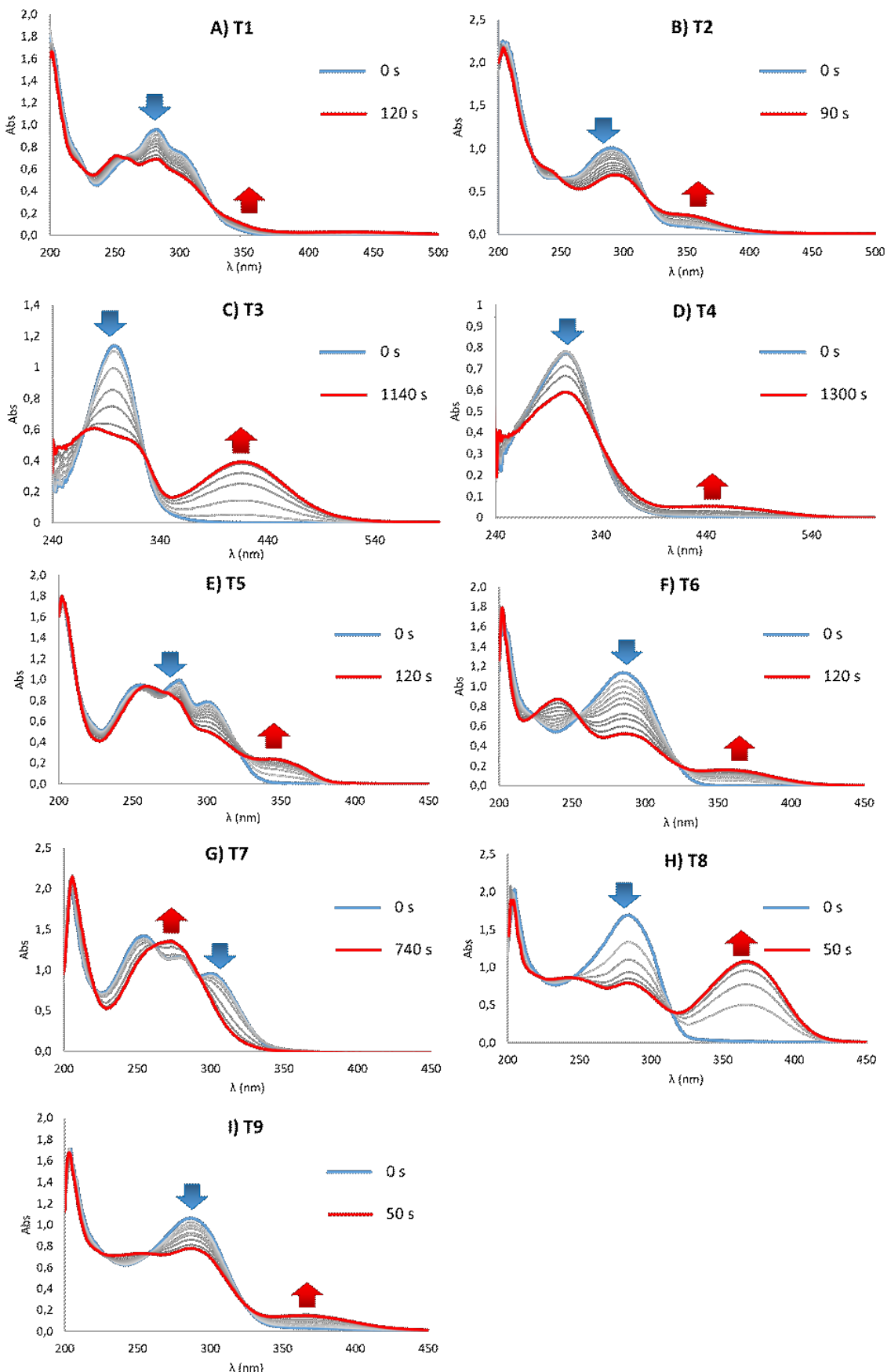


Figure 5.3 – A) UV-VIS Absorption spectra of tetrazoles **T1-T9** at different times of irradiation.

5.1.4 Fluorescent Properties of Pyrazolines

One of the most interesting properties of cycloaddition between tetrazoles and alkenes is the fluorogenicity. In fact, tetrazoles present only negligible emission, while pyrazolines arising from the cycloaddition with alkenes, including acrylamide, are fluorescent. This is a significant advantage for biological applications because it means that emission of the probe can be strictly modulated. However, it emerged that not all pyrazolines are characterized by high fluorescence emission: indeed, recently it has been reported that, to allow the visualization of the biological target, additional fluorescent probes, as coumarin¹⁹³ and cyanine derivatives¹⁹⁴, have been covalently conjugated to the tetrazole. To fully exploit the useful fluorogenicity of this photoclick reaction, and avoid conjugation with addition fluorophores, pyrazolines with intense emission should be individuated. To this aim, we have analysed the spectroscopic and fluorescent properties of pyrazolines **P1-P9**, obtained from our library of tetrazoles.

Initially, we have analysed their absorption profiles, in phosphate buffer solution (pH 7.4, 50 mM), except for **P2**, whose poor water solubility forced us to record its spectra in ACN: phosphate buffer 1:1. Pyrazolines' absorption properties are significantly different from corresponding tetrazoles (*Figure 5.4*): they present a minimum of absorbance at 290 nm, where tetrazoles display the highest absorption, and, in general, have two maximum peaks, at 250 nm and among 350 and 400 nm.

P1 had the most blue-shifted spectra, with a maximum at 320 nm, but it is also characterized by a very large band in this region. **P2**, **P5**, **P6** and **P7** display higher absorption at 320, 355 and 375 nm, respectively. **P8** and **P9** that present a most red-shifted spectra, with a maximum at 379 nm. It is interesting to note that, in this case, substituents have negligible effects on the position of absorption bands.

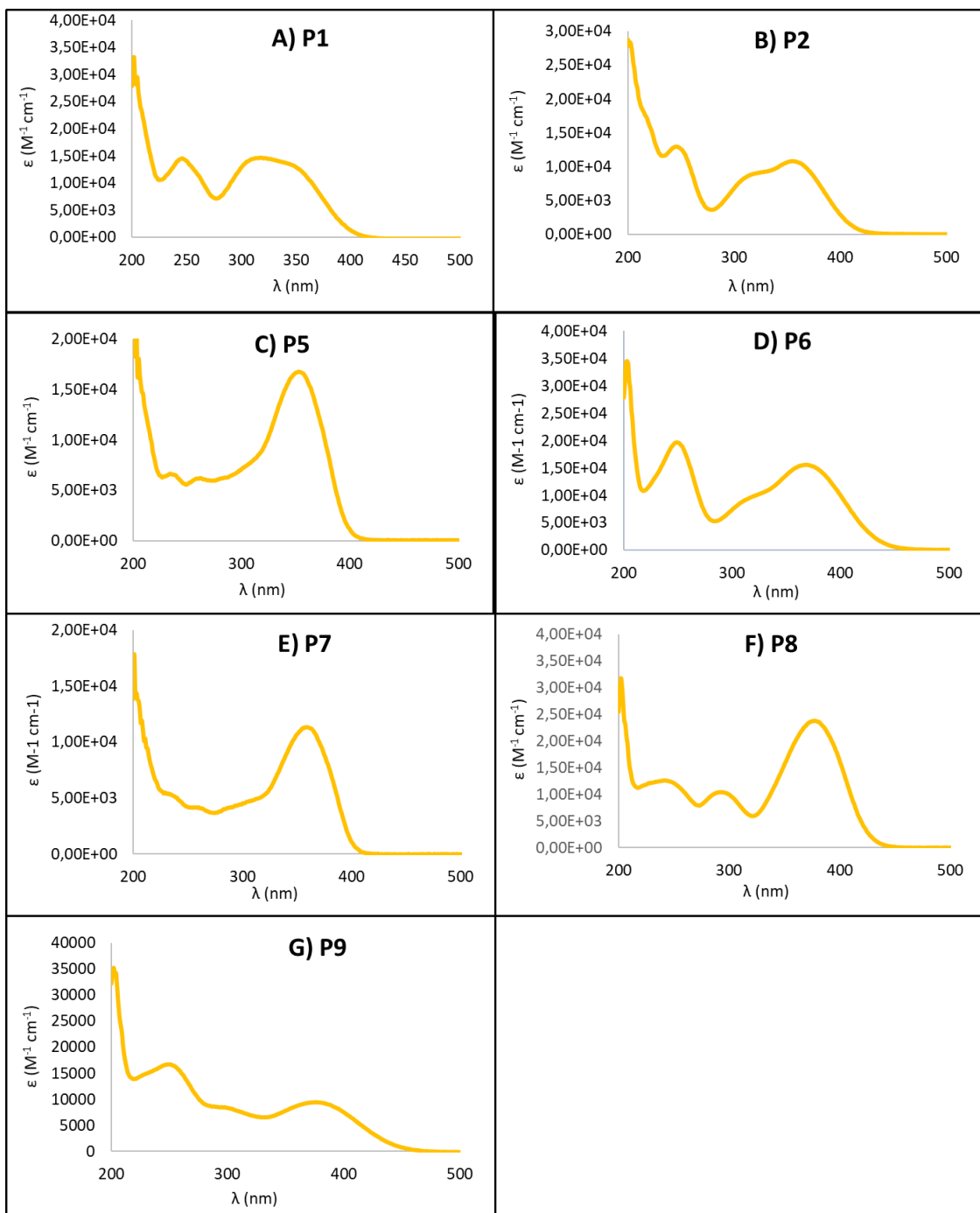


Figure 5.4 - P1-P9 molar absorptivity in PBS (50 mM, pH 7.4).

Furthermore, we have analysed the fluorescence of each compound. To find substituents able to enhance the emission, we have measured the fluorescence quantum yields, in DMSO and in water (*Table 5.3*). Pyrazoline behaviour is strictly dependent on the solvent and, in general, in DMSO we have obtained higher quantum yields, probably because, unlike water, DMSO erase self-aggregation . Moreover, the following data highlighted the remarkable effect of the substituents on pyrazoline emission properties.

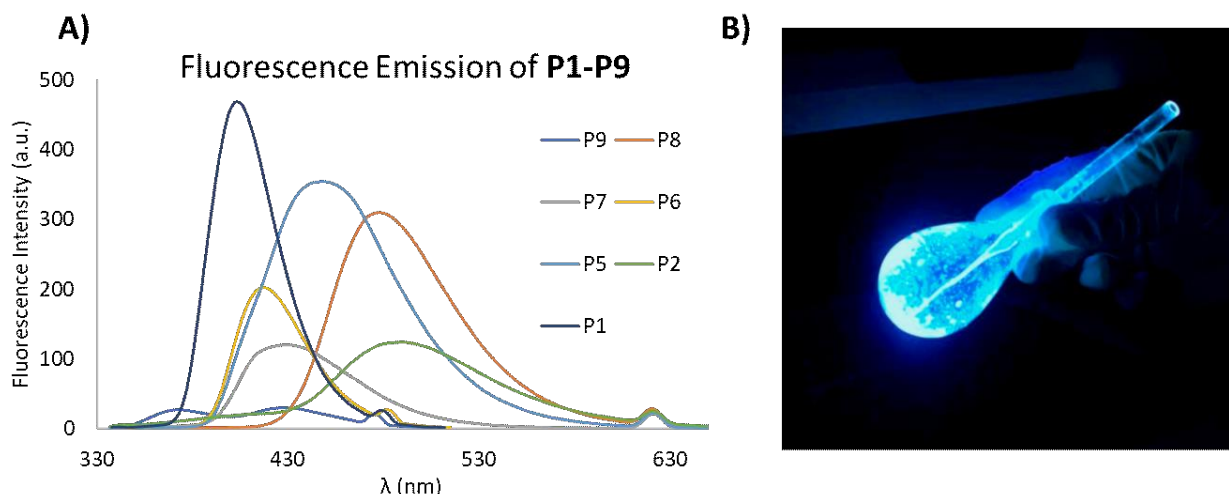


Figure 5.5 – A) Fluorescence emission of Pyrazoline **P1-P9** in DMSO solution, at $C = 2 \times 10^{-6}$ M. **B)** Fluorescence emission of **P8** upon excitation at $\lambda = 365$ nm, with a TLC lamp.

Indeed, in this case, the best outcome was achieved specifically when an electron-withdrawing substituent was introduced on N-phenyl ring of the product. In more detail, **P5** and **P7** showed excellent emission, with $\Phi = 65\%$ and 42% , respectively, but the most outstanding result was displayed by **P8**, that achieve $\Phi = 72\%$ in water solution, even higher than in DMSO (44%). These values are competitive with most common fluorescent dyes employed in biological fields, such as Rhodamines 6G ($\Phi_f = 90\%$ in water), Rhodamine B (31% in water)¹⁹⁵ and Alex-Fluor derivatives, whose quantum yields values, in water, range from 10 to 92%. Moreover, these emission efficiency is significantly higher in comparison to the photogenerated pyrazoline, reported by Lin's group¹⁷⁴. To our knowledge, these are the highest fluorescent quantum yields reported for pyrazolines in water solutions. Conversely, electron-donating groups on N-phenyl ring have detrimental effect on pyrazoline emission: in fact, for **P1**, **P2**, **P6** and **P9** afforded very low quantum yields in water, that increased significantly using DMSO as solvent, except in case of **P9**, whose emission remained negligible in all tested conditions. Then, it should be noticed that, in this case, nature of groups present on C-phenyl ring did not affect the emission properties of pyrazolines.

Another interesting consideration can be made on emission wavelengths: in general, we can observe that in water, a significant red-shift is observed for all compounds and is more pronounced for electron-rich pyrazolines, such as **P1**, **P2**, **P6** and **P9**, whose maximum is above 510 nm (*Figure 5.5*). Nevertheless, these compounds are also the ones characterized by lower quantum yields. Pyrazolines with an electron-withdrawing substituent on 2-N-Phenyl ring displayed the same behaviour, however, the emission reached its highest value at lower wavelengths, with the best result achieved with **P8** ($\lambda_{em} = 505$ nm).

An important aspect that should be underlined is that compounds that displayed highest fluorescence quantum yields, **P5**, **P7** and **P8**, are the same who were affected by lower photolysis quantum yields, while most reactive tetrazoles, as **T9** and **T5**, generate a pyrazoline with low emission intensity.

Entry	Substituent effect	Φ_f (%) H ₂ O	Φ_f (%) DMSO
P1	D-D	0.77 ± 0.04	45 ± 3
P2	D-D	0.77 ± 0.05	24 ± 3
P5	D-A	65 ± 1	44 ± 5
P6	A-D	0.41 ± 0.04	24 ± 6
P7	D-A	42 ± 1	65 ± 9
P8	A-A	72 ± 5	44 ± 0.4
P9	A-D	0.54 ± 0.04	3.0 ± 0.2

Table 5.3 - Fluorescence Quantum Yields of Pyrazolines, in water and DMSO. Fluorescence Quantum Yields (Φ_f) have been measured using 4,6-Diamidino-2-phenylindole (DAPI) as standard. Φ_f in DMSO were recorded using, as excitation wavelength, $\lambda = 310$ nm, while, in water $\lambda_{exc} = 350$ nm. Collected data are the results of three different measurements.

3.3.5 Efficiency of pyrazoline generation vs hydration

After the evaluation of spectroscopic properties of synthesized compounds, we have focused our attention on the second reaction step: cycloaddition with dipolarophiles. It is well-known that electron-donating substituents on N-phenyl ring can increase the rate of cycloaddition, however, a specific type of tetrazole scaffold, able to react selectively with alkene in physiological environment, it has not been individuated yet. Therefore, we have decided to analyse the behaviour of our library, to explore the reactivity of these new tetrazoles in presence of an alkene and the possibility to generate a highly fluorescent pyrazoline with good selectivity, in pure phosphate buffer solution. In these experiments, we have excluded **T3** and **T4**, because of their poor quantum yields and the impossibility to isolate the corresponding photoproducts.

As trapping agent, we have chosen acrylamide because it is one of the most used dipolarophile for bioconjugation. In the first set of experiment, we have irradiated tetrazoles **T1-T9** in presence of a large excess of alkene (100 equivalents), to immediately discard compounds that, even in these conditions, were unable to react preferentially with the dipolarophile. For each tetrazole, corresponding pyrazoline and acyl hydrazide, previously synthesized on a preparative scale, were used as references to determine products concentration during the analysis.

Solution of tetrazoles ($C = 10^{-5}$ M) were irradiated with a multi-lamps photoreactor (Rayonet) at 310 nm (with two 15 W lamps), in 1:1 ACN:PBS solution, in presence of 100 equivalent of acrylamide. Reactions were monitored through HPLC Analysis and UV-VIS, and little amount of solution were taken at different times in order to analyse products distribution.

For all considered substrates, we have observed clean reactions, with the formation of the only two expected products: **Pyr** and **AH**. In order to estimate cycloaddition efficiency, we have reported the ratio (indicated as $[\text{Pyr}]/[\text{AH}]$) between the concentration of generated compounds (*Table 5.4*) at high substrate conversion. Different tetrazoles were irradiated for different times, depending on their photolysis quantum yields. In general, with most of compounds, high product yields have been achieved in less than 5 minutes, while for compound **T7**, longer times (at least 12 minutes) were necessary.

Entry	Substituent effect	C (10^{-5} M)	Conversion (%)	Time (seconds)	Ratio [Pyr]/[AH]
T1	D-D	5.00	88	80	0.6
T2	D-D	6.00	93	70	^a AH n.d.
T5	D-A	4.00	93	80	3.7
T6	D-A	5.55	95	60	45.0
T7	D-A	7.67	80	720	2.7
T8	A-A	5.95	76	50	0.9
T9	A-D	7.16	73	40	AH n.d.

Table 5.4 - Conversion of tetrazoles and ratio between concentration of pyrazoline and acyl hydrazide obtained. Reaction were performed irradiating solution of tetrazole with Rayonet, in presence of 100 equivalent of acrylamide .^aAcyl Hydrazide not detected.

In such a large excess of trapping agent, almost all compounds led to the formation of higher yields of pyrazoline, compared to acyl hydrazides, except in case of **T1** and **T8**, whose ratio remained below 1. Tetrazoles **T5** and **T7**, despite their low photochemical quantum yields, formed the desired pyrazolines with good selectivity. However, most remarkable results have been observed with **T5** ([Pyr]/[AH] = 45) and, in particular, **T2** and **T9**, for whom acyl hydrazide formation was not even detected. Interestingly, best performances have been displayed by substrates with also highest rate photolysis. From these preliminary data, we can deduce that combination of acceptor-donor substituents ensures not only fast photolysis rate, but also selective formation of pyrazoline.

To verify if this selectivity can be retained decreasing concentration of acrylamide and if it is possible to perform the reaction in a more competitive environment, the same experiment has been repeated on selected tetrazoles in presence of different concentrations of acrylamide in pure buffer. We run these experiments with substrate **T9** and **T6**, which gave the best outcomes, but also with **T7**, for its good selectivity, and **T8**, for the solubility properties. Contrary, **T2** has not been included in this set of experiments, because of its poor solubility in aqueous solution. As in previous case, reactions were monitored through HPLC analysis and we have determined concentration of products at high reaction conversion. In *Table 5.5*, we have reported the ratio between concentration of pyrazoline and acyl hydrazide, at high substrate conversion.

Acrylamide Equivalents	Ratio [Pyr]/[AH]			
	T6 (95%)	T7 (90%)	T8 (85%)	T9 (70%)
5	0.9	1.0	Pyr n.d.	3.7
10	2.3	1.1	0.1	4.4
20	5.2	1.7	0.2	AH n.d.
50	11.1	2.4	0.5	AH n.d.
100	45.3	2.7	0.9	AH n.d.

Table 5.5 - Cycloaddition selectivity for T6, T7, T8 and T9. For each tetrazole, ratio between concentration of Pyr and AH are reported for different amounts of acrylamide. Percentage in brackets represent conversion of substrate at which the ratio has been measured.

As expected, decreasing the concentration of acrylamide, selectivity of the reaction diminished. The most dramatic effect can be observed on **T8**: concentration of pyrazoline decreases in a significant extent and, at only 5 equivalents of alkene, is not even detected anymore. For **T6** and **T9**, cycloaddition remained the preferred pathway at each amount of alkene. While **T6**, at only 5 equivalents of acrylamide, generated the corresponding pyrazoline in 50% yield, **T9** displayed high selectivity at each amount of trapping agent. For what concern **T7**, it didn't show outstanding performances, however, the ratio between the products is never below one, indicating a discrete selectivity. Moreover, pyrazoline generated by **T7** is highly fluorescent ($\Phi = 42\%$ in water), therefore this tetrazole can be considered a good compromise for potential biological applications, to achieve both an efficient photoreactivity and high fluorogenicity.

5.1.6 Biophysical Experiments to analyze G4 binding affinity

In order to preliminarily investigate the potential of tetrazole moiety as quadruplex photoactivatable ligands, we have considered water-soluble compounds, **T7**, **T8** and **T9** and analyzed their binding affinity through Fluorescence Resonance Energy Transfer assay (FRET Melting assay).

This experiment has been carried out with different quadruplex forming sequences: the telomeric F21T, the two quadruplex identified in the oncogene c-KIT (c-KIT1 and c-KIT2) and LTR-III and LTR-IV, associated to HIV virus. Results are summarized in *Table 5.6* and, as it's possible to observe, for each derivative, the experiment has been repeated at different ligand concentrations (5, 10 and 15 μM). It is evident that all analyzed compounds showed low affinity for G4 structures: in particular, **T8** and **T9** displayed even negative values, suggesting that they could even induce a destabilization of the target. The only exception is represented by **T7**, that, in case of LTR-III and LTR-IV, displayed moderate stabilization. The significantly different melting temperatures determined among different quadruplexes pointed out that **T7** is able to recognize selectively LTR-III and LTR-IV, representing an interesting starting point for the development of specific ligands for this target.

Compound	ΔT_m (°C)				
	F21T	c-KIT1	c-KIT2	LTR-III	LTR-IV
T7 (5 μM)	1.3	1.3	1.0	3.0	3.0
T7 (10 μM)	2.7	1.7	1.3	4.6	5.0
T7 (15 μM)	4.0	1.7	1.7	5.7	6.3
T8 (5 μM)	0.0	-0.7	0.0	0.0	-0.7
T8 (10 μM)	0.3	0.7	0.0	1.0	0.0
T8 (15 μM)	-2.3	-1.7	-3	-1.3	-2.6
T9 (5 μM)	-2.7	-2.7	-2.7	-2.0	-3.3
T9 (10 μM)	-2.7	0.7	-2.0	-1.6	-3.3
T9 (15 μM)	-2.3	-2.7	-1.3	-1.0	-3.3

Table 5.6 – FRET Melting assay, performed in presence of 0.25 μM of oligonucleotide.

However, it should be underlined that common quadruplex ligands reported in literature, induce higher stabilization of quadruplex structures and results achieved with these compounds cannot be considered competitive.

Then, in order to develop efficient ligands, further optimization of tetrazole scaffold was required, in order to improve binding affinity for the desired target.

5.1.7 Looking for biologically active scaffolds

Low affinity of 2,5-diaryl tetrazoles for quadruplex structures forced us to look for alternative strategies to improve their interactions with the selected target. To this aim, we reasonably planned to modify their structure through simple covalent conjugation to well-known quadruplex ligands, in order to ensure stronger and selective binding. In Freccero's group, several classes of ligands have been designed and synthesized, as naphthalendiimides (tri- and tetra-substituted)¹⁹⁶ and their dimers derivatives¹²⁵, core-extended naphthalendiimides¹³⁰, heptacyclic ligands¹⁹⁷ and squaraines⁹². These compounds can be considered good G4 ligands, well-suited to improve binding properties of 2,5-diaryl tetrazoles. However, the choice of the ligand depended not only on the affinity for the target, but was prompted by the necessity to achieve significant biological activity. Indeed, with the aim to develop biologically active ligands, this parameter cannot be neglected.

Therefore, we have evaluated the cytotoxicity, still unknown, of different classes of quadruplex ligands, previously produced and characterized in our laboratory, and compared their results with here synthesized, water-soluble, tetrazoles **T7-T9**. In details, we have investigated their anticancer and antiparasitic activity, testing their citotoxicity against two different cell lines, MRC5 and HT29, and two parasites, *Trypanosoma Brucei* and *Leishmania Major*. Here we present the obtained results for the following classes of compounds: tri- and tetra-substituted NDIs, core-extended NDIs and NDIs dimers and squaraines. It should be underlined

that the choice of these class of ligands was dictated also by their spectroscopic properties, in particular by their high molar absorptivity in the visible region.

Here we describe the obtained results for each class of compounds, tested on both cells and parasites and reported IC₅₀ values have been determined through MTT assay and with Alamar Blue (or Resazurin) assay for *Trypanosoma Brucei*.

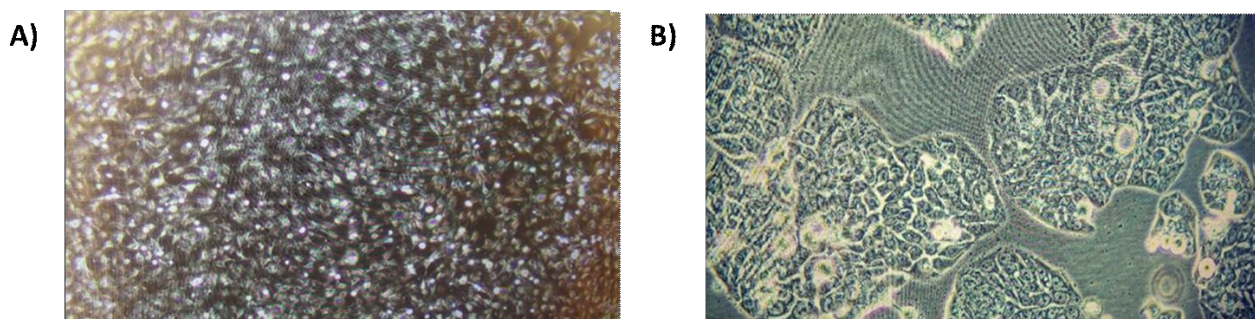


Figure 5.6 – A) MRC5 cells visualized with optical microscope; **B)** HT29 cells under optical microscope.

➤ Tri- and Tetra-Substituted Naphthalenediimides

We have analyzed twelve interesting tri- and tetra-substituted NDIs, **NDI1-12**, bearing substituents of different nature: in particular, they were mainly characterized by the presence of alkyl diamines and polyethylene glycole chains (PEG) (*Figure 5.7*). Amino groups ensure high solubility in water and strong interactions with G4s, although with often low selectivity. Conversely, PEG were introduced to maintain water solubility but increase the specificity for the target, ensured by the lack of positive charges. The influence of substitution degree on biological properties was also investigated, through the analysis of di-, tri- and tetra-substituted NDIs. Moreover, in this group we have added naphthaleniiimide **NDI11**, to verify the influence of the extension of the aromatic core, and the copper complex **NDI4**, which was not only a good quadruplex binder, but possesses catalytic activity able to selectively cleave quadruplex structures¹⁹⁸. MRC5 and HT29 cells were incubated with increasing concentration of these ligands and tetrazoles **T7-T9** and, subsequently, we have calculated their IC₅₀ values. In general, as it's possible to observe in *Table 5.7*, tetra-derivatives displayed low toxicity against HT29 cells and poor selectivity, as evidenced by their selectivity indexes. **NDI6** was the only exception, with S.I. = 12, despite its low toxicity against cancer cells. From these data, it seems that the presence of an increasing number of polyethyleneglycole chains increased the IC₅₀ values, as demonstrated by the trend reported in *Table 5.7*. In addition, these compounds displayed higher toxicity towards healthy cells MRC5 compared to cancer line, as the copper complex **NDI4**, then they cannot be considered promising anticancer agents.

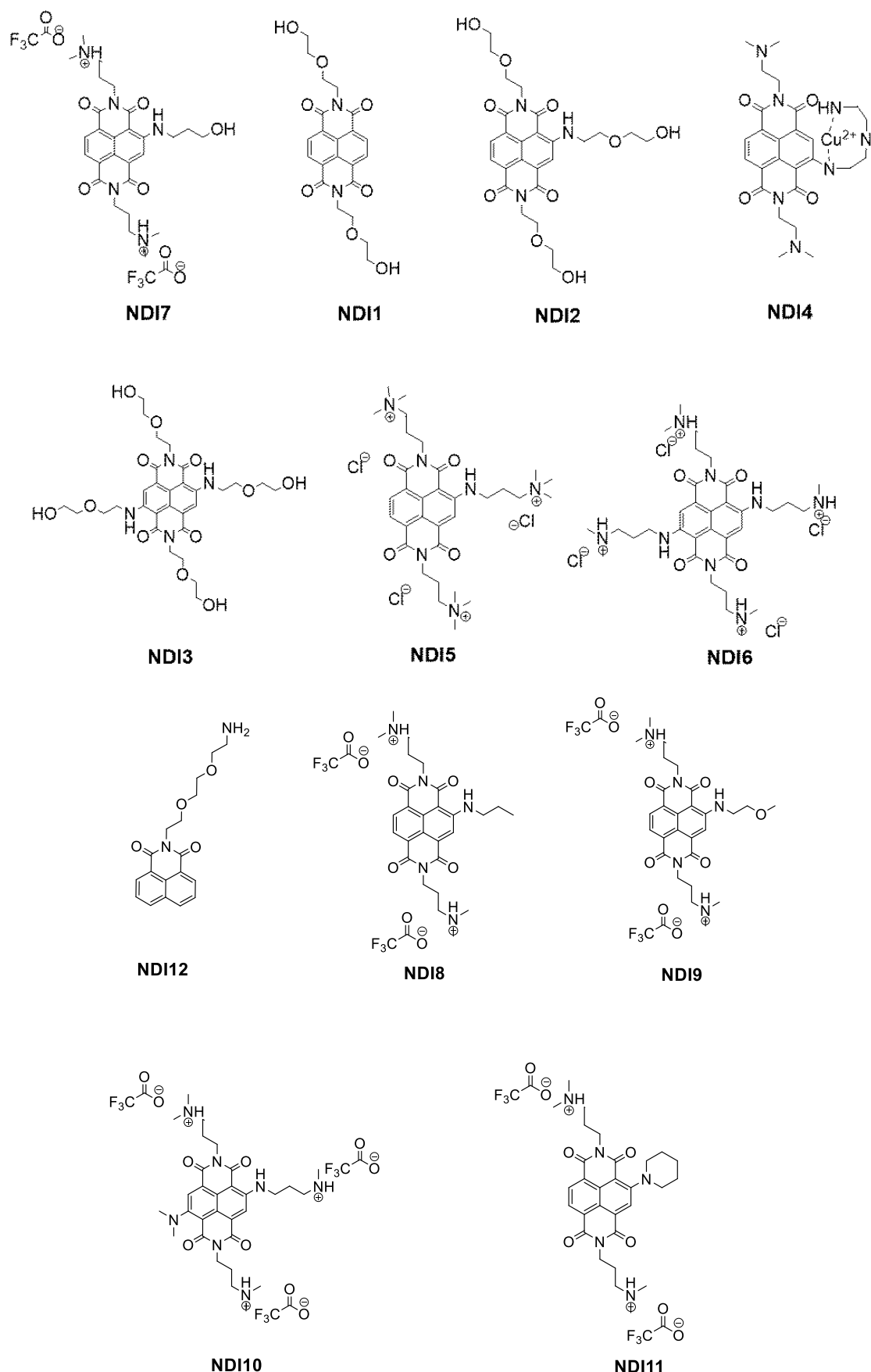


Figure 5.7 – Tri- and tetra-substituted NDIs analyzed.

The best results were accomplished with tri-substituted NDIs characterized by two or more 3-(dimethylamino)propylamine chains, in particular with **NDI10**, that was characterized by submicromolar toxicity towards HT29 cells and remarkable selectivity (S.I. = 44). This ligand was followed by **NDI9** and **NDI6**, with low IC₅₀ values and S.I. = 36 and 35, respectively. The analysis of tetrazole cytotoxicity revealed that these molecules not only were affected by poor binding properties towards G4, but they presented negligible biological activity, as proved by their high IC₅₀ values that, for **T7** and **T9**, are even above 50 µM, and low selectivity for cancer cells. This outcome further evidenced that modification of tetrazole scaffold is mandatory to optimize their performances for potential biological applications.

	HT29	MRC5	
Compound	IC ₅₀ (µM)	IC ₅₀ (µM)	Selectivity Index (S.I.)
NDI1	6 ± 1	2.1 ± 0.4	0.35
NDI2	8 ± 2	6.6 ± 0.3	0.8
NDI3	33.8 ± 0.3	> 100	-
NDI4	1.6 ± 0.4	0.5 ± 0.4	0.31
NDI5	> 80	> 100	-
NDI6	0.7 ± 0.2	12 ± 9	17
NDI7	0.080 ± 0.009	2.8 ± 0.9	35
NDI8	< 0,005	1.3 ± 0.2	-
NDI9	0.09 ± 0.01	2.0 ± 0.3	22
NDI10	0.22 ± 0.09	8 ± 6	36
NDI11	0.09 ± 0.009	4 ± 1	44
NDI12	84 ± 4	> 100	-
T7	47 ± 9	> 100	-
T8	9 ± 2	32 ± 12	1.3
T9	29 ± 1	> 50	-

Table 5.7 – IC₅₀ values of tri and tetra-substituted NDIs on MRC5 and HT29 cells.

Subsequently, we have investigated their antiparasitic activity, measuring the IC₅₀ values against *T. Brucei* and *Leishmania Major*.

The first fact that should be underlined is that, in general, all compounds showed higher toxicity towards *T. Brucei*, compared to *Leishmania*, and toxicity trend was similar to cells. For example, even in this case, increasing the number of polyethylene glycole chains, IC₅₀ decreased. More elevated toxicity was observed with tri-substituted NDIs with amines functions: the most remarkable results was displayed by **NDI7**, with an IC₅₀ in the subnanomolar range, followed by **NDI6** (IC₅₀ = 0.027 ± 0.006 µM) and **NDI8** and **NDI9**. Furthermore, **NDI7** showed also the highest toxicity against *Leishmania M*, evidencing its particular toxic effects against

parasites. Once again, tetrazoles **T7-T9** displayed low activity: only **T8** showed modest effect against *T. Brucei*, with $IC_{50} = 0.68 \pm 0.06 \mu M$.

	Leishmania M.	<i>T. Brucei</i>
Compound	$IC_{50} (\mu M)$	$IC_{50} (\mu M)$
NDI1	4 ± 2	0.99 ± 0.06
NDI2	96.6 ± 0.4	3.0 ± 0.2
NDI3	4.3 ± 0.7	11 ± 2
NDI4	56 ± 34	0.008 ± 0.001
NDI5	*	7 ± 1
NDI6	*	0.07 ± 0.02
NDI7	4 ± 3	0.027 ± 0.006
NDI8	0.008 ± 0.001	$4.38 \cdot 10^{-7} \pm 4.36 \cdot 10^{-7}$
NDI9	13 ± 7	0.031 ± 0.004
NDI10	3 ± 1	0.03 ± 0.02
NDI11	0.32 ± 0.11	0.4 ± 0.2
NDI12	63.5 ± 0.3	30 ± 2
T7	23 ± 2	19 ± 1
T8	96 ± 4	0.68 ± 0.06
T9	10 ± 0.9	17.8 ± 0.4

Table 5.8 – IC_{50} values of NDI1-NDI12 and T7-T9 on against *T. Brucei* and Leishmania M. *Values not determined because fluorescence of NDI5 and NDI6 interfered with Alamar blue assay.

➤ Core-extended Naphthalenediimides and NDI-Dimers

Subsequently, we have evaluated the toxicity of another class of naphthalenediimide derivatives: core-extended and dimers. As reported in *Figure 5.8*, we have selected four extended NDIs (**CEX1-CEX4**) and five dimers (**DIM1-DIM5**). We have explored how different substituents influence cytotoxicity properties of these scaffolds: in particular, for core-extended NDIs, we have analyzed two 3-(dimethylamino)propylamine derivatives, **CEX1** and **CEX4**, and other two compounds, one bearing morpholine moiety and the other one two polyethylene glycole chains. Morpholine has been chosen for its reduced basicity compared to propylamine function, therefore, in physiological environment, presents a lower degree of protonation, that results in higher affinity for G4s. NDI dimers involve both tri- and tetra-substituted NDIs, a core-extended derivative (**DIM1**) and, concerning substitution in the imidic positions, we have considered also a compound with two long-chain carboxylic acids.

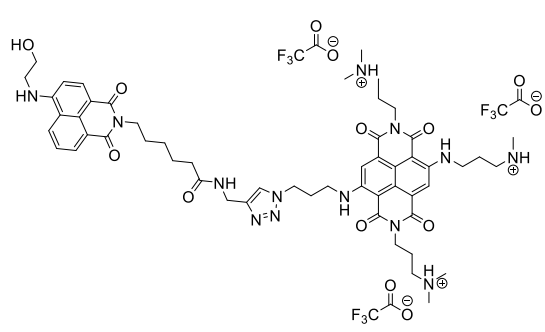
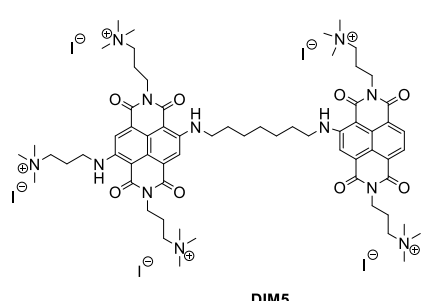
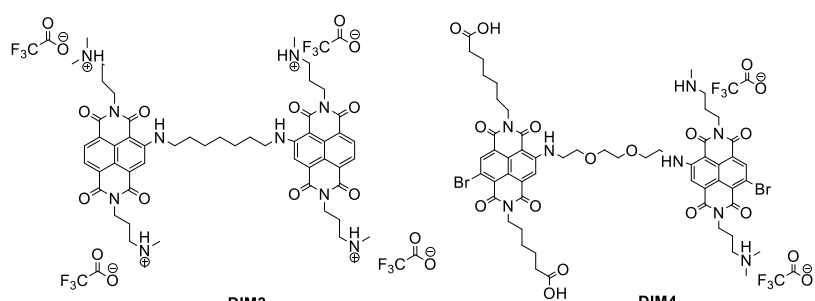
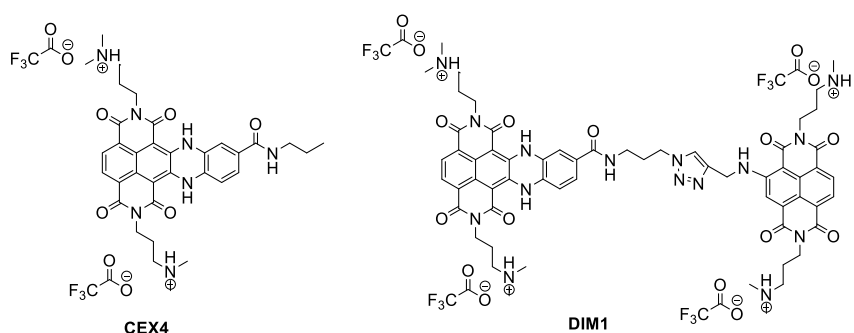
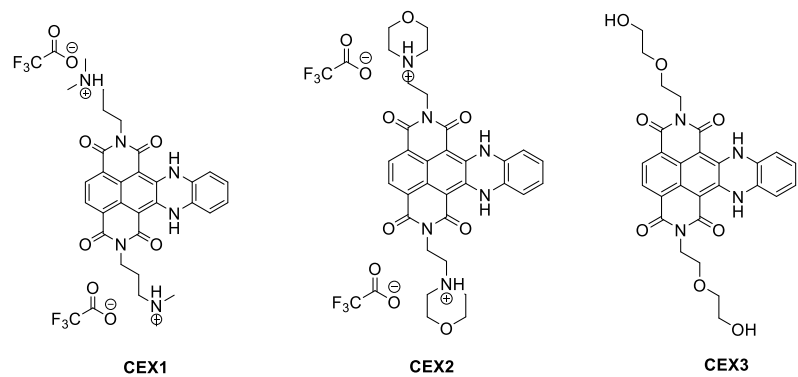


Figure 5.8 – Representation of here analyzed core-extended NDIs **CEX1-CEX4 and NDI dimers **DIM1-DIM5**.**

As described in *Table 5.9*, in the experiments on HT29 and MRC5 cells, we have observed very different outcomes, depending on the structural features of the compounds. In particular, **CEX1** and **CEX2**, with amino groups on imidic position, displayed not only the highest toxicity ($IC_{50} = 0.03 \pm 0.05$ nM and $IC_{50} = 0.03 \pm 0.01$ μ M) but also the best selectivity among healthy and cancer cells (S.I. = 150 and 63, respectively). However, it should be highlighted that, despite the unique specificity, these compounds showed elevated toxicity also against MRC5 cells, with very low IC_{50} values. **CEX4**, the only derivative presenting a functionalization of the extended aromatic core, displayed even higher toxicity compared to **CEX2**, but it had the same effect on the two cell lines, with poor selectivity.

Compounds	HT29 IC_{50} (μ M)	MRC5 IC_{50} (μ M)	Selectivity Index
CEX1	$3 \cdot 10^{-5} \pm 5 \cdot 10^{-6}$	$4.5 \cdot 10^{-3} \pm 3 \cdot 10^{-3}$	150
CEX2	$2.7 \cdot 10^{-2} \pm 1 \cdot 10^{-3}$	1.7 ± 0.4	63
CEX3	$9 \cdot 10^{-2} \pm 2 \cdot 10^{-2}$	$7 \cdot 10^{-1} \pm 3 \cdot 10^{-1}$	7.4
CEX4	$2.6 \cdot 10^{-3} \pm 4 \cdot 10^{-4}$	$6 \cdot 10^{-3} \pm 1 \cdot 10^{-3}$	2.3
DIM1	1.06 ± 0.05	43 ± 10	43
DIM2	57 ± 9	64 ± 1	1.1
DIM3	$1 \cdot 10^{-2} \pm 2 \cdot 10^{-2}$	$7 \cdot 10^{-2} \pm 6 \cdot 10^{-2}$	1
DIM4	12.8 ± 0.3	1 ± 1	12.8
DIM5	66.3 ± 0.5	>100	-

Table 5.9 - IC_{50} values of core-extended and dimers NDIs on MRC5 and HT29 cells.

Among NDI dimers, **DIM1** showed excellent selectivity index, with only moderate toxicity, (IC_{50} above 1 μ M for both cell lines). **DIM3** presented lower IC_{50} values, but with basically no specificity among HT29 and MRC5. The last two analyzed compounds, **DIM4** and **DIM5**, were affected only by low toxicity against cancer cells, therefore they don't represent promising compounds for potential anticancer therapy. Comparing these results, with tetrazoles **T7-T9**, we have observed that core-extended NDIs, as the previous tri- and tetra-substituted compounds, showed remarkable higher toxicity compared to tetrazole scaffolds, while, interestingly, dimers displayed similar activity, except for **DIM3**. Therefore, we can conclude that the presence of a larger and planar aromatic surface, is responsible of elevated toxicity towards human cell lines, regardless of the type of substituents present. However, the nature of the functional groups seems to be relevant to determine the selectivity for a specific cell line, as demonstrated by improved selectivity index obtained with the introduction of protonable amino groups. Conversely, conjugation of two naphthalenediimide units even decreased the toxicity, evidencing that this strategy, on the basis of these preliminary data, isn't particularly promising for the development of novel anticancer agents.

With these compounds, determination of the antiparasitic activity has not been possible, because the specific fluorescence emission of these compounds interfered with the Alamar blue assay, the fluorescence-based analysis used to determine citotoxicity against parasites, therefore a more suitable protocol should be developed to obtain more reliable results.

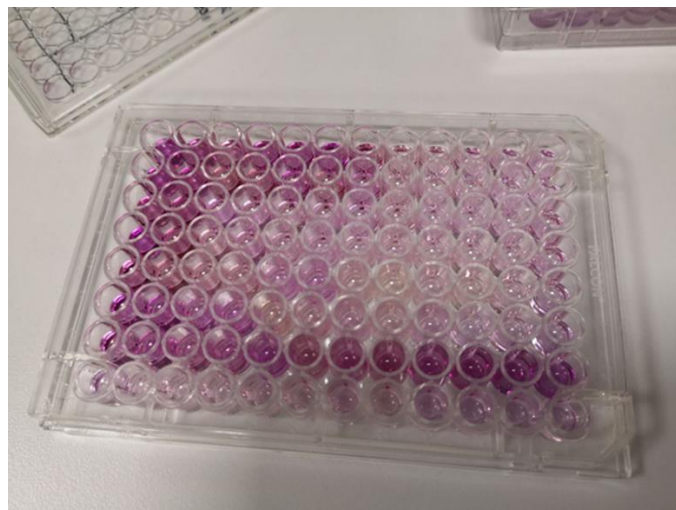


Figure 5.9 – 96-well plate of HT29 cells incubated with **CEX1-CEX3**, after the MTT assay. The colour indicate the percentage of cell survival: purple wells are associated to elevate amounts of survived cells, while white wells indicate that most of cells didn't survive.

➤ Squaraines

In the end, we have investigated the biological behaviour of a third class of previously reported quadruplex ligands, squaraines, which are cyanine derivatives with very interesting optical properties, as their intense emission in the NIR region¹⁹⁹. Coherently with previous biological investigations, we have selected compounds characterized by different substituents, in particular alkyl chains bearing terminal amine and polyethylene glycole functions, as reported in *Figure 5.10*.

With squaraines, we have obtained very different results compared to naphthalenediimide derivatives: as reported in *Table 5.10*, most of them showed IC₅₀ values above 100 µM on both cell lines, with no selectivity. Slightly better activity was observed with **V40**, bearing two polyethylene glycole chains, and **V46**, with two ester functions connected to the central core through a two-carbon atom spacer. Although these two molecules presented better results compared to other analyzed squaraines, their activity cannot be considered promising for potential anticancer applications. Moreover, if we consider the results achieved with tetrazoles **T7-T9**, we noticed that even tetrazole scaffold was characterized by better efficiency, in terms of both selectivity and IC₅₀ values, respect to squaraines. Therefore, squaraines cannot be employed to improve the biological activity of 2,5-diaryl tetrazoles. Their such low toxicity could be due to poor cellular uptake, then, further experiments should be performed to verify this hypothesis and, in case this is confirmed, modification of the structure could be performed to improve this aspect.

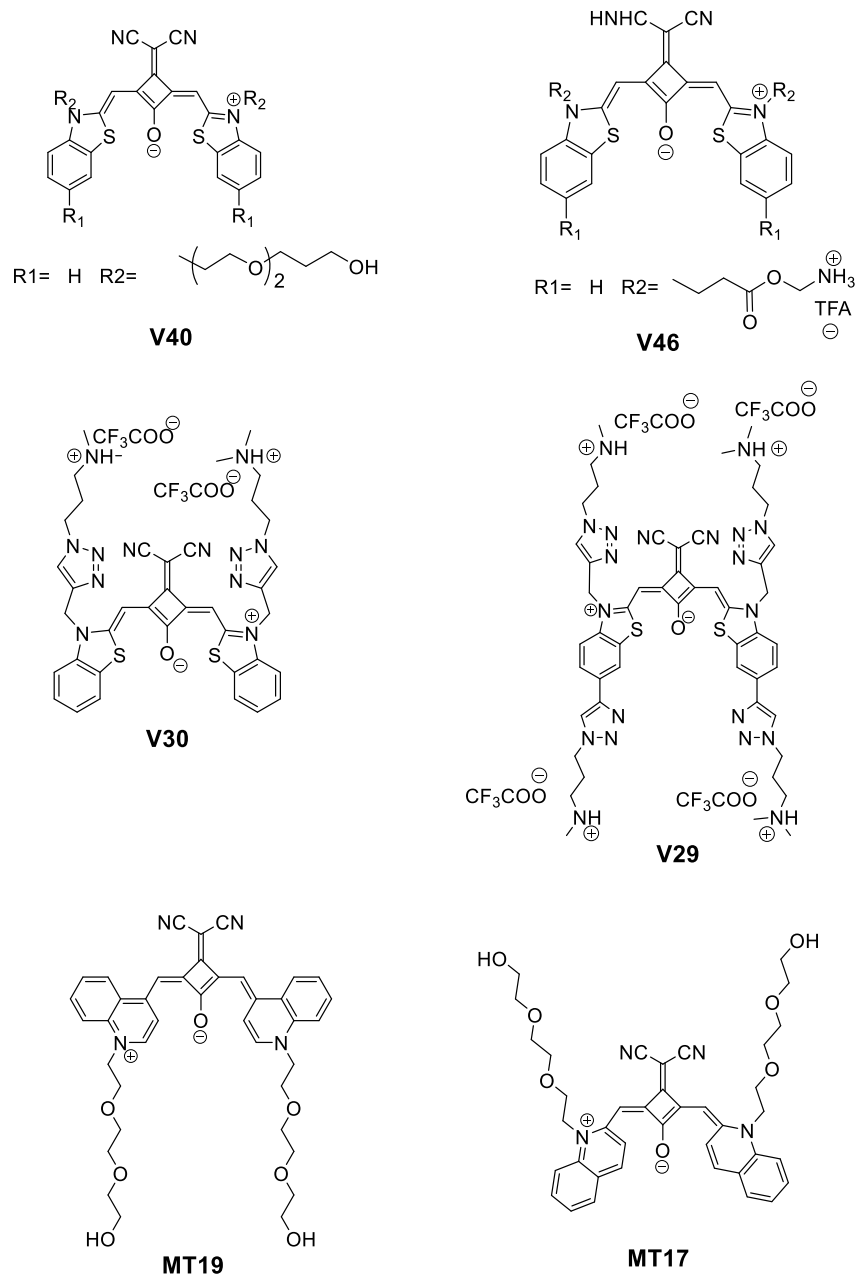


Figure 5.10 – Squaraines analyzed to determine their IC_{50} values on HT29 and MRC5 cells and on parasites *T. Brucei* and *Leishmania M*.

	HT29	MRC5
Compound	IC ₅₀ (µM)	IC ₅₀ (µM)
V29	> 90	0.2 ± 0.1
V30	> 100	> 100
V40	12 ± 6	2.7 ± 0.7
V46	7 ± 3	> 100
MT17	> 100	> 100
MT19	> 100	> 100

Table 5.10 - IC₅₀ values of squaraines on MRC5 and HT29 cells.

Subsequently, we have determined their behaviour on parasites and, as it's possible to observe in *Table 5.11*, different outcomes have been obtained with two different microorganisms: indeed, we verified complete absence of toxicity on *Leishmania M.*, for all squaraine derivatives, with IC₅₀ always above 100 µM. On *T. Brucei*, slightly better activity was recorded, with IC₅₀ ranging from 6 to 27 µM. The lowest values was displayed by **V30**, characterized by two triazoles and two alkyl amines. However, all squaraines were characterized by poor biological activity and tetrazoles **T7-T9** showed significantly higher toxicity towards both parasites, in particular against *T. Brucei*, with IC₅₀ below 1 µM.

	T. Brucei	Leishmania
Compound	IC ₅₀ (µM)	IC ₅₀ (µM)
V29	16 ± 7	> 100
V30	6 ± 3	> 100
V40	27 ± 2	> 100
V46	14 ± 7	> 100
MT17	20 ± 6	> 100
MT19	> 100	> 100

Table 5.11 - IC₅₀ values of squaraines against *T. Brucei* and *Leishmania M.*

From this preliminary screening, emerged that naphthalenediimides represent the most promising scaffold to improve the biological properties of 2,5-diaryl tetrazoles. In details, tri- and tetra-substituted NDIs and core-extended presented most interesting anticancer and antiparasitic activities. Therefore, we addressed our choice towards the first class of ligands and we decided to exclude, for the moment, core-extended NDIs, because of their low IC₅₀ values on MRC5 cells. In the end, tri-substituted NDIs resulted to be the most suitable scaffold, not only for good toxicity with excellent selectivity, but also because their activity could be easily modulated by proper choice of substituents.

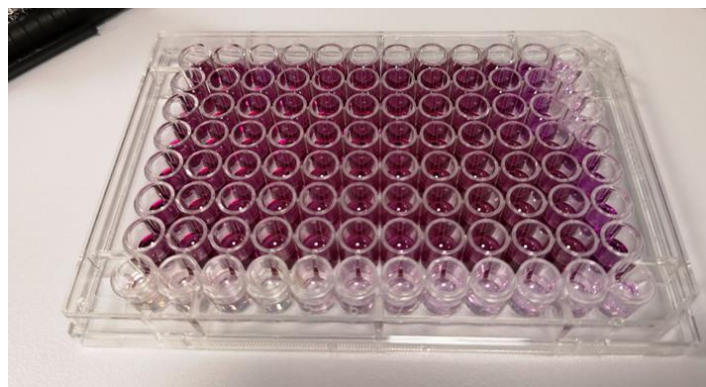


Figure 5.11 - 96-well plate of HT29 cells incubated with Squaraines, after the MTT assay. Almost all wells resulted to be of an intense purple, indicating the very low toxicity of these compounds.

5.1.8 Conclusions

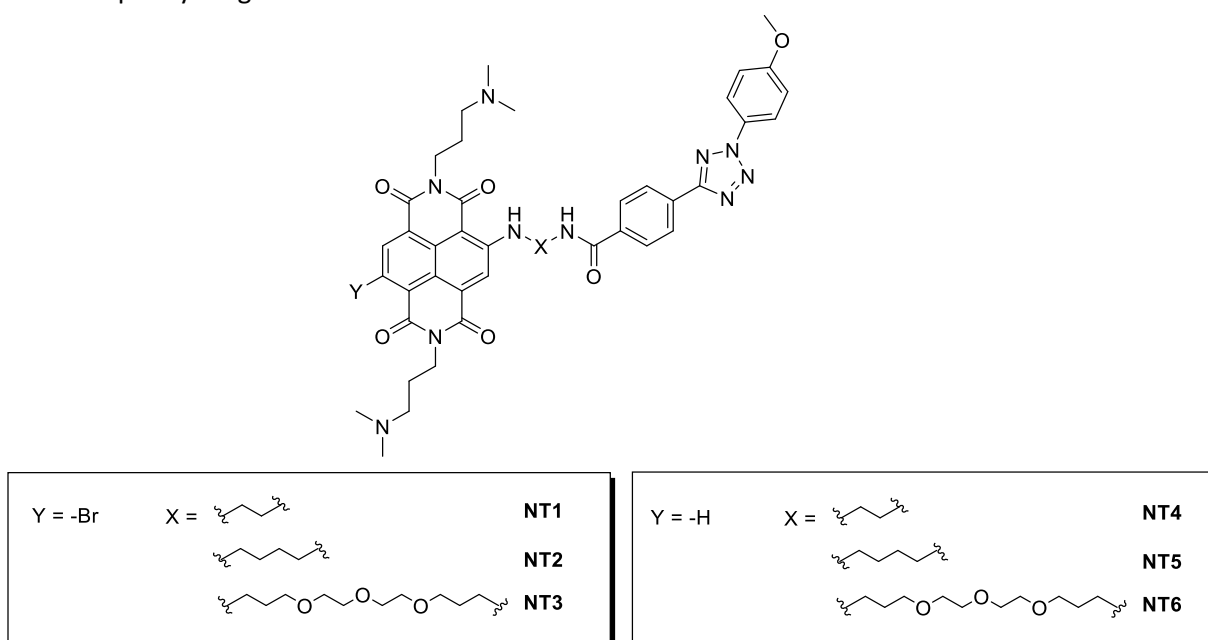
From the analysis of different substituted 2,5-diaryl tetrazoles, we have discovered that different combination of substituents strictly influence their photoreactivity. Presence of electron-donating substituents accelerate nitrile imine formation, especially if they are introduced on N-phenyl ring, and improve the selectivity of the cycloaddition, leading to the formation of high yields of pyrazolines, even at low concentration of alkene. However, the same trend has not been observed during the evaluation of fluorescent properties of their corresponding pyrazolines: indeed, intense emission are observed only for compounds bearing electron-withdrawing groups on N-phenyl ring, while introduction of electron-donating substituents in that specific position has a quenching effect on fluorescence emission. Therefore, the requirements to obtain high photoreactivity and high quantum yields are the opposite. However, in order to maximize the efficiency of the process, a compromise can be achieved: **T7**, despite the low photolysis efficiency, showed good selectivity in the cycloaddition step and its corresponding pyrazoline displayed high fluorescence quantum yield. With the aim to exploit tetrazoles to develop new quadruplex ligands, we have also preliminarily investigated the binding affinity of water soluble **T7**, **T8** and **T9** for some common quadruplex forming sequences, through FRET melting assay. Unfortunately, these compounds displayed only low stabilization of tested G4s, evidencing the impossibility to use them as efficient ligands. Then, 2,5-diaryl tetrazoles scaffold requires further modifications, in order to improve the affinity for quadruplex structures. To this aim, we planned to conjugate tetrazole moieties to previously reported G4 ligands, synthesized in Freccero's laboratory. However, the choice of the ligands has been dictated not only by affinity for the target, but also by their biological activity: indeed, we have selected three classes of compounds and analyzed their anticancer and antiparasitic activity, to individuate biologically active scaffolds, that could be employed for therapeutic applications. Moreover, we have compared these results with toxicity of tetrazoles **T7-T9**, that, as expected, resulted to be quite low. In the end, considering both their affinity for G4s and biological activity, tri-substituted NDIs appeared to be the most promising derivatives to improve properties of 2,5-diaryl tetrazoles.

5.2 Photoresponsive Tetrazoles-Based G4 ligands

5.2.1 Design of Tetrazole-based ligands

Previously described 2,5-diaryl tetrazoles exhibit interesting spectroscopic and photochemical properties, which can be exploited to develop light-responsive quadruplex ligands, after having tackled two major drawbacks: 1) they have low affinity for quadruplex structures and 2) the photo-generation of intermediate nitrile imine occurs upon irradiation with UV-light, centered at 300-350nm. For biological applications, the process should be activated, at least, with visible light, to minimize DNA damage.

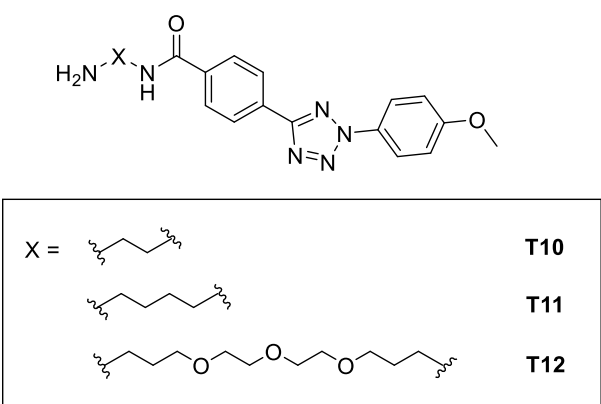
To this aim, we planned to modify tetrazoles scaffold to overcome both these issues. In details, we assumed that the conjugation of 2,5-diaryl tetrazole moiety to naphthalenediimide (NDI) core might represent a valid strategy: in fact, the planar and aromatic structure of NDI ensures strong affinity for G4 structures and, at the same time, due to its intense absorption in the visible region, upon excitation, it could trigger tetrazole photolysis through energy transfer or electron transfer, as already observed with other photoactivatable conjugates¹³⁸. To verify this hypothesis, we have synthesized six different conjugates NDI-Tetrazoles **NT1-NT6** (*Scheme 5.6*), covalently linked with alkyl spacers of two, four and twelve atoms. The longest chain was a polyethyleneglycole linker, chosen because the presence of multiple oxygen atoms improved both the solubility and affinity for the target. Concerning the synthesis of these conjugates, we have used NDIs, with 3-(dimethylamino)propylamine moiety, at the imide positions and with an alkylamino linker on the naphthalene core, for the conjugation to the tetrazole. Three of the six NDI-tetrazole conjugates are characterized by the presence of a bromine atom on naphthalene core, which is replaced by a hydrogen atom in the other three compounds. Methoxy group was chosen as electron donor substituent on N-phenyl ring of the tetrazole, with the aim to increase the efficiency of the photoreactivity, while an amide group was placed on C-phenyl ring.



Scheme 5.6 – Structure of the NDI-Tetrazole conjugates (**NT1-NT6**), synthesized and investigated in the present study.

We have optimized the synthetic protocol to efficiently obtain the designed conjugates **NT1-NT6** and, simultaneously, we have produced three novel water soluble tetrazoles, **T10**, **T11** and **T12**, to be tethered to the NDI core (*Scheme 5.7*). Subsequently, we have analyzed spectroscopic properties of all synthesized compounds, to evaluate the interaction between two chromophores. In details, we have investigated the photoactivation at 517 nm, to verify if the activation of tetrazole using visible light was possible, and analyzed the nature of generated products. Photoreactivity has been investigated even at 310 nm, not only because of the higher absorption of compounds in this spectral region (resulting in higher reactivity) but also to evaluate the reactivity by tetrazole direct irradiation.

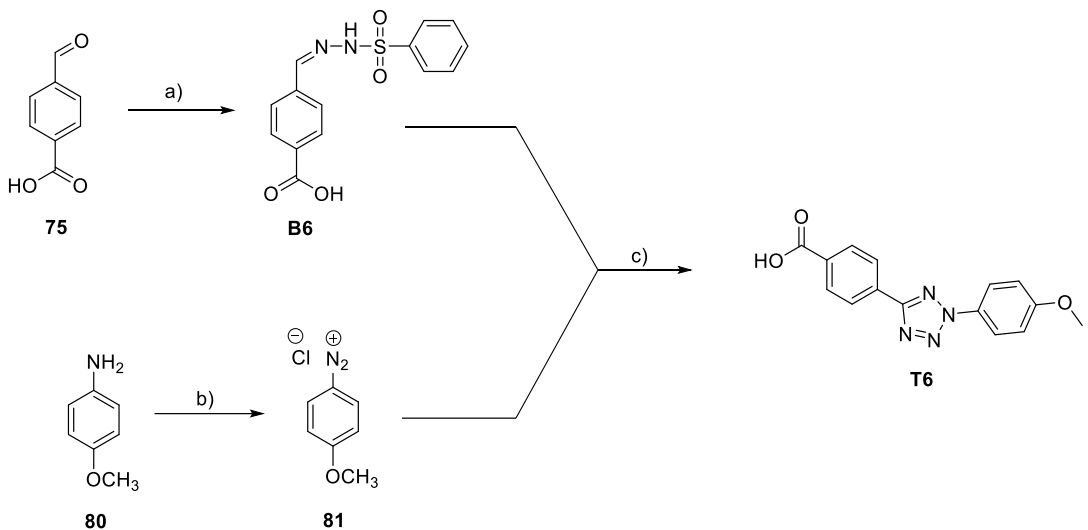
In the final part of the work, we have also investigated the affinity of these new conjugates towards different quadruplex structures, by circular dichroism (CD) analysis, to confirm their potential as novel photoactivatable ligands.



Scheme 5.7 – 2,5-Diaryl tetrazoles **T10, **T11** and **T12** synthesized for conjugation on NDIs.**

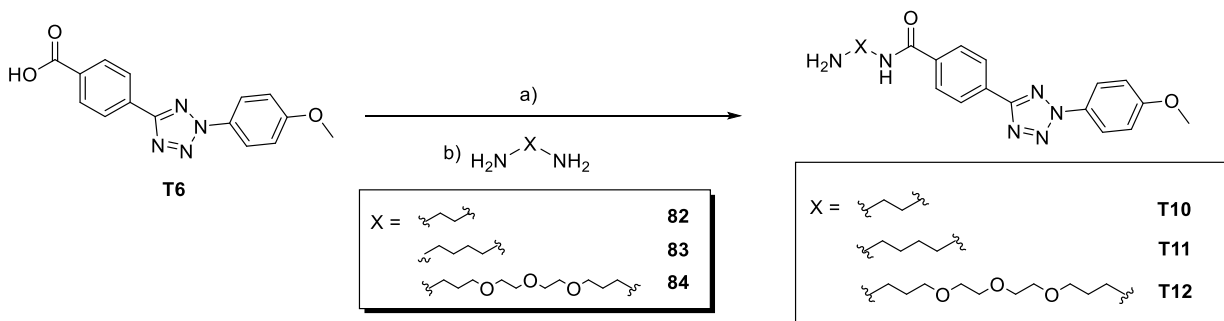
5.2.2 Synthesis of NDI-Tetrazoles conjugates

To obtain the designed compounds **NT1-NT6**, we started with the synthesis of three 2,5-diaryl tetrazoles **T10-T12**. We have exploited the same synthetic protocol described in the previous section (3.1.2), then we performed the condensation reaction between benzaldehyde **75** and commercially available benzensulphonyl hydrazide to quantitatively produce the corresponding benzensulphonyl hydrazone **B6** (*Scheme 5.8*). At the same time, we have synthesized the corresponding arenediazonium salt, from p-anisidine **80**. The arenediazonium salt has not been isolated and was used for the subsequent step without purification. Solution of **81** was added dropwise to a cooled solution of **B6**, dissolved in pyridine. Reaction was stirred at room temperature for four hours and, after this time, tetrazole **T6** was precipitated through addition of water (*Scheme 5.8*).



Scheme 5.8 – Synthesis of tetrazole **T6:** *a)* Benzenesulphonyl hydrazide (1 eq.), EtOH, r.t, 2 h; *b)* NaNO_2 , HCl 37%, EtOH 50%, 0°C, 30 min; *c)* Pyridine, 0°C-r.t., 4h.

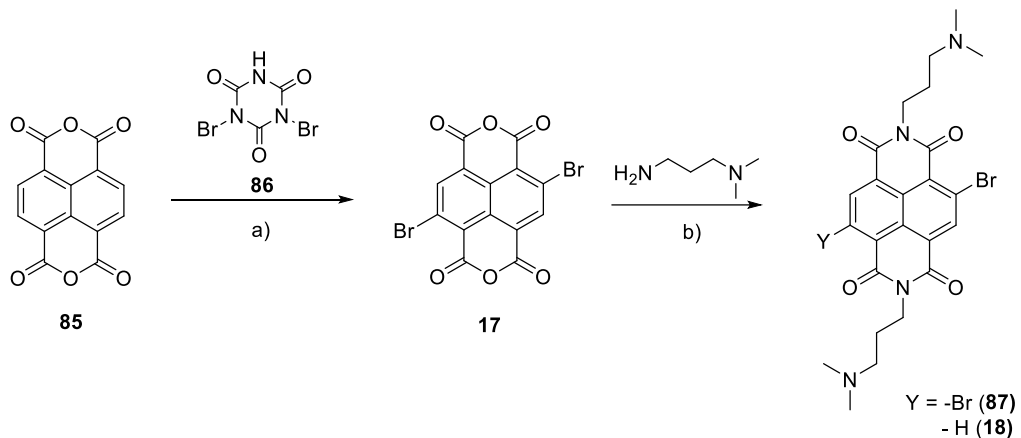
Final tetrazoles **T10-T12** were synthesized with coupling reactions, with three different amines (*Scheme 5.9*). Briefly, tetrazole **T6** was dissolved in ACN and solution was cooled to 0°C with an ice bath. PyBOP, was used as activating agent, with *N,N*-diisopropylethylamine (DIPEA), and the resulting mixture was stirred at r.t. for 30 minutes. In the meantime, in a separated flask, a large excess of amines **82-83** were dissolved in ACN and cooled to 0°C. The solution containing the carboxylic acid **T6** was transferred into a dropping funnel and added dropwise to amine, in order to avoid the formation of polymeric products. After two hours, reaction was quenched and the crude was purified through flash column chromatography to isolate **T10-T12** in moderate/good yields (40-68%).



Scheme 5.9 – General procedure for the synthesis of tetrazoles **T10-12:** *a)* DIPEA (2 eq.), PyBOP (1 eq.), ACN, 0°C, 30 min. *b)* amine (10 eq.), ACN, 0°C-r.t., 2h.

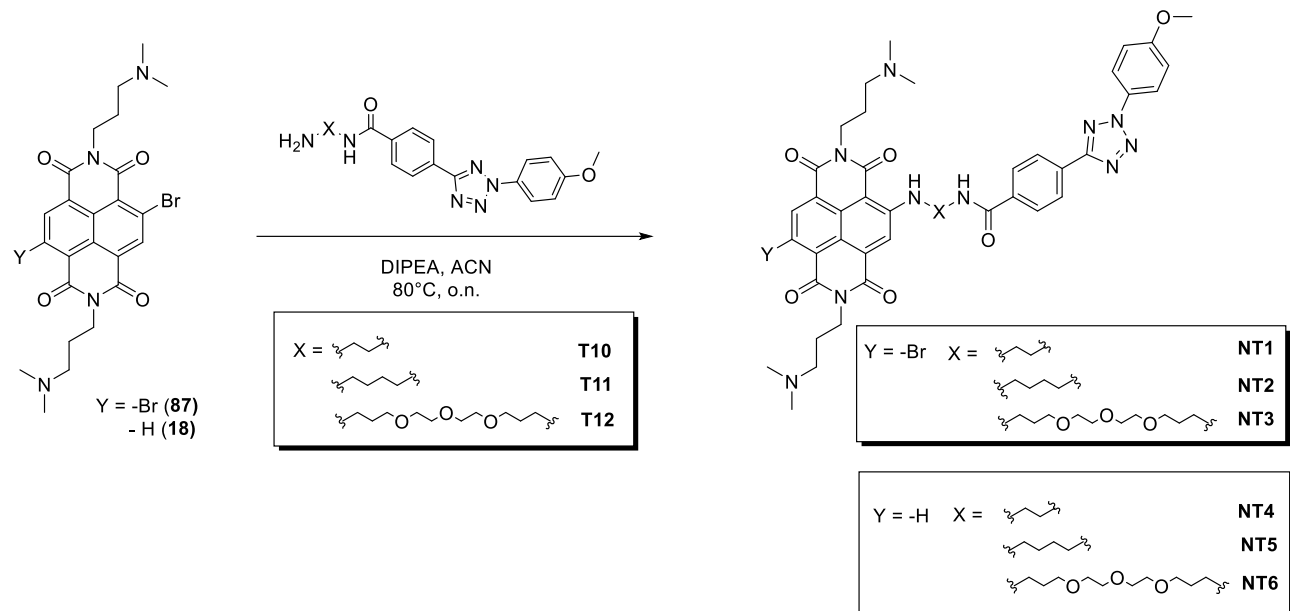
Once we have obtained the tetrazoles **T10-T12**, we proceeded with the synthesis of the NDI scaffold and we have exploited the synthetic protocol optimized by Freccero's group. Starting from commercially available 1,4,5,8-Naphthalenetetracarboxylic dianhydride **85** (*Scheme 5.10*), we performed a bromuration of naphthalene core with dibromoisocyanuric acid **86**, in pure sulfuric acid, at 130°C. After 16 hours, dibromoanhydride **17** was isolated through simple filtration of reaction mixture on Buchner funnel. Conversion of anhydrides into imides was obtained upon treatment of **17** with 3-(dimethylamino)propylamine in acetic acid, under reflux, for 30 minutes, with the same procedure

described previously. From this reaction, a mixture of products was obtained, composed for 60% of NDI with two bromine atoms (**87**) and for 30% by mono-brominated derivative **17** (while the remaining 10% was NDI without bromine). However, the crude was not purified and this mixture was employed for the subsequent synthetic step.



Scheme 5.10 – Synthesis of NDIs 18 and 87: a) dibromoiso-cyanuric acid (1.5 eq.), H_2SO_4 98%, $130^\circ C$, 16h; b) 3-(dimethylamino)propylamine (2.5 eq.), CH_3COOH , $130^\circ C$, 30 min.

Finally, the conjugation of NDIs to previously synthesized tetrazoles involved an aromatic nucleophilic substitution: the free alkylamino group on tetrazole **T10-T12** was exploited to replace the bromine atom on NDI core. Reaction occurred in acetonitrile, in presence of DIPEA. After one night under reflux, substrate was completely consumed and two products were produced: the brominated NDIs (**NT1-3**) and the dehalogenated analogues (**NT4-6**).



Scheme 5.11 – General procedure for the synthesis of NT1-NT6.

5.2.3 Spectroscopic Properties

Preliminarily, we analysed absorption properties of tetrazoles **T10-T12**, to subsequently compare their spectra with NDIs conjugates. The experiments were performed in 1:1 ACN:phosphate buffer solution, at pH = 7.4) and, as it's possible to observe, all three compounds showed the same behaviour: only one maximum peak can be individuated, centered at 290 nm, coherently with what observed with previously described 2,5-diaryl tetrazoles. These compounds are also characterized by the same type of substituents, which results in a perfect overlay of absorption profiles: indeed, as reported in *Figure 5.12-A*, they basically displayed the same molar extinction coefficients. The three tetrazoles presented also excellent absorption at 310 nm, the selected wavelength of irradiation, with $\epsilon > 1 \times 10^4 \text{ M}^{-1} \text{ cm}^{-1}$.

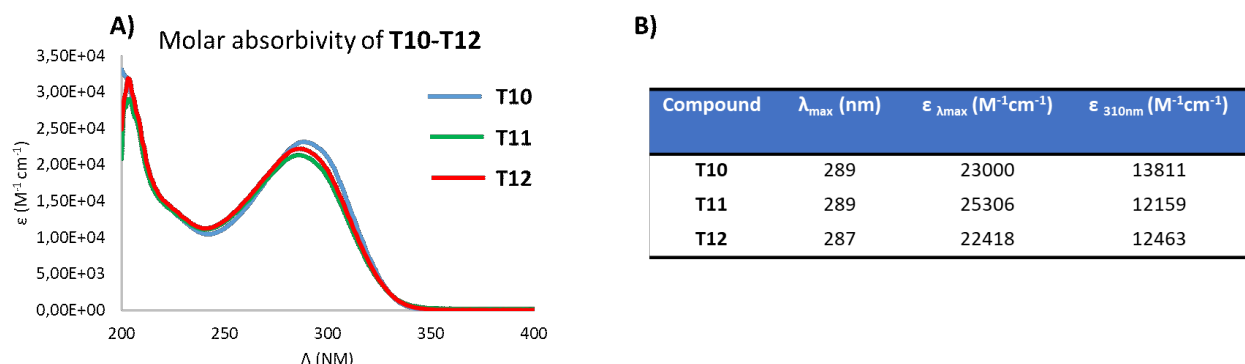


Figure 5.12 – A) Molar absorptivity of tetrazoles **T10-T11** in 1:1 ACN:PBS (50 mM, pH 7.4) and **B)** measured molar extinction coefficients at λ_{max} and $\lambda = 310 \text{ nm}$.

Then, we have analysed spectroscopic properties of conjugates **NT1-NT6** in phosphate buffer solution (PBS), at pH = 7.4, to mimic physiological conditions. However, molar absorptivity was measured in 1:1 ACN:PBS, because of their poor solubility in pure buffer. In *Figure 5.13-A*, we have overlapped the spectra of three bromine derivatives (**NT1**, **NT2** and **NT3**), while in *Figure 5.13-B* their dehalogenated analogues. As it's possible to observe, the presence of halogen atom on naphthalenediimide core doesn't induce significant differences in the absorption spectra. In particular, for each compound we can find a maximum around 270 nm, two peaks at 360 and 380 nm, which are attributed to $\pi-\pi^*$ transitions of NDI aromatic core, and the typical charge-transfer band in the visible region, extended from 450 to 600 nm, originated by the introduction of electron-rich substituents on naphthalene core. In these spectra, it's possible to notice also the presence of a "shoulder" at 290 nm, particularly pronounced in **NT4** and **NT6**, corresponding to the typical absorption of tetrazole ring.

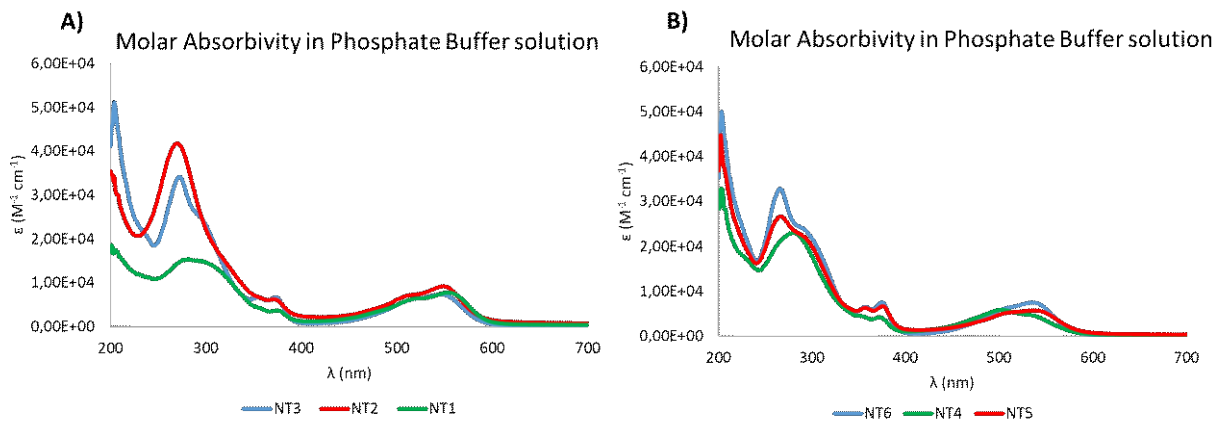


Figure 5.13 – A) Molar absorbivity of **NT1-NT3** in 1:1 ACN:PBS (50 mM, pH 7.4); **B)** molar absorbivity of **NT4-NT6** in 1.1 ACN:PBS (50 mM, pH 7.4).

From these preliminary analyses, we demonstrated that all synthesized compounds present excellent absorption properties in UV region, as expected, and in the visible region, therefore activation in more biocompatible conditions, using, for example, a green LED, could be explored. In *Table 5.12*, we have summarized the molar extinction coefficients of **NT1-NT6**, in phosphate buffer solution, at 310 nm and 517 nm, the wavelength selected for photoactivation experiments. In general, molar absorptivity is significantly higher at 310 nm, compared to visible region, indicating that photoactivation should be more efficient in these conditions. However, they present good absorption also at 517 nm, therefore tetrazole photolysis has been explored even at this wavelength.

Compound	λ _{max} (nm)	ε _{310nm} (M ⁻¹ cm ⁻¹)	ε _{517nm} (M ⁻¹ cm ⁻¹)
NT1	279, 379, 560	13421	6291
NT2	270, 352, 373, 551	17938	7298
NT3	273, 360, 373, 551	18028	6185
NT4	284, 357, 376, 505	13300	5217
NT5	268, 357, 379, 543	15732	5353
NT6	268, 357, 375, 538	17695	6712

Table 5.12 – Molar extinction coefficients of conjugates NT1-NT6 in 1:1 ACN:PBS solution (50 mM, pH 7.4) at 310 and 517 nm.

Subsequently, we have investigated the fluorescence emission of compounds **NT1-NT2**, to verify the potential fluorogenicity of the process; indeed, as previously reported, 2,5-diaryl tetrazoles are completely non fluorescent, while their corresponding pyrazolines displayed elevated fluorescent quantum yields. Tri-substituted naphthalenediimides are usually characterized by intense fluorescence in aqueous solution, therefore, if their emission remains constant during the process, no “light-up” can be observed upon product formation. NDIs **88** and its dehalogenated analogue **89** (*Figure 5.14*), present the same substitution pattern of our conjugates **NT1-NT6**, with three *N,N*-dimethylaminopropylamines groups, then we have used them as

a reference for our experiments²⁰⁰. These compounds showed good quantum yields in water solution, which was slightly lower for brominated NDI **89** ($\Phi_f = 0.11$).

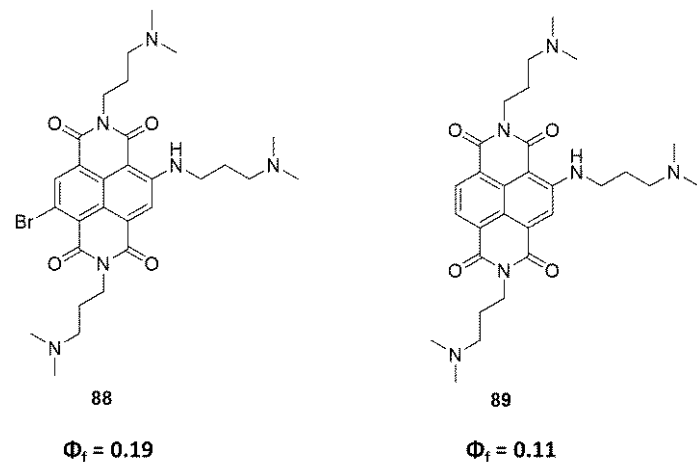


Figure 5.14 – Fluorescence Quantum yields, in buffered acidic water ($pH = 2$), of trisubstituted NDIs **88** and **89**²⁰⁰.

We have measured the fluorescence quantum yields of conjugates **NT1-NT6** in pure water and in DMSO, to eventually evaluate the influence of solvent on the emission intensity, using, as standard reference, DAPI. Obtained results are reported in *Table 5.13* and, surprisingly, all conjugates displayed very low emission intensities, with quantum yields that remain always below 4%. Lowest values, in water, have been recorded with **NT3**, characterized by the bromine atom and polyethyleneglycole chain as spacer, and dehalogenated **NT4**. However, no significant differences have been observed among all derivatives. Interestingly, in DMSO solution, quantum yield values are even lower, then we can deduce that their poor emission doesn't depend on the solvent. As described previously, tri-substituted NDIs are generally characterized by significantly higher fluorescent quantum yields, as in case of **88** and **89** ($\Phi_f = 0.19$ and 0.11 , respectively), while, in this case, we have recorded a remarkable quenching by almost one order of magnitude. Therefore, we can conclude that, despite the conjugation has been accomplished with long-chain spacers, the presence of the tetrazole moiety strongly influenced optical properties of NDI scaffold and has a quenching effect on its fluorescence emission. In the end, we can speculate that, despite the presence of NDI, fluorogenicity of the process could be maintained and intense emission should be observed upon pyrazoline formation.

A)	Compound	$\Phi_f \%$ (H ₂ O)	$\Phi_f \%$ (DMSO)
	NT1	3.3 ± 0.5	0.53 ± 0.03
	NT2	3.0 ± 0.2	0.62 ± 0.02
	NT3	1.7 ± 0.1	0.71 ± 0.03
	NT4	0.5 ± 0.2	1.5 ± 0.5
	NT5	2.7 ± 0.3	0.154 ± 0.006
	NT6	2.4 ± 0.6	0.14 ± 0.04

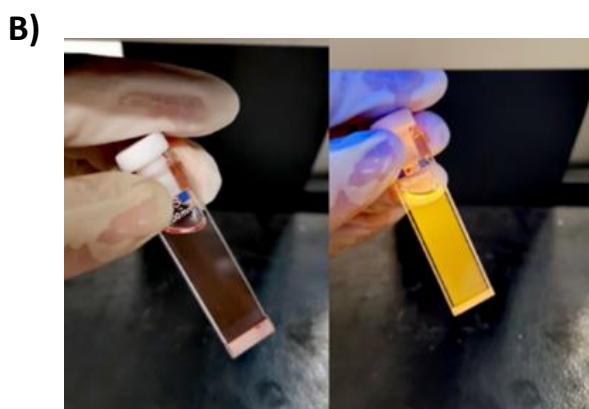


Table 5.13 – A) Fluorescence quantum yields of **NT1-NT6** in water and DMSO. These values have been measured using

DAPI as reference, $\lambda_{exc} = 350$ nm for experiments in water and $\lambda_{exc} = 310$ nm for DMSO solutions. Reported quantum yields are the results of three different measurements. B) Fluorescence emission of NT3, in water solution, upon excitation at 365 nm, with a TLC lamp.

5.2.4 Photoreactivity

After a complete analysis of spectroscopic properties of synthesized compounds, we have thoroughly studied their photochemical behavior, to evaluate the photolysis efficiency and the nature of photogenerated products. In details, we evaluated the effect of conjugation to NDI derivatives on tetrazole photoreactivity, compared their behaviour at 310 nm with free 2,5-diaryl tetrazoles **T10-T12**. Moreover, for conjugates **NT1-NT6** we have also explored the photoreactivity irradiating selectively the NDI chromophore at 517 nm, to test if tetrazole photolysis could occur in the visible region, by energy or electron transfer.

Firstly, we have focused our attention on non-conjugated 2,5-diaryl tetrazoles **T10-T12**: as described in the previous section (5.1), we have measured their photolysis quantum yields, at 313 nm, in water solution, and, subsequently, we tested their reactivity in the presence of acrylamide, to generate pyrazolines as product. Once again, nitrile imine generation efficiency has been measured in phosphate buffer solution, at pH = 7.4, irradiating at 313 nm with an optical desk. Reaction was monitored through HPLC and UV-VIS analysis (*Figure 5.15*). These tetrazoles display substituents with identical electron properties (an electron-rich group on N-phenyl ring and an electron-withdrawing one on C-phenyl-ring), which have been chosen to maximize the photolysis efficiency, according to the results described in *chapter 5.1.3*. Our hypothesis has been confirmed by experimental results: indeed, efficient photolysis has been observed for all three derivatives, with reaction quantum yields ranging from 0.17 to 0.22, in accordance with values measured in preliminary studies of *chapter 5.1.3*. From UV-VIS analysis of tetrazole photolysis, several isosbestic points can be located, indicating that the process was very clean and led to the formation of only one product. Moreover, during irradiation, absorption spectra of three compounds changed significantly: in particular, band centered at 290 nm decreased because of the rupture of tetrazole ring, while a new peak, extended from 350 to 400 nm, increased, indicating the formation of acyl hydrazide.

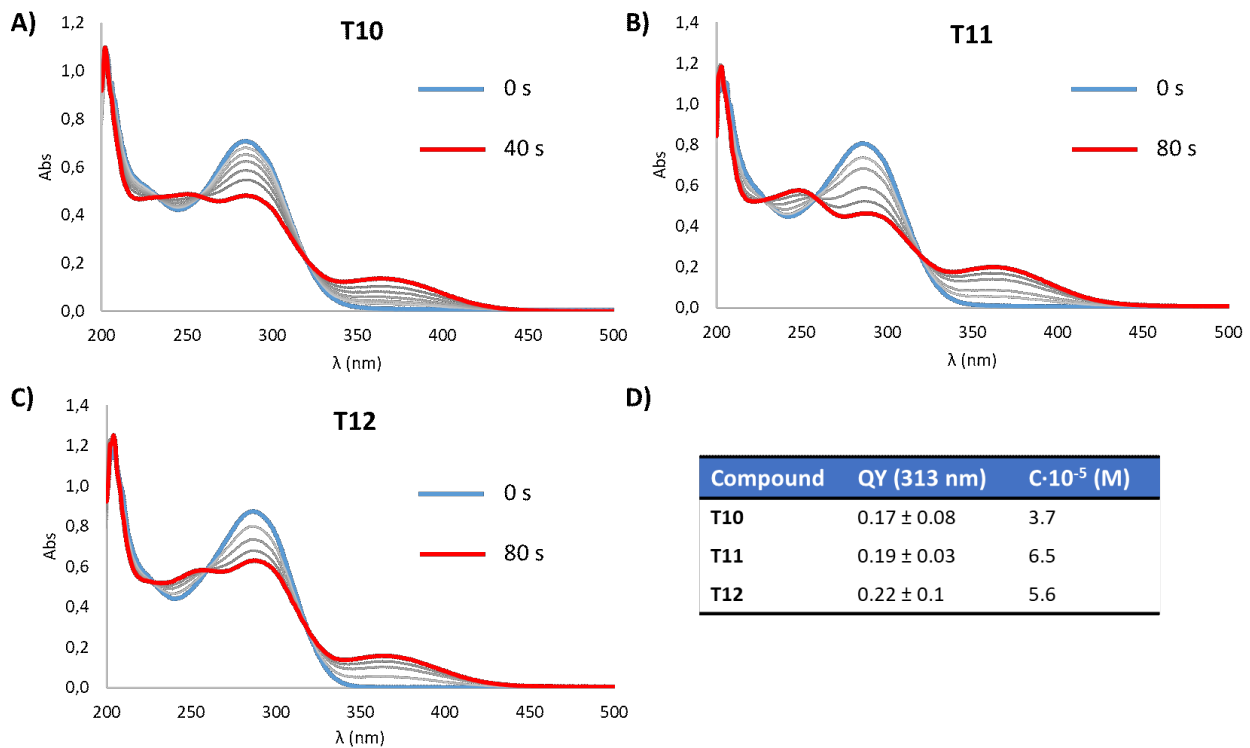


Figure 5.15 – UV-VIS analysis of photolysis of tetrazoles A) T10, B) T11 and C) T12 in phosphate buffer solution ($pH = 7.4$, 50 mM). D) Photolysis quantum yields measured for T10-T12.

These experiments were carried out in water, therefore the only product expected was the corresponding acyl hydrazide. To prove the formation of this single photoproduct, we have analyzed irradiated solution also with HPLC and LC-MS analysis. In the first case, we observed the formation of only one new peak and LC-MS analysis confirmed that it was the expected acyl hydrazide **AH10**, by mass spectrometry and NMR. In Figure 5.16, we have reported, as an example, the reaction profiles for **T10**, but the same behavior has been observed also for the other two tetrazoles, with exclusive formation of the corresponding acyl hydrazides.

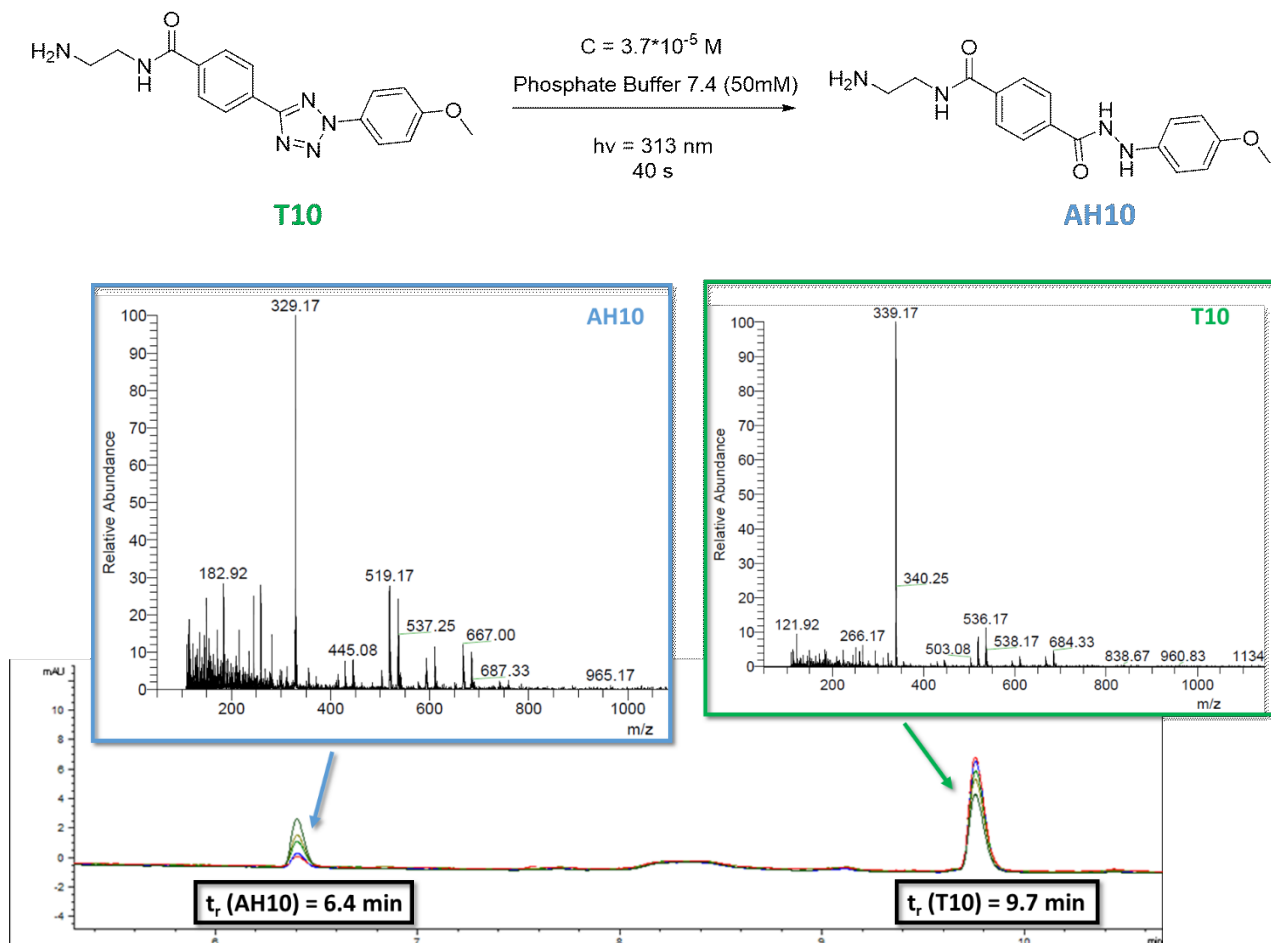


Figure 5.16 – HPLC and LC-MS analysis of **T10 solution, after 40 seconds of irradiation at 313 nm, performed with optical desk, in phosphate buffer (pH 7.4, 50 mM).**

Tetrazole photoreactivity was investigated also in presence of an alkene, acrylamide, to test their ability to generate selectively the corresponding pyrazoline. Tetrazoles **T10-T12** are perfect analogues of compound **T9**, that, in the previous section (5.1) resulted to be not only the most phoreactive derivative, but also able to generate the desired pyrazoline with excellent selectivity, even in presence of low amount of trapping agent. Therefore, for these new tetrazoles, we expected the same outcomes. To prove pyrazoline formation, we have irradiated solution of **T10-T12**, at the same concentration used in the previous experiments, at 313 nm, in phosphate buffered solution (pH 7.4) in presence of 100 equivalents of acrylamide ($C = 5 \times 10^{-3}$ M). Tetrazoles were irradiated for 40 seconds and, we have analyzed the solution through UV-VIS analysis, HPLC and LC-MS, at different reaction times, to verify product distribution and the selectivity of the cycloaddition. Once again, as an example, here we have reported the reaction profile for compound **T10**, but the same outcome has been obtained with tetrazole **T11** and **T12**. In details, we have observed, as stated before, that photoactivation in presence of a large excess of acrylamide led to exclusively formation of the desired pyrazoline. In this case, formation of acyl hydrazide was not even detected in trace, despite water was the reaction solvent, confirming the remarkable selectivity of these derivatives. As it's possible to observe in *Figure 5.17*, HPLC profile of the reaction was really clean and tetrazole consumption resulted in increase of pyrazoline concentration. Identification of the two peaks has been possible thanks to LC-MS analysis.

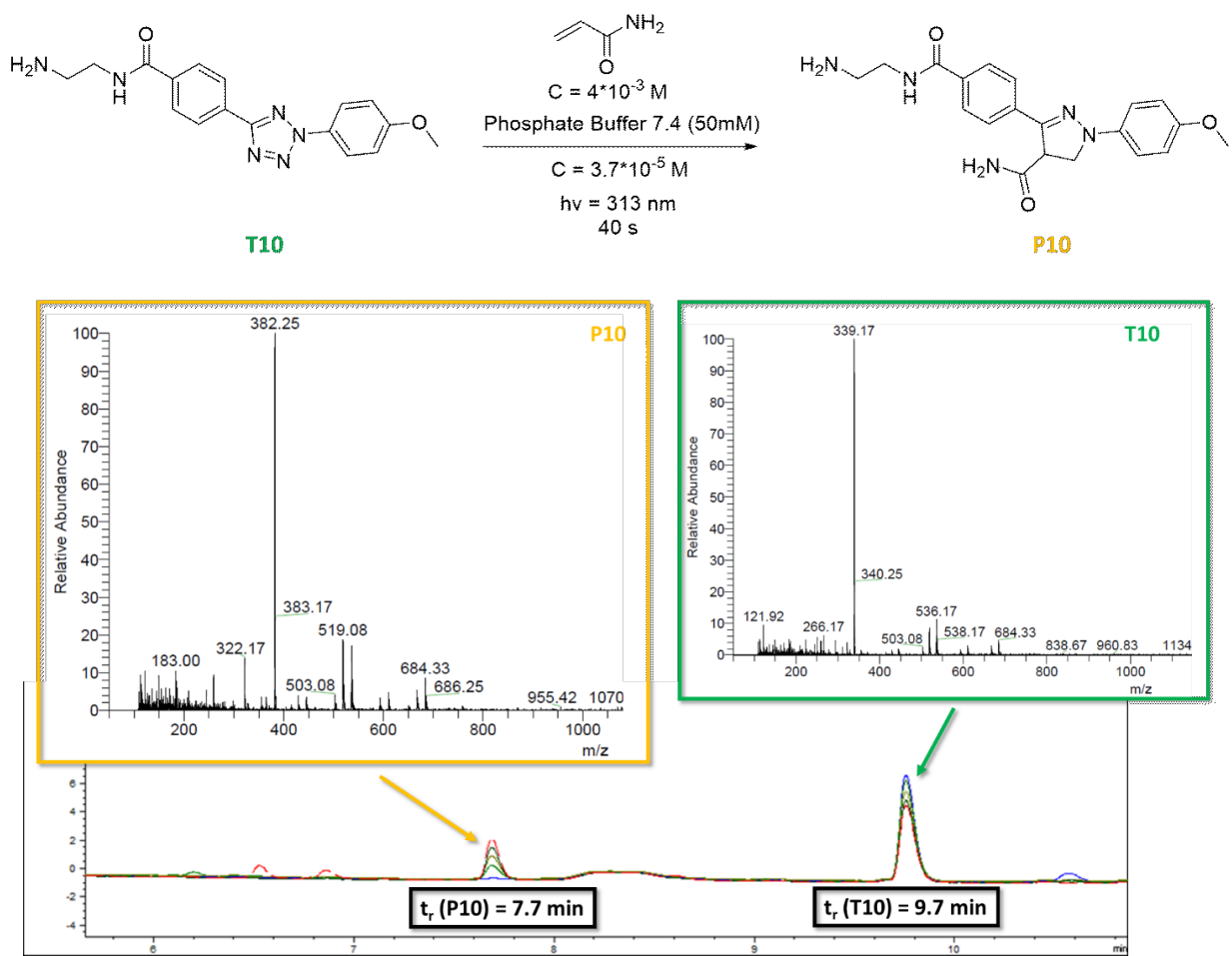
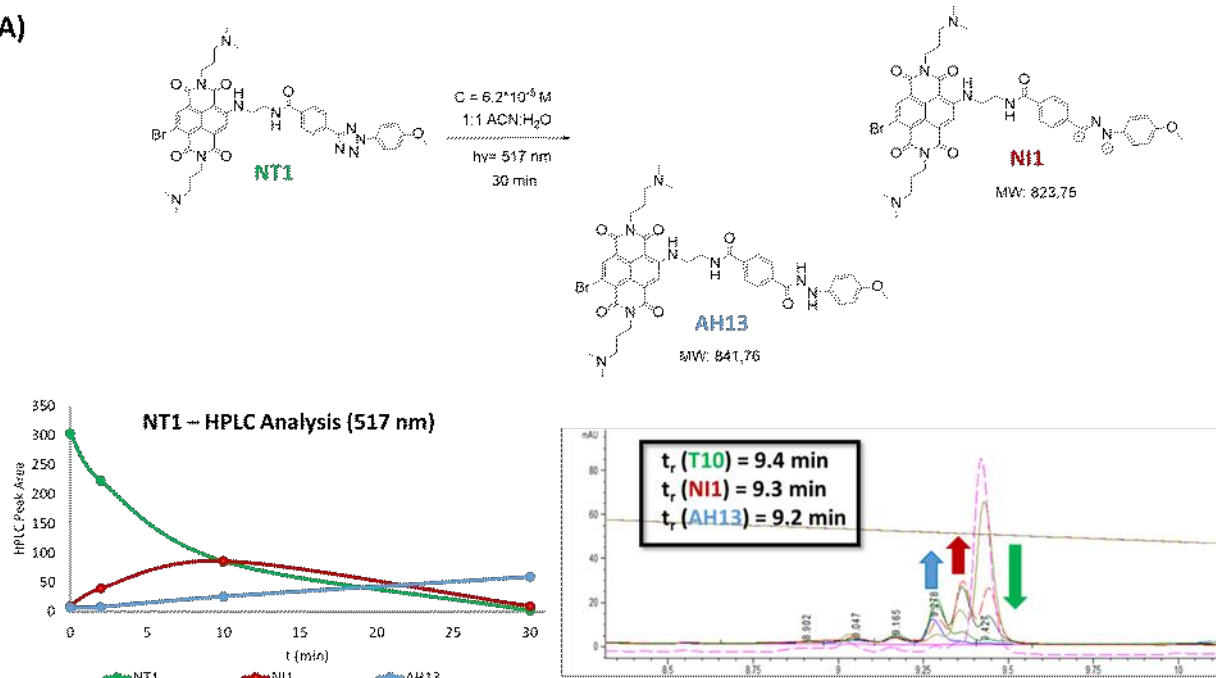


Figure 5.17 - HPLC and LC-MS analysis of **T10 solution in presence of 100 eq. of acrylamide, after 40 seconds of irradiation at 313 nm, performed with optical desk, in phosphate buffer (pH 7.4, 50 mM).**

After the evaluation of the photoreactivity of free tetrazoles, we focused our attention on conjugated NDIs-tetrazoles **NT1-NT6**. We have explored the possibility to achieve photoactivation in the visible region, using a green LED, centred at 517 nm. Experiments were performed in 10^{-5} M solution of **NT1-NT6**, in 3 ml of 1:1 ACN: water solution. Times of irradiation were different, depending on substrate reactivity, conversion and reactions were monitored through UV-VIS, HPLC and LC-MS analysis. Despite the two chromophores were not directly conjugated and they were separated by a long spacer and tetrazole displayed null absorbance in the visible region, all examined conjugates, were successfully activated upon irradiation of NDI chromophore. Then, we have determined the products generated by this photochemical process, to compare their behavior with UV-activable, non-conjugated, tetrazoles **T10-T12**. Here are reported the results obtained for **NT1**, but we have observed the same reaction profiles for all the conjugates **NT1-NT6**. Taking into account previous experiments, performed on tetrazoles **T10-T12** and on **T1-T9**, in case of successful photoactivation, we expected to observe the generation of only one product, the acyl hydrazide. However, from HPLC analysis, we have individuated the formation of two species, with retention times $t_r = 9.3$ min and $t_r = 9.2$ min, very similar to the substrate **NT1** ($t_r = 9.4$ min). Thanks to LC-MS analysis, it has been possible to assign two different masses to these new species: briefly, 9.3 min peak corresponded to $m/z = 825.33$ and $m/z = 412.17$, while the second one, to $m/z = 840.25$ and $m/z = 420.17$. Interestingly, concentration of the new adduct, with $t_r = 9.3$ min, increased in the first part of the reaction, reaching its maximum value after 10 minutes, then it started to decrease and, simultaneously, the intensity of the peak at 9.2 min increased. Based on these observations, we have associated the mass of this intermediate to nitrile imine dipole **NI1**, which evolved to

the expected acyl hydrazide **AH13** (*Figure 5.18*). Detection of nitrile imine dipole through HPLC analysis is not really a novelty, because Lin and co-workers already reported that nitrile imine can be individuated when particularly stable¹⁷⁸. These outcomes confirmed the initial hypothesis: conjugation to NDI allowed the activation of tetrazole with visible light, resulting in the formation of the expected acyl hydrazide. However, during irradiation of 2,5-diaryl tetrazoles, we have never detected 1,3-nitrile imine, only the subsequent adduct to water, suggesting that conjugation to NDI could at least influence the lifetime of this intermediate.

A)



B)

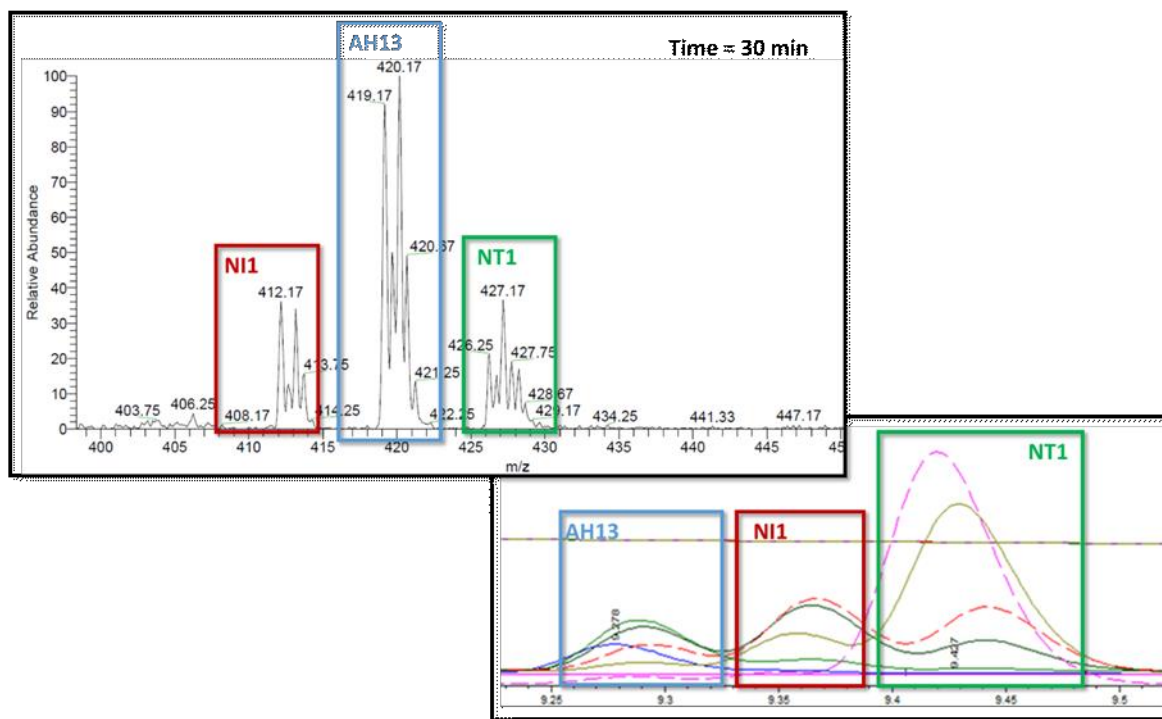


Figure 5.18 – A) HPLC profile of irradiation of **NT1**, at 517 nm, in 1:1 ACN: H₂O and detected photoproducts; **B)** LC-MS analysis of products formed upon irradiation.

In order to demonstrate that this reactivity was due to irradiation with visible light and not to thermal activation, we have performed a “dark experiment” for each conjugate: we covered the vial containing the solution of conjugate, then this was kept on the green LED, for the same time indicated for irradiation, to verify if the potential warming caused by the lamp could be responsible of the observed activation. Solutions were subsequently analyzed before and after 40 minutes: through HPLC analysis (*Figure 5.19*), it was possible to observe that the only detected peak was the substrate and no one of the previous reported products was generated. This result was confirmed also by LC-MS analysis and, indeed, in these conditions, the only m/z individuated corresponded to the substrate. Therefore, we concluded that no thermal activation occurred, and the observed products were the results of light-mediated activation of **NT1-NT6**.

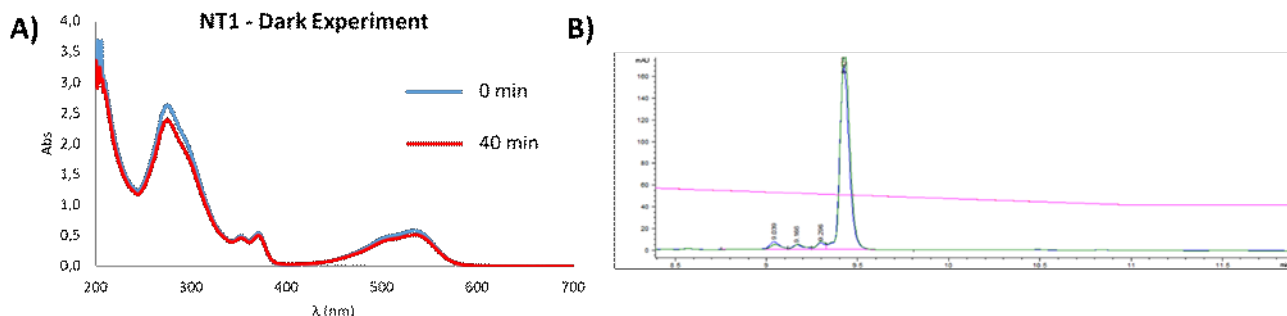


Figure 5.19 – A) UV-VIS absorption profile before and after 40 minutes of dark experiment; **B)** HPLC profile before and after 40 minutes of dark exposure: substrate's concentration remained unaltered and formation of new peak has not been observed at the end of the experiment.

The nature of products generated upon irradiation at 517 nm was the same for all synthesized conjugates, however, **NT1-NT6** displayed different photolysis efficiency. Because of the impossibility to measure photolysis quantum yields with a LED, we have reported, for compounds **NT1-NT6**, their corresponding half-lives, obtained upon irradiation at 517 nm, using the same irradiating led and conditions, to compare the efficiency of the photochemical process, as reported in *Table 5.14*. Despite their low absorption in this spectral window, photoactivation resulted to be quite effective: substrate consumption was almost quantitative in 30 minutes or less of irradiation. Another interesting fact that should be evidenced, is the clear difference in photoreactivity among brominated compounds **NT1-NT3** and dehalogenated **NT4-NT5**. In details, it seems that the presence of bromine on NDI core accelerated the photochemical reaction, resulting in significantly lower half-lives compared to non-substituted derivatives. The only exceptions were **NT2** and **NT5**, that showed comparable reactivity. These results indicated that bromine atom could have a relevant role in this photochemical process, for example promoting tetrazole activation through an energy transfer process. It is well-known, indeed, that bromine atom on NDI increase the half-life of their triplet state²⁰⁰, while it has been suggested that nitrile imine generation occurs via triplet excited state, therefore excitation of NDI with visible light could promote triplet-triplet energy transfer and, as a consequence, tetrazole photolysis, which is more efficient with long-living triplet of brominated compounds **NT1-NT3**. However, this hypothesis should be confirmed by further experiments.

Compound	$t_{1/2}$ 517 nm (min)	$C \cdot 10^{-5}$ (M)
NT1	7.0	6.2
NT2	13.0	5.8
NT3	6.0	3.8
NT4	19.0	3.8
NT5	12.5	2.3
NT6	11.0	4.3

Table 5.14 – Half-lives of compounds NT1-NT6 recorded upon irradiation at 517 nm, under identical conditions in 1:1 ACN: H₂O solution.

In *Figure 5.20*, we have reported UV-VIS spectra for **NT1-NT6** during irradiation at 517 nm. In general, it's possible to notice that, in this case, variations of the absorption profiles are less pronounced compared to irradiation of non-conjugated tetrazoles **T10-T12** (*Figure 5.15*), as the photoreaction is less efficient at 517 nm. Indeed, spectra of the starting and final solutions presented almost the same intensity, while formation of new band is not observed with no one of these compounds. The only effect that is achieved upon irradiation is the decrease of the 290 nm peak and the simultaneous reduction of intensity of the visible band: the entity of this absorption drop was more evident with **NT1-NT3**, the conjugates containing the bromine atom, and, in particular, with **NT1**. More pronounced changes in the absorption spectra of these derivatives are associated with higher reactivity, as confirmed also by their lower half-lives (*Table 5.14*). Moreover, the dehalogenated conjugates **NT4-NT6**, characterized by lower reactivity, showed only subtle variations in the UV-VIS spectra.

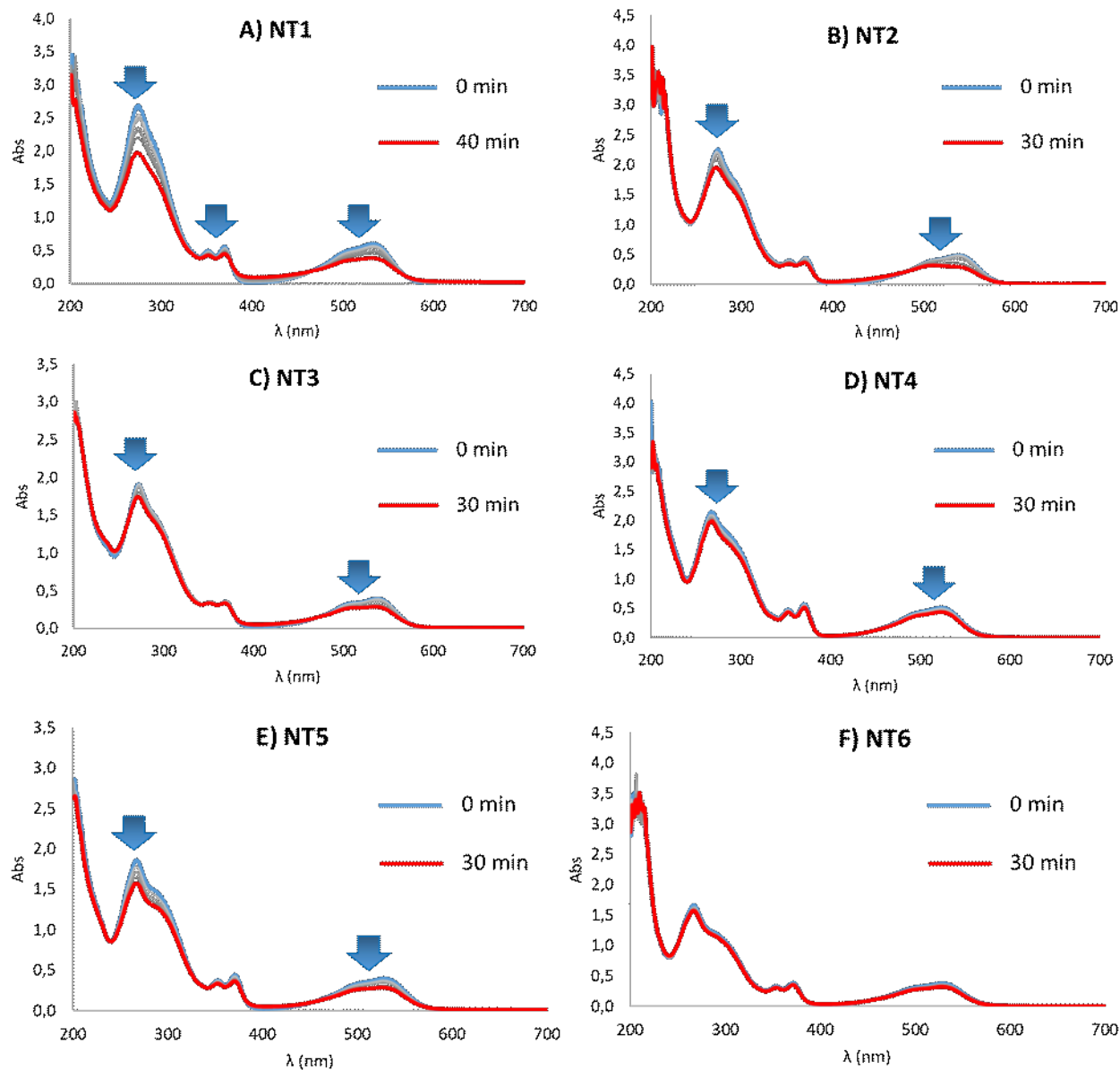


Figure 5.20 - Absorption spectra of **NT1-NT6** during irradiation at 517 nm, with a green LED, in 1:1 ACN: water solution.

With described experiments, we have demonstrated that the activation of 2,5-diaryl tetrazoles is achievable with visible light. However, photolysis efficiency, at this wavelength, is not excellent, because at least 30 minutes of irradiation were required to achieve high substrate conversions. Through irradiation of non-conjugated tetrazoles, as **T10-T12**, but also **T9** or **T6**, described in *Chapter 5.1*, elevated conversions (above 85%) were obtained in less than 3 minutes of light-exposure. We suggested that lower molar absorptivity measured at 517 nm, compared to 310 nm (*Table 5.12*), could be partially responsible of the low efficiency of the process. To verify if higher efficiency could be achieved by direct irradiation of the tetrazole, we have investigated the photochemical behaviour of conjugates **NT1-NT6** at 313 nm. In details, we have analyzed the products generated upon UV-irradiation, and measured, for each compound, the photolysis quantum yield in 1:1 ACN: water solution, to determine the efficiency of the process for different compounds. As in previous experiments, reactions were monitored through HPLC, UV-VIS and LC-MS analysis, to identify the photogenerated products, and here we have described reaction profiles of only **NT1**, because with other conjugates we have obtained the same outcomes. Due to the absence of any trapping agent, we expected to

observe the exclusive formation of the corresponding acyl hydrazide. Nevertheless, despite our previous findings, we have observed a completely unexpected outcome.

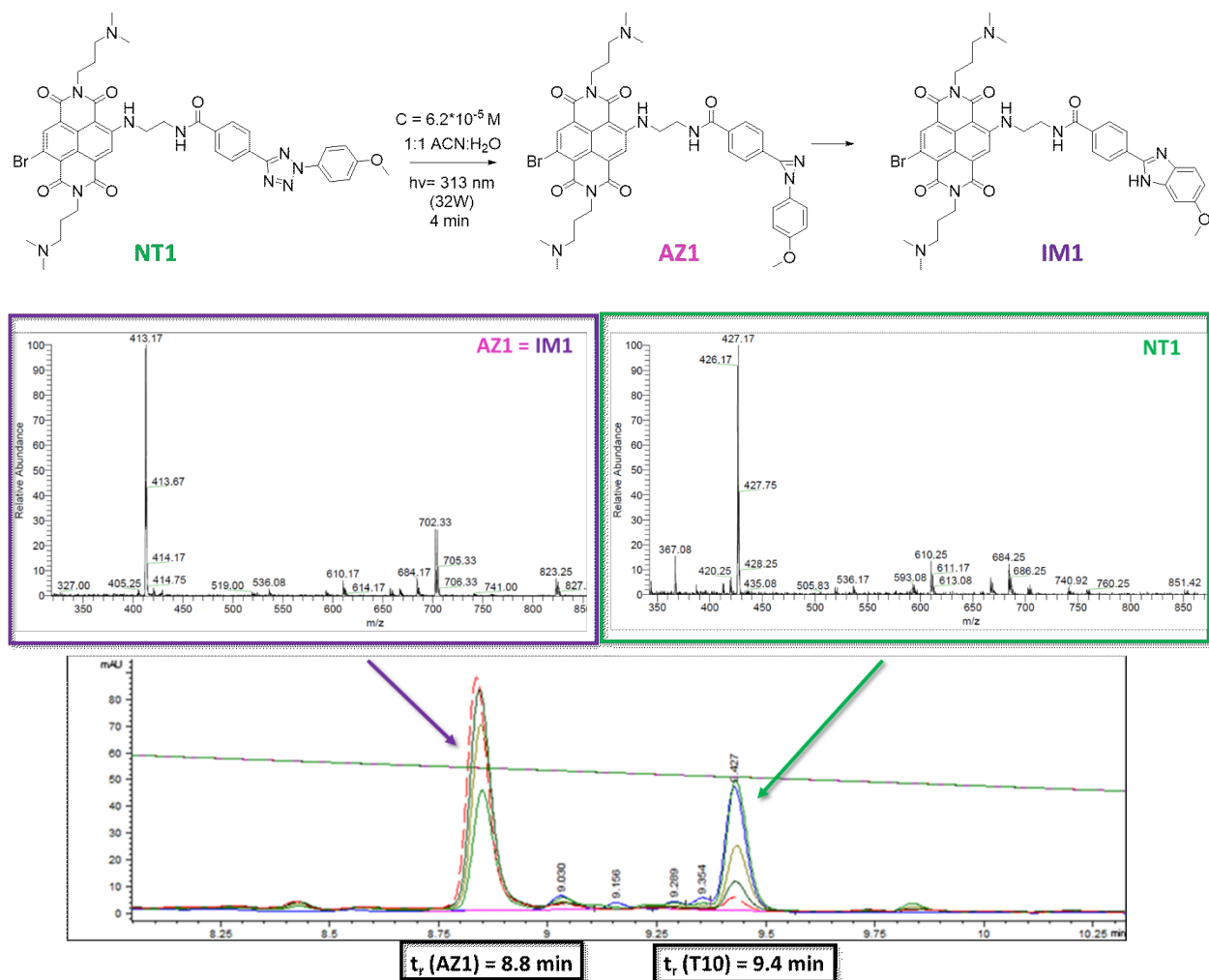


Figure 5.21 – HPLC profile and LC-MS analysis after 4 minutes of irradiation, at 313 nm, of **NT1**, performed in a multi-lamps photoreactor, with two 15W lamps.

From HPLC analysis, reaction resulted to be very clean: substrate consumption coincided with the formation of a single species (*Figure 5.21*). However, retention time of the product was significantly different from previous observed acyl hydrazide **AH13** (*Figure 5.18*). Indeed, LC-MS analysis confirmed that this derivative was not the expected acyl hydrazide. This new product was characterized by $m/z = 823.25$, that could be associated to two different species: the intermediate nitrile imine **NI1** and a self-cycloadduct, the *1H*-diazirine **AZ1** (*Figure 5.21*) that, as reported in literature, can be generated as a consequence of tetrazole photolysis¹⁶⁴. Nitrile imine is a reactive intermediate, whose transient nature was confirmed by the transformation into the acyl hydrazide, as showed by experiments at 517 nm. Conversely, in this case not only the concentration of the new product increased until complete consumption of **NT1**, but it was also stable at room temperature, for several hours since the end of photochemical process. Then, we concluded that the observed product could be attributed to the *1H*-diazirine **AZ1**, by mass spectrometry data, or to the benzimidazole **IM1** (*Figure*

5.21) resulting from the transposition of the nitrene intermediate as described in the literature¹⁶⁴. Formation of this derivative was never observed in any preliminary studies, under irradiation in aqueous solution, neither it has been never reported in literature, for studies carried out in similar conditions. Therefore, conjugation to NDI affect the tetrazole photoreactivity, leading to the generation of this unexpected product. Moreover, it emerged that, on these kinds of scaffolds, the activation wavelength strictly modulates the process, as irradiation at 313 and at 517 nm resulted in different reaction pathways. However, additional experiments are required to clarify the reaction mechanism generating the diazirine or benzimidazole.

Compound	Φ_R (ACN:H ₂ O)	Time (min)	C*10 ⁻⁵ (M)
NT1	0.13	4	6.2
NT2	0.17	4	5.8
NT3	0.10	4	3.8
NT4	0.11	4	3.8
NT5	0.09	4	2.3
NT6	0.16	3	4.3

Table 5.15 – Photolysis quantum yields of NT1-NT6, measured in 1:1 ACN:water solutions.

We have analyzed the reactivity of all conjugates, **NT1-NT6**, at 313 nm, and, for each of them, we have detected the exclusive formation of 1*H*-diazirine. Furthermore, we have found that, at this wavelength, the photochemical process displayed good efficiency. Indeed, for all compounds, we have measured photolysis quantum yields, monitoring substrate consumption upon irradiation at 313 nm, in 1:1 ACN: water solution, with an optical desk. The obtained results are summarized in *Table 5.15*. For each conjugate we have been able to measure the reaction quantum yields, $0.1 \leq \Phi_R \leq 0.17$ (*Table 5.15*). Interestingly, they showed very similar results to tetrazoles **T10-T12** (*Figure 5.15*), evidencing that conjugation to NDI did not reduce the efficiency of the UV-activated reaction. It should be highlighted that, in this case, the different nature of the alkyl chain spacer and the presence of bromine atom, did not significantly affect the photolysis efficiency, since all derivatives displayed similar reaction quantum yields.

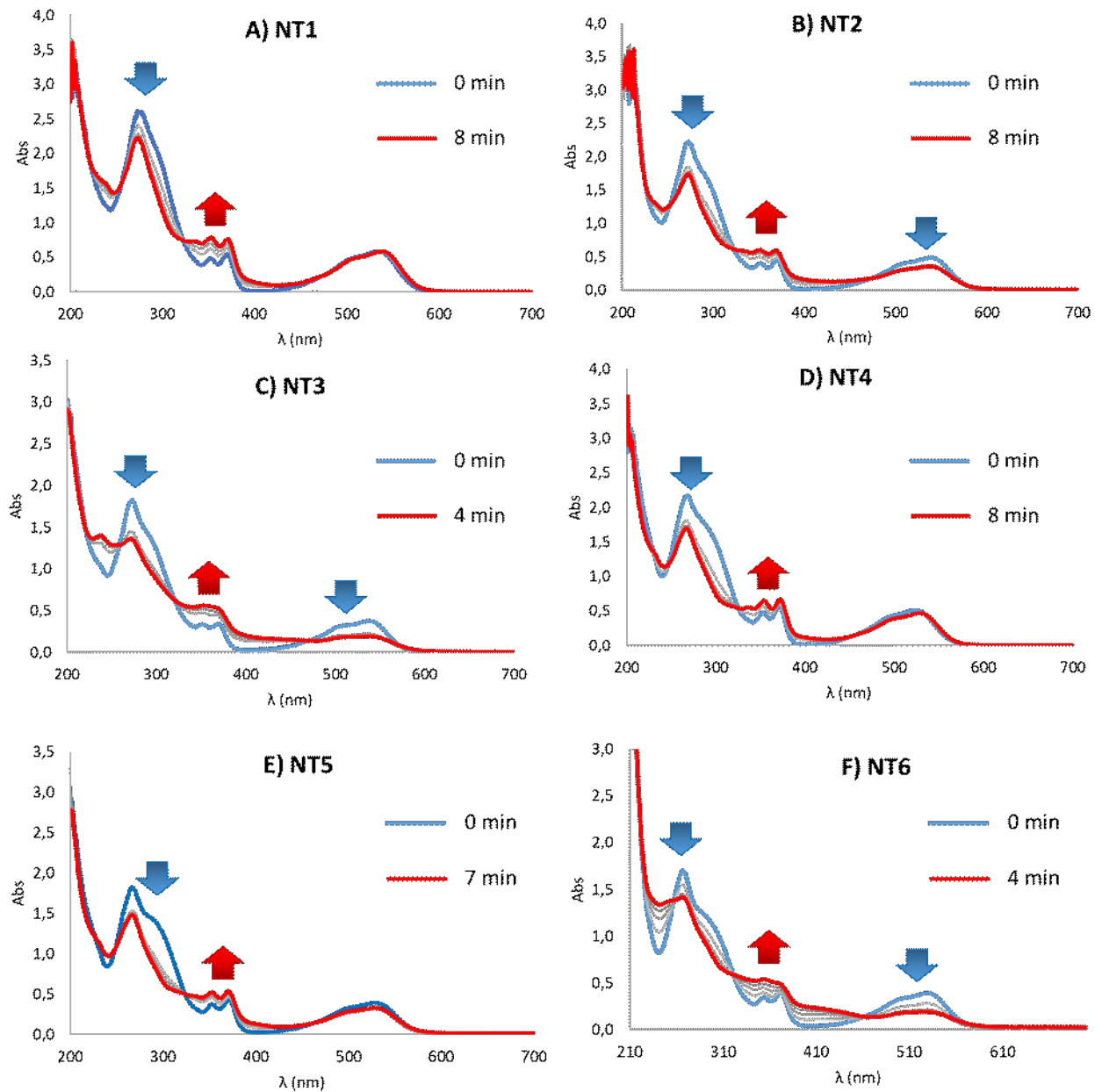


Figure 5.22 – Absorption spectra of NT1-NT6 during irradiation at 313 nm (Photon Flux = $2.66 \times 10^{-6} E \cdot cm^{-2} \cdot min^{-1}$), with optical desk, in 1:1 ACN: water solution

These photochemical reactions have been monitored also through UV-VIS analysis, to control absorption profiles during the irradiation, as reported in *Figure 5.22*. The absorption spectra of the conjugates NT1-NT6 during the irradiation exhibit isosbestic points, indicating the clear formation of a new, single product for each reaction. All the derivatives presented similar absorbance change during the irradiation: as in the case of simple 2,5-diaryl tetrazoles, 290 nm peak decreased significantly, indicating the rupture of tetrazole ring, and this “shoulder” completely disappeared at the end of the reaction. Simultaneously, the double band between 360 and 390 nm, attributed to $\pi-\pi^*$ transition of NDI aromatic core, became more intense and, in case of NT3 and NT6, characterized by polyethyleneglycole chain as a spacer, a new band at 400 nm appeared. For the conjugates with the longer spacer (NT3 and NT6) a non-negligible reduction of the peak at 500 nm was observed, suggesting that, in this case, the photoinduced reaction generate a product with different charge transfer band of the NDI. The fact that tetrazole photolysis influenced the absorption properties of NDI scaffold indicated that the two chromophores can interact with a longer spacer.

Then, despite the promising results achieved upon irradiation with visible region, photolysis efficiency is higher upon activation at 313 nm, probably because of the higher molar absorptivity of conjugates at this wavelength. Moreover, we have demonstrated that the reaction pathway and, subsequently, the nature of generated product, can be switch by the activation wavelength.

5.2.5 Binding Affinity of NDI-Tetrazoles for Quadruplexes

In order to also evaluate the affinity of the NDI-tetrazole conjugates for nucleic acid secondary structures, we have analyzed their interaction with different quadruplex forming sequences, through Circular Dichroism (CD) analysis. In particular, we have selected three different targets: LTR-III, the HIV-related quadruplex, and the telomeric 22AG in K⁺-rich solution, both characterized by (3+1) hybrid topology, and the c-MYC, with a parallel structure. For compounds **NT4-NT6** (chosen because they are less prone to hydrolysis in physiological environment, compared to brominated derivative), we have performed CD-Melting experiments: briefly, we have measured the folding temperature of each quadruplex forming sequence in presence and in absence of the ligands, to evaluate their stabilization properties towards these different targets. Moreover, we have also carried out the same experiments with tetrazoles **T10-T12**, to test the affinity of the tetrazole in the absence of NDI scaffold.

We started our analysis with LTR-III and we have determined its unfolding temperature in 10 mM K⁺ solution, in 10 mM LiCaco buffer (pH 7.2). At room temperature (T= 20°C), CD spectra of LTR-III showed, coherently with what described in literature, a broad positive band, with a maximum at $\lambda = 290$ nm and the other one at 264 nm, and a negative peak at 245 nm, typical of its unique (3+1) hybrid topology with a diagonal stem-loop in B-DNA form. In order to measure its melting temperature (T_m), we have heated the solution to 95°C and recorded CD spectra at different temperatures. Then, we have plotted the molar ellipticity at a selected wavelength, as a function of the temperature, and T_m was measured at the half height of the sigmoid curve. For LTR-III, T_m was calculated following quadruplex unfolding at both $\lambda_{max} = 264$ and 290 nm. In absence of any ligands, its T_m was 57°C and 58°C, at 264 and 290 nm, respectively, and the structure was completely unfolded before 70°C. Melting experiment was repeated in presence of 10 μ M of **NT4-NT6** and of **T10-T12**. The first thing that should be underlined is that even non-conjugates tetrazoles displayed modest affinity for the target, as proved by melting temperatures, ranging from +6°C to +10°C, with the best result obtained by compound **T11**, with the four-carbon atoms alkyl chain. The higher values observed at 264 nm, respect to 290 nm, could be explained by the fact that these compounds induce a variation of quadruplex topology, shifting the equilibrium towards the formation of a parallel structure.

LTR-III					
Compound	T _m ($\lambda=264\text{nm}$) (°C)	ΔT _m ($\lambda=264\text{nm}$) (°C)	T _m ($\lambda=290\text{nm}$) (°C)	ΔT _m ($\lambda=290\text{nm}$) (°C)	
Blank	57.0	-	58.0	-	
T10	65.2	+ 8.2	64.9	+ 6.9	
T11	67.0	+ 10	66.0	+ 8.0	
T12	65.0	+ 8.0	64.0	+ 6.0	
NT4	83.5	+ 26.5	75.0	+ 17.0	
NT5	87.0	+ 30.0	74.0	+ 16.0	
NT6	79.2	+ 22.2	76.0	+ 18.0	

Table 5.16 – Temperature melting measured for compounds **T10-T12** and **NT4-NT6** with LTR-III, at $\lambda = 264\text{ nm}$ and $\lambda = 290\text{ nm}$. Blank sample represents the melting temperature of LTR-III without ligand. Experiments were performed in 1 ml of solution, containing 2.5 μM of oligonucleotide, 10 μM of ligands, 10 mM of LiCaco (pH = 7.2) and 10 mM KCl.

Moreover, as CD melting curves (Figure 5.23), show that 2,5-diaryl tetrazoles did not affect the structure of LTR-III, which maintained the same identical topology. Different results were achieved in presence of NDI-tetrazoles conjugates: indeed, significantly higher melting temperatures have been obtained, proving that modification of tetrazole scaffold with NDI represents a straightforward strategy to improve affinity for G4s. Interestingly, significantly different T_m were obtained at 264 and 290 nm, in particular with **NT4** and **NT5**: indeed, looking at CD spectra, it is possible to notice that molar ellipticity of the band at 290 nm, dropped more rapidly compared to 264 nm peak. As in the case of tetrazoles, this behaviour could be due to the fact that NDI scaffold forces the G4 into a parallel topology, for which it has better affinity, as testified by melting temperatures. This effect was more pronounced with two and four-carbon atoms spacers, while **NT6**, characterized by the presence of polyethyleneglycole chain, showed lower stabilization at both wavelengths, but did not induce significant variations of LTR-III structure. Compound **NT5** gave the most remarkable result, with $\Delta T_m = +30^\circ\text{C}$ and, interestingly, the corresponding non-conjugated tetrazole **T11** displayed the highest stabilization among non-conjugated compounds, suggesting that the strong interactions of **NT5** could be attributed to a cooperative effect of NDI and tetrazole. On the contrary, longer spacers have a detrimental effect on the interaction with the target, while short distances between tetrazole and NDI not only increased the affinity, but also induced a structural variation of LTR-III topology.

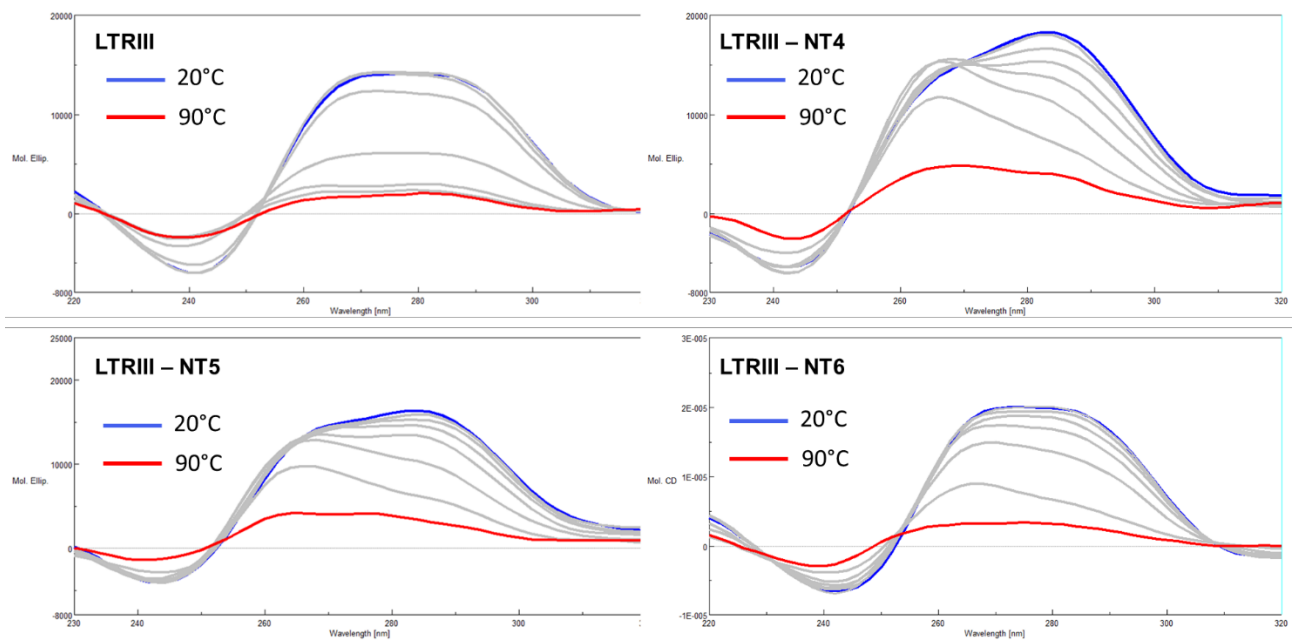


Figure 5.23 – CD Melting of compounds NT4-NT6 with LTR-III. Experiments were performed in 1 ml of solution, containing 2.5 μ M of oligonucleotide, 10 μ M of ligands, 10 mM of LiCaco (pH = 7.2) and 10 mM KCl. Solution temperature was increased from 20 to 95°C and the CD spectra was recorded every ten degrees.

Subsequently, we have performed the same experiments with telomeric 22AG that, in K^+ -rich buffer (20 mM), folded in a (3+1) topology. Analysis were carried out in presence of 2.5 μ M of oligonucleotide and 10 μ M of ligands, in lithium cacodylate buffer 10 mM (pH 7.2). CD spectra of the quadruplex showed a positive maximum at 290 nm and a shoulder at 260 nm, with a negative band at 240 nm. In absence of any ligand, melting temperature was 61°C at 264 nm and 58°C at 290 nm. Tetrazoles **T10-T12** showed low stabilization of the G4, also compared to LTR-III, and only small differences in melting temperature were observed. As in the previous case, the only exception was **T11**, with $\Delta T_m = + 8.9^\circ C$, indicating that four carbon atom alkyl chain is critical to achieve stronger interactions, probably because of a specific conformation adopted by the molecule in presence of the G4. On the contrary, addition of NDIs **NT4-NT6** determined significant variations, already at 20°C: indeed, in presence of NDI ligands, shoulder at 260 nm disappeared, while the band at 290 nm was unaltered, and a new positive band, with low intensity, appeared at 240 nm. Increasing the temperature, another structural variation was observed: the intensity of 290 nm dropped rapidly, as proved by T_m values reported in Table 5.17, but molar ellipticity increased at 264 nm, leading to the formation of a new band, that reached maximum intensity at 70°C and then decreased upon quadruplex unfolding.

22AG					
Compound	T _m ($\lambda=264\text{nm}$) (°C)	ΔT _m ($\lambda=264\text{nm}$) (°C)	T _m ($\lambda=290\text{nm}$) (°C)	ΔT _m ($\lambda=290\text{nm}$) (°C)	
Blank	61.0	-	58.0	-	
T10	65.0	+ 4.0	60.0	+ 2.0	
T11	69.9	+ 8.9	62.0	+ 4.0	
T12	64.0	+ 3.0	57.9	- 0.1	
NT4	84.0	+ 23.0	62.0	+ 4.0	
NT5	78.0	+ 17.0	60.0	+ 2.0	
NT6	77.0	+ 16.0	55.0	- 3.0	

Table 5.17 – CD melting measured for compounds **T10-T12** and **NT4-NT6** with 22AG, at $\lambda = 264\text{ nm}$ and $\lambda = 290\text{ nm}$. Blank sample represents the melting temperature of 22AG without ligand. Experiments were performed in 1 ml of solution, containing 2.5 μM of oligonucleotide, 10 μM of ligands, 10 mM of LiCaco (pH = 7.2) and 20 mM KCl. Solution temperature was increased from 20 to 95°C and the CD spectra was recorded every ten degrees.

This behaviour is paralleled by melting temperature values: indeed, at 290 nm, no significant increase was recorded and **NT6** showed even a destabilizing effect, reducing the unfolding temperature of 3°C. On the contrary, at 264 nm, ligands induced variation ranging 16°C and 23°C, with highest stabilization achieved with **NT4**, with the shortest spacer, despite the more elevated stabilization observed with tetrazole **T11** compared to **T10**. Furthermore, NDI-tetrazole conjugates are responsible of significant structural variations on telomeric 22AG. In this case, all three ligands were able to cause modification of dichroic signal of 22AG at room temperature and, before quadruplex unfolding, as in case of LTR-III, they shifted the equilibrium towards the formation of a parallel structure, confirming, once again, their preference for this particular topology.

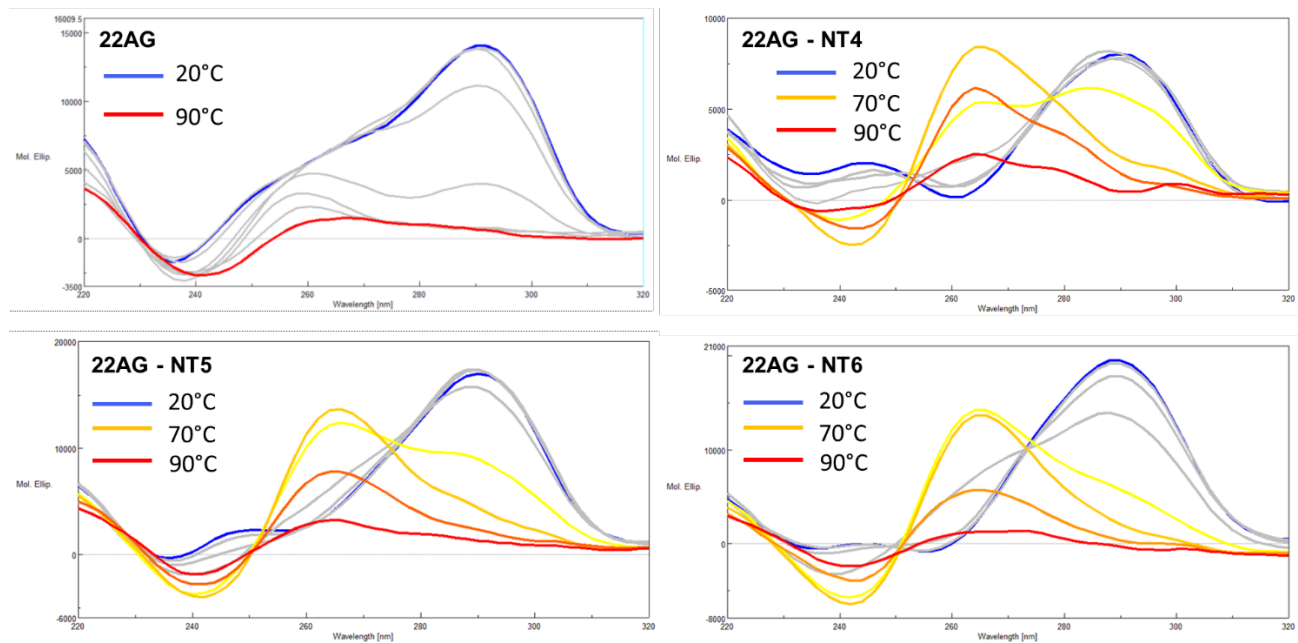


Figure 5.24 - CD Melting of compounds NT4-NT6 with 22AG. Experiments were performed in 1 ml of solution, containing 2.5 μ M of oligonucleotide, 10 μ M of ligands, 10 mM of LiCaco (pH = 7.2) and 20 mM KCl. Solution temperature was increased from 20 to 95°C and the CD spectra was recorded every ten degrees.

This consideration has been further confirmed by subsequent experiments performed on parallel c-MYC: this quadruplex is characterized by intrinsic elevated stability, as demonstrated by its elevated melting temperature ($T_m = 72^\circ\text{C}$). Once again, analyses were conducted in solutions containing 2.5 μ M of oligonucleotide and 10 μ M of ligands, in lithium cacodylate buffer (pH 7.2). In this case, unfolding was followed only at 264 nm because, for its well-defined parallel topology, CD spectra of c-MYC present only one maximum signal, at 264 nm, and a negative band at 245 nm. In presence of the ligands, higher stabilizations were observed with all compounds (Table 5.18): indeed, at the maximum achievable temperature, the quadruplex was not even completely unfolded, resulting in melting temperatures higher than 95°C and stabilizations above 23°C, with all ligands. Despite the impossibility to measure the exact entity of the interactions between NT4-NT6 and c-MYC, looking at the CD spectra (Figure 5.25) it's possible to observe that, in presence of NT4, the intensity of the signal was only slightly reduced, even at 95°C, while NT5 and NT6 induced a significant decrease of the same band, suggesting that the presence of longer spacer ensures better affinity for the target. Tetrazoles T10-T12 showed, once again, poor stabilization and lower increase of melting temperature (among 2°C and 5°C) was detected.

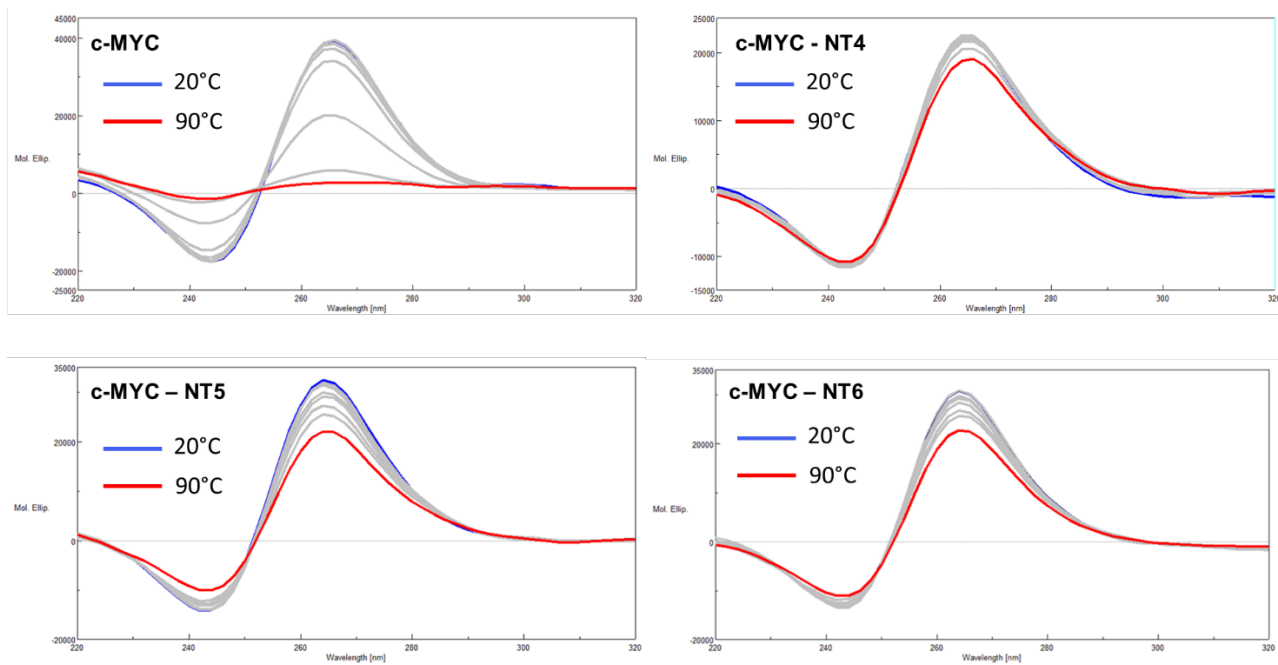


Figure 5.25 - CD Melting of compounds **NT4-NT6** with **c-MYC**. Experiments were performed in 1 ml of solution, containing 2.5 μ M of oligonucleotide, 10 μ M of ligands, 10 mM of LiCaco (pH = 7.2) and 5 mM KCl. Solution temperature was increased from 20 to 95°C and the CD spectra was recorded every ten degrees.

These preliminary investigations demonstrated that modification of 2,5-diaryl tetrazoles with NDI scaffold represent a successful strategy to improve their binding properties towards G4s. In particular, the most interesting fact is that all ligands showed marked preference for parallel topology, suggesting that they could act as topology-selective ligands. Moreover, it should be underlined that, with all oligonucleotides, highest stabilization was always achieved with **NT4**, indicating that two-carbon atoms spacer ensured stronger interactions with the target.

c-MYC		
Compound	$T_m (\lambda=264\text{nm})$ (°C)	$\Delta T_m (\lambda=264\text{nm})$ (°C)
Blank	72.0	-
T10	75.3	+ 3.3
T11	77.0	+ 5.0
T12	74.0	+ 2.0
NT4	> 95	> 23
NT5	> 95	> 23
NT6	> 95	> 23

Table 5.18 - Temperature melting measured for compounds **T10-T12** and **NT4-NT6** with **c-MYC**, at $\lambda = 264$ nm. Blank sample represents the melting temperature of **c-MYC** without ligand. Experiments were performed in 1 ml of solution, containing 2.5 μ M of oligonucleotide, 10 μ M of ligands, 10 mM of LiCaco (pH = 7.2) and 5 mM KCl. Solution temperature was increased from 20 to 95°C and the CD spectra was recorded every ten degrees.

5.2.6 Conclusions

Here we have engineered novel naphthalenediimide-tetrazole conjugates, covalently bound through spacers of different length, as innovative light-responsive quadruplex ligands. After the optimization of their synthetic protocol, we have explored their photoinduced reactivity, as their photochemical properties were completely unknown. Firstly, we have demonstrated that, all synthesized derivatives **NT1-NT6** can be activated upon photoirradiation at 517 nm, in water solution and we observed not only the generation of the expected acyl hydrazide, but also the intermediate nitrile imine dipole. However, photolysis efficiency was quite low. Then we explored the photoreactivity of all conjugates in the UV-region, at 313 nm, where the tetrazole moiety absorbs. As predicted, for all conjugates, we have measured high quantum yields, with values similar to non-conjugated 2,5-diaryl tetrazoles, evidencing their higher photolysis efficiency at this irradiation wavelength. Furthermore, within these experiments, we have obtained an unexpected outcome: activation of NDI-tetrazoles, at 313 nm, did not result in the generation of the expected acyl hydrazide, or nitrile imine, but in another chemical species, *1H*-diazirine. Although further experiments are required to confirm the structural identity and stability of this product, its generation represents an unexpected but interesting outcome. These three-membered rings are characterized by elevated reactivity, especially towards nucleophile, therefore they could be potentially employed as innovative alkylating agents, as *1H*-diazirines are expected to be strong electrophiles, and supplementary studies will be carried out in order to prove this potential application.

In the end, we have investigated the binding affinity of NDI-tetrazole **NT4-NT6** for different quadruplex structures, including LTR-III, telomeric 22AG and c-MYC. From these studies, we have observed that NDI scaffold effectively ensured higher affinity for G4s, compared to non-conjugated tetrazoles, despite the non-negligible binding properties have been determined for compounds **T10-T12**. It should be underlined that, in general, **NT6**, characterized by the longest spacer, always displayed lower affinity compared to other compounds. Furthermore, **NT4** and **NT6** were characterized by marked preference for parallel structures, suggesting that they could act as topology-selective ligands. Although other biophysical experiments need to be performed and the selectivity in presence of double and single stranded DNA should be investigated, these outcomes highlighted that we managed to develop novel light-activatable molecules, even in the visible region, which also present strong affinity for quadruplex structures and, therefore, can be potentially exploited as innovative sensors or reactive ligands delivered on G4 as target.

6. Conclusions

In the last decades, light-responsive molecules attracted a great deal of attention, for the possibility to design progressively more efficient and selective fluorescent probes, to detect specific targets in their native environment, or photoswitches, whose properties can be easily modulated upon irradiation.

The work of this thesis was focused on the development of novel optically active small-molecules for targeting G-quadruplex structures, which can be exploited both as sensors and biologically active ligands.

We designed different small libraries of 1) fluorescent and 2) photoreactive ligands.

The first class of reported compounds included a family of sixteen, highly fluorescent, naphthalenediimides (NDIs), conjugated to different types of carbohydrates. Introduction of sugar derivatives had a dual purpose: improve the affinity for G4s structures, thanks to the possibility to establish multiple hydrogen-bonds with grooves and loops, and to increase cellular uptake in cancer cells, exploiting the overexpression of GLUT receptors. The first library of NDI-sugar conjugates has been implemented with thio-modified carbohydrates, in which oxygen in position 1 was replaced with a sulphur atom, in order to increase the hydrolytic stability in physiological environment. Moreover, two series of NDIs were used, the first one characterized by the presence of 3-(dimethylamino)propylamine at the imide position, the second with 4-(2-aminoethyl)morpholine, selected for its lower basicity and, subsequently, to improve the selectivity towards the target of interest. Analysis of their cytotoxicity against cancer (HT29) and normal (MRC5) cells highlighted, in general, higher toxicity in NDIs bearing 3-(dimethylamino)propylamine and, in particular, NDI **8**, conjugated to thio-maltose, emerged for a more pronounced activity towards cancer cells, which offers a potential therapeutic window. In general, it should be underlined that introduction of thio-modified sugars resulted to be a successful strategy, because best results have been achieved with this new library of conjugates. Interestingly, FRET-melting analysis on telomeric quadruplex evidenced a correlation between cytotoxicity and binding properties: most toxic compounds displayed also the highest affinities for telomeric G4, suggesting that the observed biological activity could be due to interaction with the specific nucleic acid target. Although further experiments are necessary to effectively demonstrate this correlation, obtained results represent a solid starting point for the development of biologically active ligands. Moreover, analysis of spectroscopic properties of the potent ligand NDI **8**, revealed the excellent fluorescence emission of this type of scaffold, in water, confirming also its potential as probe to detect the target in cellular environment. The second part of this thesis work has been dedicated to the development of alternative targeting strategies, based on photoreactive units. This type of approach is still relatively unexplored in the G-quadruplex targeting scenario, therefore we decided to exploit two basically different photoreactive units to design innovative quadruplex ligands: 1) quinone methide precursors (QMPs) and 2) 2,5-diaryl tetrazoles.

Due to their high electrophilic nature, quinone methides have been selected for their ability to form a covalent bond with nucleobases, to further strengthen the interactions to the target. In details, we have designed six new “V-shaped” ligands, bearing Mannich bases or ammonium salts functions as quinone methide precursors (QMPs). Their structure was designed to achieve both strong interactions with the target and red-shift the absorption spectra, to perform photochemical activation under biocompatible conditions. The investigation of their photochemical behaviour pointed out significant differences in reactivity, evidencing the more efficient photolysis of ammonium salts precursors. CD and FRET-melting assays suggested that, in general, these types of scaffolds suffer from low affinity for quadruplex structures. Nevertheless, it should be underlined that, in presence of duplex DNA, they retained good selectivity towards quadruplex structures. Although their quite low binding properties toward quadruplex structures, during the irradiation experiments in presence of the target, formation of adducts of quinone methides to nucleobases were detected in good yields, in particular with ammonium salts **QMP2** and **QMP4**, demonstrating the efficacy of this approach. Further optimizations are required, in particular in strengthening the binding and to shift the absorption of the photoresponsive ligands towards visible region, to perform the activation in a more biologically suitable spectral window.

The low and unexpected photoreactivity of naphthalene derivatives **QMP5** and **QMP6** observed during these experiments, prompted us to investigate in depth the photochemical behaviour of naphthalene-based quinone methide precursors. We were particularly interested in this scaffold, because the presence of naphthalene unit could ensure both stronger interactions with guanine tetrads (through π - π stacking interactions), and red-shifted absorption. Therefore, we have synthesized a library of different 6-substituted 3-((dimethylamino)methyl)naphthalen-2-ol derivatives and we have evaluated their photochemical behaviour, in order to individuate most reactive compounds. Photoreactivity experiments highlighted that increasing the electron density on naphthalenic core improves the generation efficiency of the corresponding quinone methide, at 313 nm and, indeed, we have identified **N2** and **N5** as most reactive substrates, characterized by the presence of a carboxylic acid and a boronic acid, respectively. We have also demonstrated that their activation was feasible even at 365 nm, in aqueous solution and, for some compounds, was even more efficient, compared to 313 nm, as proved by their high quantum yields values,. This preliminary investigation of spectroscopic and photochemical properties represents a solid base for the development of new improved naphthalene-based ligands for nucleic acids.

The last part of this work has been focused on the development of novel compounds, based on 2,5-diaryl tetrazoles as photoreactive unit. This light-activatable moiety has never been used for applications on nucleic acids secondary structures, however it attracted our attention for some interesting properties, such as the high versatility of the photogenerated nitrile imine intermediate, and for the possibility to generate, *in situ*, a fluorescent pyrazoline, as a consequence of cycloaddition with alkenes.

Due to the complete lack of preliminary data, we have performed a thorough investigation of photochemical behaviour of a small library of substituted 2,5-diaryl tetrazoles, finding the general structural and electronic features to maximise the reactivity. From our experiments, we demonstrated that electronic properties of substituents influence substrate reactivity and product distribution. In more detail, electron-rich substituents on N-phenyl ring increased both photolysis efficiency and cycloaddition selectivity vs hydration, but unfortunately resulted in lowering the fluorescence quantum yield of the photoproduct pyrazoline. Therefore, the “most effective combination”, which guarantees both high reactivity and intense emission, has not been defined. However, a compromise can be achieved, as in case tetrazole **T7**, that was able to generate a highly fluorescent pyrazoline with moderate selectivity and good reactivity. Despite these encouraging results, FRET-melting assay, performed on water soluble **T7-T9**, evidenced low affinity of these scaffolds towards quadruplex structures and the impossibility to use them as efficient ligands.

To improve interactions with G-quadruplexes, we effectively achieved the conjugation of tetrazoles to well-known quadruplex binders. The choice of the type of ligand was dictated not only by the affinity for G4s, but also by the necessity to also induce a biological response. Therefore, we have analysed the anticancer and the antiparasitic activity of three different classes of G4 ligands, previously synthesized by Freccero’s group and, from this screening, identifying the tri-substituted NDI scaffold as most promising one.

Then, we have designed and synthesized several NDIs-tetrazole conjugates, covalently bound through alkyl spacers of different lengths, and explored their photophysical properties and photochemical reactivity. Their excellent absorption between 500 and 600 nm allowed us to explore their activation in the visible region. We have shown that tetrazole photolysis could be accomplished upon irradiation with a green LED, as confirmed by detection of photogenerated acyl hydrazide. However, in this spectral region, photolysis efficiency was significantly lower, by a magnitude order, compared to non-conjugated tetrazole. Then, for comparison sake, we have analysed their reactivity also at 313 nm, to verify if their higher molar absorptivity at this wavelength could ensure a more effective process: as expected, activation in UV-region resulted in more efficient tetrazole photolysis. Moreover, through these experiments, we have demonstrated that conjugation to NDI and the wavelength of activation modulate product distribution: upon irradiation at 313

nm, formation of expected acyl hydrazide was not detected and a new type of derivative, 1*H*-diazirine, was generated.

Our results represent a significant breakthrough in this research field, as to the best of our knowledge, activation of 2,5-diaryl tetrazoles with visible light has never been accomplished. We are confident that this outcome will further expand their range of applications. Moreover, formation of diazirine because of tetrazole photolysis was never been described under similar conditions. This somehow unexpected reactivity resulting in an electrophilic three membered ring is an interesting opportunity to explore also a different type of photoreactivity of tetrazoles, which may produce alkylation of the G-quadruplex. Photoreactivity studies of these conjugates in the presence of G-quadruplex are currently in progress.

We have also shown, by CD-melting experiments, that conjugation to NDI resulted to be a successful strategy to improve binding affinity towards quadruplex structures. Interestingly, we have discovered that these compounds showed good affinity for G4s, with a marked preference for parallel topology, indicating that they could be further developed as dual topology-selective and photoreactive ligands.

In the end, we have explored the possibility to exploit different types of photoresponsive molecules to develop novel and efficient quadruplex ligands, based on fluorescent probes or using photoreactive moieties. We conducted a deep analysis of photochemical behaviour of selected, light-activable, compounds, to fully understand their behaviour and how to efficiently exploit them for applications on quadruplex structures. Despite the optimization of these ligands is far from over, this thesis work lay the basis for the development of dual photoresponsive ligands, combining the novel photoreactivity of tetrazole and its water soluble NDI-conjugates, to the efficient emission of the pyrazoline photoadducts.

7. Experimental Section

7.1 Materials and Methods

7.1.1. Chemicals, Oligonucleotides and Cells

Reagents, solvents and chemical were purchased from Merck, TCI-Chemicals or Carlo Erba and were used as supplied without further purifications. Oligonucleotides were purchased from IBA, Merck or Eurogentec and used without further purifications. Oligonucleotide stock solutions were stored at -20°C and the exact concentrations were determined through UV-VIS analysis.

Cells and parasites used in biological assays were stored in liquid nitrogen, in DMSO solution. For culture, we have used Dulbecco's Modified Eagle Medium, with 1g/L of glucose. For HT29 cells, medium composition was 4.5 g/L of glucose.

7.1.2 Absorption, Fluorescence and Circular Dichroism Analysis

UV-visible spectra were measured in a Agilent Cary-300 spectrophotometer equipped with a Peltier temperature controller. The absorbance was recorded for 200-900 nm wavelength interval at a scan rate of 200 nm/min and a slit width of 1.5 nm, with a 3 ml quartz cell with 1 cm path length.

Fluorescence spectra were recorded with a Agilent Cary Eclipse fluorospectrometer, at room temperature, at a scan rate of 600 nm/min, in 300-800 nm interval, with band width of excitation and emission slits at 5 nm and medium voltage, in 3 ml quartz cell with 1 cm path length.

Circular Dichroism analysis were performed on a JASCO J1500 spectropolarimeter, equipped with a Peltier temperature controller, or, alternatively, with JASCO J-710 spectropolarimeter equipped with a Peltier temperature controller (Jasco PTC-348WI), in 1 mL black-walled rectangular quartz cells with 1 cm path length.

7.1.3 Compounds Characterization

¹H- and ¹³C-NMR spectra were recorded on a Bruker ADVANCE 300 MHz.

7.1.4 Compounds Purification and Analysis

TLC analysis were performed on silica gel (Merck 60F-254), with visualization at 254 nm and 366 nm. For flash column chromatography purification, we have used an Isolera ONE Flash Chromatography System (Biotage), combined with a UV/VIS detector. The proper columns (KP-SIL Pk 20 by Biotage) were used, depending on the type of compounds (SNAP 10 g – 10 ml/min, SNAP 25 g – 25 ml/ min, SNAP 50 – 45 ml/min, SNAP 100 g – 50 ml/min).

HPLC analysis were performed with an Agilent System SERIES 1260, with XSelectHSS C18 (2.5 mM) (50 x 4.6 mm) (Waters).

HPLC semi-preparative purification was carried out with a Water system composed of Delta 600 PUMP, a 2489 UV/VIS detector and a Fraction Collector III. The used column was a XSelect CSH Prep Phenyl-Hexyl 5 µm (150x30 mm) (Waters), working at flow = 27 ml/min.

Preparative HPLC purification was performed also with an Agilent Technologies 1260 Infinity, equipped with a diode array UV-VIS detector. The work-flow was 27 ml/min. Two different columns have been used: SunFire C18 OBD (5 µm, 150x30 mm) and a XSelect CSH Prep Phenyl-Hexyl OBD (5 µm, 150x30 mm).

For all the HPLC analysis and purifications, we have used, as eluents, 0.1% trifluoroacetic acid in water and acetonitrile.

All the HPLC analysis were performed through injection of 10 µl of sample solution and monitoring the absorbance at $\lambda = 256$ nm.

Here are described the principal analytical methods used to analyze solutions of synthesized compounds:

- **3A:** Flow: 1.4 ml/min; Gradient: 95% aqueous for 2 minutes, gradually increased to 40% aqueous over 8 minutes and then isocratic flow for 4 minutes.
- **4A:** Flow: 1.0 ml/min; Gradient: 95% aqueous for 2 minutes, gradually increased to 100% acetonitrile over 10 minutes, isocratic flow for 1 minute, then decreased to 5% acetonitrile in 1 minute.
- **5A:** Flow: 1.0 ml/min; Gradient 95% aqueous for 2 minutes, gradually decreased to 42% over 11 minutes, isocratic for 1 minute, then decreased to 0% in 2 minutes, then 4 minutes of isocratic flow at 100% acetonitrile and decreased to 5% of acetonitrile in 2 minutes.

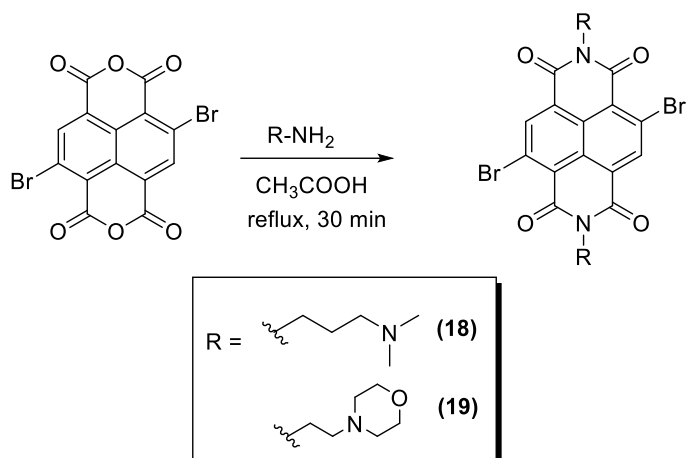
Methods used for semi-preparative and preparative purification of compounds are the following:

- **3P:** Flow: 30 ml/min; Gradient: 95% aqueous for 2 minutes, gradually increased to 70% aqueous over 20 minutes, then decreased to 60% in 4 minutes and finally increased again to 95% in other 2 minutes.
- **4P:** Flow: 30 ml/min; Gradient: 95% aqueous for 2 minutes, gradually increased to 100% aceonitrile over 13 minutes, the isocratic for 4 minutes and to 5% acetonitrile over 2 minutes.
- **5P:** Flow: 30 ml/min; Gradient: 95% aqueous for 2 minutes, gradually increased to 100% acetonitrile over 12 minutes, then isocratic flow for 2 minutes and decreased to 5% acetonitrile in 2 minutes.
- **6P:** Flow: 27 ml/min; Gradient: 95% aqueous for 2 minutes, gradually decreased to 85% in 2 minutes, then to 60% over 18 minutes and to 20% in other 2 minutes and, in the end, increased again to 95% in 2 minutes.

7.2 NDI-Carbohydrates conjugates: experimental details

7.2.1 Synthesis of Compounds

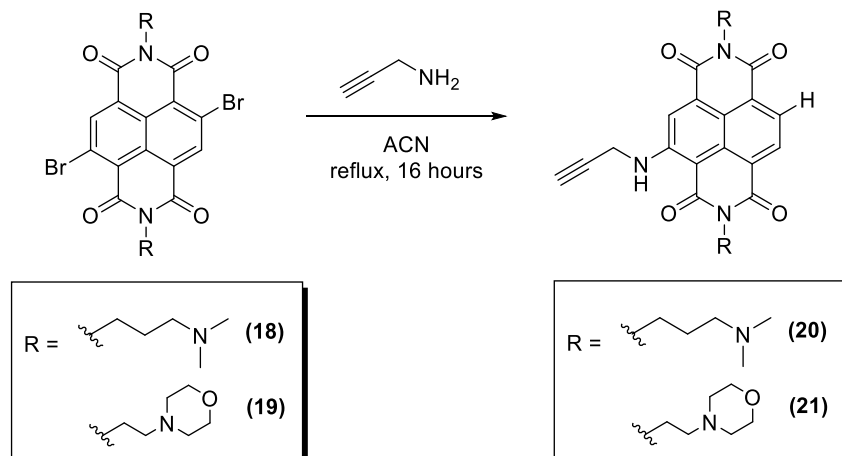
General procedure for the synthesis of NDIs 18-19



Scheme 7.1 – Synthesis of NDIs 18-19.

In a one-necked flask, 500 mg (1.18 mmol, 1 eq.) of di-bromo-1,4,5,8-naphthalenetetracarboxylic dianhydride, previously synthesized according to a published procedure, were suspended into 100 ml of acetic acid, then 0.460 ml (3.54 mmol, 3 eq.) were added to the mixture. Solution was refluxed for 30 minutes, under nitrogen atmosphere, then acid was neutralized through addition of sodium carbonate. Crude has been extracted three times with dichloromethane (3x200 ml) and used for the next step without no further purification.

General Procedure for the Synthesis of NDIs 20-21



Scheme 7.2 – General Procedure for the synthesis of NDIs 20-21.

In a round bottomed flask, 300 mg (0.46 mmol, 1 eq.) of di-bromo-disubstituted NDI were dissolved into 150 ml of acetonitrile, then 0.08 ml (1.39 mmol, 3 eq.) were added. Reaction mixture has been refluxed for 16 hours, then solvent was removed under reduced pressure. Crude has been purified with reverse phase column chromatography, using method **3P**.

20*CF₃COOH: Red solid. Yield (%) = 45%. The compound characterization coincided with the description found in literature¹⁸³.

21*CF₃COOH: Red solid. Yield (%) = 40%. **¹H-NMR (300 MHz, D₂O)** δ (ppm) = 8.16 (d, *J* = 7.8 Hz, 1H), 7.98 (d, *J* = 7.9 Hz, 1H), 7.9 (s, 1H), 4.48-4.42 (m, 4H), 4.3 (s, 2H), 4.02 (m, 4H), 3.69-3.65 (m, 8H), 3.5-3.45 (m, 4H), 3.22-3.19 (m, 4H), 2.82 (s, 1H). **¹³C-NMR (75MHz, D₂O):** δ (ppm) = 168.6, 167.3, 167.0, 166.7, 166.6, 166.1, 165.6, 154.7, 134.7, 131.7, 129.9, 128.5, 128.3, 125.7, 125.2, 123.7, 121.9, 121.4, 117.5, 113.7, 103.0, 82.2, 77.3, 67.0, 58.1, 57.8, 55.6, 38.2, 37.7, 35.9.

General Procedure for the Synthesis of Halogen-linked protected sugars 22-25



Scheme 7.3 – General Procedure for synthesis of halogen protected sugars 22-25.

To a solution of peracetylated 1-trichloroacetimide sugar (1 eq.) in anhydrous DCM, under argon atmosphere, 2-bromo ethanol (1.1 eq.) was added dropwise. Boron trifluoride diethyl etherate was then added (1 eq.) and the reaction was stirred at room temperature for 30 minutes. After TLC verification of total consumption of the initial product, an 10% aqueous solution of Na₂CO₃ was added. The organic phase was washed three times (3 x 100 mL) with the basic solution, then was concentrated and purified through flash column chromatography, using, as eluent, a mixture of Hexane: Ethyl Acetate 4:1 to 2:1.

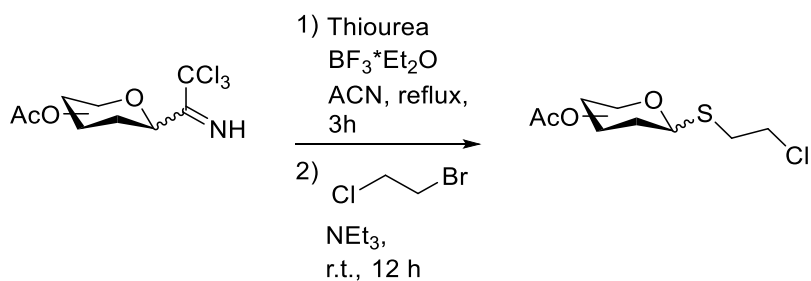
22: Yield = 20%. which was fully characterized according to the literature¹⁸³.

23: Yield = 37%. which was fully characterized according to the literature²⁰¹.

24: Yield = 30%, which was fully characterized according to the literature¹⁸³.

25: Yield = 13%, which was fully characterized according to the literature²⁰².

General Procedure for the synthesis of Halogen-linked protected thiosugars 26-29.



Scheme 7.4 – General Procedure for the synthesis of halogen-protected thiosugars 26-29

To a stirred solution of the peracetylated sugar (1 eq.) and thiourea (1.1 eq.), dissolved in 10 ml of dry acetonitrile, $\text{BF}_3\text{-Et}_2\text{O}$ (2 eq.) was added. The reaction mixture was refluxed for 3 hours, then, after cooling, 1-bromo-2-chloroethane (2.5 eq.) and triethylamine (4 eq.) were added. The resulting solution stirred at room temperature for 12 h. After this time, solvent was removed under vacuum to afford the curde, which was dissolved into 100 ml of DCM and washed with water (3 x 100 mL). The organic phase was evaporated and purified by flash column chromatography using as eluents Hexane: Ethyl Acetate – 4:1 to 2:1.

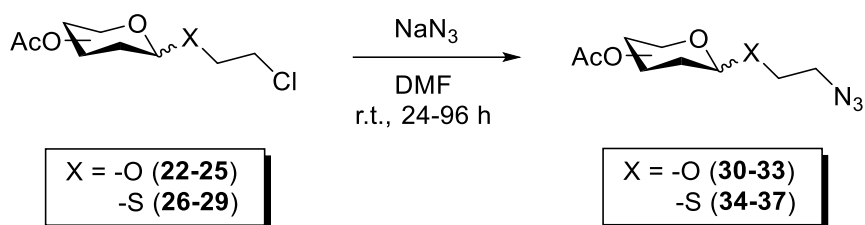
26: Yield = 79%, R_f = 0.65 (Hexane: Ethyl Acetate – 1:1), which was fully characterized according to the literature²⁰³.

27: Yield = 18 %. $^1\text{H NMR}$ (300 MHz, CDCl_3) δ (ppm) = 5.37 (d, J = 2.4 Hz, 1H), 5.16 (t, J = 9.9 Hz, 1H), 5.00 (dd, J = 10.0, 3.0 Hz, 1H), 4.51 (d, J = 9.8 Hz, 1H), 4.13 – 3.98 (m, 2H), 3.92 (t, J = 6.3 Hz, 1H), 3.74 – 3.55 (m, 2H), 3.13 – 2.77 (m, 2H), 2.10 (s, 3H), 2.00 (s, 6H), 1.92 (s, 3H). $^{13}\text{C NMR}$ (75 MHz, CDCl_3) δ (ppm) = 170.5, 170.3, 170.1, 169.7, 84.5, 74.8, 71.87, 67.5, 67.2, 61.9, 43.5, 33.0, 20.9, 20.8, 20.7.

28: Yield = 49 %. $^1\text{H NMR}$ (300 MHz, CDCl_3) δ (ppm) = 5.24 (s, 1H), 5.22 – 5.10 (m, 2H), 4.38 – 4.26 (m, 1H), 4.22 (dd, J = 11.9, 6.2 Hz, 1H), 4.05 (dd, J = 12.0, 1.5 Hz, 1H), 3.80 – 3.37 (m, 3H), 3.04 – 2.83 (m, 2H), 2.09 (s, 3H), 2.03 (s, 3H), 1.99 (s, 3H), 1.92 (s, 3H). $^{13}\text{C NMR}$ (75 MHz, CDCl_3) δ (ppm) 170.7, 170.0, 169.9, 169.9, 83.3, 70.9, 69.5, 69.4, 66.4, 62.7, 42.8, 34.1, 21.0, 20.8, 20.8.

29: Yield = 27 %. $^1\text{H NMR}$ (300 MHz, CDCl_3) δ (ppm) = 5.29 (ddd, J = 18.6, 9.6, 6.5 Hz, 3H), 4.99 (t, J = 9.8 Hz, 1H), 4.86 – 4.76 (m, 2H), 4.63 – 4.42 (m, 1H), 4.17 (ddd, J = 16.9, 12.3, 4.4 Hz, 2H), 4.07 – 3.87 (m, 3H), 3.76 – 3.50 (m, 3H), 3.38 (dt, J = 31.3, 7.7 Hz, 1H), 3.10 – 2.75 (m, 2H), 2.08 (d, J = 7.9 Hz, 3H), 2.04 (s, 3H), 1.97 (dd, J = 8.8, 3.8 Hz, 15H). $^{13}\text{C NMR}$ (75 MHz, CDCl_3) δ (ppm) = 170.7, 170.6, 170.2, 170.1, 169.8, 169.6, 95.8, 83.5, 72.9, 70.7, 70.2, 69.5, 68.8, 68.2, 63.0, 61.8, 43.6, 42.3, 32.7, 32.3, 25.6, 21.1, 21.0, 20.9, 20.8, 20.8.

General Procedure for the Synthesis of Azide-linked protected sugars 30-37



Scheme 7.5 – General Protocol for the synthesis of azide-linked protected sugars 30-37.

Solution of halogen-linked protected sugar **22-29** (1 eq.) and sodium azide (10 eq.), dissolved in 25 ml of DMF, was stirred for 24 h to 96 hours at room temperature. Reaction product was then diluted with DCM and extracted with water (6 x 100 mL). Obtained azido-sugars was used for the subsequent step without no further purification.

30: Yield = 90 %, which was fully characterized according to the literature¹⁸³.

31: Yield = 94 %, which was fully characterized according to the literature²⁰¹.

32: Yield = 92 %, which was fully characterized according to the literature¹⁸³.

33: Yield = 93 %, which was fully characterized according to the literature²⁰².

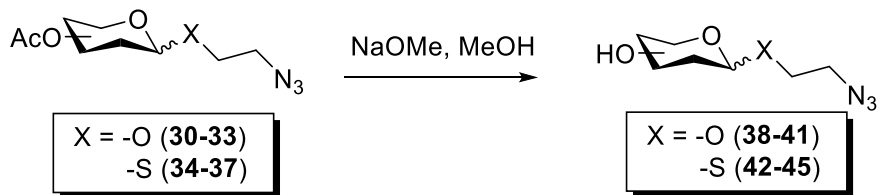
34: Yield = 50 %. **¹H NMR (500 MHz, CDCl₃) δ (ppm)** = 5.23 (t, *J* = 9.4 Hz, 1H), 5.06 (dt, *J* = 19.3, 9.7 Hz, 2H), 4.56 (d, *J* = 10.0 Hz, 1H), 4.19 (ddd, *J* = 14.7, 12.4, 3.7 Hz, 2H), 3.73 (ddd, *J* = 10.1, 5.0, 2.3 Hz, 1H), 3.60 – 3.43 (m, 2H), 2.95 (dt, *J* = 13.9, 6.9 Hz, 1H), 2.77 (dt, *J* = 13.9, 6.9 Hz, 1H), 2.09 (s, 3H), 2.06 (s, 3H), 2.03 (s, 3H), 2.01 (s, 3H). **¹³C NMR (126 MHz, CDCl₃) δ (ppm)** = 170.5, 170.1, 169.4, 169.4, 83.5, 76.0, 73.7, 69.6, 68.2, 62.0, 51.6, 29.4, 20.7, 20.7, 20.6, 20.5.

35: Yield = 99 %. **¹H NMR (300 MHz, CDCl₃) δ (ppm)** = 5.37 (d, *J* = 2.6 Hz, 1H), 5.22 – 4.93 (m, 2H), 4.54 (d, *J* = 9.8 Hz, 1H), 4.04 (t, *J* = 8.3 Hz, 2H), 3.95 (t, *J* = 6.3 Hz, 1H), 3.66 (dt, *J* = 9.6, 5.7 Hz, 1H), 3.46 (ddd, *J* = 12.3, 7.8, 4.5 Hz, 1H), 3.14 – 2.95 (m, 1H), 2.72 (dd, *J* = 13.9, 7.0 Hz, 1H), 2.09 (s, 3H), 2.00 (s, 3H), 1.98 (s, 3H), 1.91 (s, 3H). **¹³C NMR (75 MHz, CDCl₃) δ (ppm)** = 170.4, 170.2, 170.0, 169.7, 84.0, 74.7, 71.8, 67.5, 61.8, 51.6, 43.5, 29.6, 20.8, 20.7, 20.6.

36: Yield = 60 %, which was fully characterized according to the literature²⁰⁴.

37: Yield = 43 %. **¹H NMR (300 MHz, CDCl₃) δ (ppm)** = 5.44 – 5.21 (m, 3H), 5.03 (t, *J* = 9.8 Hz, 1H), 4.90 – 4.79 (m, 2H), 4.64 – 4.45 (m, 2H), 4.28 – 4.13 (m, 2H), 4.13 – 3.90 (m, 3H), 3.75 – 3.57 (m, 2H), 3.48 (dd, *J* = 10.6, 6.4 Hz, 1H), 3.10 – 2.65 (m, 2H), 2.12 (s, 3H), 2.08 (s, 3H), 2.04 – 1.97 (m, 15H). **¹³C NMR (75 MHz, CDCl₃) δ (ppm)** = 170.7, 170.7, 170.6, 170.2, 170.1, 169.8, 169.6, 95.9, 83.4, 72.8, 70.8, 70.2, 69.5, 68.8, 68.2, 63.0, 61.7, 51.7, 43.5, 32.6, 29.8, 21.1, 21.0, 21.0, 20.9, 20.8, 20.8, 20.8.

General procedure for the deprotection of the peracetylated sugars 38-45



Scheme 7.6 – General Procedure for deprotection of sugars 38-45.

In a round-bottom flask, protected peracetylated sugar (1 eq.) was dissolved in MeOH. A solution of sodium methoxide (2 mL/ 1 mmol of protected sugar, 25 % v/v in MeOH) was added dropwise and stirred until TLC verification showed complete transformation of the initial product. Solvents were evaporated and the resulting oil was resuspended in MeOH, then Amberlite [®] 120 H resin was introduced into the flask. The suspension was stirred until pH = 7, then resin was filtered off. Evaporation of the solvents afforded pure product as yellow oil or foam.

38: Yield = 90 %. The compound was fully characterized according to the literature¹⁸³.

39: Yield = 92 %. **¹H NMR (400 MHz, CD₃OD)** δ (ppm) = 4.31 (d, *J* = 6.9 Hz, 1H), 4.03 (dd, *J* = 10.8, 5.2 Hz, 1H), 3.88 (s, 1H), 3.79 - 3.73 (m, 3H), 3.59 – 3.55 (m, 1H), 3.54 (d, *J* = 2.9 Hz, 2H), 3.50 (t, *J* = 5.2 Hz, 2H). **¹³C NMR (101 MHz, CD₃OD)** δ (ppm) = 103.6, 75.2, 73.5, 71.1, 68.9, 67.9, 61.1, 50.8.

40: Yield = 93 %. The compound was fully characterized according to the literature¹⁸³.

41: Yield = 89 %. **¹H NMR (400 MHz, CD₃OD)** δ (ppm) = 4.98 (s, 2H), 4.41 (dd, *J* = 11.5, 7.3 Hz, 2H), 4.02 (dd, *J* = 10.7, 5.2 Hz, 1H), 3.91 (d, *J* = 9.6 Hz, 2H), 3.79 (dd, *J* = 11.5, 6.5 Hz, 2H), 3.65 (d, *J* = 8.1 Hz, 2H), 3.62 – 3.55 (m, 4H), 3.50 (t, *J* = 5.1 Hz, 2H), 3.33 (d, *J* = 1.4 Hz, 1H). **¹³C NMR (101 MHz, CD₃OD)** δ (ppm) = 178.6, 103.8, 102.8, 79.3, 75.7, 75.2, 73.3, 71.0, 69.0, 68.0, 61.1, 50.7, 48.5, 22.5.

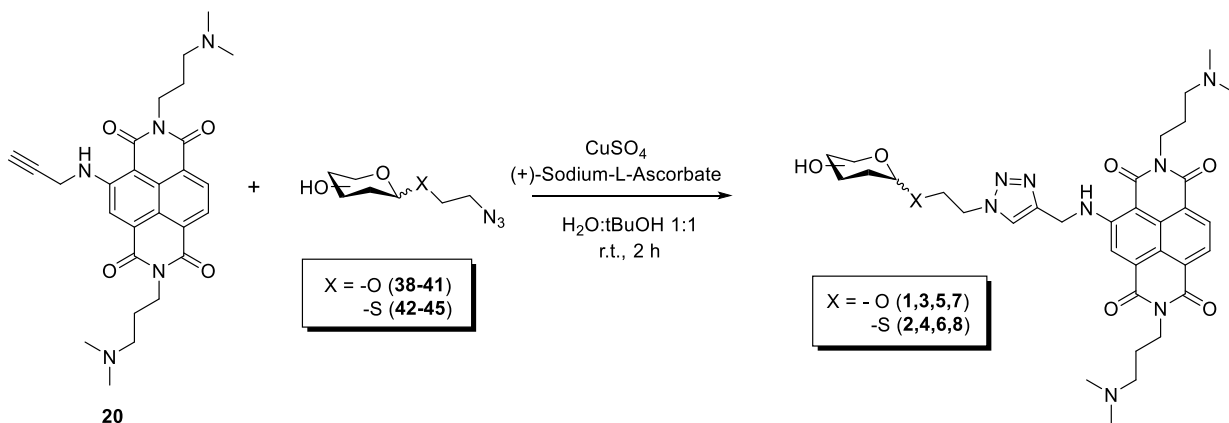
42: Yield = 97 %. **¹H NMR (300 MHz, CD₃OD)** δ (ppm) = 4.46 (d, *J* = 9.7 Hz, 1H), 3.89 (d, *J* = 11.9 Hz, 1H), 3.68 (dd, *J* = 11.6, 3.6 Hz, 1H), 3.57 (dt, *J* = 9.1, 5.9 Hz, 2H), 3.38 (d, *J* = 8.5 Hz, 1H), 3.34 (s, 2H), 3.23 (t, *J* = 9.0 Hz, 1H), 2.99 (dt, *J* = 13.9, 7.0 Hz, 1H), 2.91 – 2.78 (m, 1H). **¹³C NMR (75 MHz, CD₃OD)** δ (ppm) = 85.8, 80.6, 78.1, 73.0, 70.1, 61.5, 51.5, 29.1.

43: Yield = 95 %. **¹H NMR (400 MHz, CD₃OD)** δ (ppm) = 4.41 (d, *J* = 9.1 Hz, 1H), 3.93 (d, *J* = 2.2 Hz, 1H), 3.74 (dd, *J* = 10.3, 6.1 Hz, 3H), 3.61 – 3.52 (m, 4H), 2.98 (dd, *J* = 13.8, 6.8 Hz, 1H), 2.91 – 2.77 (m, 1H). **¹³C NMR (101 MHz, CD₃OD)** δ (ppm) = 86.3, 79.2, 74.7, 70.0, 69.1, 61.3, 51.6, 29.1.

44: Yield = 95 %. **¹H NMR (300 MHz, CD₃OD)** δ (ppm) = 5.34 (s, 1H), 3.98 – 3.83 (m, 2H), 3.83 – 3.70 (m, 2H), 3.70 – 3.65 (m, 2H), 3.56 (ddd, *J* = 12.9, 8.7, 4.8 Hz, 1H), 3.45 – 3.36 (m, 1H), 2.99 – 2.77 (m, 2H). **¹³C NMR (75 MHz, CD₃OD)** δ (ppm) = 85.5, 73.7, 72.2, 71.7, 67.4, 61.3, 50.9, 30.0.

45: Yield = 97 %. **¹H NMR (400 MHz, CD₃OD)** δ (ppm) = 5.21 (d, *J* = 3.4 Hz, 1H), 4.48 (d, *J* = 9.7 Hz, 1H), 3.94 – 3.78 (m, 4H), 3.75 – 3.54 (m, 6H), 3.50 – 3.42 (m, 2H), 3.34 – 3.25 (m, 2H), 3.03 – 2.92 (m, 1H), 2.86 (dt, *J* = 13.8, 6.8 Hz, 1H). **¹³C NMR (101 MHz, CD₃OD)** δ (ppm) = 101.4, 85.8, 79.2, 77.9, 73.7, 73.3, 72.7, 70.1, 61.3, 61.0, 51.5, 43.5, 32.3 29.1.

General Procedure for the synthesis of conjugated NDI-Sugars 1-8



Scheme 7.7 – General Procedure for the click reaction between NDI 20 and sugar 38-45.

A solution of (+)-sodium-L-ascorbate (12 mg, 0.06 mmol), copper(II) sulfate pentahydrate (1.5 mg, 0.006 mmol) and NDI **20** (30 mg, 0.06 mmol), dissolved in 2 ml of H_2O , was added to azido-glyco-derivative **38-45** (0.09 mmol, 1.5 eq.), solubilized into 2 ml of *t*BuOH. The suspension was stirred at room temperature, under argon atmosphere, for 2 hours. The resulting red solution was concentrated under vacuum and a red solid was obtained. The crude product was analysed and purified by reverse phase column chromatography, ($\text{CH}_3\text{CN}: \text{H}_2\text{O} 0.1\% \text{TFA}$) with method **3P**, described in the previous section.

1*CF₃COOH: Red solid. Yield = 80%. The compound was fully characterized according to the literature¹⁸³.

2*CF₃COOH: Red solid. Yield = 92 %. **¹H NMR (300 MHz, D₂O)**, δ (ppm) = 8.12 (d, 1H, J = 8 Hz), 8.09 (s, 1H), 7.88 (d, 1H, J = 8.0 Hz), 7.72 (s, 1H), 4.76 (s, 1H), 4.61 (s, 2H), 4.23 (d, 1H, J = 9.7 Hz), 4.01 (bs, 4H), 3.69 (d, 1H, J = 12 Hz), 3.44 (dd, 1H, J = 6, 12 Hz), 3.24-3.18 (m, 8H), 3.06-3.00 (m, 2H), 2.99 (t, 1H, J = 9 Hz), 2.84 (s, 12H), 2.04 (m, 4H). **¹³C NMR (75 MHz, D₂O)** δ (ppm) = 165.1, 163.5, 163.3, 162.8, 151.3, 143.3, 130.9, 128.1, 126.4, 125.0, 124.9, 122.1, 119.8, 118.2, 118.1, 114.2, 99.2, 85.2, 79.6, 76.9, 72.2, 69.3, 60.7, 55.1, 50.5, 42.7, 38.0, 37.6, 37.0, 22.7.

3*CF₃COOH: Red solid. Yield = 85%. The compound was fully characterized according to the literature¹⁸³.

4*CF₃COOH: Red solid. Yield = 92 %. **¹H NMR (300 MHz, D₂O)** δ (ppm) = 8.12 (s, 1H), 8.11 (d, 1H, J = 8.0 Hz), 7.88 (d, 1H, J = 8.0 Hz), 7.72 (s, 1H), 5.11 (s, 1H), 4.82 (s, 2H), 4.01 (t, 4H, J = 7 Hz), 3.78 (d, 1H, J = 2 Hz), 3.59-3.55 (m, 2H), 3.45 (t, 1H, J = 9 Hz), 3.34 (dd, 1H, J = 3, 8 Hz), 3.23-3.15 (m, 8H), 3.07 (m, 2H), 2.85 (s, 12H), 2.05 (m, 4H). **¹³C NMR (75 MHz, D₂O)** δ (ppm) = 165.16, 163.6, 163.3, 162.9, 151.3, 143.5, 130.9, 128.1, 126.5, 124.9, 124.6, 122.2, 119.6, 118.2, 114.2, 110.3, 99.3, 85.0, 73.3, 71.4, 70.8, 66.6, 60.6, 55.2, 55.1, 49.7, 42.7, 38.0, 37.6, 37.0, 31.2, 22.7.

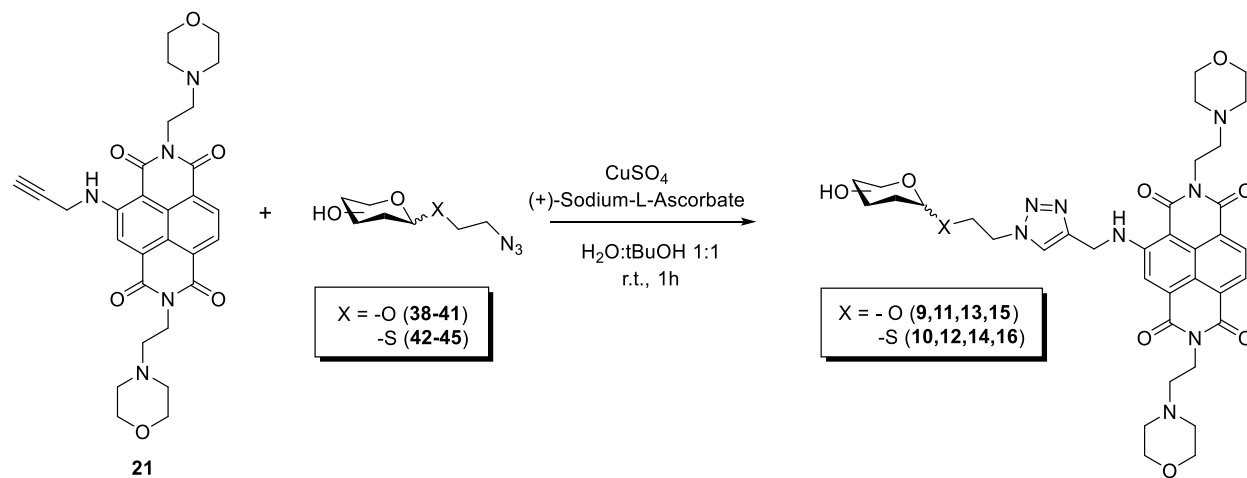
5*CF₃COOH: Red solid. Yield = 91 %. **¹H NMR (300 MHz, D₂O)** δ (ppm) = 8.21 (d, 1H, J = 7.8 Hz), 8.13 (s, 1H), 7.97 (d, 1H, J = 7.8 Hz), 7.88 (s, 1H), 4.79 (s, 1H), 4.63 (s, 2H), 4.25 (d, 1H, J = 7.9 Hz), 4.20 (m, 1H), 4.04 (bs, 4H), 3.74 (d, 1H, J = 3.3 Hz), 3.56-3.47 (m, 4H), 3.44 (d, 1H, J = 3.3 Hz), 3.33 (t, 1H, J = 7.9 Hz), 3.20-3.12 (m, 4H), 3.05 (d, 1H, J = 6.8 Hz), 2.82 (s, 12H), 2.05-2.03 (m, 4H). **¹³C NMR (75 MHz, D₂O)** δ (ppm) = 165.4, 163.9, 163.7, 163.3, 151.5, 143.5, 130.9, 128.3, 126.8, 124.7, 124.4, 122.3, 119.8, 118.5, 102.9, 99.4, 75.0, 72.4, 70.4, 69.9, 68.3, 67.9, 60.7, 55.1, 50.4, 42.6, 37.8, 37.6, 36.9, 22.7.

6*CF₃COOH: Red solid. Yield = 89 %. **¹H NMR (300 MHz, D₂O)** δ (ppm) = 8.18 (d, *J* = 9.0 Hz, 1H), 8.11 (s, 1H), 7.94 (d, *J* = 9.0 Hz, 1H), 7.83 (d, *J* = 12Hz, 1H), 4.80 (s, 4H), 4.22 (d, *J* = 9.0 Hz, 1H), 4.04 (m, 4H), 3.77 (d, *J* = 3 Hz, 1H), 3.57-3.55 (m, 2H), 3.50 – 3.42 (m, 2H), 3.33-3.15 (m, 7H), 2.85 (s, 6H), 2.83 (s, 6H), 2.63 (s, 1H), 2.09-2.01 (m, 4H), 1.97 (s, 1H). **¹³C NMR (75 MHz, D₂O)** δ (ppm) = 164.9, 163.4, 163.2, 162.7, 151.1, 130.6, 127.8, 126.3, 124.7, 124.2, 121.9, 118.07, 99.0, 85.3, 85.3, 78.5, 73.4, 69.1, 68.1, 60.6, 54.8, 54.8, 50.1, 42.3, 37.3, 36.6, 29.9, 22.3.

7*CF₃COOH: Red solid. Yield = 86 %. **¹H NMR (300 MHz, D₂O)** δ (ppm) = 8.18 (d, 1H, *J* = 7.8 Hz), 8.12 (s, 1H), 7.94 (d, 1H, *J* = 7.8 Hz), 7.80 (s, 1H), 4.77 (s, 2H), 4.61 (m, 2H), 4.20 (d, 1H, *J* = 8 Hz), 4.19-4.17 (m, 1H), 4.02 (m, 4H), 4.0-3.97 (m, 2H), 3.80 (d, 1H, *J* = 3.1 Hz), 3.66-3.62 (m, 3H), 3.50-3.45 (m, 3H), 3.36-3.23 (m, 3H), 3.22-3.14 (m, 4H), 3.11-2.91 (m, 2H), 2.83 (s, 12H), 2.08-2.0 (m, 4H). **¹³C NMR (75 MHz, D₂O)** δ (ppm) = 167.0, 165.4, 165.2, 164.7, 153.2, 143.6, 132.8, 130.0, 128.4, 126.9, 126.4, 24.0, 121.5, 120.2, 119.9, 116.0, 104.8, 103.8, 101.1, 80.8, 77.1, 76.2, 75.8, 74.3, 74.2, 72.4, 70.1, 69.7, 62.6, 61.8, 57.0, 56.9, 52.2, 44.5, 44.4, 39.7, 39.5, 38.9, 24.6.

8*CF₃COOH: Red solid. Yield = 74 %. **¹H NMR (300 MHz, D₂O)** δ (ppm) = 8.19 (d, 1H, *J* = 8.0 Hz), 8.13 (s, 1H), 7.96 (d, 1H, *J* = 8.0 Hz), 7.75 (s, 1H), 5.18 (s, 2H), 4.74 (m, 2H), 4.27 (d, 1H, *J* = 9.2 Hz), 3.89 (m, 4H), 3.66-3.35 (m, 12H), 3.18 (t, 1H, *J* = 9.2 Hz), 3.15 (bs, 4H), 3.11-2.98 (m, 2H), 2.77 (s, 12H), 1.93 (bs, 4H). **¹³C NMR (75 MHz, D₂O)** δ (ppm) = 165.0, 163.4, 163.1, 151.1, 148.6, 132.8, 130.0, 128.4, 126.9, 126.4, 24.0, 121.5, 120.2, 119.9, 116.0, 104.8, 99.7, 99.2, 85.2, 78.2, 77.1, 72.7, 72.6, 72.0, 71.5, 69.2, 69.1, 60.6, 60.3, 55.1, 55.0, 54.1, 50.4, 42.6, 42.3, 30.3, 22.7.

General Procedure for the synthesis of conjugates NDI-sugars 9-16



Scheme 7.8 – General Procedure for the click reaction between NDI 21 and sugars 38-45.

A 2 ml solution of (+)-sodium-L-ascorbate (7.3 mg, 0.04 mmol), copper(II) sulfate pentahydrate (0.9 mg, 0.006 mmol) and NDI 21 (20 mg, 0.04 mmol), in water, was added to azido-glyco-derivative 38-45 (0.06 mmol, 1.5 eq.), dissolved into 2 ml of *t*BuOH. The suspension was stirred at r.t. under nitrogen atmosphere for 2 hours. The resulting red solution was concentrated under vacuum and a red solid was obtained. The crude product was analysed and purified by reverse phase column chromatography, (CH₃CN: H₂O 0.1%TFA), with method 3P, described in the previous section.

9*CF₃COOH: Red solid. Yield = 81 %. **¹H NMR (300 MHz, D₂O)** δ (ppm) = 8.33 (d, *J* = 7.9 Hz, 1H), 8.11 (d, *J* = 6.43 Hz, 1H), 8.08 (s, 1H), 8.03 (s, 1H), 4.85 (s, 2H), 4.65-4.62 (m, 4H), 4.48-4.46 (m, 4H), 4.28 (d, *J* = 7.88 Hz, 1H), 4.06 (m, 6H), 3.74-3.69 (m, 10H), 3.51-3.46 (m, 6H), 3.30-3.22 (m, 6H), 3.03 (m, 2H), 1.26 (d, *J* = 6.68 Hz, 1H). **¹³C NMR (75 MHz, D₂O)** δ (ppm) = 165.5, 164.1, 164.0, 163.5, 163.0, 162.5, 151.7, 143.7, 131.2, 128.7, 126.9, 125.3, 124.7, 122.5, 121.9, 120.2, 118.8, 114.2, 102.2, 99.5, 75.7, 75.4, 72.8, 69.4, 67.8, 63.5, 60.5, 54.6, 54.3, 52.2, 50.4, 37.9, 34.7, 34.2.

10*CF₃COOH: Red solid. Yield = 83%. **¹H NMR (300 MHz, D₂O)** δ (ppm) = 8.40 (d, *J* = 7.9 Hz, 1H), 8.16 (d, *J* = 7.9 Hz, 1H), 8.10 (m, 2H), 4.90 (s, 2H), 4.60 (m, 4H) 4.50-4.49 (m, 4H), 4.19 (d, *J* = 9.88 Hz, 1H), 4.07 (m, 4H), 3.7-3.69 (m, 10H), 3.47 (m, 6H), 3.28-3.12 (m, 10H), 3.02 (d, *J* = 9.19 Hz, 1H). **¹³C NMR (75 MHz, D₂O)**, δ (ppm) = 168.7, 167.3, 166.7, 154.9, 134.5, 131.9, 130.1, 128.5, 127.9, 127.8, 125.7, 123.5, 122.0, 102.8, 88.1, 82.7, 79.9, 75.2, 72.2, 66.6, 63.7, 57.7, 57.3, 55.2, 53.5, 40.9, 37.6, 37.3, 33.1.

11*CF₃COOH: Red solid. Yield = 90 %. **¹H NMR (300 MHz, D₂O)** δ (ppm) = 8.3 (d, *J* = 7.83 Hz, 1H), 8.08 (s, 1H), 8.04 (d, *J* = 9.48 Hz, 1H), 4.84 (s, 2H), 4.78 (s, 1H), 4.65 (m, 4H), 4.59 (m, 2H), 4.42-4.41 (m, 4H), 3.86 (m, 8H), 3.67 (m, 1H), 3.48-3.31 (m, 20H). **¹³C NMR (75 MHz, D₂O)** δ (ppm) = 165.5, 164.2, 163.5, 160.8, 151.8, 136.5, 135.2, 131.2, 131.1, 130.6, 128.8, 124.6, 124.5, 122.6, 113.4, 103.5, 99.4, 99.3, 72.6, 70.2, 69.7, 66.1, 65.4, 63.7, 60.4, 60.4, 54.7, 54.3, 53.4, 53.4, 52.2, 50.1, 43.2, 43.1, 37.8, 34.9, 34.4, 33.9, 33.8.

12*CF₃COOH: Red solid. Yield = 75 %. **¹H NMR (300 MHz, D₂O)** δ (ppm) = 8.08 (d, *J* = 6 Hz, 1H), 8.05 (s, 1H), 7.85 (d, *J* = 4 Hz, 1H), 7.76 (s, 1H), 5.02 (s, 1H), 4.55 (m, 2H), 4.32 (m, 4H), 3.98-3.92 (m, 4H), 3.76 (s, 1H), 3.60-3.36 (m, 19H), 3.14-3.01 (m, 6H). **¹³C NMR (75 MHz, D₂O)** δ (ppm) = 165.4, 164.0, 163.9, 163.3, 151.7, 131.1, 128.6, 126.8, 125.2, 124.7, 122.4, 120.2, 118.7, 99.5, 84.8, 73.2, 71.4, 70.8, 66.6, 63.5, 60.6, 54.6, 54.2, 52.1, 49.6, 37.9, 34.6, 34.2, 30.9.

13*CF₃COOH: Red solid. Yield = 67 %. **¹H NMR (300 MHz, D₂O)** δ (ppm) = 8.23 (d, *J* = 7.9 Hz, 1H), 8.16 (s, 1H), 8.0 (d, *J* = 7.85 Hz, 1H), 7.93 (s, 1H), 4.8 (s, 2H), 4.66-4.63 (m, 4H), 4.45-4.43 (m, 4H), 4.28-4.26 (m, 3H), 4.08-4.04 (m, 6H), 3.78-3.46 (m, 17H), 3.37 (m, 2H), 3.22 (m, 4H). **¹³C NMR (75 MHz, D₂O)** δ (ppm) = 165.2, 163.9, 163.7, 163.2, 151.5, 143.3, 131.1, 128.4, 126.6, 125.0, 124.8, 124.7, 122.3, 120.1, 118.5, 118.0, 114.1, 102.9, 99.2, 75.0, 72.5, 70.5, 68.4, 67.9, 63.5, 60.8, 54.6, 54.3, 52.1, 50.4, 37.9, 34.6, 34.2.

14*CF₃COOH: Red solid. Yield = 80 %. **¹H NMR (300 MHz, D₂O)** δ (ppm) = 8.3 (d, *J* = 7.89 Hz, 1H), 8.13 (s, 1H), 8.07 (d, *J* = 7.86 Hz, 1H), 7.99 (s, 1H), 4.85 (s, 2H), 4.7 (m, 4H), 4.46-4.44 (m, 4H), 4.24-4.21 (d, *J* = 9.47 Hz, 1H), 4.05 (m, 4H), 3.79-3.10 (m, 23H). **¹³C NMR (75 MHz, D₂O)** δ (ppm) = 168.5, 167.1, 167.0, 166.4, 154.7, 146.5, 134.2, 131.7, 129.9, 128.3, 127.7, 125.5, 123.4, 122.0, 121.8, 121.1, 117.2, 102.5, 88.7, 81.9, 76.7, 72.5, 71.5, 66.5, 63.9, 57.7, 57.3, 57.2, 55.2, 53.5, 45.4, 40.9, 37.6, 37.2, 33.2, 20.6, 19.1, 15.0.

15*CF₃COOH: Red solid, Yield = 77 %. **¹H NMR (300 MHz, D₂O)** δ (ppm) = 8.3 (d, *J* = 7.88 Hz, 1H), 8.08-8.05 (m, 2H), 7.95 (s, 1H), 5.02 (d, *J* = 3.59 Hz, 1H), 4.84 (s, 2H), 4.7-4.62 (m, 6H), 4.43-4.4 (m, 4H), 4.28 (d, *J* = 9.84 Hz, 2H), 3.88 (m, 8H), 3.68 (d, *J* = 10.1 Hz, 1H), 3.52-3.2 (m, 28H), 2.97 (m, 1H). **¹³C NMR (75 MHz, D₂O)** δ (ppm) = 165.4, 164.0, 164.0, 163.4, 151.7, 131.2, 128.6, 126.8, 125.3, 125.0, 124.7, 122.5, 120.4, 118.7, 99.7, 99.6, 85.1, 78.1, 77.1, 77.0, 72.7, 72.6, 72.1, 71.4, 69.1, 63.7, 63.7, 60.6, 60.3, 54.6, 54.2, 52.2, 50.3, 37.9, 34.8, 34.4, 30.4, 30.1.

16*CF₃COOH: Red solid, Yield = 70%. **¹H NMR (300 MHz, D₂O)** δ (ppm) = 8.22 (d, *J* = 12 Hz, 1H), 8.03 (s, 1H), 7.98 (d, *J* = 8.0 Hz, 1H), 7.87 (s, 1H), 5.00 (d, *J* = 4.0 Hz, 1H), 4.76 (m, 2H), 4.57 (s, 2H), 4.38 (s, 4H), 4.24 (d, *J* = 10 Hz, 1H), 4.02-3.96 (m, 4H), 3.64-2.91 (m, 28H), 2.95 (t, *J* = 10 Hz, 2H). **¹³C NMR (75 MHz, D₂O)** δ (ppm) = 165.5, 164.1, 164.0, 163.5, 163.0, 162.5, 151.8, 143.6, 131.3, 128.7, 126.9, 125.3, 125.0, 124.8, 122.6, 120.5, 118.8, 118.1, 114.2, 99.8, 99.6, 85.2, 78.2, 77.2, 77.1, 72.7, 72.6, 72.1, 71.5, 69.2, 63.6, 60.7, 60.4, 54.7, 54.3, 52.2, 50.4, 38.0, 34.7, 34.2, 30.4.

7.2.2 Cell Culture

Human MRC5-cell line (fibroblast derived from lung tissue) was cultured in DMEM (Invitrogen) medium plus 10% Fetal Bovine Serum Albumin (FBSA), 2 mM Gluthamine and 100 U/ml penicillin. Cells were grown in monolayer (5% CO₂, 37°C) in DMEM medium with 4.5 g/L of glucose for HT29 and 1 g/L for MRC5. Cells were plated and passaged according to ATCC recommendations and were used for the experiments while in the exponential growth phase.

'Single marker' (S16) BSF *Trypanosoma Brucei* (Lister 427, antigenic type MiTat 1.2, clone 221a) were cultured at 37°C, 5% CO₂ in HMI-9 medium supplemented with 20% heat-inactivated fetal bovine serum (hiFBS, Invitrogen). *Leishmania Major* (MHOM/IL/80/Friedlin) promastigotes were cultured at 28 °C in RPMI-1640 medium (Invitrogen, Carlsbad, CA) modified with fetal bovine serum (hiFBS, Invitrogen).

7.2.3 Citotoxicity Assays

- **MTT Test on cells:** Toxicity against cells has been determined through incubation of 4*10⁶ HT29 cells and MRC5 cells in 96-wells plates, in 100 µl of DMEM solution, with increasing concentrations of selected compounds. Cells were stored at 37°C (with 5% CO₂) for 72 hours. After this time, IC₅₀ values were measured through MTT (3-(4,5-Dimethylthiazol-2-yl)-2,5-Diphenyltetrazolium Bromide) assay: briefly, reduction of MTT to insoluble formazan by cellular oxidoreductase enzymes allow the evaluation of cellular viability, through spectrophotometric analysis of formazan absorbance. After 3 days of incubation, 10 µl of 5 mg/ml solution of MTT were added to each well, then solution were centrifugated and stored at 37°C for 4 hours. Cell media was removed and cells were dissolved into 100 µl of DMSO, then analyzed at the plate reader, recording the absorbance at λ= 590 nm.
- **MTT Test on Leishmania Major:** Activity of compounds against Leishmania Major has been determined upon incubation of 2*10⁵ parasites, in 96-wells plates, in 100 µl of culture media, in presence of increasing concentrations of compounds. After an incubation period of 3 days, 10 µl of 5mg/ml of MTT solution were added to each well, then parasites were stored for further 4 hours at 28°C. Then, each solution was treated with 50 µl of 20% Sodium Dodecyl Sulphate and incubated at 37°C overnight. In the end, all plates were analyzed at the plate reader, recording the absorbance at λ = 590 nm.
- **Alamar Blue Assay on Trypanosoma Brucei:** Toxicity on *T. Brucei* was determined through incubation of 3*10⁵ parasites in 96-wells plates, in 100 µl of solutions, adding increasing concentrations of ligands. After 3 days of incubation at 37°C, Alamar Blue Assay (or Resazurin Assay) was performed to measure IC₅₀ values: briefly, Resazurin is reduced by the metabolic activity of parasites, forming fluorescent derivative Resorufin. In details, 20 µl of Alamar Blue solution (5 g/L) were added to each

plate, then they were incubated at 37°C for 4 hours. Later, 50 µl of sodium dodecyl sulfate solution (3%) were added to each well, then plates were incubated again for one hour at 37°C. In the end, fluorescence analysis of each solution was performed with plate reader.

- **Cellular permeability:** Cellular uptake was determined through confocal microscopy analysis. In details, $2,25 \times 10^5$ cells were incubated with NDIs (10 µM) in 750 µl of DMEM medium, at 37°C, for 2 hours. After this time, solutions were centrifuged, the supernatant was removed and cells resuspended in 750 µl of sodium dodecyl sulfate (0.4%). Fluorescence was detected with a TECAN infinite F200 fluorescence-intensity multiplate reader (excitation wavelength: 485 nm, emission wavelength: 535 nm). Fluorescence values were normalized via protein quantification assay using Pierce BCA test (ThermoFisher Scientific) and concentration values were extrapolated from a fluorescence – NDI-concentration calibration curve.

7.2.4 FRET-Melting Assay

FRET Melting assays were performed on Stratagene MX3005P qPCR, with a procedure previously described in literature²⁰⁵. All oligonucleotides were annealed for 2 minutes at 90°C before the experiment. Analysis were performed on DNA concentrations equal to 0.2 µM, in presence of 10 mM LiCaco, 10 mM of KCl, LiCl 90 mM and 1 or 2 µM of ligand. Data processing was carried out using Origin 9, with ΔT_{\max} used to represent ΔT_m . For the experiment, the following oligonucleotide sequence was employed:

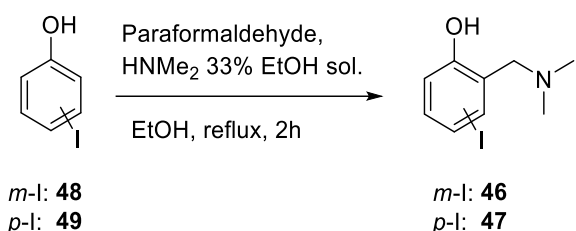
F21T (Human Telomeric G4): 5'-FAM-GGGTTAGGGTTAGGGTTAGGGTAMRA-3'

7.3 Quinone Methides

7.3.1 Bi-Functional Photo-Alkylating Ligands: Experimental Details

7.3.1.1 Synthesis and Characterization of Compounds

Synthesis of 2-((dimethylamino)methyl)iodophenols **46** and **47**



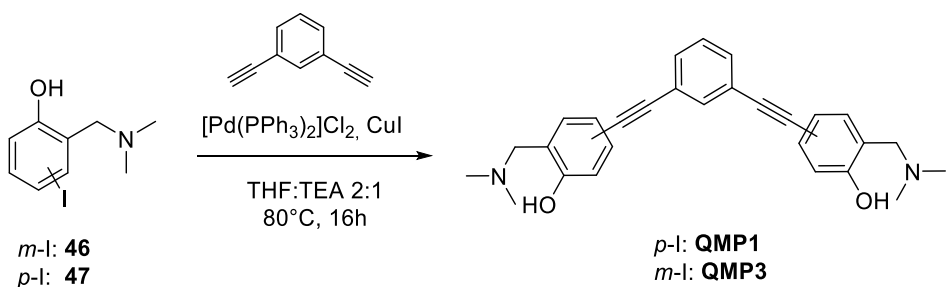
Scheme 7.9 – Mannich reaction for the synthesis of **46 and **47**.**

In a round bottomed flask, iodophenol **48** or **49** (11 mmol, 1 eq.) have been dissolved into 140 ml of EtOH, then 6 g (0.2 mol, 18 eq.) of paraformaldehyde and 14 ml of dimethylamine in 33% ethanol solution were added. Mixture was refluxed two hours, then solvent was removed under vacuum. Product has been isolated through purification on column chromatography, using DCM: MeOH 95:5 as eluent.

46: Yield (%) = 40%. The compound was fully characterized according to the literature²⁰⁶.

47: Yield (%) = 55%. The compound was fully characterized according to the literature²⁰⁶.

Synthesis of QMP1 and QMP3:



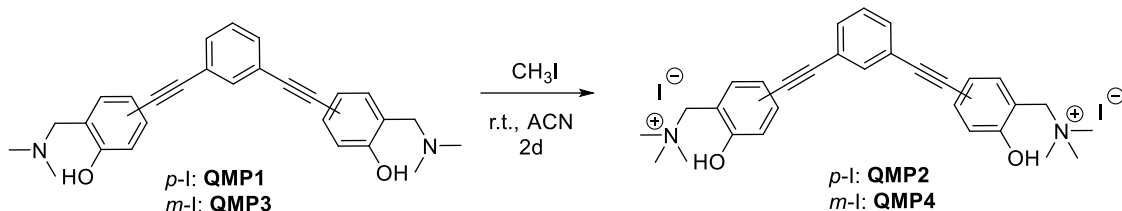
Scheme 7.10 – Synthesis of QMP1 and QMP3.

The previously synthesized 2-((dimethylamino)methyl)-4-iodophenol (0.61 mmol, 3 eq.), Bis(triphenylphosphine) palladium chloride [Pd(PPh₃)₂]Cl₂ (0.06 mmol, 10%), copper iodide (0.06 mmol, 10%) and 1,3-diethynylbenzene (0.2 mmol, 1 eq.) were introduced into a three-necked flask, and stored under argon flux for 5 minutes. Then, 36 ml of THF:Triethylamine 2:1 solution were added to the mixture with a syringe, then the resulting solution was heated 60°C and stirred for 16 hours. Once substrate was completely consumed, solvent was removed under vacuum and the crude was filtered on silica gel. The resulting mixture was purified through reverse phase column chromatography, with method **4P**.

QMP1: Yield (%) = 39%. **¹H-NMR (300 MHz, CDCl₃)** δ (ppm) = 10.28 (bs, 2H), 7.65 (s, 1H), 7.45–7.28 (m, 5H), 7.19 (d, *J* = 1.7 Hz, 2H), 6.84 (d, *J* = 8.4 Hz, 2H), 3.66 (s, 4H), 2.36 ppm (s, 12H). **¹³C-NMR (75 MHz, CDCl₃)** δ (ppm) = 158.7, 134.0, 132.4, 131.7, 130.5, 128.3, 123.9, 121.9, 116.3, 113.1, 90.1, 86.8, 62.3, 44.3.

QMP2: Yield (%) = 20%. **¹H-NMR (300 MHz, CDCl₃)** δ (ppm) = 8.64 (bs, 2H), 7.71 (s, 1H), 7.49 (d, *J* = 7.8 Hz, 2H), 7.34 (t, *J* = 7.3 Hz, 1H), 7.02–6.96 (m, 6H), 3.67 (s, 4H), 2.35 ppm (s, 12H). **¹³C-NMR (75 MHz, CDCl₃)** δ (ppm) = 159.7, 136.3, 132.9, 130.1, 130.0, 125.4, 124.9, 124.5, 124.3, 120.7, 91.7, 89.9, 64.4, 46.2.

Synthesis of QMP2 and QMP4:



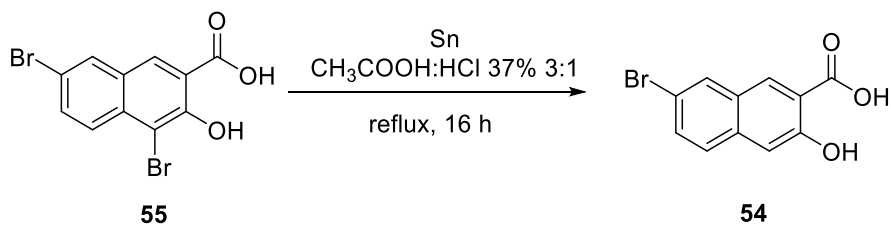
Scheme 7.11 – Synthesis of QMP2 and QMP4.

Iodomethane (0.23 mmol, 5 eq.) was added, in one portion, to a stirred solution of **QMP1** or **QMP2** (0.047 mmol, 1 eq.) dissolved into 1 ml of ACN, in presence of sodium acetate (0,08 mmol, 2 eq.). Reaction mixture was stirred at room temperature for two days. In order to favour product formation, after one day, another addition of iodomethane (0.23 mmol, 5 eq.) was done. After complete substrate consumption, products were isolated through reverse phase column chromatography, with method **4P**.

QMP2: Yield (%) = 97%. **¹H-NMR (300 MHz, CD₃OD)** δ (ppm) = 7.67 (s, 2H), 7.65 (s, 1H), 7.60–7.56 (m, 2H), 7.5–7.49 (m, 3H), 7.04–6.97 (m, 2H), 4.6 (s, 4H), 3.2 (s, 18H). **¹³C-NMR (75 MHz, CD₃OD)** δ (ppm) = 159.5, 139.4, 137.2, 135.3, 132.3, 130.2, 125.4, 117.9, 116.6, 116.0, 90.4, 88.7, 65.2, 53.9.

QMP4: Yield (%) = 98%. **¹H-NMR (300 MHz, CD₃OD)** δ (ppm) = 7.70 (s, 1H), 7.59 (s, 1H), 7.56–7.49 (m, 4H), 7.18–7.16 (m, 4H), 4.60 (s, 4H), 3.19 (s, 18H). **¹³C-NMR (75 MHz, CD₃OD)** δ (ppm) = 159.0, 136.3, 135.7, 133.2, 130.5, 128.6, 124.9, 124.5, 120.1, 116.8, 90.8, 90.3, 65.4, 54.0, 53.9.

Synthesis of 7-bromo-3-hydroxy-2-naphthoic acid **54**:

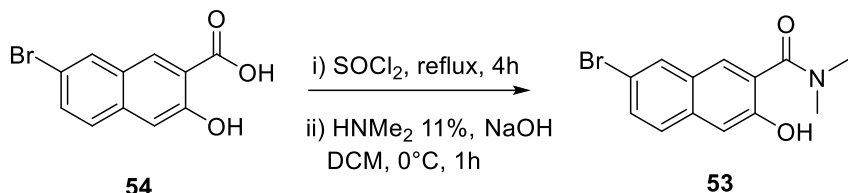


Scheme 7.12 – Reductive dehalogenation for the synthesis of **54.**

In one-necked flask, 4,7-dibromo-3-hydroxy-2-naphthoic acid **55** (0.014 mol, 1 eq.) was suspended in 76 ml of CH₃COOH: HCl 37% 3:1 solution, then tin powder (0.014 mol, 1.3 eq.) was added. Reaction mixture was stirred at reflux for 16 hours, then was cooled at room temperature until precipitation of a yellow solid. Product was filtered on a Buchner funnel and used for the subsequent step with no further purification.

54: Yield (%) = 94%. The compound was fully characterized according to the literature²⁰⁷.

Synthesis of 7-bromo-3-hydroxy-N,N-dimethyl-2-naphthamide 53:

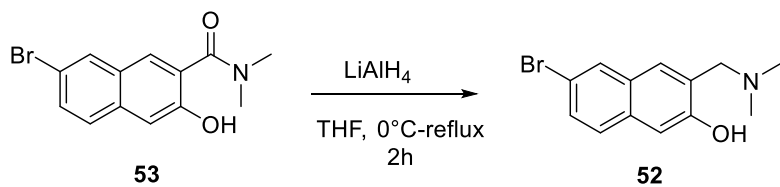


Scheme 7.13 – Two-step procedure for the synthesis of 55.

Bromo-3-hydroxynaphthalene-2-carboxylic acid **54** (0.0075 mol, 1 eq.) was dissolved into 20 ml of thionyl chloride, the reaction mixture was stirred at 80°C for four hours. Later, thionyl chloride was removed under vacuum, with a water pump, collecting the condensed liquid with a cold finger. The obtained red solid was dissolved into 8 ml of dichloromethane. In the meantime, in one-necked flask, sodium hydroxide (0.009 mol, 1.2 eq.) was dissolved in 30 ml (0.9 mol, 100 eq.) of dimethylamine solution (11% in ethanol) and cooled to 0°C with an ice bath. Acyl chloride was transferred into a dropping funnel and added dropwise to dimethylamine solution. Reaction mixture was stirred for one hour at 0°C , then 100 ml of HCl 10% were added to induce product precipitation. Suspension was filtered in a Buchner funnel and 2.01 g of product were collected and used for the subsequent step without no further purification.

53: Yield (%) = 93%. **$^1\text{H-NMR}$ (300 MHz, DMSO- d_6)** δ (ppm) = 10.35 (s, 1H), 8.09 (s, 1H), 7.71 (m, 2H), 7.52 (d, J = 8.86 Hz, 1H), 7.23 (s, 1H), 3.00 (s, 3H), 2.80 (s, 3H). **$^{13}\text{C-NMR}$ (75 MHz, DMSO- d_6)** δ (ppm) = 167.8, 152.0, 132.8, 129.5, 129.0, 128.5, 128.1, 126.4, 115.9, 109.2, 37.6, 34.1.

Synthesis of 6-bromo-3-((dimethylamino)methyl)naphthalen-2-ol 52:

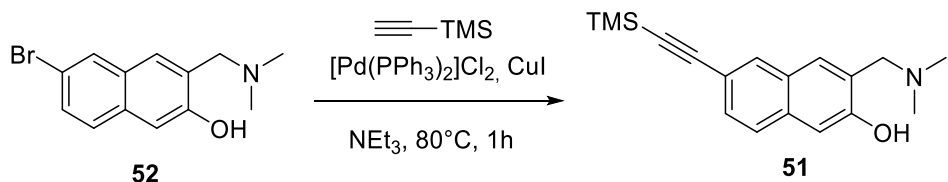


Scheme 7.14 – Reduction with lithium aluminium hydride to synthesize 52.

7-bromo-3-hydroxy-N,N-dimethyl-2-naphthamide **53** (30.2 mmol, 1 eq.) was suspended in anhydrous THF (250 mL) and the mixture was cooled at 0°C . Lithium aluminium hydride (75.5 mmol, 2.5 eq.) was added in one portion under stirring and the reaction mixture was heated at 70°C and refluxed for 2 hours. Hence, the mixture was cooled in an ice bath and quenched with a saturated aqueous NaHCO_3 solution (100 mL). The organic solvent was removed under reduced pressure and the aqueous phase was extracted with DCM (3x50 mL). The combined organic phases were washed with brine and dried over Na_2SO_4 . The solvent was removed under reduced pressure, and the residue was purified by recrystallization in ethanol.

52: Yield (%) = 96%. **¹H-NMR (300 MHz, DMSO-d₆)** δ (ppm) = 8.11 (s, 1H), 7.77–7.72 (m, 2H), 7.57 (d, *J* = 8.79 Hz), 7.24 (s, 1H), 3.85 (s, 2H), 2.39 (s, 6H). **¹³C-NMR (75 MHz, DMSO-d₆)** δ (ppm) = 156.1, 132.4, 129.0, 128.8, 128.7, 128.6, 128.0, 127.3, 126.9, 115.3, 111.6, 109.0, 60.4, 44.3.

Synthesis of 3-((dimethylamino)methyl)-6-((trimethylsilyl)ethynyl)naphthalen-2-ol **51**:

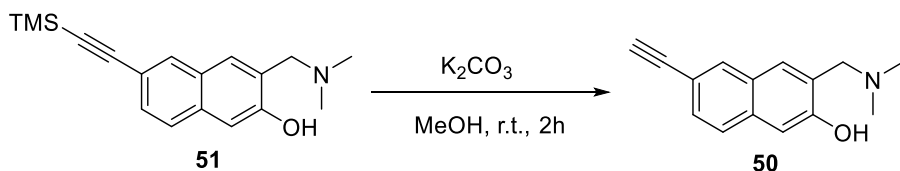


Scheme 7.15 – Sonogashira Cross-coupling for the synthesis of **51.**

In a three-necked flask, 6-bromo-3-((dimethylamino)methyl)naphthalene-2-ol **52** (1.78 mmol, 1 eq.), $PdCl_2(PPh_3)_2$ (4% mol), copper (I) iodide (4% mol) were stored under argon flux for 10 minutes. Then, trimethylsilylacetylene (2.68 mmol, 1.5 eq.) was dissolved in triethylamine (20 mL), degassed with Ar for 5 minutes, and added in the reaction flask. The mixture was stirred at $80^\circ C$ for 1 hour, then was filtered through a thin pad of celite, washed with chloroform (3x20 mL), and the solvent was removed under reduced pressure. The crude was purified by flash chromatography with Cyclohexane/AcOEt gradient.

51: Yield (%) = 86%. **¹H-NMR (300 MHz, CDCl₃)** δ (ppm) = 7.86 (s, 1H), 7.60 (d, *J* = 8.5 Hz, 1H), 7.46–7.39 (m, 2H), 7.16 (s, 1H), 3.83 (s, 2H), 2.40 (s, 6H), 0.30 (s, 9H); **¹³C-NMR (75 MHz, CDCl₃)** δ (ppm) = 157.0, 134.1, 131.4, 128.7, 127.3, 127.2, 126.0, 125.2, 117.3, 110.3, 105.9, 93.2, 62.7, 44.3, 0.0.

Synthesis of 3-((dimethylamino)methyl)-6-ethynylnaphthalen-2-ol **50**:

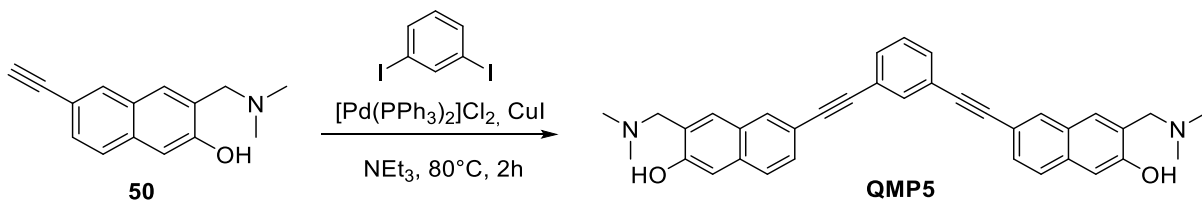


Scheme 7.16 – Trimethylsilyl basic deprotection to synthesize **50.**

3-((dimethylamino)methyl)-6-((trimethylsilyl)ethynyl)naphthalen-2-ol **51** (1.34 mmol, 1 eq.) was dissolved in methanol (25 mL) and potassium carbonate (5.36 mmol, 4 eq.) was added in one portion. The suspension was stirred at room temperature for 2 hours. The solvent was removed under reduced pressure, the crude was treated with 1% HCl (10 mL) and neutralized with $NaHCO_3$. The product was extracted in DCM (3x20 mL), the combined organic phases were dried over Na_2SO_4 and the solvent was removed under reduced pressure. The crude was purified by flash chromatography with Cyclohexane/AcOEt gradient.

50: Yield (%) = 59%. **¹H-NMR (300 MHz, CDCl₃)** δ (ppm) = 9.85 (s, 1H), 7.88 (s, 1H), 7.63 (d, *J* = 8.5 Hz, 1H), 7.45 (d, *J* = 7.8, 1H), 7.44 (s, 1H), 7.17 (s, 1H), 3.82 (s, 2H), 3.11 (s, 1H), 2.38 ppm (s, 6H). **¹³C-NMR (75 MHz, CDCl₃)** δ (ppm) = 156.9, 133.9, 131.3, 128.3, 128.0, 126.9, 125.8, 125.1, 115.8, 109.9, 84.0, 76.0, 62.5, 44.0.

Synthesis of QMP5:

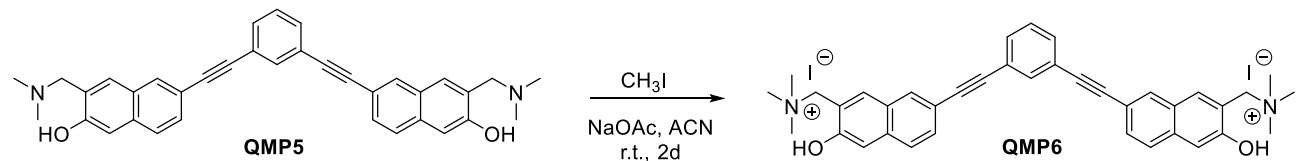


Scheme 7.18 – Sonogashira cross-coupling for the synthesis of QMP5.

In a three-necked flask, 1,3-diiodobenzene (0.22 mmol, 0.5 eq.), $PdCl_2(PPh_3)_2$ (0.018, 4% mol), copper (I) iodide (0.018, 4% mol) were kept under argon atmosphere for 10 minutes, then 3-((dimethylamino)methyl)-6-ethynylnaphthalen-2-ol **50** (0.44 mmol, 1 eq.) was dissolved in triethylamine (10 mL), degassed with argon for 5 minutes and added in the flask. The reaction mixture was stirred at $80^\circ C$ for 2 hours. The suspension was dissolved in DCM (25 mL) and washed with 1% $NaHCO_3$ (3x20 mL). The organic phase was dried over Na_2SO_4 and the solvent was removed under reduced pressure. The crude was purified by reverse phase HPLC (H_2O 0.1% TFA/ACN gradient) with method **4P**.

QMP5: Yield (%) = 81%. **¹H-NMR (300 MHz, DMSO-d₆)** δ (ppm) = 8.06 (s, 2H), 7.77–7.74 (m, 5H), 7.62 (d, *J* = 7.2 Hz, 2H), 7.53–7.49 (m, 3H), 7.19 (s, 2H), 3.89 (s, 4H), 2.39 ppm (s, 12H); **¹³C-NMR (75 MHz, DMSO-d₆)** δ (ppm) = 156.6, 133.8, 133.7, 131.2, 131.1, 129.4, 128.7, 128.2, 127.0, 126.3, 125.9, 123.2, 116.0, 109.2, 91.0, 87.8, 59.6, 44.0.

Synthesis of QMP6:



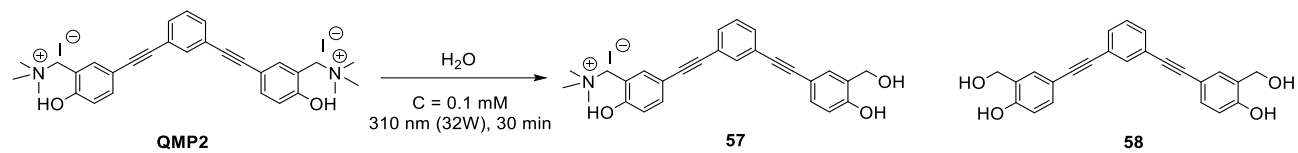
Scheme 7.19 – Synthesis of QMP6.

Iodomethane (0.9 mmol, 5 eq.) and sodium acetate (0.36 mmol, 2 eq.) were added to a stirred solution of **QMP5** (0.18 mmol) in 1 ml of ACN and the reaction mixture was stirred at room temperature for 24 hours. After this time, further iodomethane (0.9 mmol, 5 eq.) was added and the suspension was stirred at room temperature for additional 16 hours. Hence, the solvent and excess iodomethane were removed under

reduced pressure. The product was purified by reverse phase HPLC (H_2O 0.1% TFA/ACN gradient) with method **4P**.

QMP6: Yield (%) = 68%. **$^1\text{H-NMR}$ (300 MHz, CD_3OD)** δ (ppm) = 8.06 (s, 4H), 7.73–7.69 (m, 3H), 7.59–7.52 (m, 4H), 7.41 (dd, $J=8.3, 7.0$ Hz, 1H), 7.33 (s, 2H), 4.72 (s, 4H), 3.21 (s, 18H). **$^{13}\text{C-NMR}$ (75 MHz, CD_3OD)**: δ (ppm)= 156.7, 137.4, 137.0, 135.5, 133.3, 132.7, 131.6, 130.3, 129.0, 127.7, 125.4, 119.7, 119.6, 111.6, 91.5, 89.7, 65.6, 53.9.

Synthesis of Photoproducts **57** and **58**:



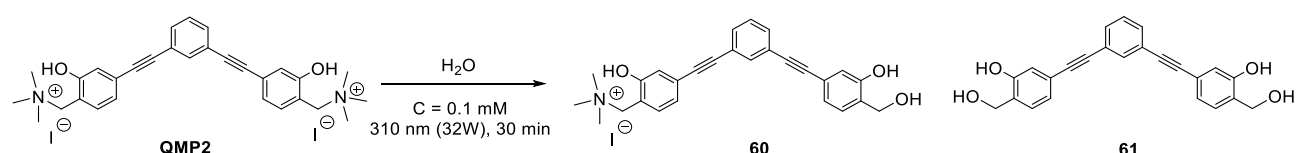
Scheme 5.20 -Photogeneration of water-adducts **57** and **58**.

Compound **QMP2** (0.02 mmol) has been dissolved into 200 ml of distilled water, to achieve concentration of 0.1 mM. Solution has been transferred into a quartz tube and irradiated with Rayonet at 310 nm (32W, 2 lamps) for 30 minutes. Then solvent removed under vacuum and crude was purified through reverse phase HPLC (H_2O 0.1% TFA/ACN gradient) with method **4P**.

57: Yield (%) = 62%. **$^1\text{H-NMR}$ (300 MHz, DMSO-d_6)** δ (ppm) = 10.96 (s, 1H), 9.91 (s, 1H), 7.66–7.45 (m, 7H), 7.27–7.26 (m, 1H), 7.05 (d, $J=8.51$ Hz, 1H), 6.82 (d, $J=8.3$ Hz, 1H), 4.48 (s, 2H), 4.4.46 (s, 2H), 3.07 (s, 9H). **$^{13}\text{C-NMR}$ (75 MHz, DMSO-d_6)** δ (ppm) = 158.1, 158.0, 155.0, 138.0, 135.3, 131.0, 130.9, 130.6, 129.4, 129.3, 123.7, 123.1, 116.8, 115.5, 114.9, 112.7, 111.8, 91.3, 89.7, 87.2, 86.1, 62.6, 57.7, 52.2, 47.7.

58: Yield (%) = 8%. **$^1\text{H-NMR}$ (300 MHz, DMSO-d_6)** δ (ppm) = 9.95 (s, 2H), 7.60 (s, 1H), 7.50–7.40 (m, 5H), 7.28 (d, $J=8.29$ Hz, 2H), 6.81 (d, $J=8.27$ Hz, 2H), 4.48 (s, 4H). **$^{13}\text{C-NMR}$ (75 MHz, DMSO-d_6)** δ (ppm) = 163.0, 157.9, 155.0, 152.1, 133.2, 130.9, 130.7, 130.6, 129.4, 129.2, 123.6, 114.9, 111.9, , 99.7, 90.6, 86.3, 60.1, 57.7, 56.2.

Synthesis of Photoproducts **60** and **61**:



Scheme 7.21 – Photogeneration of water-adducts **60** and **61**.

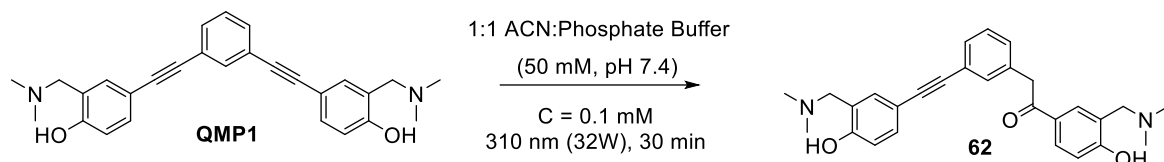
Compound **QMP4** (0.2 mmol) has been dissolved into 250 ml of distilled water, to achieve concentration of 1 mM. Solution has been transferred into a quartz tube and irradiated with Rayonet at 310 nm (32W, 2 lamps)

for one hour. Then solvent removed under vacuum and crude was purified through reverse phase HPLC (H_2O 0.1% TFA/ACN gradient) with method **4P**.

60: Yield (%) = 12%. **¹H-NMR (300 MHz, DMSO-d₆)** δ (ppm) = 10.79 (s, 1H), 7.73 (s, 1H), 7.62-7.43 (m, 4H), 7.36 (d, *J*= 8.29 Hz, 1H), 7.15-7.13 (m, 2H), 7.03 (d, *J*= 8.70 Hz, 1H), 6.94 (s, 1H), 4.50 (s, 2H), 4.47 (s, 2H), 3.05 (s, 9H). **¹³C-NMR (75 MHz, DMSO-d₆)** δ (ppm) = 157.3, 154.0, 135.1, 133.9, 131.8, 131.5, 130.6, 129.4, 127.4, 125.3, 123.2, 122.5, 122.3, 120.4, 118.4, 116.8, 115.9, 90.6, 89.2, 87.1, 62.7, 57.9, 52.1.

61: Yield (%) = 5%. **¹H-NMR (300 MHz, DMSO-d₆)** δ (ppm) = 9.73 (s, 2H), 7.69 (s, 1H), 7.57 (d, *J*= 7.2 Hz, 2H), 7.50-7.44 (m, 1H), 7.35 (d, *J*= 7.8 Hz, 2H), 7.03 (d, *J*= 7.77 Hz, 2H), 6.93 (s, 2H), 4.50 (s, 4H). **¹³C-NMR (75 MHz, DMSO-d₆)** δ (ppm) = 161.1, 153.9, 133.7, 131.3, 130.5, 129.3, 127.4, 123.1, 122.3, 120.5, 116.8, 90.5, 87.3, 57.9.

Synthesis of Hydrated alkyne **62**:



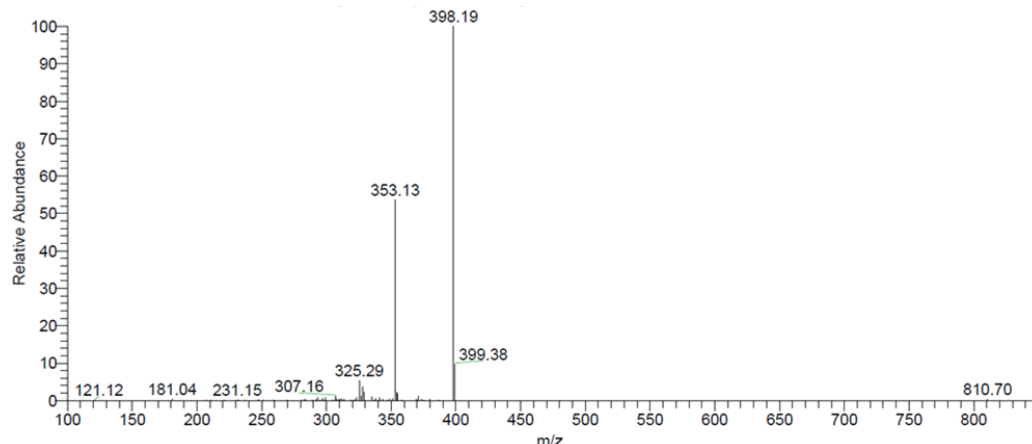
Scheme 7.22 – Photogeneration of hydrated alkyne **62.**

Compound **QMP1** (0.13 mmol) has been dissolved into 200 ml of 1:1 ACN: phosphate buffer (50mM, pH 7.4), to achieve concentration of 7 mM. Solution has been transferred into a quartz tube and irradiated with Rayonet at 310 nm (32W, 2 lamps) for one hour. Then solvent removed under vacuum and crude was purified through reverse phase HPLC (H_2O 0.1% TFA/ACN gradient) with method **4P**.

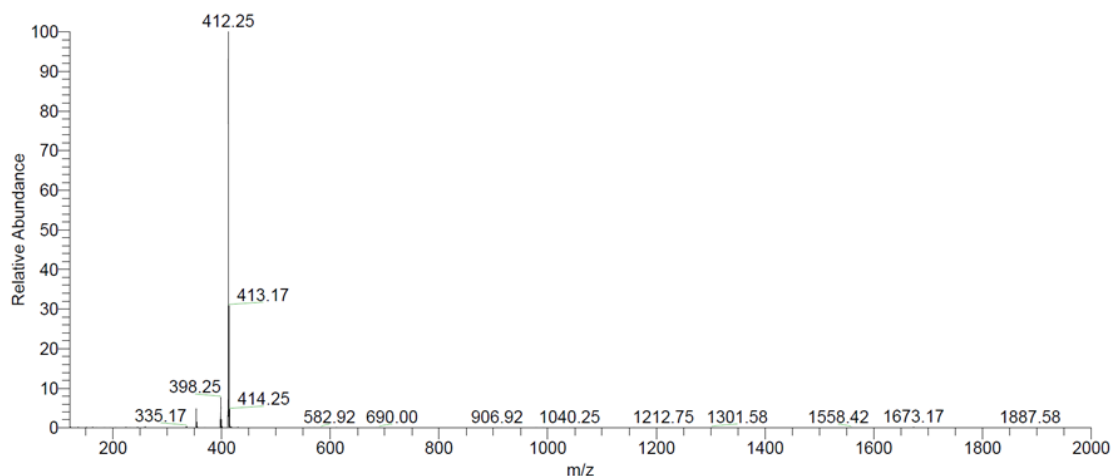
62: Yield (%) = 80%. **¹H-NMR (300 MHz, DMSO-d₆)** δ (ppm) = 8.36 (s, 1H), 8.04-8.01 (m, 1H), 7.79-7.75 (m, 1H), 7.66-7.60 (m, 1H), 7.52-7.51 (m, 2H), 7.22-7.14 (m, 2H), 7.03 (m, 2H), 6.95-6.92 (m, 1H), 4.35 (s, 2H), 4.12 (s, 2H), 4.19 (s, 2H), 2.76 (s, 6H), 2.74 (s, 6H). **¹³C-NMR (75 MHz, DMSO-d₆)** δ (ppm) = 197.3, 158.1, 157.7, 157.5, 155.2, 136.8, 136.1, 135.3, 134.4, 133.8, 132.6, 130.6, 129.4, 128.2, 125.4, 123.1, 117.6, 116.4, 116.2, 115.5, 112.4, 90.1, 87.0, 55.2, 54.6, 42.3, 42.1, 34.3.

ESI-MS Data for Photoproducts 56-63:

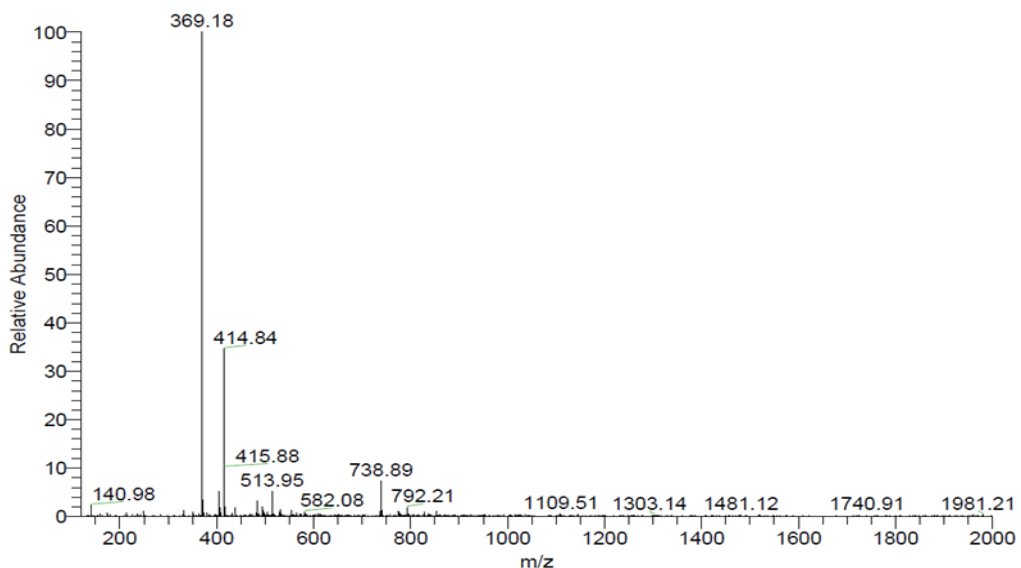
56. Mol. Wt: 397.47 u.m.a. (Positive mode)



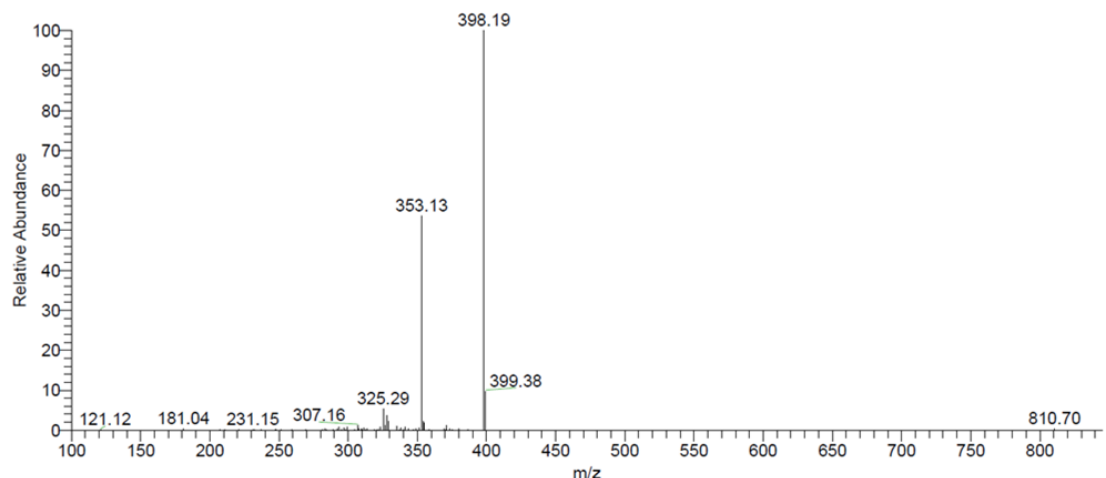
57. Mol. Wt: 412.51 u.m.a. (Positive mode)



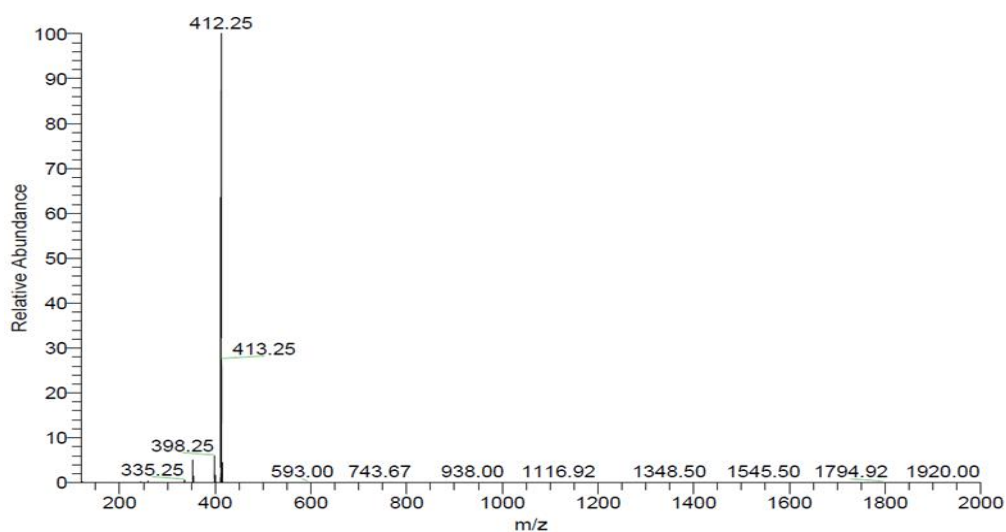
58. Mol. Wt: 370.40 (Negative mode)



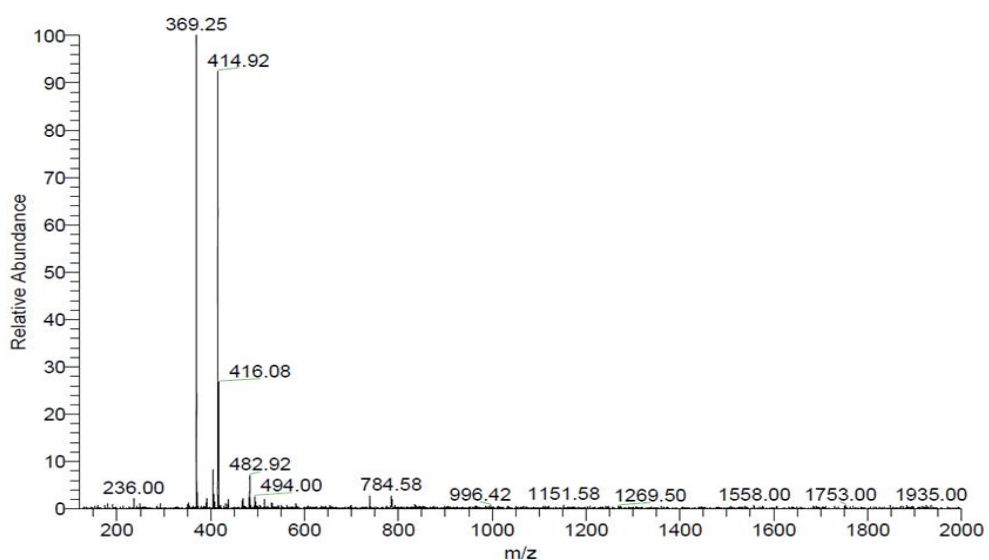
59. Mol. Wt: 397.47 u.m.a. (Positive mode)



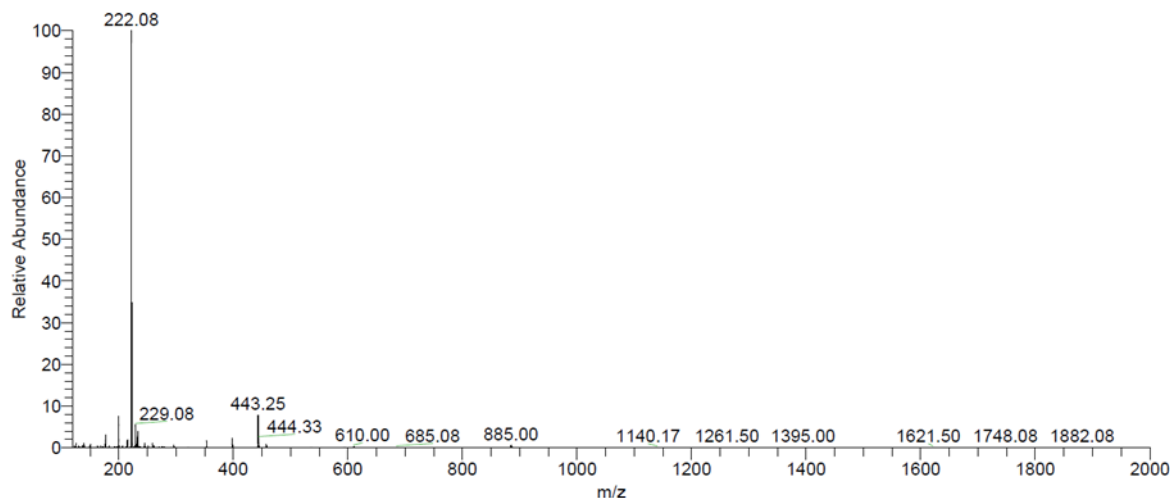
60. Mol. Wt: 412.51 u.m.a. (Positive mode)



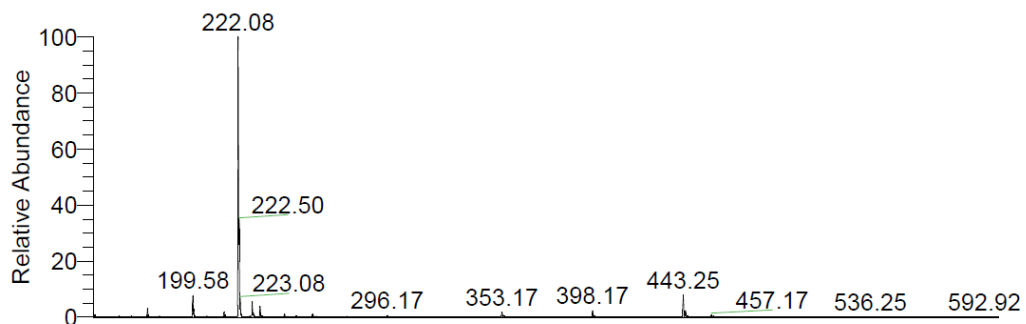
61. Mol. Wt: 370.4 u.m.a. (Negative Mode)



62. Mol Wt.: 442.46 u.m.a. (Positive Mode)



63. Mol Wt.: 442.46 u.m.a. (Positive Mode)



7.3.1.2 Photochemical Quantum Yields:

Reaction quantum yields (Φ) were obtained by irradiating a 3mL solution (1:1 ACN:PBS 50mM pH=7.4) of **QMP1-QMP6** (concentration 10^{-4} to 10^{-5}) in a 1 cm optical path cuvette and monitoring the consumption of the QMP by reverse-phase HPLC, using method **4A**, described in the previous section. Lamp source was a focalized 150 W high-pressure mercury arc equipped with a transmittance filter (transmission 313nm) and a single-photon detector (photon flux $q_p=2.6 \times 10^{-7}$ Einstein/cm $^2 \cdot$ min $^{-1}$). Calibration of the apparatus was performed using the photochemical decomposition of potassium ferrioxalate as actinometer. Conversion of substrate was measured through HPLC analysis, at different time of irradiation.

7.3.1.3 FRET-Melting Experiments

Fret melting experiments were performed using fluorophore-labelled oligonucleotide sequences, with FAM (6-carboxyfluorescein) 5'-end- and TAMRA (6-carboxy-tetramethylrhodamine) 3'-end. Solutions of 0.2 μ M

DNA, in 10 mM lithium cacodylate buffer (pH 7.2), 99 mM LiCl and 1 mM KCl (90 mM LiCl and 10 mM KCl for F21T and F(21CTA)T), were heated to 95°C for 5 minutes and cooled at 4°C overnight. Before the analysis, DNA competitor (ds26) was added, followed by the ligand (concentrations ranging from 1 µM to 20 µM) or water, used for blank experiments. Fluorescence melting curves were measured with a 7900HT Fast Real-Time quantitative PCR machine (Applied Biosystems, Thermo Fischer Scientific), using 96-well plates and a total reaction volume of 25 µL. Solutions were kept at 25°C for 5 minutes, then a temperature gradient of 0.5°C/30 seconds was applied to achieve 95°C. Measurements were performed with $\lambda_{\text{exc}} = 492$ nm and monitoring fluorescence emission at $\lambda_{\text{em}} = 516$ nm. The melting temperature (T_m) has been measured at the inflection point of the sigmoid curve obtained by plot of normalized fluorescence intensity versus temperature.

Labelled sequences for FRET-melting assays:

F21T	5'-Fam-GGGTTAGGGTTAGGGTAGGG-Tamra-3'
F(21CTA)T	5'-Fam-GGGCTAGGGCTAGGGCTAGGG-Tamra-3'
F(Pu24T)T	5'-Fam-TGAGGGTGGTGAGGGTGGGAAGG-Tamra-3'
F(c-Myc)T	5'-Fam-TTGAGGGTGGGTAGGGTGGGTAA-Tamra-3'
F(c-Kit2)T	5'-Fam-GGGCGGGCGCGAGGGAGGGG-Tamra-3'
F(Bcl2)T	5'-Fam-AGGGCGGGCGCGGGAGGAAGGGGGCGGGA-Tamra-3'
F(CEB25wt)T	5'-Fam-AAGGGTGGGTGTAAGTGTGGGTGGGT-Tamra-3'
Competitor ds DNA sequence:	
ds26	5'-CAATCGGATCGAATTGATCCGATTG-3'

7.3.1.4 Circular Dichroism Analysis

CD titrations were performed using a JASCO J-710 spectropolarimeter equipped with a Peltier temperature controller (Jasco PTC-348WI) and black-walled rectangular quartz cells with 1 cm path length. A 1 ml solution of 3 µM oligonucleotide (2µM for control ds26) in 10 mM lithium cacodylate buffer (pH 7.2) and 100 mM KCl or NaCl was heated for 5 min at 95°C and subsequently cooled to 0°C for 30 minutes. This solution was titrated with 2 mM solution of the tested compound to get a final concentration in the range of 1–10, 12, or 14 eq. of ligand. Spectra were recorded from 220 to 450 nm, with 50 nm min-1 scan speed, 1.0 nm band width, 0.5 s integration time, 0.5 nm data pitch, and were corrected by a baseline obtained from the buffer in the same conditions.

7.3.1.5 Irradiation Experiments with Oligonucleotides

Photochemical experiments in presence of oligonucleotides have been carried out with a MAX-303 Xenon light source (Asahi), bearing a 365 nm filter, a quartz light guide and a collimator lens. The instruments were setup in order to expose an opened 1.5 ml Eppendorf, cooled into an ice-bath, to the UV beam, positioned 120 mm from the collimator extremity to the Eppendorf top (at this distance, the irradiance is approximately 1.8 mW/cm² at 365 nm). Solutions with ³²P-5'-end-labelled (.ca 100 Bq/µL) and 10 µM of cold 22AG in 10 mM lithium cacodylate buffer (pH 7.2) and 100 mM KCl, in a total volume of 18 µL, were heated at 95°C for 5 minutes, then at room temperature over a period of 3 hours. Before irradiation, folded oligonucleotide was incubated with the compounds (2 µL to reach the total volume of 20 µL) and the competitor, for 30 minutes, at room temperature. Before the analysis, the sample volumes were reduced and 3 µL of dye solution (80%

formamide, 0.1 M EDTA, 0.1% xylene cyanol and 0.1% bromophenol blue (blue loading dye) were added. The 15% polyacrylamide gel was run at 20 W. The gel was exposed to a storage phosphor screen and converted to a digital image with a Typhoon Trio variable-mode imager (GE Healthcare).

The yield of alkylation was determined as the ratio between the counts corresponding to the alkylation band and the sum of the counts corresponding to both the alkylation and the non-modified DNA bands, corrected by the background noise. The background has been subtracted, from the relative dark control, because they derived both from the same starting sample. The values given in % are the average of three distinct measurements.

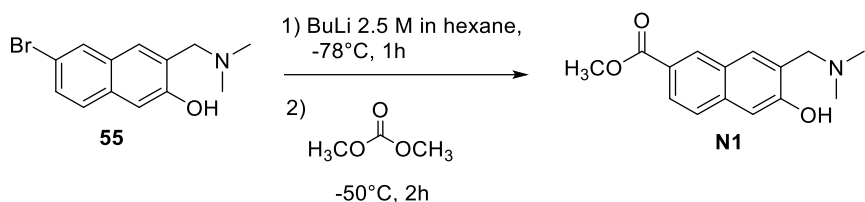
7.3.1.6 Exonuclease Digestion

PAGE-purified alkylated DNA was digested with two different concentration of Phosphodiesterase I from *Crotalus adamanteus* venom (0.2 U / μ L, Tris-HCl 110 mM, NaCl 100 mM, MgCl₂ 15 mM, 50%v/v Glycerol), an enzyme whose digestion stops at mono-alkylated sites. Products were incubated in 10 mM Tris-HCl buffer (pH = 8.0), in the presence of 2 mM MgCl₂ and 0.5 mg/mL transfer RNA with the 3'- Phosphodiesterase I from *Crotalus adamanteus* venom at 0.04 U/ μ L or 0.2 U/ μ L to a final volume of 5 μ L for 25 min at 37 °C. The partial digestion of non-alkylated DNA was run with 0.01 and 0.007 U/ μ L. Alkylated products were incubated with increasing concentrations of enzyme, to bypass the first alkylated base faced at the 3'-end. For each quinone methide precursor, both treated and untreated samples were analyzed by urea denaturing 20% polyacrylamide gel electrophoresis, along with treated and untreated unmodified DNA and a reference ladder. The main bands, associated to an arrest of the exonuclease activity have been isolated, eluted, and precipitated in ethanol. The entity of the migration of the oligonucleotides depended on the formation of the covalent bond with the quinone methide. Then, each alkylated adduct was heated at 95°C for 15 minutes to obtain partial thermal reversion of the alkylation. After precipitation, the dealkylated fragments were migrated on 20% denaturing gel. For the ladder, an amount of PAGE-purified unmodified DNA, characterized byradioactivity twice as high asthe most concentrated sample, was added with 1 μ L of reaction buffer and 1 μ L of 0.01 U/ μ L or 0.07 U/ μ L exonuclease solutions, and if necessary, water was used to achieve the final volume of 5 μ L. The solution was kept at 37°C for 25 minutes, then cooled down to 0°C and, finally, 3 μ L of blue loading dye were added.

7.3.2 Naphthalene-based Quinone Methide Precursors

7.3.2.1 Synthesis of compounds

Synthesis of Methyl 7-((dimethylamino)methyl)-6-hydroxy-2-naphthoate N1:

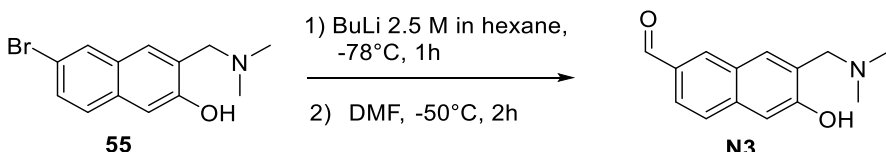


Scheme 7.23 – Synthesis of methyl ester N1.

In three-necked flask, compound **55** (0.75 mmol, 1 eq.) was dissolved in 15 ml of dry THF, under argon atmosphere. The mixture was cooled to -78°C, then butyllithium solution 2.5 M in hexane (1.9 mmol, 2.5 eq.) was added dropwise with a dropping funnel. After one hour, dimethyl carbonate (7.5 mmol, 10 eq.) was dissolved into 10 ml of dry THF, under argon atmosphere, and cannulated into reaction mixture. The solution was stirred for further two hours at -50°C. After this time, the crude was heated to 0°C and poured into a becker containing ice and 50 ml of HCl 10%. Subsequently, the suspension was transferred into an extracting funnel and the product was extracted three times with ethyl acetate (3x50 ml). Organic phase was dried over sodium sulphate, filtered and solvent removed under vacuum. Product was isolated after purification with reverse phase column chromatography (eluent: H₂O with 0.1% TFA:ACN) with method **4P**.

N1: Yield (%) = 60%, white solid. ¹H-NMR (300 MHz, CDCl₃) δ (ppm) = 8.48 (s, 1H), 7.98 (dd, J = 8.6 Hz, 1.6 Hz, 1H), 7.71 (d, J = 8.7 Hz, 1H), 7.60 (s, 1H), 7.23 (s, 1H), 3.97 (s, 3H), 3.88 (s, 2H), 2.42 (s, 6H). ¹³C-NMR (75 MHz, CDCl₃) δ (ppm) = 167.4, 158.4, 137.0, 130.6, 129.0, 126.7, 126.1, 125.4, 125.3, 124.5, 110.2, 62.6, 51.9, 44.3.

Synthesis of 7-((dimethylamino)methyl)-6-hydroxy-2-naphthaldehyde N3:



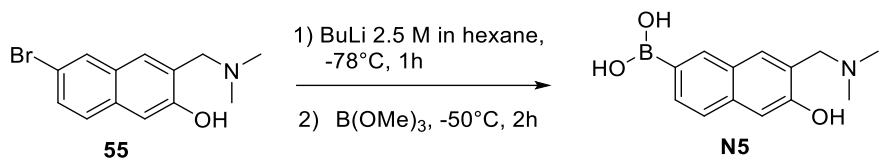
Scheme 7.24 – Organolithium coupling performed to obtain aldehyde N3.

In three-necked flask, compound **55** (3.56 mmol, 1 eq.) was dissolved in 25 ml of dry THF, under argon atmosphere. The mixture was cooled to -78°C, then butyllithium solution 2.5 M in hexane (7.85 mmol, 2.2 eq.) was added dropwise with a dropping funnel. After one hour, dimethyl formamide (35.6 mmol, 10 eq.) was dissolved into 10 ml of dry THF, under argon atmosphere, and cannulated into reaction mixture. The solution was stirred for further two hours at -50°C. After this time, the crude was heated to 0°C and poured into a beaker containing ice and 50 ml of HCl 10%. Subsequently, the suspension was transferred into an

extracting funnel and the product was extracted three times with ethyl acetate (3x50 ml). Organic phase was dried over sodium sulphate, filtered and solvent removed under vacuum. Product was isolated after purification with reverse phase column chromatography (eluent: H₂O with 0.1% TFA:ACN) with method **4P**.

N3: Yield (%) = 71%, white solid. **¹H-NMR (300 MHz, DMSO-d₆)** δ (ppm) = 10.07 (s, 1H), 8.18 (s, 1H), 7.87 (dd, J = 8.6 Hz, J = 1.3 Hz, 1H), 7.75 (d, J = 8.6 Hz, 1H), 7.64 (s, 1H), 7.23 (s, 1H), 3.88 (s, 2H), 2.41 (s, 6H). **¹³C-NMR (75 MHz, DMSO-d₆)** δ (ppm) 191.5, 159.1, 137.7, 133.6, 131.4, 128.7, 126.7, 126.4, 125.4, 122.8, 110.3, 62.3, 44.0.

Synthesis of (7-((dimethylamino)methyl)-6-hydroxynaphthalen-2-yl)boronic acid N5:

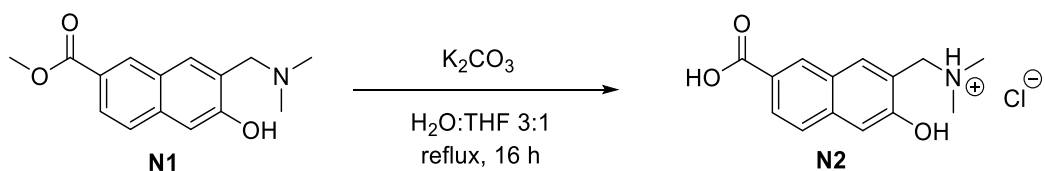


Scheme 7.25 – Organolithium coupling performed to obtain aldehyde N5.

In three-necked flask, compound **55** (1.7 mmol, 1 eq.) was dissolved in 8 ml of dry THF, under argon atmosphere. The mixture was cooled to -78°C, then butyllithium solution 2.5 M in hexane (5.12 mmol, 3 eq.) was added dropwise with a dropping funnel. After one hour, trimethylborate (17 mmol, 10 eq.) was dissolved into 10 ml of dry THF, under argon atmosphere, and cannulated into reaction mixture. The solution was stirred for further two hours at -50°C. After this time, the crude was heated to 0°C and poured into a becker containing ice and 50 ml of HCl 10%. The resulting suspension was stirred at room temperature for 30 minutes, then was transferred into an extracting funnel and the product was extracted three times with ethyl acetate (3x50 ml). Organic phase was dried over sodium sulphate, filtered and solvent removed under vacuum. Product was isolated after purification with reverse phase column chromatography (eluent: H₂O with 0.1% TFA:ACN) with method **4P**.

N5: Yield (%) = 49%, white solid. **¹H-NMR (300 MHz, DMSO-d₆)** δ (ppm) = 10.96 (s, 1H), 10.39 (bs, 1H), 8.38 (s, 1H), 8.17 (s, 1H), 7.93 (d, *J* = 8.3 Hz, 1H), 7.75 (d, *J* = 8.3 Hz, 1H), 7.44 (s, 1H), 4.50 (s, 2H), 2.85 (s, 6H). **¹³C-NMR (75 MHz, DMSO-d₆)** δ (ppm) = 154.6, 136.1, 135.2, 133.7, 131.9, 128.7, 126.7, 124.5, 119.3, 109.0, 54.8, 42.0.

Synthesis of 7-((dimethylamino)methyl)-6-hydroxy-2-naphthoic acid N2:

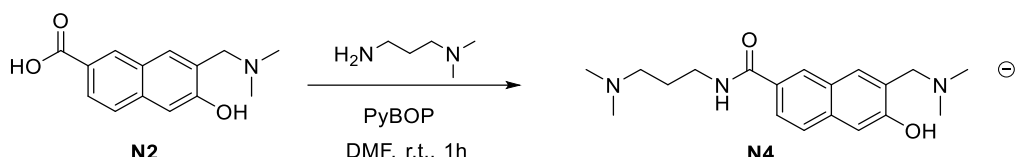


Scheme 7.26 – Basic hydrolysis of methyl ester, to obtain carboxylic acid N2.

Previously synthesized compound **N1** (0.38 mmol, 1 eq.) was poured into one-necked flask and dissolved into 20 ml of water/THF 3:1 and potassium carbonate (0.86 mmol, 2.2 eq.) was added. Mixture was stirred 16 hours under reflux and, subsequently, was quenched with 1 ml of HCl 10%. Solvent was removed under vacuum and crude was dissolved in water and purified through reverse phase column chromatography (H_2O 0.1 % TFA: ACN gradient), with method **4P**.

N2: Yield (%) = 84%, white solid. **1H -NMR (300 MHz, CD₃OD)** δ (ppm) = 8.59 (s, 1H), 8.09 (s, 1H), 8.05 (d, J = 8.7, 1H), 7.79 (d, J = 8.6 Hz, 1H), 7.34 (s, 1H), 4.53 (s, 2H), 2.94 (s, 6H). **^{13}C -NMR (75 MHz, CD₃OD)** δ (ppm) = 170.1, 157.3, 140.0, 135.7, 132.8, 128.7, 128.5, 127.7, 127.7, 121.8, 110.8, 59.0, 43.9.

Synthesis of 7-((dimethylamino)methyl)-N-(3-(dimethylamino)propyl)-6-hydroxy-2-naphthamide **N4**:

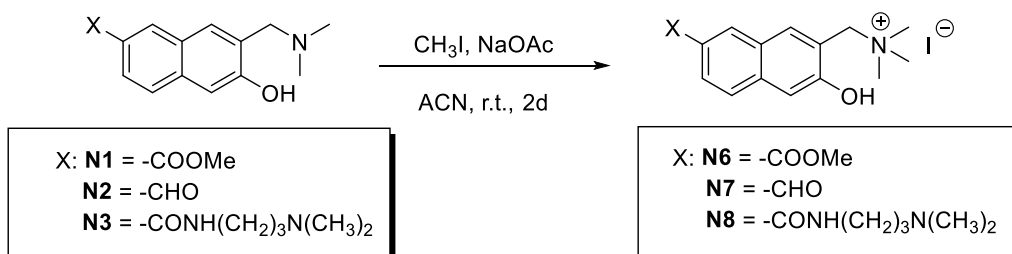


Scheme 7.27 – Coupling reaction performed to obtain amide **N4.**

Carboxylic acid **N2** (0.35 mmol, 1 eq.) was dissolved in 5 ml of dry DMF, then PyBOP (0.35 mmol, 1 eq.) and 3-(dimethylamino)propylamine (0.106 mmol, 3 eq.) were added to the solution, in one portion. Solution was stirred at room temperature for one hour, then solvent was removed under vacuum and the crude was purified through reverse phase column chromatography (H_2O 0.1% TFA: ACN gradient), with method **4P**. The aqueous phase was neutralized with NaHCO₃, extracted in DCM (3x10 mL), the combined organic phases were dried over Na₂SO₄, and the solvent was removed under reduced pressure.

N4: Yield (%) = 79%, white solid. **1H -NMR (300 MHz, CDCl₃)** δ (ppm) = 8.54 (s, 1H), 8.38 (s, 1H), 7.87-7.79 (m, 2H), 7.67 (s, 1H), 7.30 (s, 1H), 3.95 (s, 2H), 3.74 (q, J = 5.4 Hz, 2H), 2.76 (t, J = 5.9 Hz, 2H), 2.54 (s, 6H), 2.49 (s, 6H), 2.00 (q, J = 6.0 Hz, 2H). **^{13}C -NMR (75 MHz, CDCl₃)** δ (ppm) = 167.2, 157.5, 135.9, 128.8, 128.5, 127.3, 127.0, 126.2, 125.5, 123.5, 110.0, 62.8, 58.5, 44.9, 44.4, 39.7, 25.0.

General procedure for the synthesis of ammonium salts **N6-N8**:



Scheme 7.28 – General procedure for methylation of compounds **N6-N8.**

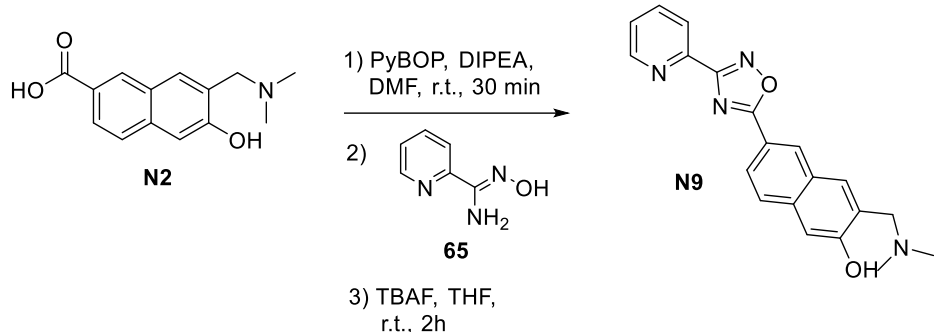
Mannich bases (0.15 mmol, 1 eq.) was dissolved into 10 ml of ACN, then sodium acetate (0.22 mmol, 1.5 eq.) and iodomethane (0.75 mmol) were added to the mixture. Solution was stirred for two days at room temperature, then solvent was removed under vacuum and the crude purified by reverse phase column chromatography (H_2O 0.1% TFA: ACN gradient) with method **4P**, described in the previous section.

N6: Yield (%) = 95%, white solid. **1H -NMR (300 MHz, CD₃OD)** δ (ppm) = 8.60 (s, 1H), 8.21 (s, 1H), 8.02 (d, J = 8.6 Hz, 1H), 7.78 (d, J = 8.7 Hz, 1H), 7.37 (s, 1H), 4.75 (s, 2H), 3.96 (s, 3H), 3.22 (s, 6H). **^{13}C -NMR (75 MHz, CD₃OD)** δ (ppm) = 168.8, 158.0, 140.2, 138.7, 132.9, 128.37, 128.35, 127.7, 127.0, 119.9, 111.4, 65.6, 54.0, 53.0.

N7: Yield (%) = 98%, white solid. **1H -NMR (300 MHz, DMSO-d₆)** δ (ppm) = 11.57 (s, 1H), 10.08 (s, 1H), 8.50 (s, 1H), 8.30 (s, 1H), 7.86 (s, 2H), 7.56 (s, 1H), 4.71 (s, 2H), 3.14 (s, 9H). **^{13}C -NMR (75 MHz, DMSO-d₆)** δ (ppm) = 192.4, 157.6, 138.6, 137.4, 135.3, 131.8, 126.9, 126.0, 123.9, 119.2, 110.3, 62.6, 52.2.

N8: Yield (%) = 96%, white solid. **1H -NMR (300 MHz, CD₃OD)** δ (ppm) = 8.44 (s, 1H), 8.16 (s, 1H), 7.94 (dd, J = 8.7, 1H), 7.82 (d, J = 8.8 Hz, 1H), 7.38 (s, 1H), 4.75 (s, 2H), 3.57 (t, J = 6.7 Hz, 2H), 3.52–3.46 (m, 2H), 3.21 (s, 9H), 3.18 (s, 9H), 2.18 (quint, J = 8.4 Hz, 2H). **^{13}C -NMR (75 MHz, CD₃OD)** δ (ppm) = 170.5, 157.6, 139.5, 138.3, 130.9, 130.0, 128.5, 127.7, 127.1, 119.9, 111.4, 66.2, 65.6, 54.0, 53.9, 38.3, 24.9.

Synthesis of 3-((dimethylamino)methyl)-6-(3-(pyridin-2-yl)-1,2,4-oxadiazol-5-yl)naphthalen-2-ol **N9**

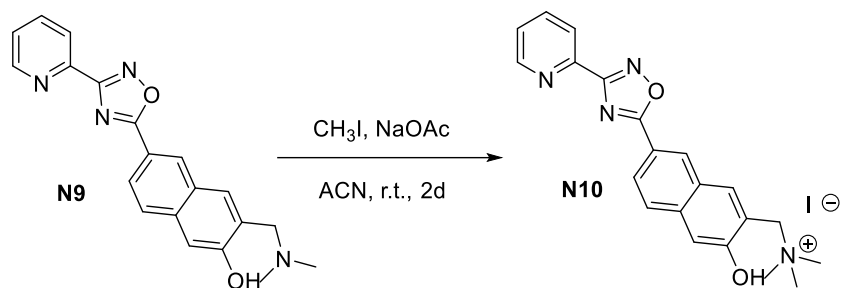


Scheme 7.29 – Synthesis of compound N9.

Carboxylic acid **N2** (0.35 mmol, 1 eq.) was dissolved in 5 ml of DMF, then DIPEA (0.71 mmol, 2 eq.) and PyBOP (0.35 mmol, 1 eq.) were added in one portion and solution was stirred at room temperature for 30 minutes. After this time, *N'*-hydroxypicolinimidamide **65** (0.35 mmol, 1 eq.) was added and the mixture was stirred for 6 days. Once substrate consumption was completed, product precipitation was induced upon addition of 20 ml of water. The precipitate was filtered on Buchner funnel, then was resuspended in 10 ml of THF and *tert*-butylammonium fluoride (0.7 mmol, 2 eq.) was added. Solution was stirred 2 hours at room temperature, then solvent was removed under vacuum and the product purified through reverse phase column chromatography (H_2O 0.1% TFA: ACN gradient) with method **4P**.

N9: Yield (%) = 61%, white solid. **1H -NMR (300 MHz, CD₃OD)** δ (ppm) = 9.00 (d, J = 4.2 Hz, 1H), 8.81 (s, 1H), 8.72–8.68 (m, 2H), 8.24–8.16 (m, 3H), 7.95 (d, J = 8.6 Hz, 1H), 7.39 (s, 1H), 4.58 (s, 2H), 2.97 (s, 6H). **^{13}C -NMR (75 MHz, CD₃OD)** δ (ppm) = 179.3, 166.1, 158.1, 146.9, 146.7, 142.6, 140.0, 136.0, 131.6, 130.1, 129.0, 128.7, 127.1, 126.6, 122.8, 119.9, 111.1, 58.7, 44.0.

Synthesis of 1-(3-hydroxy-7-(3-(pyridin-2-yl)-1,2,4-oxadiazol-5-yl)naphthalen-2-yl)-N,N,N-trimethylmethanaminium iodide N10

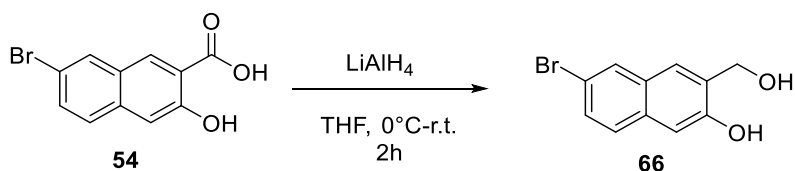


Scheme 7.29 – Methylation procedure to obtain compound N10.

Mannich base **N9** (0.15 mmol, 1 eq.) was dissolved in 10 ml of ACN, then sodium acetate (0.22, 1.5 eq.) and iodomethane (0.75 mmol, 5 eq.) were added to the mixture. Solution was stirred at room temperature for two days, then solvent was removed under vacuum and crude purified by reverse phase column chromatography (H₂O 0.1% TFA: ACN gradient) with method **4P**.

N10: Yield (%) = 90%, yellow solid. **¹H-NMR (300 MHz, CD₃OD)** δ (ppm) = 8.88 (s, 2H), 8.40–8.32 (m, 3H), 8.19 (t, *J* = 7.8 Hz, 1H), 8.02 (d, *J* = 8.7 Hz, 1H), 7.76 (t, *J* = 5.3 Hz, 1H), 7.48 (s, 1H), 4.85 (s, 2H), 3.33 (s, 9H). **¹³C-NMR (75 MHz, CD₃OD)** δ (ppm) = 178.2, 169.9, 158.4, 151.3, 147.5, 140.0, 139.8, 138.6, 131.3, 128.7, 128.6, 127.9, 127.0, 125.1, 120.7, 120.5, 111.7, 65.5, 58.9.

Synthesis of 6-bromo-3-(hydroxymethyl)naphthalen-2-ol 66:

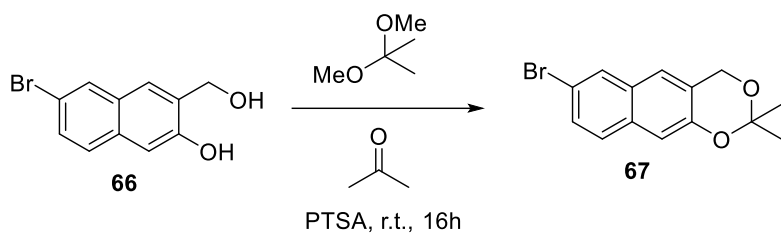


Scheme 7.30 – Reduction of 54 with lithium aluminium hydride.

Carboxylic acid **54** (4.9 mmol, 1 eq.) was dissolved in 15 ml of dry THF and cooled to 0°C. Then, LiAlH₄ (12 mmol, 2.4 eq.) was added, under argon atmosphere. Reaction was stirred two hours under reflux, until substrate was completely consumed. Reaction mixture was cooled again in an ice-bath and saturated solution of sodium bicarbonate was added dropwise. Then, crude was transferred into an extracting funnel and extracted three times with ethyl acetate (3x100 ml). Organic phase was dried over sodium sulphate, filtered and solvent removed under vacuum. Product was used for the subsequent step without no further purification.

66: Yield (%) 90%, white solid. **¹H-NMR (300 MHz, DMSO-d₆)** δ (ppm) 10.01 (s, 1H), 8.02 (s, 1H), 7.80 (s, 1H), 7.63 (d, *J*=9 Hz, 1H), 7.42 (dd, *J*=9 Hz, 1H), 7.10 (s, 1H), 5.22 (bs, 1H), 4.61 (s, 2H).

Synthesis of 7-bromo-2,2-dimethyl-4H-naphtho[2,3-d][1,3]dioxine 67:

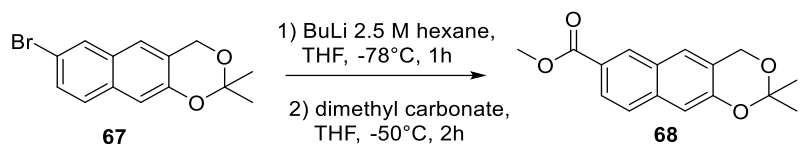


Scheme 7.31 – Protection procedure for compound 66.

In a one-necked flask, 6-bromo-3-(hydroxymethyl)naphthalen-2-ol **66** (19.8 mmol, 1 eq.) and 2,2-dimethoxypropane (203.3 mmol, 10 eq.) were dissolved in 50 ml of acetone, then a catalytic amount of p-toluenesulfonic acid (0.99 mmol, 0.5 eq.) was added. Reaction mixture was stirred at room temperature for 16 hours, then solvent was removed under vacuum. The crude was dissolved in chloroform and washed two times with saturated solution of sodium carbonate (2x50 ml). Organic phase was dried over sodium sulphate, filtered and the solvent distilled at reduced pressure. The product obtained has been used without no further purification.

67: Yield (%) = 97%, white solid. **¹H-NMR (300 MHz, DMSO-d₆)** δ (ppm) = 8.06 (s, 1H), 7.72 (d, J = 8.85 Hz, 1H), 7.65 (s, 1H), 7.51 (dd, J¹ = 8.79 Hz, J³ = 1.77 Hz, 1H), 7.29 (s, 1H), 5.06 (s, 2H), 1.53 (s, 6H). **¹³C-NMR (75 MHz, DMSO-d₆)** δ (ppm) = 149.9, 131.8, 129.1, 129.0, 128.8, 128.6, 123.1, 122.6, 116.5, 111.3, 99.8, 60.3, 24.8.

Synthesis of 7-bromo-2,2-dimethyl-4H-naphtho[2,3-d][1,3]dioxine 68:



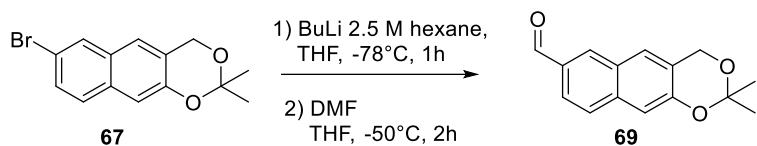
Scheme 7.32 – Organolithium-based coupling to obtain compound 68.

In a three-necked flask, 7-bromo-2,2-dimethyl-4H-naphtho[2,3-d][1,3]dioxine **67** (0.68 mmol, 1 eq.), was dissolved in 10 ml of dry THF, under argon atmosphere. Solution was cooled to -78°C, then butyllithium solution, 2.5 M in hexane (1.70 mmol, 2.5 eq.) was added dropwise with a dropping funnel. Solution was stirred at -78°C for one hour, then, in another three-necked flask, dimethyl carbonate (6.8 mmol, 10 eq.) was dissolved in 10 ml of dry THF and cooled to -78°C. Then, butyllithium solution was cannulated in this second flask, under argon atmosphere. Reaction mixture was stirred for other two hours, then heated to 0°C and poured into a becker containing ice. The crude was transferred into an extracting funnel and extracted three times with ethyl acetate (3x50 ml). Product has been purified through flash column chromatography (Cyclohexane: CHCl₃ 8:1).

68: Yield (%) = 50%, white solid. **¹H-NMR (300 MHz, CDCl₃)** δ (ppm) = 8.49 (s, 1H), 7.99 (d, J = 8.66, 1.29 Hz, 1H), 7.72 (d, J = 8.69 Hz, 1H), 7.58 (s, 1H), 7.25 (s, 1H), 5.09 (s, 2H), 3.98 (s, 3H), 1.63 (s, 6H). **¹³C-NMR (75**

MHz, CDCl₃) δ (ppm) = 167.2, 151.8, 135.9, 130.6, 127.2, 126.5, 125.3, 125.2, 126.1, 121.9, 111.8, 100.1, 77.6, 77.4, 76.9, 76.5, 60.9, 52.0, 24.9.

Synthesis of 2,2-dimethyl-4H-naphtho[2,3-d][1,3]dioxine-7-carbaldehyde 69:

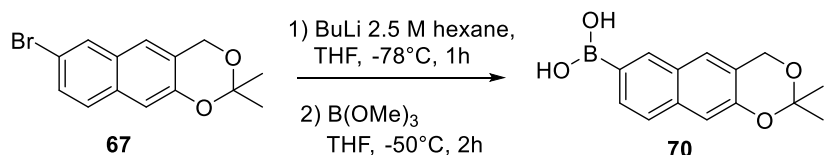


Scheme 7.33 – Organolithium-based coupling to obtain compound 69.

In a three-necked flask, 7-bromo-2,2-dimethyl-4H-naphtho[2,3-d][1,3]dioxine **67** (10.2 mmol, 1 eq.) was dissolved in 90 mL of dry THF under an argon atmosphere. The magnetically stirred solution was cooled to -78 °C and a solution of n-butyllithium 2.5 M in n-hexane (12.3 mmol, 1.2 eq) was added dropwise. After 1 h, dry N,N-dimethylformamide (100 mmol, 10 eq) was dissolved in dry THF and was added dropwise to the mixture. After two hours, solution was heated to room temperature and the solvent was removed under reduced pressure. The oil residue was suspended in 100 ml of distilled water, then ammonium formate and HCl 10% were added slowly, until pH 5. The precipitated formed during this operation was filtered on a Buchner funnel and washed with water. The product was used for the subsequent step without no further purification.

69: Yield (%) = 69%, white solid. ¹H-NMR (300 MHz, CDCl₃) δ (ppm) = 10.07 (s, 1H), 8.19 (s, 1H), 7.86 (dd, *J* = 8.6, 1.6 Hz, 1H), 7.75 (d, *J* = 8.6 Hz, 1H), 7.62 (s, 1H), 7.26 (s, 1H), 5.09 (s, 2H), 1.62 (s, 7H).

Synthesis of (2,2-dimethyl-4H-naphtho[2,3-d][1,3]dioxin-7-yl)boronic acid 70:



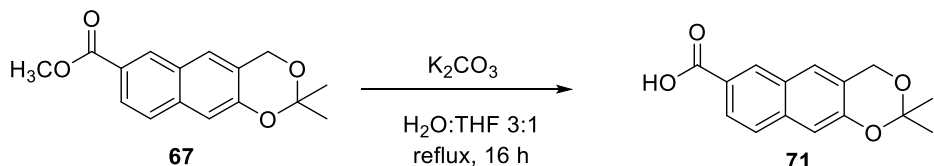
Scheme 7.34 – Organolithium-based coupling to obtain compound 70.

In a three necked-flask, 7-bromo-2,2-dimethyl-4H-naphtho[2,3-d][1,3]dioxine **67** (0.85 mmol, 1 eq.) was dissolved in 15 ml of dry THF, under argon atmosphere. Solution was cooled to -78°C, then n-butyllithium solution 2.5 M in n-hexane (8.5 mmol, 3 eq.) was added dropwise, with a dropping funnel. Solution was stirred for one hour at -78°C, then trimethyl borate (8.5 mmol, 10 eq.) was dissolved in 5 ml of dry THF and added dropwise, under argon atmosphere. Reaction mixture was stirred for further two hours at -50°C, then was heated to 0°C and poured into a mixture of ice and HCl 10%. The resulting suspension was transferred

into an extracting funnel and extracted three times with ethyl acetate (3x70 ml). The product was purified with flash column chromatography (CHCl_3 : AcOEt 4:1).

70: Yield (%) = 46%, white solid. **$^1\text{H-NMR}$ (300 MHz, CDCl_3)** δ (ppm) = 8.71-8.68 (m, 1H), 8.17-8.15 (m, 1H), 7.80-7.76 (m, 2H), 7.66 (s, 1H), 5.1 (s, 2H), 1.66 (s, 6H).

Synthesis of methyl 2,2-dimethyl-4H-naphtho[2,3-d][1,3]dioxine-7-carboxylate 71:

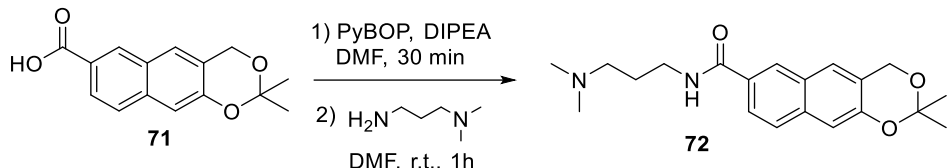


Scheme 7.35 – Basic hydrolysis of methyl ester 67.

Methyl ester **67** (0.062 mmol, 1 eq.) and potassium carbonate (0.075 mmol, 1.2 eq.) were suspended in H_2O : THF 3:1, then the resulting mixture was refluxed for 16 hours. Once reaction was completed, solvent was removed under vacuum and the crude diluted in HCl 10% and extracted three times with ethyl acetate (3x30 ml). The crude was purified through column chromatography ($\text{AcOEt}:\text{MeOH}$ gradient).

71: Yield (%) = 95%, white solid. **$^1\text{H-NMR}$ (300 MHz, Acetone- d_6)** δ (ppm) = 8.55 (s, 1H), 7.98 (d, J = 8.7, 1H), 7.85-7.83 (m, 2H), 7.31 (s, 1H), 5.14 (s, 2H), 1.59 (s, 6H). **$^{13}\text{C-NMR}$ (75 MHz, Acetone- d_6)** δ (ppm) 168.2, 153.4, 137.3, 131.9, 128.7, 127.8, 127.0, 126.8, 126.6, 123.8, 112.7, 101.4, 61.9, 25.6.

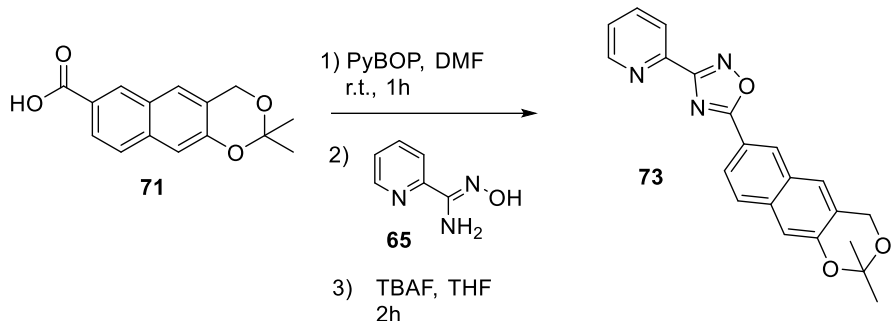
Synthesis of N-(3-(dimethylamino)propyl)-2,2-dimethyl-4H-naphtho[2,3-d][1,3]dioxine-7-carboxamide 72:



Scheme 7.36 – Coupling procedure to obtain amide 72.

Carboxylic acid **71** (0.39 mmol, 1 eq.) was dissolved in 1 ml of DMF, then DIPEA (0.8 mmol, 2 eq.) and PyBOP (0.39 mmol, 1 eq.) were added and solution was stirred at room temperature for 30 minutes. After this time, 3-(dimethylamino)propylamine (0.39 mmol, 1 eq.) was introduced in the mixture, that was stirred for another hour, at room temperature. When reaction was completed, solvent was removed under reduced pressure and the crude was dissolved in 50 ml of CHCl_3 and washed three time with saturated solution of sodium bicarbonate (3x20 ml). Product has been used for the following step without no further purification.

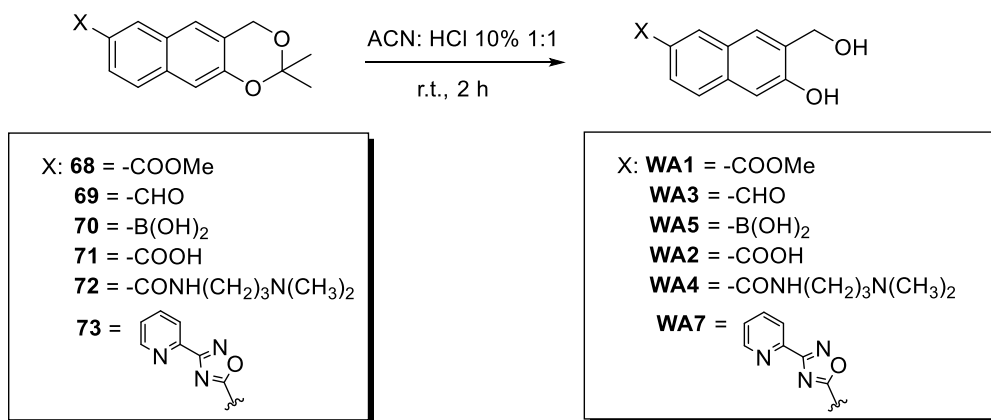
Synthesis of Oxadiazole 73:



Scheme 7.37 – Procedure for the synthesis of oxadiazole-based ligand 73.

Carboxylic acid **71** (0.38 mmol, 1 eq.) was dissolved in 10 ml of DMF, then PyBOP (0.38 mmol, 1 eq.) was added in one portion and the mixture was stirred one hour at room temperature. *N*'-hydroxypicolinimidamide **65** (0.38 mmol, 1 eq.) was introduced into the solution, which was stirred for 6 days at room temperature. After substrate consumption, solvent was removed and the crude was dissolved in 2 ml of THF and TBAF (0.76 mmol, 2 eq.) was added. After two hours, solvent was distilled under reduced pressure and the crude was suspended in water. Product precipitated immediately, then was filtered on a Buchner funnel and used for the final step without further purification.

General Procedure for deprotection and synthesis of WA1-WA7:



Scheme 7.38 – General procedure for deprotection of compounds WA1-WA7.

Protected acetal (0.39 mmol, 1 eq.) was dissolved in 10 ml of ACN:HCl 10% 1:1 and the resulting solution was stirred at room temperature for two hours. Crude has been diluted in water and purified through reverse phase column chromatography (H₂O 0.1% TFA: ACN gradient) with method **4P**, described in the previous section.

WA1: Yield (%) = 80%, white solid. **¹H-NMR (300 MHz, DMSO-d₆)** δ (ppm) = 10.44 (s, 1H), 8.56 (s, 1H), 8.08 (s, 1H), 7.94 (dd, J = 8.62, 1.49 Hz, 1H), 7.86 (d, J = 8.65 Hz, 1H), 4.7 (s, 2H), 3.98 (s, 3H). **¹³C-NMR (75 MHz, DMSO-d₆)** δ (ppm) = 166.6, 155.6, 135.9, 133.2, 130.2, 127.0, 126.6, 126.0, 124.4, 123.6, 107.9, 58.4, 52.0.

WA2: Yield (%) = 68%, white solid. **¹H-NMR (300 MHz, CD₃OD)** δ (ppm) = 8.50 (s, 1H), 7.95–7.88 (m, 2H), 7.67 (d, J = 8.6 Hz, 1H), 7.15 (s, 1H), 4.81 (s, 2H). **¹³C-NMR (75 MHz, CD₃OD)** δ (ppm) = 169.3, 157.8, 134.2, 130.1, 129.5, 127.8, 127.6, 126.1, 125.4, 124.6, 107.8, 58.9.

WA3: Yield (%) = 95%, white solid. **¹H-NMR (300 MHz, DMSO-d₆ + DCl in D₂O)** δ (ppm) = 9.95 (s, 1H), 8.38 (s, 1H), 7.98 (s, 1H), 7.74 (s, 2H), 7.21 (s, 1H), 4.63 (s, 2H). **¹³C-NMR (75 MHz, DMSO-d₆ + DCl in D₂O)** δ (ppm) = 194.6, 157.0, 138.1, 136.0, 133.4, 132.3, 128.9, 127.8, 127.7, 123.3, 109.6, 59.4.

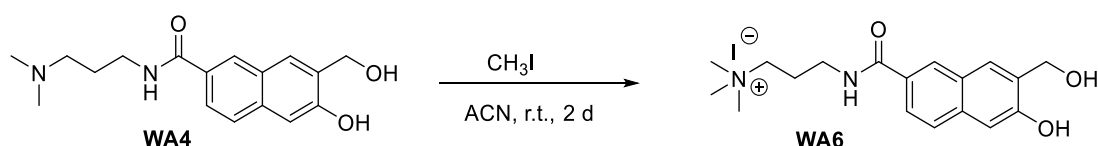
WA4: Yield (%) = 90%, white solid. **¹H-NMR (300 MHz, CDCl₃)** δ (ppm) = 8.22 (bs, 1H), 7.80 (s, 1H), 7.57–7.45 (m, 2H), 7.26 (s, 1H), 7.09 (s, 1H), 4.88 (s, 2H), 3.56 (t, J = 5.6 Hz, 2H), 2.56 (t, J = 6.2 Hz, 2H), 2.34 (s, 6H), 1.82 (q, J = 6.0 Hz, 2H). **¹³C-NMR (75 MHz, CDCl₃)** δ (ppm) = 167.5, 157.6, 131.8, 131.2, 130.9, 130.2, 128.2, 127.9, 126.1, 123.2, 108.9, 59.1, 58.7, 47.2, 37.2, 25.9.

WA5: Yield (%) = 89%, white solid. **¹H-NMR (300 MHz, DMSO-d₆)** δ (ppm) = 9.86 (s, 1H), 8.22 (s, 1H), 7.98 (s, 1H), 7.78 (s, 1H), 7.72 (d, J = 8.08 Hz, 1H), 7.58 (d, J = 8.12 Hz, 1H), 7.07 (s, 1H), 4.63 (s, 2H). **¹³C-NMR (75 MHz, DMSO-d₆)** δ (ppm) = 153.8, 134.6, 134.5, 131.5, 130.3, 127.1, 126.0, 124.2, 107.8, 58.6.

WA7: Yield (%) = 70%, white solid. **¹H-NMR (300 MHz, DMSO-d₆)** δ (ppm) = 10.57 (s, 1H), 8.91 (d, J = 4.48 Hz, 1H), 8.83 (s, 1H), 8.31 (d, J = 7.9 Hz, 1H), 8.17 (m, 2H), 8.02 (d, J = 8.88 Hz, 1H), 7.75 (t, J = 4.99 Hz, 1H), 7.09 (s, 1H), 4.77 (s, 2H). **¹³C-NMR (75 MHz, DMSO-d₆)** δ (ppm) = 168.3, 155.9, 150.3, 137.7, 135.8, 133.8, 128.7, 127.0, 126.9, 126.1, 123.4, 123.2, 108.2, 58.4.

Synthesis of 3-(6-hydroxy-7-(hydroxymethyl)-2-naphthamido)-N,N,N-trimethylpropan-1-aminium iodide

WA6:

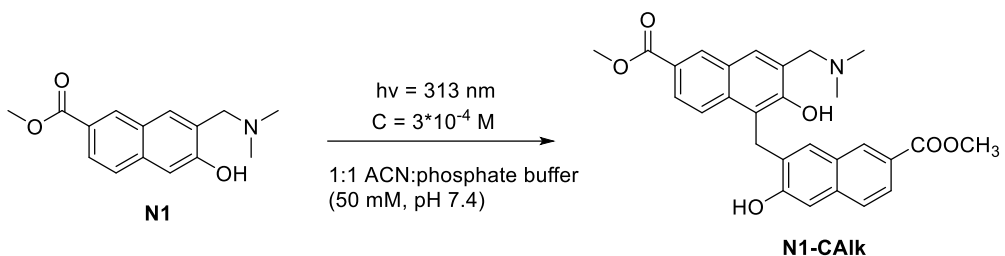


Scheme 7.39 – Procedure for methylation of compound WA4.

Amide **WA4** (0.16 mmol, 1 eq.) was dissolved into 10 ml of ACN, then iodomethane (0.8 mmol, 5 eq.) was added in one portion. Solution was stirred at room temperature for 2 days, then solvent was removed under reduced pressure. Crude was purified by reverse phase column chromatography (H₂O 0.1% TFA: ACN gradient) with method **4P**, described in the previous section.

WA6: Yield (%) = 85%, yellow oil. **¹H-NMR (300 MHz, CD₃OD)** δ (ppm) = 8.31 (s, 1H), 7.93 (s, 1H), 7.81 (dd, J = 8.6, 1.7 Hz, 1H), 7.71 (d, J = 8.7 Hz, 1H), 7.16 (s, 1H), 4.83 (s, 2H), 3.56 (t, J = 6.6 Hz, 2H), 3.50–3.44 (m, 2H), 3.17 (s, 9H), 2.17 (p, J = 6.7 Hz, 2H). **¹³C-NMR (75 MHz, CD₃OD)** δ (ppm) = 171.2, 157.1, 137.8, 133.5, 129.7, 129.1, 129.0, 128.8, 127.4, 125.0, 109.6, 66.2, 61.2, 53.9, 38.2, 25.0.

Synthesis of alkylation adduct N1-CAlk:



Scheme 7.40 – Photochemical preparation of quinone methide adduct N1-CAlk.

Quinone methide precursor **N1** (0.032 mmol, 1 eq.) was dissolved in 100 ml of 1:1 ACN:phosphate buffer solution and distributed in different quartz tubes. Then, mixture was irradiated at 310 nm with multi-lamps photoreactor (Rayonet). After 20 minutes, solvent was removed under vacuum and the crude was purified with reverse phase column chromatography (H_2O 0.1% TFA/ACN gradient) with method **4P**.

N1-CAlk: Yield (%) = 48%. **¹H-NMR (300 MHz, DMSO-d₆)** δ (ppm) = 10.87 (bs, 1H), 10.10 (bs, 2H), 8.57 (s, 1H), 8.30 (s, 1H), 8.12 (s, 1H), 7.88 (d, *J* = 8.9 Hz, 1H), 7.76–7.72 (m, 3H), 7.34 (s, 1H), 7.11 (s, 1H), 4.57 (s, 2H), 4.53 (s, 2H), 3.88 (s, 3H), 3.78 (s, 3H), 2.86 (s, 6H). **¹³C-NMR (75 MHz, DMSO-d₆)** δ (ppm) = 166.4, 166.2, 156.5, 154.1, 136.3, 135.6, 133.7, 131.4, 130.7, 129.9, 128.4, 127.1, 126.5, 126.2, 125.9, 124.5, 124.4, 123.8, 123.5, 121.9, 118.9, 108.2, 55.9, 52.1, 51.8, 42.3, 25.2.

7.3.2.2 Spectroscopic and Photochemical Analysis

- **Molar Absorbivity:** Molar extinction coefficients of compounds **N1-N10** were measured by adding increasing concentrations of compound stock solution to 3 ml of 1:1 ACN:PBS (50 mM, pH 7.4) solution in 3.5 ml quartz cuvette and recording UV-VIS spectra after each addition.
- **Spectrophotometric Titrations:** Stock solutions of compounds **QMP1-QMP6** were used to prepare $1 \cdot 10^{-5}$ solutions, in 2.5 ml of water, in presence of $1 \cdot 10^{-3}$ M of NaCl. HCl 0.1 M was used to decrease solution pH, while 0.1 and 0.01 M solutions of NaOH were used to gradually increase pH up to 12. At each addition, UV-VIS spectra of the sample was recorded. pK_a values were measured by plotting the molar absorptivity, at a fixed wavelength, versus the pH, and the resulting curve was fitted with Origin software.
- **Reaction quantum yields (Φ)** were obtained by irradiating a 3mL solution (1:1 ACN:PBS 50mM pH=7.4) of **QMP1-QMP6** (concentration 10^{-4} to 10^{-5}) in a 1 cm optical path cuvette and monitoring the consumption of the QMP by reverse-phase HPLC, using method **4A**, described in the previous section. Lamp source was a focalized 150 W high-pressure mercury arc equipped with a transmittance filter (transmission 313nm) and a single-photon detector (photon flux $q_p=2.6 \cdot 10^{-7}$ Einstein/cm²*min⁻¹). Calibration of the apparatus was performed using the photochemical decomposition of potassium ferrioxalate as actinometer. Conversion of substrate was measured through HPLC analysis, at different time of irradiation. The same procedure was applied to measure photochemical quantum yields at 366 nm, using the proper filter on the optical desk.

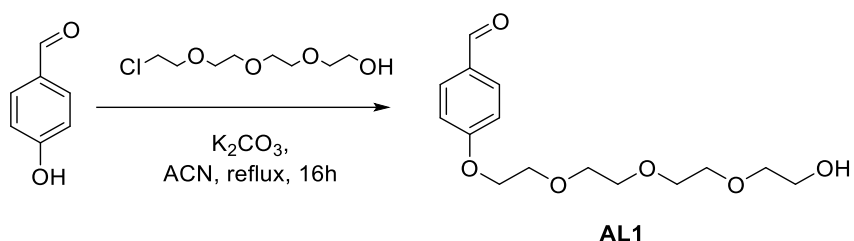
- **Analysis of N1-Calk formation:** Different 3 ml solutions of compound **N1**, with concentration 500, 100, 50 and 10 μ M, in 1:1 ACN:PBS (50 mM, pH 7.4), were irradiated with multi-lamps photoreactors, at 310 nm (32W), for 60 seconds. Then, solution was checked through HPLC analysis, with method 4A, and the ration between peak area of **N1-Calk** and **WA1** was measured.

7.4 2,5-Diaryl Tetrazoles

7.4.1 Synthesis and Photochemical behaviour of 2,5-diaryl tetrazoles

7.4.1.1 Synthesis of Compounds

Synthesis of 4-((2-(2-hydroxyethoxy)ethoxy)ethoxy)methyl)benzaldehyde B1:

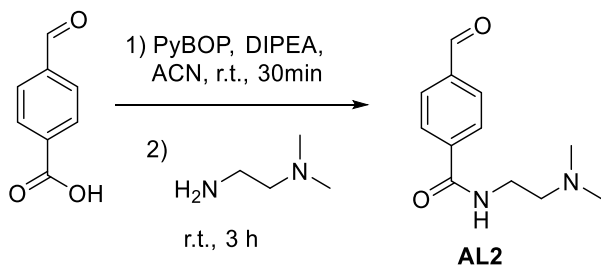


Scheme 7.41 – Synthesis of benzaldehyde AL1.

Hydroxybenzaldehyde (6.5 mmol, 1 eq.) was dissolved into 6 ml of anhydrous ACN, then potassium carbonate (9.8 mmol, 1.5 eq.) and (2-(2-chloroethoxy)ethoxy)methanol (6.55 mmol, 1 eq.) were added to the solution. Reaction was heated to 80°C and stirred at this temperature overnight. After 18 hours, crude was diluted into 30 ml of 0.05 M NaOH solution and extracted four times with diethyl ether. Organic phase was dried over sodium sulphate, solvent removed under vacuum and pure product was isolated as yellow oil.

AL1: Yield (%) = 64%. $^1\text{H-NMR}$ (300MHz, CDCl_3) δ (ppm) = 9.9 (s, 1H), 7.87 (d, J = 8.71 Hz, 2H), 7.06 (d, J = 7.15 Hz, 2H), 4.5 (t, J = 4.69 Hz, 2H), 4.26-3.66 (m, 10H). $^{13}\text{C-NMR}$ (75MHz, CDCl_3) δ (ppm) = 191.0, 163.6, 132.0, 114.7, 70.8, 70.7, 70.2, 69.4, 69.3, 68.1, 67.6, 67.5, 66.8, 61.6.

Synthesis of N-(2-(dimethylamino)ethyl)-4-formylbenzamide B2:



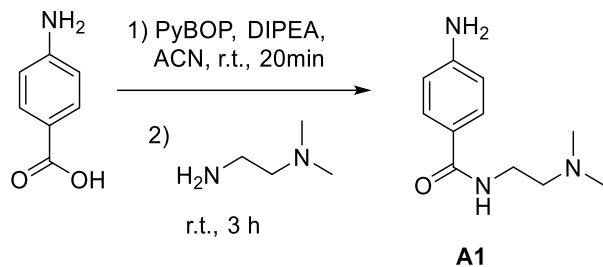
Scheme 7.42 – Synthesis of Benzaldehyde AL2

500 mg of 4-formylbenzoic acid (3.33 mmol, 1 eq.), were dissolved into 20 ml of ACN, then 1.15 ml (6.66 mmol, 2 eq.) of DIPEA and 1.7 g of PyBOP (3.33 mmol, 1 eq.) were added. Solution was stirred for 30 minutes at room temperature, then N,N' -dimethylethylenediamine was introduced into reaction flask. After 3 hours, solvent was removed under vacuum and crude was diluted with 20 ml of 0.05 M NaOH solution

and extracted three times with ethyl acetate. Product was purified by MPLC (Gradient DCM:MeOH 15%, SNAP 25 g) and product was isolated in 65% yield.

AL2: Yield (%) = 55%. This compound was fully characterized according to literature²⁰⁸.

Synthesis of 4-amino-N-(2-(dimethylamino)ethyl)benzamide A1:

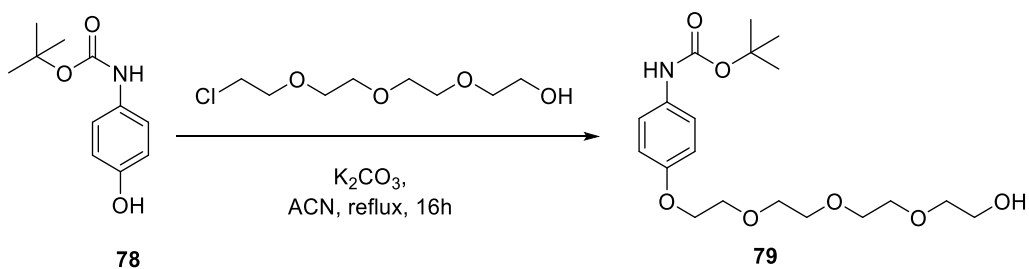


Scheme 7.43 -Synthesis of Aniline A1

p-Amino benzoic acid (0.73 mmol, 1 eq.) was dissolved into 5 ml of anhydrous THF, then DIPEA (1.16 mmol, 1.6 eq.) and PyBOP (0.73 mmol, 1 eq.) were added to the reaction mixture. Solution was stirred for 20 minutes at room temperature, then *N,N*-dimethylethylenediamine (0.73 mmol, 1 eq.) was introduced into the flask. Reaction was stirred for 3 hours at room temperature, then solvent was removed under vacuum. Crude was diluted with 5 ml of 0.05 M NaOH solution and extracted three times with ethyl acetate. Organic phase was dried over sodium sulphate, solvent removed with rotary evaporator. Crude was purified through reverse phase liquid chromatography (H_2O 0.1% TFA/ACN gradient) with method **5P**.

A1: Yield (%) = 76%. The compound was fully characterized according to the literature²⁰⁹.

Synthesis of tert-butyl (4-(2-(2-hydroxyethoxy)ethoxy)ethoxy)phenyl)carbamate 79:

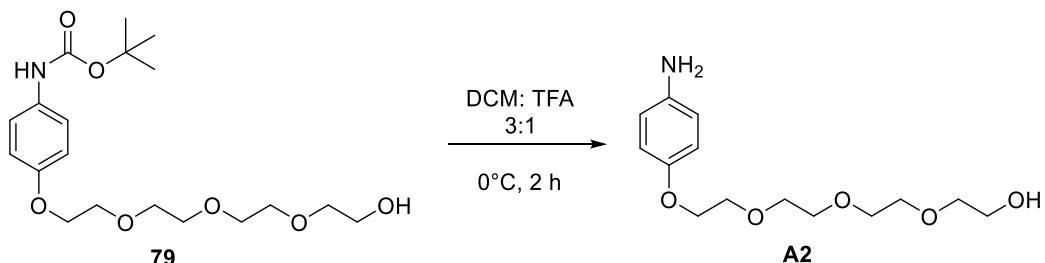


Scheme 7.44 – Synthesis of aniline 79.

Tert-butyl (4-hydroxyphenyl)carbamate **78** (3.5 mmol, 1 eq.) was dissolved into 10 ml of ACN anhydrous and potassium carbonate (5.23 mmol, 1.5 eq.) and (2-(2-chloroethoxy)ethoxy)methanol (5.23 mmol, 1.5 eq.) were added. Solution was stirred at 80°C, in nitrogen atmosphere, for 24 hours, then, diluted with 30 ml of 0.05 M NaOH solution and extracted four times with diethyl ether. Organic phase was dried over sodium sulphate, solvent removed under vacuum and pure product was isolated.

79: Yield (%) = 54%. **¹H-NMR (300MHz, CDCl₃):** δ (ppm) = 7.18 (d, *J* = 8.05 Hz, 2H), 6.76 (d, *J* = 8.9 Hz, 2H), 4.01 (t, *J* = 4.36 Hz, 2H), 3.76 (q, *J* = 4.81 Hz, 2H), 3.65-3.48 (m, 8H), 1.40 (s, 9H). **¹³C-NMR (75 MHz, CDCl₃):** δ (ppm) = 154.3, 131.8, 120.3, 114.7, 77.5, 77.2, 77.1, 76.6, 72.4, 70.5, 70.3, 69.9, 69.5, 67.4, 67.3, 61.1, 28.1.

Synthesis of 2-(2-(4-aminophenoxy)ethoxy)ethoxyethanol A2:

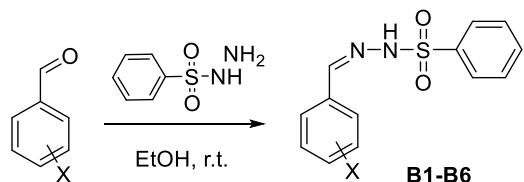


Scheme 7.45 – Synthesis of aniline A2.

Tert-butyl (4-(2-(2-hydroxyethoxy)ethoxy)phenyl)carbamate (0.85 mmol, 1 eq.) has been dissolved into 3 ml of DCM. Solution was cooled to 0°C into an ice-bath and 1.3 ml of TFA (17 mmol, 20 eq.) have been added slowly. Reaction mixture was stirred for two hours at 0°C, then has been neutralised with saturated solution of sodium carbonate. Product was extracted three times with ethyl acetate and organic phase was dried over sodium sulphate. After solvent evaporation, 150 mg of pure product were obtained.

A2: Yield (%) = 73%. **¹H-NMR (300MHz, DMSO-d₆):** δ (ppm) = 7.18 (d, *J* = 8.8 Hz, 2H), 6.97 (d, *J* = 8.82 Hz, 2H), 4.05 (t, *J* = 4.65 Hz, 2H), 3.73 (q, *J* = 4.75 Hz, 2H), 3.58-3.39 (m, 8H). **¹³C-NMR (75 MHz, DMSO-d₆):** δ (ppm) = 156.5, 127.5, 122.7, 119.1, 115.4, 115.1, 111.1, 72.3, 69.9, 69.7, 68.8, 67.5, 62.7, 60.1.

General Procedure for the synthesis of benzensulphonyl hydrazone B1-B6



Scheme 7.46 – General Procedure for the synthesis of benzensulphonylhydrazones B1-B6.

According to procedure previously reported in literature¹⁷², benzensulphonyl hydrazones were obtained by dissolving the corresponding benzaldehyde (1.7 mmol, 1 eq.) into 14 ml of ethanol, then benzensulphonyl hydrazide (1.7 mmol, 1 eq.) was introduced in the reaction flask. Solution was stirred for four hours at room temperature, then solvent was removed under vacuum to obtain the desired pure product.

B1: Yield (%) = 86%. **¹H-NMR (300MHz, DMSO-d₆)** δ (ppm) = 11.3 (s, 1H), 7.66 (m, 5H), 7.49 (d, *J* = 8.7 Hz, 2H), 6.96 (d, *J* = 8.68 Hz), 4.12 (t, *J* = 4.14 Hz, 2H), 4.08 (q, *J* = 2.8 Hz, 2H), 3.58-3.41 (m, 10H). **¹³C-NMR (75 MHz, DMSO-d₆)** δ (ppm) = 150.0, 147.2, 139.1, 132.9, 129.2, 128.4, 127.2, 126.3, 114.7, 72.34, 69.9, 69.7, 68.8, 67.3, 50.2.

B2: Yield (%) = 80%. **¹H-NMR (300MHz, D₂O)** δ (ppm) = 7.56 (m, 3H), 7.36 (d, *J* = 6.0 Hz), 7.10 (m, 5H), 3.57 (m, 2H), 3.23 (d, *J* = 6.0 Hz, 2H), 2.8 (s, 6H). **¹³C-NMR (75 MHz, D₂O)** δ (ppm) = 169.5, 148.1, 136.8, 136.1, 133.7, 133.6, 129.1, 127.3, 127.0, 126.9.

B3: Yield (%) = 90%. **¹H-NMR (300MHz, CDCl₃)** δ (ppm) = 8.44 (q, *J* = 9.2 Hz, 4H), 8.40 (d, *J* = 9.2 Hz, 2H), 8.14 (m, 2H), 7.11 (m, 2H). **¹³C-NMR (75 MHz, CDCl₃)** δ (ppm) = 160.8, 148.9, 133.1, 130.0, 127.7, 124.2, 121.4, 114.7.

B4: Yield (%) = 94%. **¹H-NMR (300MHz, DMSO-d₆)** δ (ppm) = 11.58 (s, 1H), 7.92-7.89 (m, 3H), 7.66-7.6 (m, 3H), 7.30 (t, *J* = 7.86 Hz, 1H), 7.15-7.10 (m, 2H), 6.94 (d, *J* = 2.44 Hz, 1H), 3.75 (s, 3H). **¹³C-NMR (75 MHz, DMSO-d₆)** δ (ppm) = 159.4, 147.0, 139.0, 135.0, 133.0, 129.9, 129.2, 127.2, 119.0, 115.9, 111.6, 55.1.

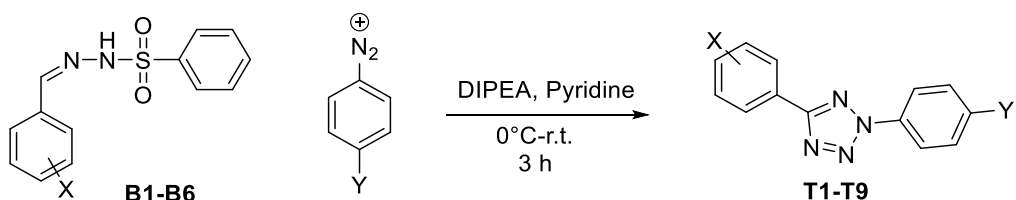
B5: Yield (%) = 89%. **¹H-NMR (300MHz, DMSO-d₆)** δ (ppm) = 12 (s, 1H), 8.2 (d, *J* = 8.6 Hz, 2H), 8.04 (s, 1H), 7.9 (d, *J* = 7.46 Hz, 2H), 7.83 (d, *J* = 8.69 Hz, 2H), 7.65 (m, 3H). **¹³C-NMR (75 MHz, DMSO-d₆)** δ (ppm) = 147.9, 144.6, 139.7, 138.8, 133.3, 129.4, 127.7, 127.1, 124.0.

B6: Yield (%) = 93%. **¹H-NMR (300MHz, DMSO-d₆)** δ (ppm) = 11.77 (s, 1H), 7.99-7.88 (m, 5H), 7.69-7.6 (m, 4H). **¹³C-NMR (75 MHz, DMSO-d₆)** δ (ppm) = 166.8, 145.9, 138.9, 137.5, 133.1, 131.7, 129.7, 129.3, 127.1, 126.8.

General Procedure for the synthesis of arene diazonium salts:

For the synthesis of arendiazonium salts, 2 ml of 37% HCl were added to a cooled solution of the aniline (7.3 mmol, 1 eq.) in 10 ml of 50% ethanol solution. Sodium nitrite (7.3 mmol, 1 eq.) was dissolved into 1 ml of water and transferred slowly into reaction mixture. Solution was stirred for 30 minutes at 0°C, then was used immediately, without purification or product isolation, to synthesize the corresponding tetrazole.

General Procedure for the synthesis of 2,5-diaryl tetrazoles T1-T9:



Scheme 7.47. -General procedure for synthesis of tetrazoles **T1-T9**.

2,5-Diaryl tetrazoles have been synthesised with procedure previously reported in literature¹⁹². Benzensulphonyl hydrazone (3.65 mmol, 0.5 eq.) was dissolved into 25 ml of Pyridine, then solution was

cooled to 0°C and DIPEA (7.3 mmol, 1 eq.) was added. Mixture has been stirred for 5 minutes, then solution of freshly prepared diazonium salt was dropped slowly into the flask. After three hours, solvent was removed under vacuum and crude was diluted with 30 ml of 10% HCl solution and extracted three times with ethyl acetate. Organic phase was dried over sodium sulphate and solvent removed with rotary evaporator. Crude was purified through flash column chromatography (DCM:MeOH 9:1) or, for water soluble tetrazoles, with reverse phase column chromatography (H₂O 0.1% TFA/ACN gradient) with method **5P**, described in the previous section.

T1: Yield (%) = 30%. **¹H-NMR (300MHz, DMSO-d₆)** δ (ppm) = 10.05 (s, 1H), 8.05-7.97 (m, 4H), 7.02 (d, *J* = 8.95 Hz, 2H), 6.9 (d, *J* = 8.49 Hz, 2H), 3.86 (s, 3H). **¹³C-NMR (75 MHz, DMSO-d₆)** δ (ppm) = 164.5, 159.7, 159.6, 132.1, 129.7, 128.3, 121.5, 117.4, 116.0, 115.9, 115.8, 115.1.

T2: Yield (%) = 64%. The compound was fully characterized according to the literature²¹⁰.

T3: Yield (%) = 43%. **¹H-NMR (300MHz, CDCl₃)** δ (ppm) = 8.5-8.41 (m, 4H), 8.36-8.28 (m, 4H), 4.01 (s, 3H). **¹³C-NMR (75 MHz, CDCl₃)** δ (ppm) = 165.6, 163.6, 149.1, 139.3, 132.5, 131.5, 131.2, 127.9, 124.2, 119.6, 52.5.

T4: Yield (%) = 80%. **¹H-NMR (300MHz, CDCl₃)** δ (ppm) = 8.48-8.39 (m, 4H), 8.14 (d, *J* = 9.06 Hz, 2H), 7.11 (d, *J* = 9.06 Hz, 2H), 3.9 (s, 3H). **¹³C-NMR (75 MHz, CDCl₃)** δ (ppm) = 163.0, 160.8, 148.9, 133.1, 130.0, 127.7, 126.8, 124.2, 121.4, 114.7, 55.6.

T5: Yield (%) = 48%. **¹H-NMR (300MHz, DMSO-d₆)** δ (ppm) = 8.2-8.17 (m, 4H), 8.08 (d, *J* = 8.56 Hz, 2H), 7.1 (d, *J* = 8.61 Hz, 2H), 3.83 (s, 3H). **¹³C-NMR (75 MHz, DMSO-d₆)** δ (ppm) = 166.2, 164.6, 161.3, 138.8, 131.7, 131.2, 128.3, 119.6, 118.5, 114.7, 55.3.

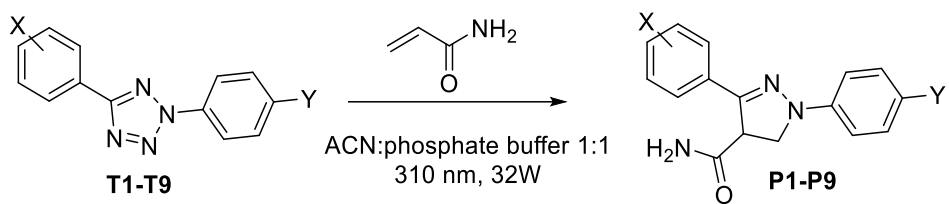
T6: Yield (%) = 40%. The compound was fully characterized according to the literature²¹¹.

T7: Yield (%) = 35%. **¹H-NMR (300MHz, D₂O)** δ (ppm) = 8.36 (d, *J* = 8.76 Hz, 2H), 8.19 (m, 4H), 7.17 (d, *J* = 8.84 Hz, 2H), 4.27 (t, *J* = 4.39 Hz), 3.92-3.61 (m, 10H), 3.01 (s, 6H). **¹³C-NMR (75 MHz, D₂O)** δ (ppm) = 169.9, 167.0, 162.9, 140.7, 136.1, 130.7, 130.0, 121.1, 120.9, 116.6, 74.0, 72.1, 71.8, 71.1, 69.1, 62.6, 59.1, 44.3, 36.8.

T8: Yield (%) = 46%. **¹H-NMR (300MHz, D₂O)** δ (ppm) = 8.36 (m, 4H), 8.2 (d, *J* = 8.71 Hz, 2H), 8.11 (d, *J* = 8.38 Hz, 2H), 3.85 (t, *J* = 1.5 Hz, 4H), 3.45 (t, *J* = 5.69 Hz, 4H), 3.03 (s, 12H). **¹³C-NMR (75 MHz, D₂O)** δ (ppm) = 170.4, 169.7, 166.2, 140.5, 137.1, 136.4, 134.8, 131.7, 130.7, 129.7, 129.6, 128.5, 128.4, 121.2, 59.0, 58.9, 58.8, 44.2, 36.8.

T9: Yield (%) = 54%. **¹H-NMR (300MHz, D₂O)** δ (ppm) = 8.36 (d, *J* = 8.27 Hz, 2H), 8.12 (m, 4H), 7.24 (d, *J* = 9.11 Hz, 2H), 4.27 (t, *J* = 4.67 Hz, 2H), 3.94 (q, *J* = 4.6 Hz, 2H), 3.91-3.59 (m, 8H), 2.99 (s, 6H). **¹³C-NMR (75 MHz, D₂O)** δ (ppm) = 182.9, 168.4, 163.4, 159.8, 134.7, 129.9, 129.8, 127.4, 126.1, 120.8, 114.8, 71.8, 69.9, 69.6, 68.8, 67.3, 60.3, 57.0, 42.2, 38.5, 34.8.

General Procedure for the synthesis of 2,5-diaryl pyrazolines P1-P9:



Scheme 7.48 – General Procedure for synthesis of pyrazolines P1-P9.

Preparative synthesis of pyrazolines has been performed dissolving the corresponding tetrazole in ACN: H₂O 1:1 or pure water, in order to prepare a solution with concentration around 5×10^{-3} M. Acrylamide (20 eq.) was added to the mixture, then solution was divided into different quartz tubes and irradiated with Rayonet at 310 nm (with two 15W lamps). Crude was purified with flash chromatography (DCM:MeOH 8:1) or, in case of water soluble tetrazoles, with reverse phase column chromatography (H₂O 0.1% TFA/ACN gradient) with method **5P**, described in the previous section.

P1: Yield (%) = 29%. **¹H-NMR (300MHz, DMSO-d₆)** δ (ppm) = 7.67 (s, 1H), 7.55 (d, *J* = 9.0 Hz, 2H), 7.27 (s, 1H), 6.96-6.80 (m, 6H), 4.42 (dd, *J* = 12.4, 8.7 Hz, 1H), 3.70 (s, 3H), 3.66 (d, *J* = 5.2 Hz, 1H), 3.14 (dd, *J* = 17.3, 8.7 Hz, 1H). **¹³C-NMR (75 MHz, DMSO-d₆)** δ (ppm) = 173.3, 158.1, 152.6, 147.2, 140.0, 127.3, 123.1, 115.4, 114.4, 113.8, 63.6, 55.3.

P2: Yield (%) = 25%. **¹H-NMR (300MHz, DMSO-d₆)** δ (ppm) = 7.68 (s, 1H), 7.37-7.25 (m, 4H), 7.01-6.87 (m, 5H), 4.55 (dd, *J* = 12.6, 8.4 Hz, 1H), 3.81 (s, 3H), 3.71 (s, 3H), 3.32-3.10 (m, 1H). **¹³C-NMR (75 MHz, DMSO-d₆)** δ (ppm) = 172.9, 159.4, 152.9, 146.5, 139.2, 133.5, 129.7, 118.1, 114.5, 114.4, 113.9, 110.5, 63.4, 55.3, 55.1.

P5: Yield (%) = 11%. **¹H-NMR (300MHz, DMSO-d₆)** δ (ppm) = 7.84-7.70 (m, 5H), 7.36 (s, 1H), 7.03-6.99 (m, 4H), 4.77 (dd, 12.4, 6.18 Hz, 1H), 3.8 (s, 3H), 3.72 (m, 1H). **¹³C-NMR (75 MHz, DMSO-d₆)** δ (ppm) = 172.1, 167.3, 160.2, 149.7, 147.5, 130.9, 127.6, 124.1, 119.6, 114.2, 111.3, 61.2, 55.3.

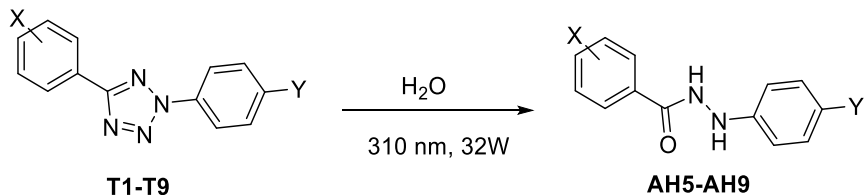
P6: Yield (%) = 13%. **¹H-NMR (300MHz, DMSO-d₆)** δ (ppm) = 7.98 (d, *J* = 9.16 Hz, 2H), 7.8-7.78 (m, 3H), 7.41 (s, 1H), 7.01 (d, *J* = 9.03 Hz, 2H), 6.91 (d, *J* = 9.05 Hz, 2H), 4.66 (dd, *J* = 12.6, 8.02 Hz, 1H), 3.78 (m, 1H), 3.7 (s, 3H), 3.28-3.2 (m, 1H). **¹³C-NMR (75 MHz, DMSO-d₆)** δ (ppm) = 172.6, 167.0, 153.1, 145.4, 138.5, 136.2, 129.8, 129.6, 125.3, 114.5, 113.9, 113.7, 63.2, 55.3.

P7: Yield (%) = 15%. **¹H-NMR (300MHz, D₂O)** δ (ppm) = 7.52 (d, *J* = 5.7 Hz, 2H), 7.32 (d, *J* = 8.5 Hz), 6.73 (m, 4H), 4.37 (m, 1H), 3.9 (m, 2H), 3.64-3.29 (m, 11H), 3.23 (m, 1H), 3.06 (m, 2H), 3.02-2.85 (m, 2H), 2.81 (s, 6H). **¹³C-NMR (75 MHz, D₂O)** δ (ppm) = 175.6, 170.0, 159.1, 150.9, 146.9, 128.8, 127.7, 123.7, 122.2, 118.0, 114.6, 114.2, 111.7, 71.6, 69.7, 69.3, 68.8, 66.9, 61.3, 60.2, 56.8, 42.9, 34.8.

P8: Yield (%) = 16%. **¹H-NMR (300MHz, DMSO-d₆)** δ (ppm) = 9.0 (s, 1H), 8.68 (s, 1H), 8.0 (d, *J* = 7.8 Hz, 2H), 7.9-7.83 (m, 5H), 7.4 (s, 1H), 7.08 (d, *J* = 8.6 Hz, 2H), 4.91 (dd, *J* = 12.5, 6.1 Hz, 1H), 3.78 (t, *J* = 4.7 Hz, 1H), 3.63 (m, 4H), 3.36 (d, *J* = 6.39 Hz, 1H), 3.26 (m, 4H), 2.83 (s, 6H). **¹³C-NMR (75 MHz, DMSO-d₆)** δ (ppm) = 173.4, 171.7, 155.5, 80.2, 78.0, 54.0, 31.3, 28.2, 27.9, 27.6, 26.3.

P9: Yield (%) = 12%. **¹H-NMR (300MHz, DMSO-d₆)** δ (ppm) = 8.01-7.87 (m, 5H), 7.17-7.08 (m, 3H), 6.98-6.93 (m, 2H), 4.23 (t, *J* = 4.6 Hz, 1H) 4.11 (m, 2H), 3.92 (t, *J* = 4.5 Hz, 1H), 3.85 (m, 2H), 3.81-3.67 (m, 10H), 3.59 (dt, *J* = 6.8, 3.4 Hz, 3H), 3.02 (s, 6H). **¹³C-NMR (75 MHz, DMSO-d₆)** δ ppm 170.3, 140.2, 134.4, 129.4, 129.1, 129.0, 128.6, 127.9, 127.6, 127.3, 127.1, 117.0, 116.9, 116.3, 116.1, 116.0, 107.8, 74.9, 74.0, 72.1, 72.1, 71.7, 71.3, 71.1, 69.4, 69.3, 66.1, 62.5, 59.3, 44.3, 40.2, 36.8, 31.1.

General Procedure for the synthesis of Acyl Hydrazides AH5-AH9.



Scheme 7.49 – General Procedure for the synthesis of acyl hydrazides AH5-AH9.

Preparative synthesis of pyrazolines has been performed dissolving the corresponding tetrazole in water or in 1:1 ACN: H₂O mixture, in order to prepare a solution with concentration around 5*10⁻³ M. Solution was divided into different quartz tubes and irradiated with Rayonet at 310 nm (with two 15W lamps) for not more than 2 hours. Crude was purified with reverse phase column chromatography (H₂O 0.1% TFA/ACN gradient) with method **5P**, described in the previous section.

AH5: Yield (%) = 7%. **¹H-NMR (300MHz, DMSO-d₆)** δ (ppm) = 10.3 (s, 1H), 8.52 (s, 1H), 7.9 (d, *J* = 8.49 Hz, 2H), 7.77 (d, *J* = 8.49 Hz, 2H), 7.06 (d, *J* = 8.52 Hz, 2H), 6.78 (d, *J* = 8.39 Hz, 2H), 3.83 (s, 1H). **¹³C-NMR (75 MHz, DMSO-d₆)** δ (ppm) = 167.3, 165.8, 162.0, 153.4, 130.9, 129.2, 124.8, 119.9, 113.7, 110.9, 55.4.

AH6: Yield (%) = 10%. **¹H-NMR (300MHz, DMSO-d₆)** δ (ppm) = 13.2 (s, 1H), 10.5 (s, 1H), 8.06-7.98 (m, 4H), 7.64 (s, 1H), 6.78 (s, 4H), 3.68 (s, 3H). **¹³C-NMR (75 MHz, DMSO-d₆)** δ (ppm) = 166.7, 165.6, 152.8, 143.1, 136.9, 133.3, 129.3, 127.5, 114.3, 113.9, 55.3.

AH7: Yield (%) = 15%. **¹H-NMR (300MHz, D₂O)** δ (ppm) = 7.8 (d, *J* = 8.76 Hz, 2H), 7.66 (d, *J* = 8.65 Hz, 2H), 7.07 (d, *J* = 8.77 Hz, 2H), 6.90 (d, *J* = 8.66 Hz), 4.22 (t, *J* = 4.05 Hz, 2H), 3.86 (t, *J* = 4.2 Hz, 2H), 3.70-3.62 (m, 10H), 3.55 (m, 2H), 3.32 (t, *J* = 5.82 Hz, 2H), 2.89 (s, 6H). **¹³C-NMR (75 MHz, D₂O)** δ (ppm) = 170.8, 170.3, 161.5, 151.3, 129.3, 128.9, 124.1, 124.1, 114.7, 112.2, 71.6, 69.7, 69.3, 68.8, 67.1, 60.2, 56.9, 43.0, 34.9.

AH8: Yield (%) = 14%. **¹H-NMR (300MHz, D₂O)** δ (ppm) = 7.94 (m, 4H), 7.75 (d, *J* = 8.22 Hz, 2H), 7.00 (d, *J* = 8.29 Hz, 2H), 3.82-3.75 (m, 4H), 3.46-3.37 (m, 4H), 2.98 (s, 6H), 2.96 (s, 6H). **¹³C-NMR (75 MHz, D₂O)** δ (ppm) = 170.8, 170.4, 170.1, 151.0, 135.0, 128.9, 127.7, 127.2, 124.3, 112.3, 56.9, 56.6, 43.0, 35.1, 34.9.

AH9: Yield (%) = 11%. **¹H-NMR (300MHz, D₂O)** δ (ppm) = 7.91 (s, 4H), 6.96 (s, 4H), 4.15 (m, 2H), 3.87-3.62 (m, 12H), 3.45 (t, *J* = 5.99 Hz, 2H), 2.95 (s, 6H). **¹³C-NMR (75 MHz, D₂O)** δ (ppm) = 170.3, 169.8, 152.7, 141.3, 136.2, 135.2, 129.8, 127.6, 127.3, 116.0, 115.2, 71.5, 69.6, 69.3, 69.0, 67.7, 60.2, 56.5, 42.9, 35.0.

7.4.1.2 Spectroscopic and Photochemical Studies

- **Molar Absorbivity:** Molar extinction coefficients of compounds **T1-T9, AH5-AH9, P1,P2** and **P5-P9** were measured by adding increasing concentrations of compound stock solution to 3 ml of 1:1 ACN:PBS (50 mM, pH 7.4) or pure PBS (50 mM, pH 7.4) solution in 3.5 ml quartz cuvette and recording UV-VIS spectra after each addition.
- **Reaction quantum yields (Φ)** were measured by irradiating 3 mL of 10^{-5} M solutions of tetrazoles **T1-T9** in 1 cm optical path quartz cuvettes. The lamp source was a focalized 150 W high-pressure mercury arc fitted with a transmittance filter (transmission, 313 nm) and a single-photon detector (photon flux $q_p=2.6*10^{-7}$ Einstein/cm²*min⁻¹). Potassium ferrioxalate was used as the actinometer to measure photon flux at desired wavelength. Tetrazole consumption was monitored through HPLC analysis, at different times of irradiation, with method **5A**, described in the previous section.
- **Fluorescence Quantum Yields (Φ_f):** Fluorescence quantum yields in water were measured in a 1 cm optical path cuvettes, using 4',6-Diamidino-2-phenylindole (DAPI) as standard, with $\lambda_{exc}=350$ nm. For experiments in DMSO, the same reference has been used, but here we have used $\lambda_{exc}=310$ nm. Increasing volumes of pyrazoline stock solution were added to 3 ml of solvent, then absorption and emission spectra were recorded. Quantum yields have been measured applying the following equation:

$$\Phi_f = (A_x/A_{std}) * (n_x/n_{std}) * \Phi_{std}$$

- **Trapping experiments:** Photoreactivity in presence of acrylamide was measured upon irradiation of 10^{-5} M solution of tetrazoles, in 6 ml of 1:1 ACN:PBS (50 mM, pH 7.4) or pure PBS (50 mM, pH 7.4), in presence of 100, 50, 20, 10 or 5 equivalents of acrylamide. Irradiation experiments were performed with multi-lamps photoreactor, equipped with two 15W lamps with emission at 310 nm. Reactions were monitored through HPLC and UV-VIS analysis, at different conversions, and the amount of reagent and products were determined through a calibration curve, realized using synthesized tetrazoles, acyl hydrazides and pyrazolines as references.

7.4.1.3 Fret-Melting Assay

FRET melting experiments were carried out on a Stratagene Mx3005P real-time PCR equipment in 96 wells plates. Experiments were performed in $1*10^{-2}$ M lithium cacodylate buffer (pH 7.2), with $1*10^{-2}$ M KCl and $9*10^{-2}$ M LiCl concentrations, depending on the T_m of the G4s alone. The DNA concentration was $2*10^{-7}$ M. The stabilization (T_m) induced by compounds was calculated as the difference between the mid-transition temperature of the nucleic acid (NA) alone and measured with the relevant ligand concentration. Data were recorded with the same instrument parameters: $\lambda_{exc}=492$ nm, $\lambda_{em}=516$ nm, T interval = 25–95°C, ramp: 25°C for 5 min, then 1°C/min, measurements every 1°C, 8x magnification of the fluorescence signal).

For the experiments, the following oligonucleotide sequences were used:

LTRIII: FAM-TGGGAGGCGTGGCCTGGCGGGACTGGGGT-TAMRA

LTRIV: FAM-TGGGCAGGACTGGGGAGTGGT-TAMRA

F21T: FAM-GGGTTAGGGTTAGGGTTAGGG-TAMRA

c-KIT2: FAM-GGGCGGGCGCGAGGGAGGGG-TAMRA

7.4.1.4 Cells and Parasites Protocols

- **Cell and Parasites culture protocols:** Human MRC5-cell line (fibroblast derived from lung tissue) was cultured in DMEM (Invitrogen) medium plus 10% Fetal Bovine Serum Albumin (FBSA), 2 mM Gluthamine and 100 U/ml penicillin. Cells were grown in monolayer (5% CO₂, 37°C) in DMEM medium with 4.5 g/L of glucose for HT29 and 1 g/L for MRC5. Cells were plated and passaged according to ATCC recommendations and were used for the experiments while in the exponential growth phase. ‘Single marker’ (S16) BSF *Trypanosoma Brucei* (Lister 427, antigenic type MiTat 1.2, clone 221a) were cultured at 37°C, 5% CO₂ in HMI-9 medium supplemented with 20% heat-inactivated fetal bovine serum (hiFBS, Invitrogen). *Leishmania Major* (MHOM/IL/80/Friedlin) promastigotes were cultured at 28 °C in RPMI-1640 medium (Invitrogen, Carlsbad, CA) modified with fetal bovine serum (hiFBS, Invitrogen).
- **MTT Test on cells:** Toxicity against cells has been determined through incubation of 4*10⁶ HT29 cells and 7*10⁵ MRC5 cells in 96-wells plates, in 100 µl of DMEM solution, with increasing concentrations of selected compounds. Cells were stored at 37°C (with 5% CO₂) for 72 hours. After this time, IC₅₀ values were measured through MTT assay. After 3 days of incubation, 10 µl of 5 mg/ml solution of MTT were added to each well, then solution were centrifugated and stored at 37°C for 4 hours. Cell media was removed and cells were dissolved into 100 µl of DMSO, then analyzed at the plate reader, recording the absorbance at λ= 590 nm.
- **MTT Test on *Leishmania Major*:** Activity of compounds against *Leishmania Major* has been determined upon incubation of 2*10⁵ parasites, in 96-wells plates, in 100 µl of culture media, in presence of increasing concentrations of compounds. After an incubation period of 3 days, 10 µl of 5mg/ml of MTT solution were added to each well, then parasites were stored for further 4 hours at 28°C. Then, each solution was treated with 50 µl of 20% Sodium Dodecyl Sulphate and incubated at 37°C overnight. In the end, all plates were analyzed at the plate reader, recording the absorbance at λ = 590 nm.
- **Alamar Blue Assay on *Trypanosoma Brucei*:** Toxicity on *T. Brucei* was determined through incubation of 3*10⁵ parasites in 96-wells plates, in 100 µl of solutions, adding increasing concentrations of ligands. After 3 days of incubation at 37°C, Alamar Blue Assay (or Resazurin Assay) was performed to measure IC₅₀ values. In details, 20 µl of Alamar Blue solution (5 g/L) were added to each plate, then they were incubated at 37°C for 4 hours. Later, 50 µl of sodium dodecyl sulfate solution (3%) were added to each well, then plates were incubated again for one hour at 37°C. In the end, fluorescence analysis of each solution was performed with plate reader.

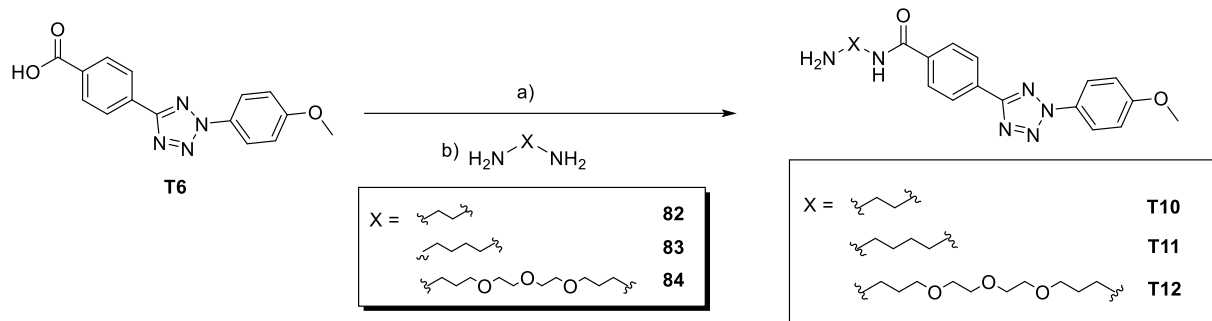
7.4.2 NDI-Tetrazole conjugates

7.4.2.1 Synthesis of compounds

Procedure for the synthesis of Tetrazole T6:

Tetrazole **T6** has been synthesized and characterized according to the procedure described in Section 7.4.1.1.

General Procedure for the synthesis of tetrazoles **T10-T12**:



Scheme 7.50 – General procedure for the synthesis of Tetrazoles **T10-T12.**

In a round-bottomed flask, tetrazole **T6** (1.35 mmol, 1 eq.) was suspended in 10 ml of acetonitrile, then solution was cooled to 0°C in an ice-bath. Then, DIPEA (2.7 mmol, 2 eq.) and PyBOP (1.35 mmol, 1 eq.) were added to the mixture in one portion. Suspension was stirred for 30 minutes at 0°C. In the meantime, in another one-necked flask, amine **82-84** (13.5 mmol, 10 eq.) were dissolved in 5 ml of acetonitrile and cooled in an ice-bath. Subsequently, solution containing activated tetrazole **T6** was transferred into a dropping funnel and added dropwise to the excess of amine, to avoid polymerization reactions. After two hours, solvent was removed under vacuum, then the crude was resuspended in 1M NaOH solution and extracted three times with ethyl acetate (3x30 ml). Product was purified through flash column chromatography, using 9:1 DCM:MeOH (with 1% NEt₃) as eluent.

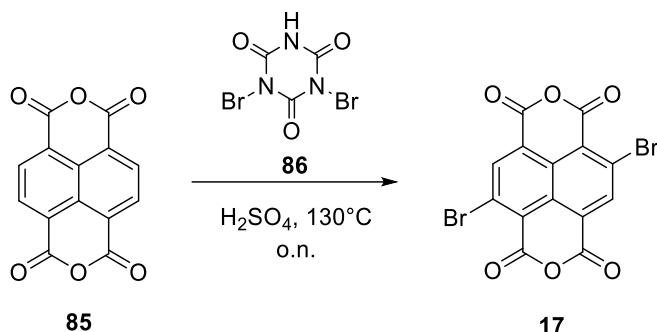
T10: Yield (%) = 41%, white solid. **¹H-NMR (300 MHz, DMSO-d₆)** δ (ppm) = 8.81 (1H, s), 8.29 (2H, d, J=8.2 Hz), 8.11 (2H, d, J=8.6Hz), 7.83 (2H, s), 7.24 (2H, d, J=8.9 Hz), 3.88 (3H, s), 3.02 (2H, s), 2.51 (2H, s). **¹³C-NMR (75 MHz, DMSO-d₆)** δ (ppm) = 166.2, 163.6, 160.5, 135.9, 129.5, 129.1, 128.4, 126.5, 121.8, 115.1, 55.7, 53.6, 45.8, 45.7, 25.9, 8.6.

T11: Yield (%) = 66%, white solid. **¹H-NMR (300 MHz, DMSO-d₆)** δ (ppm) = 8.71 (1H, s), (8.24 (2H, d, J=8.1 Hz), 8.07 (4H, t, J=9.3), 7.23 (2H, d, J=8.9 Hz), 3.88 (3H, s), 3.27 (2H, t, J=5.9 Hz), 2.58 (3H, t, J=6.7 Hz), 1.57-1.40 (5H, m). **¹³C-NMR (75 MHz, DMSO-d₆)** δ (ppm) = 165.3, 163.7, 160.5, 136.6, 129.5, 128.7, 128.1, 126.4, 121.7, 115.1, 55.7, 41.3, 30.4, 26.6.

T12: Yield (%) = 38%, white solid. **¹H-NMR (300 MHz, D₂O)** δ (ppm) = 7.16 (m, 4H), 6.89 (d, J= 8.00 Hz, 2H), 6.15 (d, J= 9.06 Hz, 2H), 3.57 (s, 3H), 3.55-3.53 (m, 10H), 3.44 (t, J= 5.9 Hz, 2H), 3.22-3.15 (m, 4H), 3.03 (t, J=

7.09 Hz, 2H), 1.87 (q, J = 6.51 Hz, 2H), 1.69-1.65 (m, 2H). $^{13}\text{C-NMR}$ (75 MHz, D_2O) δ (ppm) = 167.2, 162.3, 159.4, 134.3, 128.3, 128.1, 127.0, 125.8, 119.7, 113.9, 69.5, 69.4, 69.3, 68.6, 68.2, 54.9, 37.6, 37.1, 28.4, 26.4.

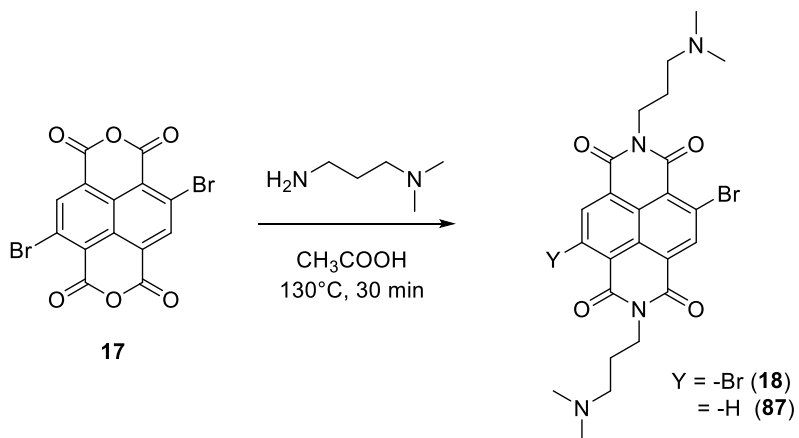
Synthesis of dibromo-1,4,5,8-Naphthalenetetracarboxylic dianhydride 17:



Scheme 7.51 – Bromination reaction to obtain dibromoanhydride 85.

In a round-bottomed flask, 1,4,5,8-Naphthalenetetracarboxylic dianhydride **85** (7 mmol, 1 eq.) was suspended in 40 ml of concentrated H_2SO_4 , then dibromoiso-cyanuric acid **86** (10.5 mmol, 1.5 eq.) were added. Reaction was stirred at 130°C overnight. After this time, mixture was cooled down to room temperature and poured in a becker containing ice and a 5% solution of sodium thiosulphate. The desired product precipitated as yellow solid, therefore was filtered on a Buchner funnel and dried with a mechanical pump. The obtained dibromo-1,4,5,8-Naphthalenetetracarboxylic dianhydride was used for the subsequent step without no further purification.

Synthesis of Naphthalenediimide 18 and 87:

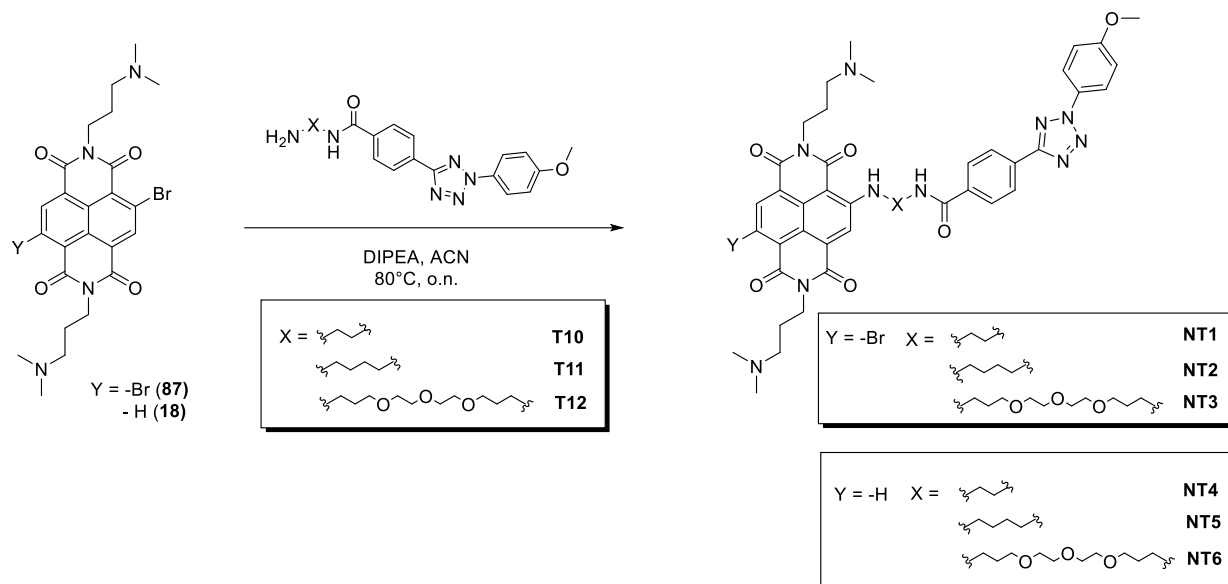


Scheme 7.52 – Immidation reaction of dianhydride 17.

Dibromo-1,4,5,8-Naphthalenetetracarboxylic dianhydride **17** (3.5 mmol, 1 eq.) was suspended in 100 ml of CH_3COOH and kept for two minutes in an ultrasonic bath, to favour its dissolution. Then, 3-(dimethylamino)propylamine (7 mmol, 2 eq.) was added and the mixture was heated to 130°C and refluxed for 30 minutes. After this time, solution was cooled to room temperature, poured into a becker containing ice and sodium carbonate. Further addition of sodium carbonate were made until pH 8 was achieved.

Solution was transferred into an extracting funnel and extracted four times with dichloromethane (4x100 ml). Organic phase was dried over sodium sulphate and solvent removed under vacuum. The mixture of products was used for the subsequent step without no further purification.

General Procedure for the synthesis of NDI-Tetrazoles conjugates NT1-NT6:



Scheme 7.53 – General procedure for the synthesis of NDI-Tetrazoles NT1-NT6.

In a round-bottomed flask, NDI 87 (0.74 mmol, 2.5 eq.) was dissolved in 70 ml of ACN and DIPEA (0.3 mmol, 1 eq.) and tetrazole T10-T12 (0.3 mmol, 1 eq.) were added. Solution was stirred at 80°C overnight, until complete substrate consumption. Solvent was removed under vacuum and the crude was purified through reverse phase column chromatography (H_2O 0.1% TFA/ACN gradient) with method **6P**, to afford compounds **NT1-NT6** and anion was exchanged with HCl 10% solution.

NT1*Cl: Yield (%) = 19%, red solid. **1H NMR (300 MHz, DMSO-d₆)** δ (ppm) = 10.16 (1H, s), 9.88 (1H, s), 8.56 (1H, s), 8.36 (1H, s), 8.18 (2H, d, *J*=8.2 Hz), 8.05 (4H, t, *J*=9.0 Hz), 7.24 (2H, d, *J*=8.9 Hz), 4.11 (4H, t, *J*=7 Hz), 3.93 (2H, d, *J*=5.14 Hz), 3.89 (3H, s), 3.67 (2H, d, *J*=5.1 Hz), 2.06 (4H, m), 2.76 (12H, s). **13C-NMR (75 MHz, DMSO-d₆)** δ (ppm) = 166.1, 165.2, 163.5, 161.6, 161.5, 161.0, 160.5, 160.2, 157.7, 151.8, 136.4, 135.9, 129.5, 128.9, 128.4, 128.2, 127.5, 126.3, 123.3, 123.0, 121.7, 121.4, 120.4, 119.1, 118.4, 117.6, 115.2, 99.4, 55.7, 54.5, 42.1, 42.1, 41.9, 37.8, 37.1, 22.8, 22.7.

NT2*Cl: Yield (%) = 10%, red solid. **1H NMR (300 MHz, DMSO-d₆)** δ (ppm) = 10.20 (1H, s), 10.03 (1H, s), 8.76 (1H, s), 8.16 (1H, s), 8.10 (4H, d, *J*=8.7 Hz), 7.96 (2H, d, *J*= 8.2 Hz), 7.25 (2H, d, *J*= 8.9 Hz), 4.11 (4H, d, *J*=7.0 Hz), 3.89 (3H, s), 3.19 (4H, s), 2.75 (12H, s), 2.08 (4H, s), 1.81 (4H, s). **13C-NMR (75 MHz, DMSO-d₆)** δ (ppm) = 165.3, 165.1, 163.5, 161.6, 161.4, 161.0, 160.5, 151.2, 136.0, 129.5, 128.6, 128.1, 128.0, 127.4, 126.1, 122.9, 121.8, 121.2, 118.3, 115.1, 99.0, 55.7, 54.4, 42.0, 26.3, 26.1, 22.8, 22.6.

NT3*Cl: Yield (%) = 15%. **¹H NMR (300 MHz, D₂O)** δ (ppm) = 7.85 (d, *J*= 7.77 Hz, 1H), 7.59 (d, *J* = 7.85 Hz, 1H), 7.38 (s, 1H), 7.33 (d, *J* = 8.14 Hz, 2H), 7.15 (d, *J*= 8.14 Hz, 2H), 7.09 (d, *J*= 8.9 Hz, 2H), 6.67 (d, *J*= 8.97 Hz, 2H), 3.8-3.5 (m, 17H), 3.36 (m, 2H), 3.2-3.08 (m, 8H), 2.8 (s, 12H), 1.99-0.85 (m, 8H). **¹³C-NMR (75 MHz, DMSO-d₆)** δ (ppm) = 166.7, 164.3, 163.0, 162.3, 161.6, 159.6, 151.0, 134.3, 130.2, 127.8, 127.6, 127.1, 126.8, 125.9, 125.2, 124.2, 123.3, 121.1, 119.5, 119.3, 114.1, 97.4, 69.3, 69.2, 69.1, 69.0, 68.9, 67.6, 55.2, 54.7, 54.7, 53.9, 42.3, 39.5, 37.4, 28.0, 27.7, 22.3, 17.2, 15.7.

NT4*Cl: Yield (%) = 18%, red solid. **¹H NMR (300 MHz, DMSO-d₆)** δ (ppm) = 10.56 (1H, s), 10.15 (1H, s), 9.07 (1H, s), 8.47 (1H, d, *J*=7.2 Hz), 8.48 (1H, s), 8.18 (2H, d, *J*=8.2 Hz), 8.06 (4H, t, *J*= 8.75 Hz), 7.23 (2H, d, *J*=9.0 Hz), 4.09 (4H, t, *J*=5.43 Hz), 3.88 (3H, s), 3.66 (2H, d, *J*= 4.41 Hz), 3.35 (12H, s), 3.17 (4H, d, *J*=7.2 Hz), 2.08 (4H, s). **¹³C-NMR (74.5 MHz, DMSO-d₆)** δ (ppm) = 166.1, 165.3, 163.6, 162.9, 162.4, 160.5, 152.2, 136.0, 130.6, 129.5, 128.9, 128.8, 128.2, 127.7, 126.4, 125.9, 123.7, 122.6, 121.7, 119.6, 118.9, 115.1, 99.0, 55.7, 54.3, 54.2, 41.9, 41.8, 37.5, 37.0, 22.8, 22.7.

NT5*Cl: Yield (%) = 9%, red solid. **¹H NMR (300 MHz, DMSO-d₆)** δ (ppm) = 7.91 (1H, d, *J*=7.72 Hz), 7.59 (1H, d, *J*=7.7 Hz), 7.28-7.10 (5H, m), 7.10 (2H, d, *J*=5.16 Hz), 6.58 (2H, d, *J*=6.84 Hz), 3.84 (4H, s), 3.64 (3H, s), 3.29-3.07 (8H, m), 2.87 (12H, s), 1.91 (4H, s) 1.64 (4H, s). **¹³C-NMR (75 MHz, DMSO-d₆)** δ (ppm) = 186.2, 167.3, 164.8, 163.2, 163.0, 162.6, 162.2, 162.1, 159.9, 151.3, 134.7, 130.7, 127.9, 127.9, 127.3, 126.3, 125.7, 124.5, 123.9, 121.6, 119.9, 117.8, 114.3, 97.9, 55.5, 55.1, 55.0, 54.2, 42.7, 25.7, 22.7, 17.6, 16.1, 12.0.

NT6*Cl: Yield (%) = 10%, red solid. **¹H NMR (300 MHz, DMSO-d₆)** δ (ppm) = 7.78 (1H, s), 7.54 (1H, s), 7.36 (2H, d, *J*=8.2 Hz), 7.19 (4H, t, *J*=6.58), 6.73 (2H, d, *J*=8.16 Hz), 3.84 (4H, t, *J*=6.1 Hz), 3.75 (3H, s), 3.63-3.53 (14H, m), 3.26-3.19 (8H, m), 2.88 (12H, s), 2.00 (4H, s), 1.85-1.81 (4H, m). **¹³C-NMR (75 MHz, DMSO)** δ (ppm) = 167.1, 164.4, 162.1, 161.6, 161.6, 160.9, 160.1, 150.8, 136.6, 134.7, 128.2, 127.5, 127.2, 127.0, 125.6, 125.5, 121.5, 121.4, 120.6, 120.0, 119.7, 119.2, 114.5, 99.5, 97.9, 69.7, 69.6, 69.5, 60.1, 68.0, 55.6, 55.1, 55.0, 42.7, 40.0, 38.0, 37.6, 37.1, 28.3, 28.1, 22.6, 22.5.

7.4.2.2. Spectroscopic and Photochemical Studies

- **Molar Absorbivity:** Molar extinction coefficients of compounds **T10-T12** and **NT1-NT6** were measured by adding increasing concentrations of compound stock solution to 3 ml of 1:1 ACN:PBS (50 mM, pH 7.4) solution in 3.5 ml quartz cuvette and recording UV-VIS spectra after each addition.
- **Reaction quantum yields (Φ)** were measured by irradiating 3 mL of 10⁻⁵ M solutions of tetrazoles **T10-T12** and **NT1-NT6**, in 1:1 ACN:water , in 1 cm optical path quartz cuvettes. The lamp source was focalized 150 W high-pressure mercury arc fitted with a transmittance filter (transmission, 313 nm) and a single-photon detector (photon flux q_p=2.6*10⁻⁷ Einstein/cm²*min⁻¹). Potassium ferrioxalate was used as the actinometer to measure photon flux at desired wavelength. Tetrazole consumption was monitored through HPLC analysis, at different times of irradiation, with method **5A**, described in the previous section. Product formation was detected through LC-MS analysis, at different times of irradiation.

- **Fluorescence Quantum Yields (Φ_f):** Fluorescence quantum yields in water were measured in a 1 cm optical path cuvettes, using 4',6-Diamidino-2-phenylindole (DAPI) as standard, with $\lambda_{exc}=350$ nm. For experiments in DMSO, the same reference has been used, but here we have used $\lambda_{exc} = 310$ nm. Increasing volumes of pyrazoline stock solution were added to 3 ml of solvent, then absorption and emission spectra were recorded. Quantum yields have been measured applying the following equation:

$$\Phi_f = (A_x/A_{std}) * (n_x/n_{std}) * \Phi_{std}$$

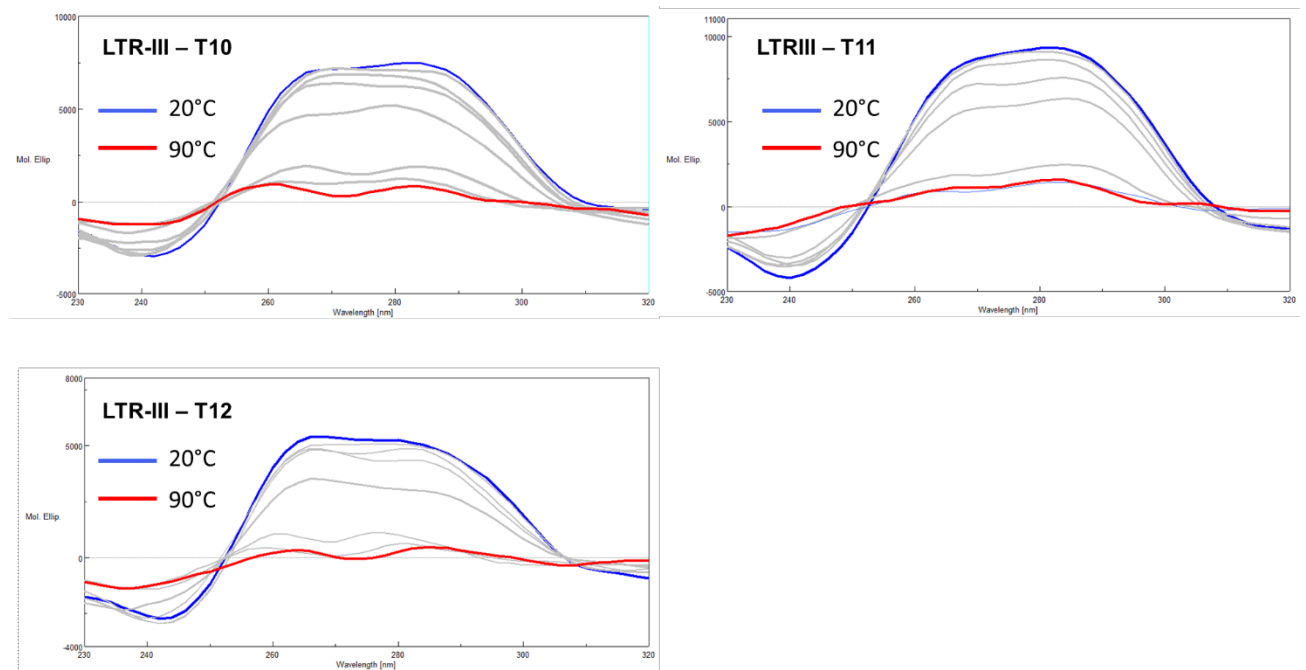
- **Photoreactivity at 517 nm:** Photochemical behaviour at 517 nm has been determined by irradiating 10^{-5} M solution of **NT1-NT6**, dissolved in 6 ml of 1:1 ACN:water solution, with a green LED, centered at 517 nm. Solutions were kept in front of the LED, covered in aluminium foil, for 30 minutes and, for each sample, a dark experiment was performed, to exclude that photoreactivity was induced by thermal activation. Reaction was monitored at different times of irradiations through UV-VIS, HPLC and LC-MS analysis, to identify photogenerated products. For HPLC analysis, method **5A** was used, while, for LC-MS, product identification has been accomplished.

7.4.2.3 CD-Melting Experiments

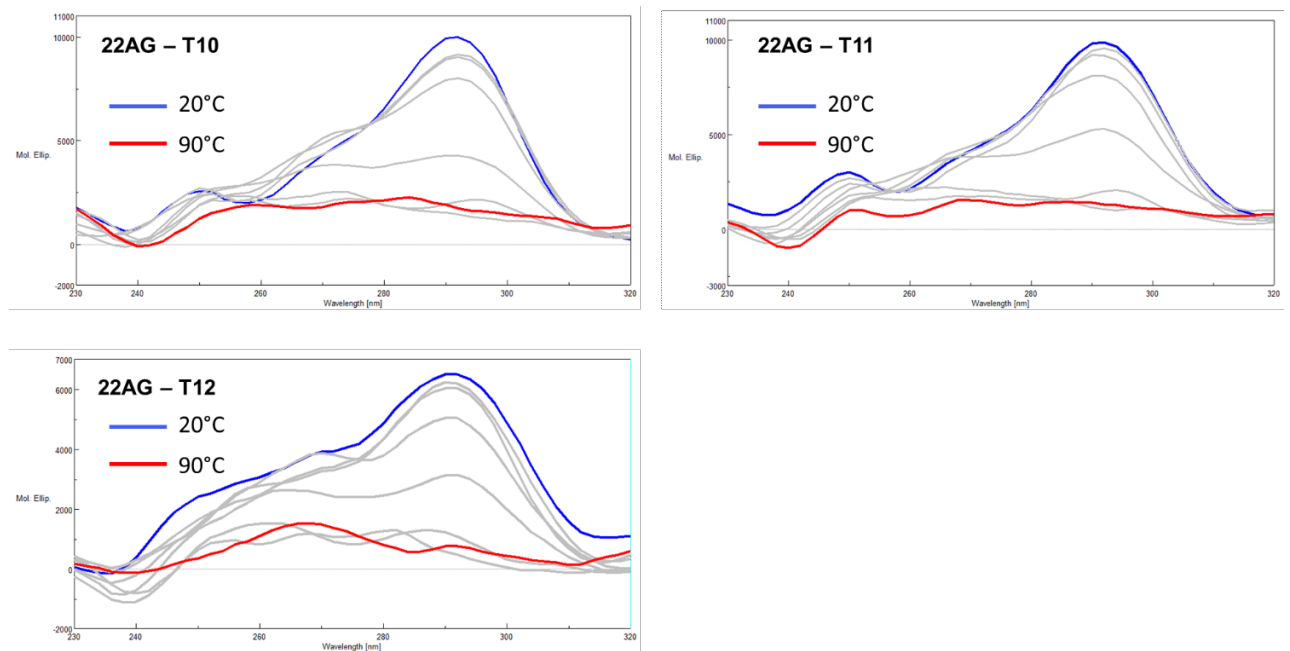
CD titrations were performed using a JASCO J1500 spectropolarimeter equipped with a Peltier temperature controller and black-walled rectangular quartz cells with 1 cm path length.

- A 1 ml solution of 2.5 μ M oligonucleotide in 10 mM lithium cacodylate buffer (pH 7.2) and KCl (10 mM for LTRIII, 20 mM for 22AG and 5 mM for c-MYC) was heated for 5 min at 95°C and subsequently cooled to 4°C for 16 hours. To this solution, volumes of stock solution of ligands **NT4-NT6** and **T10-T12** were added to achieve concentration of 10 μ M. Spectra were recorded from 230 to 320 nm, with temperature gradient from 20°C to 95°C, increased of 1°C / min. Spectra were recorded every ten degrees and were corrected by a baseline obtained from the buffer in the same conditions.

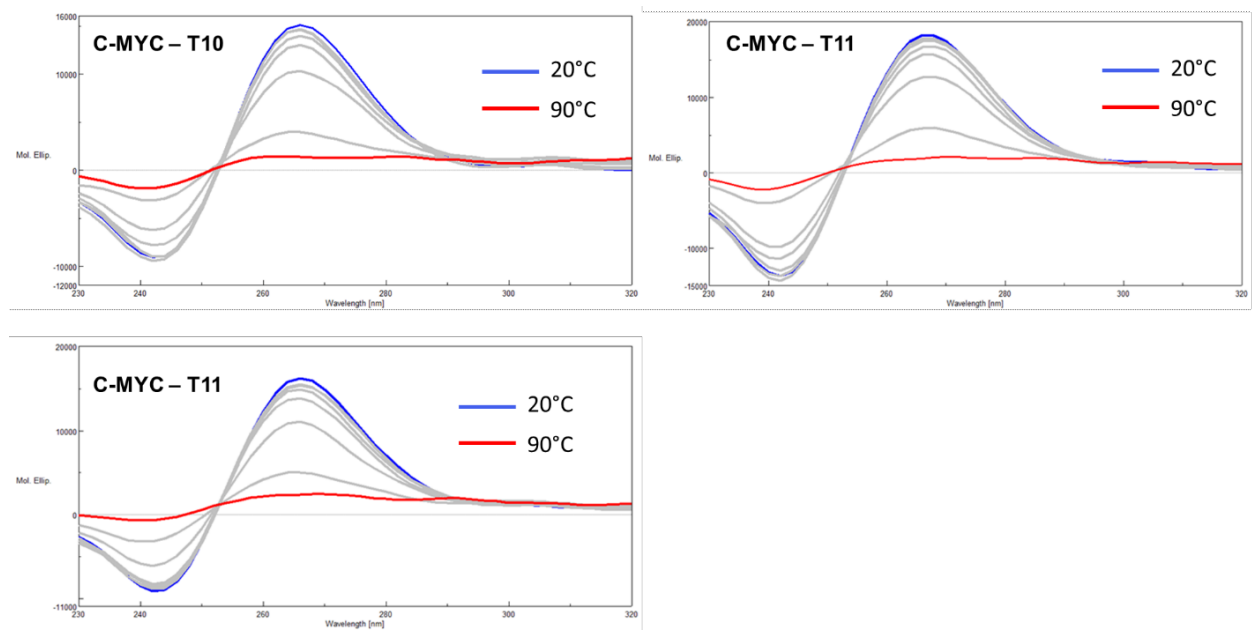
- CD-Melting Spectra of T10-T12 with LTR-III:



- CD-Melting Spectra of T10-T12 with 22AG:



- CD-Melting Spectra of T10-T12 with c-MYC:



References:

1. Travers, A.; Muskhelishvili, G., DNA structure and function. *The FEBS Journal* **2015**, 282 (12), 2279-2295.
2. Kaushik, M.; Kaushik, S.; Roy, K.; Singh, A.; Mahendru, S.; Kumar, M.; Chaudhary, S.; Ahmed, S.; Kukreti, S., A bouquet of DNA structures: Emerging diversity. *Biochem Biophys Rep* **2016**, 5, 388-395.
3. Wang, G.; Vasquez, K. M., Impact of alternative DNA structures on DNA damage, DNA repair, and genetic instability. *DNA Repair* **2014**, 19, 143-151.
4. Ida, R.; Kwan, I. C.; Wu, G., Direct ^{23}Na NMR observation of mixed cations residing inside a G-quadruplex channel. *Chem Commun (Camb)* **2007**, (8), 795-7.
5. Cesare Marincola, F.; Virno, A.; Randazzo, A.; Mocci, F.; Saba, G.; Lai, A., Competitive binding exchange between alkali metal ions (K^+ , Rb^+ , and Cs^+) and Na^+ ions bound to the dimeric quadruplex [$d(\text{G4T4G4})_2$]: a ^{23}Na and ^1H NMR study. *Magn Reson Chem* **2009**, 47 (12), 1036-42.
6. Sen, D.; Gilbert, W., [10] Guanine quartet structures. In *Methods in Enzymology*, Academic Press: 1992; Vol. 211, pp 191-199.
7. Burge, S.; Parkinson, G. N.; Hazel, P.; Todd, A. K.; Neidle, S., Quadruplex DNA: sequence, topology and structure. *Nucleic Acids Res* **2006**, 34 (19), 5402-15.
8. Ma, Y.; Iida, K.; Nagasawa, K., Topologies of G-quadruplex: Biological functions and regulation by ligands. *Biochem Biophys Res Commun* **2020**, 531 (1), 3-17.
9. Neidle, S., The structures of quadruplex nucleic acids and their drug complexes. *Curr Opin Struct Biol* **2009**, 19 (3), 239-50.
10. Hazel, P.; Huppert, J.; Balasubramanian, S.; Neidle, S., Loop-Length-Dependent Folding of G-Quadruplexes. *Journal of the American Chemical Society* **2004**, 126 (50), 16405-16415.
11. Joachimi, A.; Benz, A.; Hartig, J. S., A comparison of DNA and RNA quadruplex structures and stabilities. *Bioorg Med Chem* **2009**, 17 (19), 6811-5.
12. Chen, Y.; Yang, D., Sequence, stability, and structure of G-quadruplexes and their interactions with drugs. *Curr Protoc Nucleic Acid Chem* **2012**, Chapter 17, Unit17.5.
13. Bhattacharyya, D.; Mirihana Arachchilage, G.; Basu, S., Metal Cations in G-Quadruplex Folding and Stability. *Front Chem* **2016**, 4, 38.
14. Largy, E.; Mergny, J. L.; Gabelica, V., Role of Alkali Metal Ions in G-Quadruplex Nucleic Acid Structure and Stability. *Met Ions Life Sci* **2016**, 16, 203-58.
15. Chen, X. C.; Chen, S. B.; Dai, J.; Yuan, J. H.; Ou, T. M.; Huang, Z. S.; Tan, J. H., Tracking the Dynamic Folding and Unfolding of RNA G-Quadruplexes in Live Cells. *Angew Chem Int Ed Engl* **2018**, 57 (17), 4702-4706.
16. Chaires, J. B., Human telomeric G-quadruplex: thermodynamic and kinetic studies of telomeric quadruplex stability. *Febs j* **2010**, 277 (5), 1098-106.
17. Rigo, R.; Palumbo, M.; Sissi, C., G-quadruplexes in human promoters: A challenge for therapeutic applications. *Biochimica et Biophysica Acta (BBA) - General Subjects* **2017**, 1861 (5, Part B), 1399-1413.
18. Bugaut, A.; Balasubramanian, S., 5'-UTR RNA G-quadruplexes: translation regulation and targeting. *Nucleic Acids Research* **2012**, 40 (11), 4727-4741.
19. Huppert, J. L.; Balasubramanian, S., Prevalence of quadruplexes in the human genome. *Nucleic Acids Research* **2005**, 33 (9), 2908-2916.
20. Besnard, E.; Babled, A.; Lapasset, L.; Milhavet, O.; Parrinello, H.; Dantec, C.; Marin, J. M.; Lemaitre, J. M., Unraveling cell type-specific and reprogrammable human replication origin signatures associated with G-quadruplex consensus motifs. *Nat Struct Mol Biol* **2012**, 19 (8), 837-44.
21. Hirashima, K.; Seimiya, H., Telomeric repeat-containing RNA/G-quadruplex-forming sequences cause genome-wide alteration of gene expression in human cancer cells *in vivo*. *Nucleic Acids Res* **2015**, 43 (4), 2022-32.
22. Tian, T.; Chen, Y.-Q.; Wang, S.-R.; Zhou, X., G-Quadruplex: A Regulator of Gene Expression and Its Chemical Targeting. *Chem* **2018**, 4 (6), 1314-1344.

23. Brázda, V.; Hároníková, L.; Liao, J. C.; Fojta, M., DNA and RNA quadruplex-binding proteins. *Int J Mol Sci* **2014**, *15* (10), 17493-517.
24. Biffi, G.; Tannahill, D.; McCafferty, J.; Balasubramanian, S., Quantitative visualization of DNA G-quadruplex structures in human cells. *Nat Chem* **2013**, *5* (3), 182-6.
25. Moye, A. L.; Porter, K. C.; Cohen, S. B.; Phan, T.; Zyner, K. G.; Sasaki, N.; Lovrecz, G. O.; Beck, J. L.; Bryan, T. M., Telomeric G-quadruplexes are a substrate and site of localization for human telomerase. *Nature Communications* **2015**, *6* (1), 7643.
26. Chambers, V. S.; Marsico, G.; Boutell, J. M.; Di Antonio, M.; Smith, G. P.; Balasubramanian, S., High-throughput sequencing of DNA G-quadruplex structures in the human genome. *Nature Biotechnology* **2015**, *33* (8), 877-881.
27. Schmutz, I.; de Lange, T., Shelterin. *Current Biology* **2016**, *26* (10), R397-R399.
28. Dai, J.; Carver, M.; Yang, D., Polymorphism of human telomeric quadruplex structures. *Biochimie* **2008**, *90* (8), 1172-1183.
29. Ambrus, A.; Chen, D.; Dai, J.; Bialis, T.; Jones, R. A.; Yang, D., Human telomeric sequence forms a hybrid-type intramolecular G-quadruplex structure with mixed parallel/antiparallel strands in potassium solution. *Nucleic Acids Res* **2006**, *34* (9), 2723-35.
30. Phan, A. T.; Luu, K. N.; Patel, D. J., Different loop arrangements of intramolecular human telomeric (3+1) G-quadruplexes in K⁺ solution. *Nucleic Acids Res* **2006**, *34* (19), 5715-9.
31. Dai, J.; Carver, M.; Punchihewa, C.; Jones, R. A.; Yang, D., Structure of the Hybrid-2 type intramolecular human telomeric G-quadruplex in K⁺ solution: insights into structure polymorphism of the human telomeric sequence. *Nucleic Acids Res* **2007**, *35* (15), 4927-40.
32. Kolesnikova, S.; Curtis, E. A., Structure and Function of Multimeric G-Quadruplexes. *Molecules* **2019**, *24* (17).
33. Yu, H. Q.; Miyoshi, D.; Sugimoto, N., Characterization of structure and stability of long telomeric DNA G-quadruplexes. *J Am Chem Soc* **2006**, *128* (48), 15461-8.
34. Petraccone, L.; Trent, J. O.; Chaires, J. B., The tail of the telomere. *J Am Chem Soc* **2008**, *130* (49), 16530-2.
35. Schaffitzel, C.; Berger, I.; Postberg, J.; Hanes, J.; Lipps, H. J.; Plückthun, A., In vitro generated antibodies specific for telomeric guanine-quadruplex DNA react with *Styloynchia lemnae* macronuclei. *Proc Natl Acad Sci U S A* **2001**, *98* (15), 8572-7.
36. Koole, W.; van Schendel, R.; Karambelas, A. E.; van Heteren, J. T.; Okihara, K. L.; Tijsterman, M., A Polymerase Theta-dependent repair pathway suppresses extensive genomic instability at endogenous G4 DNA sites. *Nature Communications* **2014**, *5* (1), 3216.
37. Kang, H.-J.; Cui, Y.; Yin, H.; Scheid, A.; Hendricks, W. P. D.; Schmidt, J.; Sekulic, A.; Kong, D.; Trent, J. M.; Gokhale, V.; Mao, H.; Hurley, L. H., A Pharmacological Chaperone Molecule Induces Cancer Cell Death by Restoring Tertiary DNA Structures in Mutant hTERT Promoters. *Journal of the American Chemical Society* **2016**, *138* (41), 13673-13692.
38. Wu, W.-Q.; Hou, X.-M.; Li, M.; Dou, S.-X.; Xi, X.-G., BLM unfolds G-quadruplexes in different structural environments through different mechanisms. *Nucleic Acids Research* **2015**, *43* (9), 4614-4626.
39. Drosopoulos, W. C.; Kosiyatrakul, S. T.; Schildkraut, C. L., BLM helicase facilitates telomere replication during leading strand synthesis of telomeres. *Journal of Cell Biology* **2015**, *210* (2), 191-208.
40. Mullins, M. R.; Rajavel, M.; Hernandez-Sanchez, W.; de la Fuente, M.; Biendarra, S. M.; Harris, M. E.; Taylor, D. J., POT1-TPP1 Binding and Unfolding of Telomere DNA Discriminates against Structural Polymorphism. *Journal of Molecular Biology* **2016**, *428* (13), 2695-2708.
41. Harley, C. B., Telomerase and cancer therapeutics. *Nature Reviews Cancer* **2008**, *8* (3), 167-179.
42. De Cian, A.; Cristofari, G.; Reichenbach, P.; De Lemos, E.; Monchaud, D.; Teulade-Fichou, M.-P.; Shin-ya, K.; Lacroix, L.; Lingner, J.; Mergny, J.-L., Reevaluation of telomerase inhibition by quadruplex ligands and their mechanisms of action. *Proceedings of the National Academy of Sciences* **2007**, *104* (44), 17347.
43. Ravichandran, S.; Ahn, J.-H.; Kim, K. K., Unraveling the Regulatory G-Quadruplex Puzzle: Lessons From Genome and Transcriptome-Wide Studies. *Frontiers in Genetics* **2019**, *10*, 1002.
44. Maizels, N.; Gray, L. T., The G4 Genome. *PLOS Genetics* **2013**, *9* (4), e1003468.

45. Simonsson, T.; Pecinka, P.; Kubista, M., DNA tetraplex formation in the control region of c-myc. *Nucleic Acids Res* **1998**, 26 (5), 1167-72.
46. González, V.; Guo, K.; Hurley, L.; Sun, D., Identification and characterization of nucleolin as a c-myc G-quadruplex-binding protein. *J Biol Chem* **2009**, 284 (35), 23622-35.
47. Cox, A. D.; Fesik, S. W.; Kimmelman, A. C.; Luo, J.; Der, C. J., Drugging the undruggable RAS: Mission possible? *Nat Rev Drug Discov* **2014**, 13 (11), 828-51.
48. Cogoi, S.; Paramasivam, M.; Membrino, A.; Yokoyama, K. K.; Xodo, L. E., The KRAS promoter responds to Myc-associated zinc finger and poly(ADP-ribose) polymerase 1 proteins, which recognize a critical quadruplex-forming GA-element. *J Biol Chem* **2010**, 285 (29), 22003-16.
49. Cogoi, S.; Paramasivam, M.; Filichev, V.; Géci, I.; Pedersen, E. B.; Xodo, L. E., Identification of a new G-quadruplex motif in the KRAS promoter and design of pyrene-modified G4-decoys with antiproliferative activity in pancreatic cancer cells. *J Med Chem* **2009**, 52 (2), 564-8.
50. Cogoi, S.; Shchekotikhin, A. E.; Xodo, L. E., HRAS is silenced by two neighboring G-quadruplexes and activated by MAZ, a zinc-finger transcription factor with DNA unfolding property. *Nucleic Acids Research* **2014**, 42 (13), 8379-8388.
51. Saha, D.; Singh, A.; Hussain, T.; Srivastava, V.; Sengupta, S.; Kar, A.; Dhapola, P.; Dhople, V.; Ummanni, R.; Chowdhury, S., Epigenetic suppression of human telomerase (hTERT) is mediated by the metastasis suppressor NME2 in a G-quadruplex-dependent fashion. *J Biol Chem* **2017**, 292 (37), 15205-15215.
52. Brooks, T. A.; Kendrick, S.; Hurley, L., Making sense of G-quadruplex and i-motif functions in oncogene promoters. *Febs J* **2010**, 277 (17), 3459-69.
53. Yip, K. W.; Reed, J. C., Bcl-2 family proteins and cancer. *Oncogene* **2008**, 27 (50), 6398-6406.
54. Dai, J.; Dexheimer, T. S.; Chen, D.; Carver, M.; Ambrus, A.; Jones, R. A.; Yang, D., An Intramolecular G-Quadruplex Structure with Mixed Parallel/Antiparallel G-Strands Formed in the Human BCL-2 Promoter Region in Solution. *Journal of the American Chemical Society* **2006**, 128 (4), 1096-1098.
55. Onel, B.; Carver, M.; Wu, G.; Timonina, D.; Kalarn, S.; Larriva, M.; Yang, D., A New G-Quadruplex with Hairpin Loop Immediately Upstream of the Human BCL2 P1 Promoter Modulates Transcription. *Journal of the American Chemical Society* **2016**, 138 (8), 2563-2570.
56. Hsu, S.-T. D.; Varnai, P.; Bugaut, A.; Reszka, A. P.; Neidle, S.; Balasubramanian, S., A G-Rich Sequence within the c-kit Oncogene Promoter Forms a Parallel G-Quadruplex Having Asymmetric G-Tetrad Dynamics. *Journal of the American Chemical Society* **2009**, 131 (37), 13399-13409.
57. Phan, A. T.; Kuryavyi, V.; Burge, S.; Neidle, S.; Patel, D. J., Structure of an Unprecedented G-Quadruplex Scaffold in the Human c-kit Promoter. *Journal of the American Chemical Society* **2007**, 129 (14), 4386-4392.
58. Carmeliet, P., VEGF as a key mediator of angiogenesis in cancer. *Oncology* **2005**, 69 Suppl 3, 4-10.
59. Shi, Q.; Le, X.; Abbruzzese, J. L.; Peng, Z.; Qian, C. N.; Tang, H.; Xiong, Q.; Wang, B.; Li, X. C.; Xie, K., Constitutive Sp1 activity is essential for differential constitutive expression of vascular endothelial growth factor in human pancreatic adenocarcinoma. *Cancer Res* **2001**, 61 (10), 4143-54.
60. Bhattacharjee, S.; Chakraborty, S.; Chorell, E.; Sengupta, P. K.; Bhowmik, S., Importance of the hydroxyl substituents in the B-ring of plant flavonols on their preferential binding interactions with VEGF G-quadruplex DNA: Multi-spectroscopic and molecular modeling studies. *Int J Biol Macromol* **2018**, 118 (Pt A), 629-639.
61. Fleming, A. M.; Ding, Y.; Burrows, C. J., Oxidative DNA damage is epigenetic by regulating gene transcription via base excision repair. *Proceedings of the National Academy of Sciences* **2017**, 114 (10), 2604.
62. Murat, P.; Zhong, J.; Lekieffre, L.; Cowieson, N. P.; Clancy, J. L.; Preiss, T.; Balasubramanian, S.; Khanna, R.; Tellam, J., G-quadruplexes regulate Epstein-Barr virus-encoded nuclear antigen 1 mRNA translation. *Nature Chemical Biology* **2014**, 10 (5), 358-364.
63. Tlučková, K.; Marušić, M.; Tóthová, P.; Bauer, L.; Šket, P.; Plavec, J.; Viglasky, V., Human Papillomavirus G-Quadruplexes. *Biochemistry* **2013**, 52 (41), 7207-7216.
64. Artusi, S.; Perrone, R.; Lago, S.; Raffa, P.; Di Iorio, E.; Palù, G.; Richter, S. N., Visualization of DNA G-quadruplexes in herpes simplex virus 1-infected cells. *Nucleic Acids Res* **2016**, 44 (21), 10343-10353.

65. Perrone, R.; Nadai, M.; Frasson, I.; Poe, J. A.; Butovskaya, E.; Smithgall, T. E.; Palumbo, M.; Palù, G.; Richter, S. N., A Dynamic G-Quadruplex Region Regulates the HIV-1 Long Terminal Repeat Promoter. *Journal of Medicinal Chemistry* **2013**, *56* (16), 6521-6530.
66. Butovskaya, E.; Heddi, B.; Bakalar, B.; Richter, S. N.; Phan, A. T., Major G-Quadruplex Form of HIV-1 LTR Reveals a (3 + 1) Folding Topology Containing a Stem-Loop. *Journal of the American Chemical Society* **2018**, *140* (42), 13654-13662.
67. Tosoni, E.; Frasson, I.; Scalabrin, M.; Perrone, R.; Butovskaya, E.; Nadai, M.; Palù, G.; Fabris, D.; Richter, S. N., Nucleolin stabilizes G-quadruplex structures folded by the LTR promoter and silences HIV-1 viral transcription. *Nucleic Acids Res* **2015**, *43* (18), 8884-97.
68. Scalabrin, M.; Frasson, I.; Ruggiero, E.; Perrone, R.; Tosoni, E.; Lago, S.; Tassinari, M.; Palù, G.; Richter, S. N., The cellular protein hnRNP A2/B1 enhances HIV-1 transcription by unfolding LTR promoter G-quadruplexes. *Scientific Reports* **2017**, *7* (1), 45244.
69. Kharel, P.; Balaratnam, S.; Beals, N.; Basu, S., The role of RNA G-quadruplexes in human diseases and therapeutic strategies. *Wiley Interdiscip Rev RNA* **2020**, *11* (1), e1568.
70. Decorsière, A.; Cayrel, A.; Vagner, S.; Millevoi, S., Essential role for the interaction between hnRNP H/F and a G quadruplex in maintaining p53 pre-mRNA 3'-end processing and function during DNA damage. *Genes Dev* **2011**, *25* (3), 220-5.
71. Gomez, D.; Lemarteleur, T.; Lacroix, L.; Mailliet, P.; Mergny, J. L.; Riou, J. F., Telomerase downregulation induced by the G-quadruplex ligand 12459 in A549 cells is mediated by hTERT RNA alternative splicing. *Nucleic Acids Res* **2004**, *32* (1), 371-9.
72. Blice-Baum, A. C.; Mihailescu, M. R., Biophysical characterization of G-quadruplex forming FMR1 mRNA and of its interactions with different fragile X mental retardation protein isoforms. *Rna* **2014**, *20* (1), 103-14.
73. Bhattacharyya, D.; Diamond, P.; Basu, S., An Independently Folding RNA G-Quadruplex Domain Directly Recruits the 40S Ribosomal Subunit. *Biochemistry* **2015**, *54* (10), 1879-1885.
74. Haeusler, A. R.; Donnelly, C. J.; Periz, G.; Simko, E. A.; Shaw, P. G.; Kim, M. S.; Maragakis, N. J.; Troncoso, J. C.; Pandey, A.; Sattler, R.; Rothstein, J. D.; Wang, J., C9orf72 nucleotide repeat structures initiate molecular cascades of disease. *Nature* **2014**, *507* (7491), 195-200.
75. Cusanelli, E.; Chartrand, P., Telomeric repeat-containing RNA TERRA: a noncoding RNA connecting telomere biology to genome integrity. *Front Genet* **2015**, *6*, 143.
76. Stanton, A.; Harris, L. M.; Graham, G.; Merrick, C. J., Recombination events among virulence genes in malaria parasites are associated with G-quadruplex-forming DNA motifs. *BMC Genomics* **2016**, *17* (1), 859.
77. Leeder, W. M.; Hummel, N. F. C.; Göringer, H. U., Multiple G-quartet structures in pre-edited mRNAs suggest evolutionary driving force for RNA editing in trypanosomes. *Scientific Reports* **2016**, *6* (1), 29810.
78. Belmonte-Reche, E.; Martínez-García, M.; Guédin, A.; Zuffo, M.; Arévalo-Ruiz, M.; Doria, F.; Campos-Salinas, J.; Maynadier, M.; López-Rubio, J. J.; Freccero, M.; Mergny, J.-L.; Pérez-Victoria, J. M.; Morales, J. C., G-Quadruplex Identification in the Genome of Protozoan Parasites Points to Naphthalene Diimide Ligands as New Antiparasitic Agents. *Journal of Medicinal Chemistry* **2018**, *61* (3), 1231-1240.
79. Schaffitzel, C.; Berger, I.; Postberg, J.; Hanes, J.; Lipps, H. J.; Pluckthun, A., In vitro generated antibodies specific for telomeric guanine-quadruplex DNA react with *Stylocystis lemnae* macronuclei. *Proc Natl Acad Sci U S A* **2001**, *98* (15), 8572-7.
80. Biffi, G.; Tannahill, D.; McCafferty, J.; Balasubramanian, S., Quantitative visualization of DNA G-quadruplex structures in human cells. *Nature Chemistry* **2013**, *5* (3), 182-186.
81. Pirota, V.; Stasi, M.; Benassi, A.; Doria, F., Chapter Six - An overview of quadruplex ligands: Their common features and chemotype diversity. In *Annual Reports in Medicinal Chemistry*, Neidle, S., Ed. Academic Press: 2020; Vol. 54, pp 163-196.
82. Zuffo, M.; Pirota, V.; Doria, F., Photoresponsive molecular devices targeting nucleic acid secondary structures. In *Photochemistry: Volume 46*, The Royal Society of Chemistry: 2019; Vol. 46, pp 281-318.
83. Gabelica, V.; Maeda, R.; Fujimoto, T.; Yaku, H.; Murashima, T.; Sugimoto, N.; Miyoshi, D., Multiple and Cooperative Binding of Fluorescence Light-up Probe Thioflavin T with Human Telomere DNA G-Quadruplex. *Biochemistry* **2013**, *52* (33), 5620-5628.

84. Chen, X.; Wang, J.; Jiang, G.; Zu, G.; Liu, M.; Zhou, L.; Pei, R., The development of a light-up red-emitting fluorescent probe based on a G-quadruplex specific cyanine dye. *RSC Advances* **2016**, *6* (74), 70117-70123.
85. Lin, D.; Fei, X.; Gu, Y.; Wang, C.; Tang, Y.; Li, R.; Zhou, J., A benzindole substituted carbazole cyanine dye: a novel targeting fluorescent probe for parallel c-myc G-quadruplexes. *Analyst* **2015**, *140* (16), 5772-5780.
86. Liu, L. Y.; Liu, W.; Wang, K. N.; Zhu, B. C.; Xia, X. Y.; Ji, L. N.; Mao, Z. W., Quantitative Detection of G-Quadruplex DNA in Live Cells Based on Photon Counts and Complex Structure Discrimination. *Angew Chem Int Ed Engl* **2020**.
87. Chen, S.-B.; Hu, M.-H.; Liu, G.-C.; Wang, J.; Ou, T.-M.; Gu, L.-Q.; Huang, Z.-S.; Tan, J.-H., Visualization of NRAS RNA G-Quadruplex Structures in Cells with an Engineered Fluorogenic Hybridization Probe. *Journal of the American Chemical Society* **2016**, *138* (33), 10382-10385.
88. Hu, M.-H.; Chen, X., New fluorescent light-up quinoxalines differentiate between parallel and nonparallel G-quadruplex topologies using different excitation/emission channels. *Chemical Communications* **2020**.
89. Xie, X.; Reznichenko, O.; Chaput, L.; Martin, P.; Teulade-Fichou, M. P.; Granzhan, A., Topology-Selective, Fluorescent "Light-Up" Probes for G-Quadruplex DNA Based on Photoinduced Electron Transfer. *Chemistry* **2018**, *24* (48), 12638-12651.
90. Hestand, N. J.; Spano, F. C., Expanded Theory of H- and J-Molecular Aggregates: The Effects of Vibronic Coupling and Intermolecular Charge Transfer. *Chemical Reviews* **2018**, *118* (15), 7069-7163.
91. Jin, B.; Zhang, X.; Zheng, W.; Liu, X.; Zhou, J.; Zhang, N.; Wang, F.; Shangguan, D., Dicyanomethylene-Functionalized Squaraine as a Highly Selective Probe for Parallel G-Quadruplexes. *Analytical Chemistry* **2014**, *86* (14), 7063-7070.
92. Grande, V.; Doria, F.; Freccero, M.; Würthner, F., An Aggregating Amphiphilic Squaraine: A Light-up Probe That Discriminates Parallel G-Quadruplexes. *Angewandte Chemie International Edition* **2017**, *56* (26), 7520-7524.
93. Jiang, G.; Chen, X.; Xu, L.; Cao, Y.; Hong, S.; Liu, M.; Cao, W.; Pei, R., Design and Synthesis of a Dimethylindole Red Trimer: A New Light-Up Red-Emitting Fluorescent Probe for G-Quadruplexes. *ChemistrySelect* **2017**, *2* (9), 2783-2788.
94. Pont, I.; González-García, J.; Inclán, M.; Reynolds, M.; Delgado-Pinar, E.; Albelda, M. T.; Vilar, R.; García-España, E., Aza-Macrocyclic Triphenylamine Ligands for G-Quadruplex Recognition. *Chemistry – A European Journal* **2018**, *24* (42), 10850-10858.
95. Hu, M.-H.; Zhou, J.; Luo, W.-H.; Chen, S.-B.; Huang, Z.-S.; Wu, R.; Tan, J.-H., Development of a Smart Fluorescent Sensor That Specifically Recognizes the c-MYC G-Quadruplex. *Analytical Chemistry* **2019**, *91* (3), 2480-2487.
96. Liao, G.-L.; Chen, X.; Ji, L.-N.; Chao, H., Visual specific luminescent probing of hybrid G-quadruplex DNA by a ruthenium polypyridyl complex. *Chemical Communications* **2012**, *48* (87), 10781-10783.
97. Lin, S.; Lu, L.; Liu, J. B.; Liu, C.; Kang, T. S.; Yang, C.; Leung, C. H.; Ma, D. L., A G-quadruplex-selective luminescent iridium(III) complex and its application by long lifetime. *Biochim Biophys Acta Gen Subj* **2017**, *1861* (5 Pt B), 1448-1454.
98. Gray, R. D.; Petraccone, L.; Trent, J. O.; Chaires, J. B., Characterization of a K⁺-induced conformational switch in a human telomeric DNA oligonucleotide using 2-aminopurine fluorescence. *Biochemistry* **2010**, *49* (1), 179-94.
99. Manna, S.; Sarkar, D.; Srivatsan, S. G., A Dual-App Nucleoside Probe Provides Structural Insights into the Human Telomeric Overhang in Live Cells. *J Am Chem Soc* **2018**, *140* (39), 12622-12633.
100. Nuthanakanti, A.; Ahmed, I.; Khatik, S. Y.; Saikrishnan, K.; Srivatsan, S. G., Probing G-quadruplex topologies and recognition concurrently in real time and 3D using a dual-app nucleoside probe. *Nucleic Acids Res* **2019**, *47* (12), 6059-6072.
101. Tahara, H.; Shin-ya, K.; Seimiya, H.; Yamada, H.; Tsuruo, T.; Ide, T., G-Quadruplex stabilization by telomestatin induces TRF2 protein dissociation from telomeres and anaphase bridge formation accompanied by loss of the 3' telomeric overhang in cancer cells. *Oncogene* **2006**, *25* (13), 1955-1966.

102. Gunaratnam, M.; Swank, S.; Haider, S. M.; Galesa, K.; Reszka, A. P.; Beltran, M.; Cuenca, F.; Fletcher, J. A.; Neidle, S., Targeting human gastrointestinal stromal tumor cells with a quadruplex-binding small molecule. *J Med Chem* **2009**, *52* (12), 3774-83.
103. Teulade-Fichou, M.-P.; Carrasco, C.; Guittat, L.; Bailly, C.; Alberti, P.; Mergny, J.-L.; David, A.; Lehn, J.-M.; Wilson, W. D., Selective Recognition of G-Quadruplex Telomeric DNA by a Bis(quinacridine) Macrocyclic. *Journal of the American Chemical Society* **2003**, *125* (16), 4732-4740.
104. Salvati, E.; Leonetti, C.; Rizzo, A.; Scarsella, M.; Mottolese, M.; Galati, R.; Sperduti, I.; Stevens, M. F. G.; D'Incalci, M.; Blasco, M.; Chiorino, G.; Bauwens, S.; Horard, B.; Gilson, E.; Stoppacciaro, A.; Zupi, G.; Biroccio, A., Telomere damage induced by the G-quadruplex ligand RHPS4 has an antitumor effect. *The Journal of Clinical Investigation* **2007**, *117* (11), 3236-3247.
105. Zhou, J. M.; Zhu, X. F.; Lu, Y. J.; Deng, R.; Huang, Z. S.; Mei, Y. P.; Wang, Y.; Huang, W. L.; Liu, Z. C.; Gu, L. Q.; Zeng, Y. X., Senescence and telomere shortening induced by novel potent G-quadruplex interactive agents, quindoline derivatives, in human cancer cell lines. *Oncogene* **2006**, *25* (4), 503-11.
106. Katsuda, Y.; Sato, S.; Asano, L.; Morimura, Y.; Furuta, T.; Sugiyama, H.; Hagihara, M.; Uesugi, M., A Small Molecule That Represses Translation of G-Quadruplex-Containing mRNA. *J Am Chem Soc* **2016**, *138* (29), 9037-40.
107. Xu, H.; Di Antonio, M.; McKinney, S.; Mathew, V.; Ho, B.; O'Neil, N. J.; Santos, N. D.; Silvester, J.; Wei, V.; Garcia, J.; Kabeer, F.; Lai, D.; Soriano, P.; Banath, J.; Chiu, D. S.; Yap, D.; Le, D. D.; Ye, F. B.; Zhang, A.; Thu, K.; Soong, J.; Lin, S. C.; Tsai, A. H.; Osako, T.; Algara, T.; Saunders, D. N.; Wong, J.; Xian, J.; Bally, M. B.; Brenton, J. D.; Brown, G. W.; Shah, S. P.; Cescon, D.; Mak, T. W.; Caldas, C.; Stirling, P. C.; Hieter, P.; Balasubramanian, S.; Aparicio, S., CX-5461 is a DNA G-quadruplex stabilizer with selective lethality in BRCA1/2 deficient tumours. *Nat Commun* **2017**, *8*, 14432.
108. Verga, D.; N'Guyen, C.-H.; Dakir, M.; Coll, J.-L.; Teulade-Fichou, M.-P.; Molla, A., Polyheteroaryl Oxazole/Pyridine-Based Compounds Selected in Vitro as G-Quadruplex Ligands Inhibit Rock Kinase and Exhibit Antiproliferative Activity. *Journal of Medicinal Chemistry* **2018**, *61* (23), 10502-10518.
109. Hu, M.-H.; Wang, Y.-Q.; Yu, Z.-Y.; Hu, L.-N.; Ou, T.-M.; Chen, S.-B.; Huang, Z.-S.; Tan, J.-H., Discovery of a New Four-Leaf Clover-Like Ligand as a Potent c-MYC Transcription Inhibitor Specifically Targeting the Promoter G-Quadruplex. *Journal of Medicinal Chemistry* **2018**, *61* (6), 2447-2459.
110. Rodriguez, R.; Müller, S.; Yeoman, J. A.; Trentesaux, C.; Riou, J. F.; Balasubramanian, S., A novel small molecule that alters shelterin integrity and triggers a DNA-damage response at telomeres. *J Am Chem Soc* **2008**, *130* (47), 15758-9.
111. O'Hagan, M. P.; Haldar, S.; Duchi, M.; Oliver, T. A. A.; Mulholland, A. J.; Morales, J. C.; Galan, M. C., A Photoresponsive Stiff-Stilbene Ligand Fuels the Reversible Unfolding of G-Quadruplex DNA. *Angewandte Chemie International Edition* **2019**, *58* (13), 4334-4338.
112. Dixon, I. M.; Lopez, F.; Tejera, A. M.; Estève, J.-P.; Blasco, M. A.; Pratviel, G.; Meunier, B., A G-Quadruplex Ligand with 10000-Fold Selectivity over Duplex DNA. *Journal of the American Chemical Society* **2007**, *129* (6), 1502-1503.
113. Ramos, C. I. V.; Almeida, S. P.; Lourenço, L. M. O.; Pereira, P. M. R.; Fernandes, R.; Faustino, M. A. F.; Tomé, J. P. C.; Carvalho, J.; Cruz, C.; Neves, M., Multicharged Phthalocyanines as Selective Ligands for G-Quadruplex DNA Structures. *Molecules* **2019**, *24* (4).
114. Chen, Z.-F.; Qin, Q.-P.; Qin, J.-L.; Liu, Y.-C.; Huang, K.-B.; Li, Y.-L.; Meng, T.; Zhang, G.-H.; Peng, Y.; Luo, X.-J.; Liang, H., Stabilization of G-Quadruplex DNA, Inhibition of Telomerase Activity, and Tumor Cell Apoptosis by Organoplatinum(II) Complexes with Oxoisoaporphine. *Journal of Medicinal Chemistry* **2015**, *58* (5), 2159-2179.
115. Kobaisi, M. A.; Bhosale, S. V.; Latham, K.; Raynor, A. M., Functional Naphthalene Diimides: Synthesis, Properties, and Applications. *Chem Rev* **2016**, *116* (19), 11685-11796.
116. Sakai, N.; Mareda, J.; Vauthey, E.; Matile, S., Core-substituted naphthalenediimides. *Chem Commun (Camb)* **2010**, *46* (24), 4225-37.
117. Kishore, R. S. K.; Ravikumar, V.; Bernardinelli, G.; Sakai, N.; Matile, S., Rapid and Mild Synthesis of Functionalized Naphthalenediimides. *The Journal of Organic Chemistry* **2008**, *73* (2), 738-740.
118. Bhosale, S. V.; Kalyankar, M. B.; Bhosale, S. V.; Langford, S. J.; Reid, E. F.; Hogan, C. F., The synthesis of novel core-substituted naphthalene diimides via Suzuki cross-coupling and their properties. *New Journal of Chemistry* **2009**, *33* (12), 2409-2413.

119. Röger, C.; Würthner, F., Core-Tetrasubstituted Naphthalene Diimides: Synthesis, Optical Properties, and Redox Characteristics. *The Journal of Organic Chemistry* **2007**, 72 (21), 8070-8075.
120. Li, C.; Xiao, C.; Li, Y.; Wang, Z., Synthesis and Properties of Heterocyclic Acene Diimides. *Organic Letters* **2013**, 15 (3), 682-685.
121. Cai, K.; Xie, J.; Zhao, D., NIR J-Aggregates of Hydroazaheptacene Tetraimides. *Journal of the American Chemical Society* **2014**, 136 (1), 28-31.
122. Hampel, S. M.; Sidibe, A.; Gunaratnam, M.; Riou, J. F.; Neidle, S., Tetrasubstituted naphthalene diimide ligands with selectivity for telomeric G-quadruplexes and cancer cells. *Bioorg Med Chem Lett* **2010**, 20 (22), 6459-63.
123. Micco, M.; Collie, G. W.; Dale, A. G.; Ohnmacht, S. A.; Pazitna, I.; Gunaratnam, M.; Reszka, A. P.; Neidle, S., Structure-based design and evaluation of naphthalene diimide G-quadruplex ligands as telomere targeting agents in pancreatic cancer cells. *J Med Chem* **2013**, 56 (7), 2959-74.
124. Perrone, R.; Doria, F.; Butovskaya, E.; Frasson, I.; Botti, S.; Scalabrin, M.; Lago, S.; Grande, V.; Nadai, M.; Freccero, M.; Richter, S. N., Synthesis, Binding and Antiviral Properties of Potent Core-Extended Naphthalene Diimides Targeting the HIV-1 Long Terminal Repeat Promoter G-Quadruplexes. *J Med Chem* **2015**, 58 (24), 9639-52.
125. Doria, F.; Salvati, E.; Pompili, L.; Pirota, V.; D'Angelo, C.; Manoli, F.; Nadai, M.; Richter, S. N.; Biroccio, A.; Manet, I.; Freccero, M., Dyads of G-Quadruplex Ligands Triggering DNA Damage Response and Tumour Cell Growth Inhibition at Subnanomolar Concentration. *Chemistry* **2019**, 25 (47), 11085-11097.
126. Pirota, V.; Platella, C.; Musumeci, D.; Benassi, A.; Amato, J.; Pagano, B.; Colombo, G.; Freccero, M.; Doria, F.; Montesarchio, D., On the binding of naphthalene diimides to a human telomeric G-quadruplex multimer model. *International Journal of Biological Macromolecules* **2020**.
127. Doria, F.; Oppi, A.; Manoli, F.; Botti, S.; Kandoth, N.; Grande, V.; Manet, I.; Freccero, M., A naphthalene diimide dyad for fluorescence switch-on detection of G-quadruplexes. *Chemical Communications* **2015**, 51 (44), 9105-9108.
128. Zuffo, M.; Doria, F.; Spalluto, V.; Ladame, S.; Freccero, M., Red/NIR G-Quadruplex Sensing, Harvesting Blue Light by a Coumarin–Naphthalene Diimide Dyad. *Chemistry – A European Journal* **2015**, 21 (49), 17596-17600.
129. Doria, F.; Nadai, M.; Zuffo, M.; Perrone, R.; Freccero, M.; Richter, S. N., A red-NIR fluorescent dye detecting nuclear DNA G-quadruplexes: in vitro analysis and cell imaging. *Chemical Communications* **2017**, 53 (14), 2268-2271.
130. Zuffo, M.; Guédin, A.; Leriche, E.-D.; Doria, F.; Pirota, V.; Gabelica, V.; Mergny, J.-L.; Freccero, M., More is not always better: finding the right trade-off between affinity and selectivity of a G-quadruplex ligand. *Nucleic Acids Research* **2018**, 46 (19), e115-e115.
131. Fuchter, M. J., On the Promise of Photopharmacology Using Photoswitches: A Medicinal Chemist's Perspective. *Journal of Medicinal Chemistry* **2020**, 63 (20), 11436-11447.
132. Lerch, M. M.; Hansen, M. J.; van Dam, G. M.; Szymanski, W.; Feringa, B. L., Emerging Targets in Photopharmacology. *Angewandte Chemie International Edition* **2016**, 55 (37), 10978-10999.
133. Dong, M.; Babalhavaeji, A.; Samanta, S.; Beharry, A. A.; Woolley, G. A., Red-Shifting Azobenzene Photoswitches for in Vivo Use. *Accounts of Chemical Research* **2015**, 48 (10), 2662-2670.
134. Murat, P.; Gormally, M. V.; Sanders, D.; Antonio, M. D.; Balasubramanian, S., Light-mediated in cell downregulation of G-quadruplex-containing genes using a photo-caged ligand. *Chemical Communications* **2013**, 49 (76), 8453-8455.
135. O'Hagan, M. P.; Ramos-Soriano, J.; Haldar, S.; Sheikh, S.; Morales, J. C.; Mulholland, A. J.; Galan, M. C., Visible-light photoswitching of ligand binding mode suggests G-quadruplex DNA as a target for photopharmacology. *Chemical Communications* **2020**, 56 (38), 5186-5189.
136. Ghosh, A. K.; Samanta, I.; Mondal, A.; Liu, W. R., Covalent Inhibition in Drug Discovery. *ChemMedChem* **2019**, 14 (9), 889-906.
137. Verga, D.; Hamon, F.; Poyer, F.; Bombard, S.; Teulade-Fichou, M.-P., Photo-Cross-Linking Probes for Trapping G-Quadruplex DNA. *Angewandte Chemie International Edition* **2014**, 53 (4), 994-998.
138. Nadai, M.; Doria, F.; Germani, L.; Richter, S. N.; Freccero, M., A photoreactive G-quadruplex ligand triggered by green light. *Chemistry* **2015**, 21 (6), 2330-4.

139. Singh, M. S.; Nagaraju, A.; Anand, N.; Chowdhury, S., ortho-Quinone methide (o-QM): a highly reactive, ephemeral and versatile intermediate in organic synthesis. *RSC Advances* **2014**, *4* (99), 55924-55959.
140. Bruins, J. J.; Albada, B.; van Delft, F., ortho-Quinones and Analogues Thereof: Highly Reactive Intermediates for Fast and Selective Biofunctionalization. *Chemistry – A European Journal* **2018**, *24* (19), 4749-4756.
141. Mauro, F., Quinone Methides as Alkylating and Cross-Linking Agents. *Mini-Reviews in Organic Chemistry* **2004**, *1* (4), 403-415.
142. Toteva, M. M.; Richard, J. P., The generation and reactions of quinone methides. In *Advances in Physical Organic Chemistry*, Richard, J. P., Ed. Academic Press: 2011; Vol. 45, pp 39-91.
143. Li, Q.; Dong, T.; Liu, X.; Lei, X., A bioorthogonal ligation enabled by click cycloaddition of o-quinolinone quinone methide and vinyl thioether. *J Am Chem Soc* **2013**, *135* (13), 4996-9.
144. Claudia, P.; Filippo Doria and Mauro, F., Quinone Methides as DNA Alkylating Agents: An Overview on Efficient Activation Protocols for Enhanced Target Selectivity. *Current Organic Chemistry* **2014**, *18* (1), 19-43.
145. Basarić, N.; Došlić, N.; Ivković, J.; Wang, Y. H.; Mališ, M.; Wan, P., Very efficient generation of quinone methides through excited state intramolecular proton transfer to a carbon atom. *Chemistry* **2012**, *18* (34), 10617-23.
146. Brousmiche, D. W.; Xu, M.; Lukeman, M.; Wan, P., Photohydration and Photosolvolyysis of Biphenyl Alkenes and Alcohols via Biphenyl Quinone Methide-type Intermediates and Diarylmethyl Carbocations. *Journal of the American Chemical Society* **2003**, *125* (42), 12961-12970.
147. Škalamera, Đ.; Bohne, C.; Landgraf, S.; Basarić, N., Photodeamination Reaction Mechanism in Aminomethyl p-Cresol Derivatives: Different Reactivity of Amines and Ammonium Salts. *J Org Chem* **2015**, *80* (21), 10817-28.
148. Ma, J.; Zhang, X.; Basarić, N.; Phillips, D. L., Direct Observation of Photoinduced Ultrafast Generation of Singlet and Triplet Quinone Methides in Aqueous Solutions and Insight into the Roles of Acidic and Basic Sites in Quinone Methide Formation. *Journal of the American Chemical Society* **2017**, *139* (50), 18349-18357.
149. Arumugam, S.; Popik, V. V., Photochemical Generation and the Reactivity of o-Naphthoquinone Methides in Aqueous Solutions. *Journal of the American Chemical Society* **2009**, *131* (33), 11892-11899.
150. Weinert, E. E.; Dondi, R.; Colloredo-Melz, S.; Frankenfield, K. N.; Mitchell, C. H.; Freccero, M.; Rokita, S. E., Substituents on Quinone Methides Strongly Modulate Formation and Stability of Their Nucleophilic Adducts. *Journal of the American Chemical Society* **2006**, *128* (36), 11940-11947.
151. Liu, J.; Li, S.; Aslam, N. A.; Zheng, F.; Yang, B.; Cheng, R.; Wang, N.; Rozovsky, S.; Wang, P. G.; Wang, Q.; Wang, L., Genetically Encoding Photocaged Quinone Methide to Multitarget Protein Residues Covalently in Vivo. *Journal of the American Chemical Society* **2019**, *141* (24), 9458-9462.
152. Liu, J.; Cai, L.; Sun, W.; Cheng, R.; Wang, N.; Jin, L.; Rozovsky, S.; Seiple, I. B.; Wang, L., Photocaged Quinone Methide Crosslinkers for Light-Controlled Chemical Crosslinking of Protein–Protein and Protein–DNA Complexes. *Angewandte Chemie International Edition* **2019**, *58* (52), 18839-18843.
153. Fakhari, F.; Rokita, S. E., A walk along DNA using bipedal migration of a dynamic and covalent crosslinker. *Nature Communications* **2014**, *5* (1), 5591.
154. Huang, C.; Liu, Y.; Rokita, S. E., Targeting duplex DNA with the reversible reactivity of quinone methides. *Signal Transduction and Targeted Therapy* **2016**, *1* (1), 16009.
155. Deeyaa, B. D.; Rokita, S. E., Migratory ability of quinone methide-generating acridine conjugates in DNA. *Org Biomol Chem* **2020**, *18* (8), 1671-1678.
156. Richter, S. N.; Maggi, S.; Mels, S. C.; Palumbo, M.; Freccero, M., Binol Quinone Methides as Bisalkylating and DNA Cross-Linking Agents. *Journal of the American Chemical Society* **2004**, *126* (43), 13973-13979.
157. Nadai, M.; Doria, F.; Di Antonio, M.; Sattin, G.; Germani, L.; Percivalle, C.; Palumbo, M.; Richter, S. N.; Freccero, M., Naphthalene diimide scaffolds with dual reversible and covalent interaction properties towards G-quadruplex. *Biochimie* **2011**, *93* (8), 1328-1340.

158. Doria, F.; Nadai, M.; Folini, M.; Di Antonio, M.; Germani, L.; Percivalle, C.; Sissi, C.; Zaffaroni, N.; Alcaro, S.; Artese, A.; Richter, S. N.; Freccero, M., Hybrid ligand-alkylating agents targeting telomeric G-quadruplex structures. *Org Biomol Chem* **2012**, *10* (14), 2798-806.
159. Neochoritis, C. G.; Zhao, T.; Dömling, A., Tetrazoles via Multicomponent Reactions. *Chemical Reviews* **2019**, *119* (3), 1970-2042.
160. Dhiman, N.; Kaur, K.; Jaitak, V., Tetrazoles as anticancer agents: A review on synthetic strategies, mechanism of action and SAR studies. *Bioorganic & Medicinal Chemistry* **2020**, *28* (15), 115599.
161. Matta, C. F.; Arabi, A. A.; Weaver, D. F., The bioisosteric similarity of the tetrazole and carboxylate anions: Clues from the topologies of the electrostatic potential and of the electron density. *European Journal of Medicinal Chemistry* **2010**, *45* (5), 1868-1872.
162. Wong, M. W.; Leung-Toung, R.; Wentrup, C., Tautomeric equilibrium and hydrogen shifts of tetrazole in the gas phase and in solution. *Journal of the American Chemical Society* **1993**, *115* (6), 2465-2472.
163. Frija, L. M. T.; Cristiano, M. L. S.; Gómez-Zavaglia, A.; Reva, I.; Fausto, R., Genesis of rare molecules using light-induced reactions of matrix-isolated tetrazoles. *Journal of Photochemistry and Photobiology C: Photochemistry Reviews* **2014**, *18*, 71-90.
164. Abe, M.; Bégué, D.; Silva, H. S.; Dargelos, A.; Wentrup, C., Triplet States of Tetrazoles, Nitrenes, and Carbenes from Matrix Photolysis of Tetrazoles, and Phenylcyanamide as a Source of Phenylnitrene. *The Journal of Physical Chemistry A* **2018**, *122* (37), 7276-7283.
165. Wentrup, C.; Fischer, S.; Maquestiau, A.; Flammang, R., Nitrile Imines: Thermal Generation, Direct Observation, and Subsequent Trapping. *Angewandte Chemie International Edition in English* **1985**, *24* (1), 56-57.
166. Wong, M. W.; Wentrup, C., Structure of nitrilimine: allenic or propargylic? *Journal of the American Chemical Society* **1993**, *115* (17), 7743-7746.
167. Mawhinney, R. C.; Muchall, H. M.; Peslherbe, G. H., The electronic structure of nitrilimines revisited. *Chemical Communications* **2004**, (16), 1862-1863.
168. Zheng, S.-L.; Wang, Y.; Yu, Z.; Lin, Q.; Coppens, P., Direct Observation of a Photoinduced Nonstabilized Nitrile Imine Structure in the Solid State. *Journal of the American Chemical Society* **2009**, *131* (50), 18036-18037.
169. Li, Y.; Fu, H., Bioorthogonal Ligations and Cleavages in Chemical Biology. *ChemistryOpen* **2020**, *9* (8), 835-853.
170. Devaraj, N. K., The Future of Bioorthogonal Chemistry. *ACS Central Science* **2018**, *4* (8), 952-959.
171. Song, W.; Wang, Y.; Qu, J.; Madden, M. M.; Lin, Q., A photoinducible 1,3-dipolar cycloaddition reaction for rapid, selective modification of tetrazole-containing proteins. *Angew Chem Int Ed Engl* **2008**, *47* (15), 2832-5.
172. Wang, Y.; Song, W.; Hu, W. J.; Lin, Q., Fast alkene functionalization in vivo by Photoclick chemistry: HOMO lifting of nitrile imine dipoles. *Angew Chem Int Ed Engl* **2009**, *48* (29), 5330-3.
173. Yu, Z.; Ho, L. Y.; Lin, Q., Rapid, Photoactivatable Turn-On Fluorescent Probes Based on an Intramolecular Photoclick Reaction. *Journal of the American Chemical Society* **2011**, *133* (31), 11912-11915.
174. An, P.; Yu, Z.; Lin, Q., Design of oligothiophene-based tetrazoles for laser-triggered photoclick chemistry in living cells. *Chemical Communications* **2013**, *49* (85), 9920-9922.
175. Yu, Z.; Ohulchanskyy, T. Y.; An, P.; Prasad, P. N.; Lin, Q., Fluorogenic, two-photon-triggered photoclick chemistry in live mammalian cells. *J Am Chem Soc* **2013**, *135* (45), 16766-9.
176. Zhou, M.; Hu, J.; Zheng, M.; Song, Q.; Li, J.; Zhang, Y., Photo-click construction of a targetable and activatable two-photon probe imaging protease in apoptosis. *Chemical Communications* **2016**, *52* (11), 2342-2345.
177. Li, Z.; Qian, L.; Li, L.; Bernhammer, J. C.; Huynh, H. V.; Lee, J. S.; Yao, S. Q., Tetrazole Photoclick Chemistry: Reinvestigating Its Suitability as a Bioorthogonal Reaction and Potential Applications. *Angew Chem Int Ed Engl* **2016**, *55* (6), 2002-6.
178. An, P.; Lewandowski, T. M.; Erbay, T. G.; Liu, P.; Lin, Q., Sterically Shielded, Stabilized Nitrile Imine for Rapid Bioorthogonal Protein Labeling in Live Cells. *Journal of the American Chemical Society* **2018**, *140* (14), 4860-4868.

179. An, P.; Lewandowski, T. M.; Lin, Q., Design and Synthesis of a BODIPY-Tetrazole Based "Off-On" in-Cell Fluorescence Reporter of Hydrogen Peroxide. *Chembiochem* **2018**, *19* (12), 1326-1333.
180. Lehmann, B.; Wagenknecht, H. A., Fluorogenic "photoclick" labelling of DNA using a Cy3 dye. *Org Biomol Chem* **2018**, *16* (41), 7579-7582.
181. Zhou, Z.; Yi, Q.; Xia, T.; Yin, W.; Kadi, A. A.; Li, J.; Zhang, Y., A photo-degradable supramolecular hydrogel for selective delivery of microRNA into 3D-cultured cells. *Org Biomol Chem* **2017**, *15* (10), 2191-2198.
182. Estupiñán, D.; Gegenhuber, T.; Blinco, J. P.; Barner-Kowollik, C.; Barner, L., Self-Reporting Fluorescent Step-Growth RAFT Polymers Based on Nitrile Imine-Mediated Tetrazole-ene Cycloaddition Chemistry. *ACS Macro Letters* **2017**, *6* (3), 229-234.
183. Arévalo-Ruiz, M.; Doria, F.; Belmonte-Reche, E.; De Rache, A.; Campos-Salinas, J.; Lucas, R.; Falomir, E.; Carda, M.; Pérez-Victoria, J. M.; Mergny, J.-L.; Freccero, M.; Morales, J. C., Synthesis, Binding Properties, and Differences in Cell Uptake of G-Quadruplex Ligands Based on Carbohydrate Naphthalene Diimide Conjugates. *Chemistry – A European Journal* **2017**, *23* (9), 2157-2164.
184. Gómez-Pinto, I.; Vengut-Climent, E.; Lucas, R.; Aviñó, A.; Eritja, R.; González, C.; Morales, J. C., Carbohydrate-DNA interactions at G-quadruplexes: folding and stability changes by attaching sugars at the 5'-end. *Chemistry* **2013**, *19* (6), 1920-7.
185. Adekola, K.; Rosen, S. T.; Shanmugam, M., Glucose transporters in cancer metabolism. *Curr Opin Oncol* **2012**, *24* (6), 650-4.
186. Zuffo, M.; Stucchi, A.; Campos-Salinas, J.; Cabello-Donayre, M.; Martinez-Garcia, M.; Belmonte-Reche, E.; Perez-Victoria, J. M.; Mergny, J. L.; Freccero, M.; Morales, J. C.; Doria, F., Carbohydrate-naphthalene diimide conjugates as potential antiparasitic drugs: Synthesis, evaluation and structure-activity studies. *Eur J Med Chem* **2019**, *163*, 54-66.
187. Quagliotto, P.; Viscardi, G.; Barolo, C.; D'Angelo, D.; Barni, E.; Compari, C.; Duce, E.; Fisicaro, E., Synthesis and Properties of New Glucocationic Surfactants: Model Structures for Marking Cationic Surfactants with Carbohydrates. *The Journal of Organic Chemistry* **2005**, *70* (24), 9857-9866.
188. Doria, F.; Lena, A.; Bargiggia, R.; Freccero, M., Conjugation, Substituent, and Solvent Effects on the Photogeneration of Quinone Methides. *The Journal of Organic Chemistry* **2016**, *81* (9), 3665-3673.
189. Renciuk, D.; Kejnovská, I.; Skoláková, P.; Bednárová, K.; Motlová, J.; Vorlícková, M., Arrangements of human telomere DNA quadruplex in physiologically relevant K⁺ solutions. *Nucleic Acids Res* **2009**, *37* (19), 6625-34.
190. Hwang, J. Y.; Arnold, L. A.; Zhu, F.; Kosinski, A.; Mangano, T. J.; Setola, V.; Roth, B. L.; Guy, R. K., Improvement of Pharmacological Properties of Irreversible Thyroid Receptor Coactivator Binding Inhibitors. *Journal of Medicinal Chemistry* **2009**, *52* (13), 3892-3901.
191. Forshaw, S.; Matthews, A. J.; Brown, T. J.; Diorazio, L. J.; Williams, L.; Wills, M., Asymmetric Transfer Hydrogenation of 1,3-Alkoxy/Aryloxy Propanones Using Tethered Arene/Ru(II)/TsDPEN Complexes. *Organic Letters* **2017**, *19* (11), 2789-2792.
192. Ito, S.; Tanaka, Y.; Kakehi, A.; Kondo, K.-i., A Facile Synthesis of 2,5-Disubstituted Tetrazoles by the Reaction of Phenylsulfonylhydrazones with Arenediazonium Salts. *Bulletin of the Chemical Society of Japan* **1976**, *49* (7), 1920-1923.
193. Wu, Y.; Guo, G.; Zheng, J.; Xing, D.; Zhang, T., Fluorogenic "Photoclick" Labeling and Imaging of DNA with Coumarin-Fused Tetrazole in Vivo. *ACS Sens* **2019**, *4* (1), 44-51.
194. Krell, K.; Wagenknecht, H.-A., Fluorogenic and Bioorthogonal Modification of RNA Using Photoclick Chemistry. *Biomolecules* **2020**, *10* (3).
195. Würth, C.; González, M. G.; Niessner, R.; Panne, U.; Haisch, C.; Genger, U. R., Determination of the absolute fluorescence quantum yield of rhodamine 6G with optical and photoacoustic methods--providing the basis for fluorescence quantum yield standards. *Talanta* **2012**, *90*, 30-7.
196. Platella, C.; Pirota, V.; Musumeci, D.; Rizzi, F.; Iachettini, S.; Zizza, P.; Biroccio, A.; Freccero, M.; Montesarchio, D.; Doria, F., Trifunctionalized Naphthalene Diimides and Dimeric Analogues as G-Quadruplex-Targeting Anticancer Agents Selected by Affinity Chromatography. *Int J Mol Sci* **2020**, *21* (6).
197. Petenzi, M.; Verga, D.; Largy, E.; Hamon, F.; Doria, F.; Teulade-Fichou, M.-P.; Guédin, A.; Mergny, J.-L.; Mella, M.; Freccero, M., Cationic Pentaheteroaryls as Selective G-Quadruplex Ligands by Solvent-Free Microwave-Assisted Synthesis. *Chemistry – A European Journal* **2012**, *18* (45), 14487-14496.

198. Nadai, M.; Doria, F.; Scalabrin, M.; Pirota, V.; Grande, V.; Bergamaschi, G.; Amendola, V.; Winnerdy, F. R.; Phan, A. T.; Richter, S. N.; Freccero, M., A Catalytic and Selective Scissoring Molecular Tool for Quadruplex Nucleic Acids. *Journal of the American Chemical Society* **2018**, *140* (44), 14528-14532.
199. Grande, V.; Shen, C.-A.; Deiana, M.; Dudek, M.; Olesiak-Banska, J.; Matczyszyn, K.; Würthner, F., Selective parallel G-quadruplex recognition by a NIR-to-NIR two-photon squaraine. *Chemical Science* **2018**, *9* (44), 8375-8381.
200. Doria, F.; Manet, I.; Grande, V.; Monti, S.; Freccero, M., Water-Soluble Naphthalene Diimides as Singlet Oxygen Sensitizers. *The Journal of Organic Chemistry* **2013**, *78* (16), 8065-8073.
201. Yarlagadda, V.; Konai, M. M.; Manjunath, G. B.; Ghosh, C.; Haldar, J., Tackling vancomycin-resistant bacteria with 'lipophilic–vancomycin–carbohydrate conjugates'. *The Journal of Antibiotics* **2015**, *68* (5), 302-312.
202. Park, S.; Shin, I., Carbohydrate Microarrays for Assaying Galactosyltransferase Activity. *Organic Letters* **2007**, *9* (9), 1675-1678.
203. Morales-Sanfrutos, J.; Lopez-Jaramillo, J.; Ortega-Muñoz, M.; Megia-Fernandez, A.; Perez-Balderas, F.; Hernandez-Mateo, F.; Santoyo-Gonzalez, F., Vinyl sulfone: a versatile function for simple bioconjugation and immobilization. *Organic & Biomolecular Chemistry* **2010**, *8* (3), 667-675.
204. Wang, J.-X.; Chen, Q.; Bian, N.; Yang, F.; Sun, J.; Qi, A.-D.; Yan, C.-G.; Han, B.-H., Sugar-bearing tetraphenylethylene: novel fluorescent probe for studies of carbohydrate–protein interaction based on aggregation-induced emission. *Organic & Biomolecular Chemistry* **2011**, *9* (7), 2219-2226.
205. De Cian, A.; Guittat, L.; Kaiser, M.; Saccà, B.; Amrane, S.; Bourdoncle, A.; Alberti, P.; Teulade-Fichou, M. P.; Lacroix, L.; Mergny, J. L., Fluorescence-based melting assays for studying quadruplex ligands. *Methods* **2007**, *42* (2), 183-95.
206. Percivalle, C.; Sissi, C.; Greco, M. L.; Musetti, C.; Mariani, A.; Artese, A.; Costa, G.; Perrore, M. L.; Alcaro, S.; Freccero, M., Aryl ethynyl anthraquinones: a useful platform for targeting telomeric G-quadruplex structures. *Org Biomol Chem* **2014**, *12* (22), 3744-54.
207. Liu, P.; Fan, S.; Wang, B.; Cao, R.; Wang, X.; Li, S.; Lu, Y.; Zhong, W., Design, synthesis and biological evaluation of novel triaryldimethylaminobutan-2-ol derivatives against Mycobacterium tuberculosis. *Bioorganic Chemistry* **2020**, *102*, 104054.
208. Peat, A. J.; Boucheron, J. A.; Dickerson, S. H.; Garrido, D.; Mills, W.; Peckham, J.; Preugschat, F.; Smalley, T.; Schweiker, S. L.; Wilson, J. R.; Wang, T. Y.; Zhou, H. Q.; Thomson, S. A., Novel pyrazolopyrimidine derivatives as GSK-3 inhibitors. *Bioorganic & Medicinal Chemistry Letters* **2004**, *14* (9), 2121-2125.
209. Dalu, F.; Scorciapino, M. A.; Cara, C.; Luridiana, A.; Musinu, A.; Casu, M.; Secci, F.; Cannas, C., A catalyst-free, waste-less ethanol-based solvothermal synthesis of amides. *Green Chemistry* **2018**, *20* (2), 375-381.
210. Ortiz-Rojano, L.; Rojas-Martín, J.; Rodríguez-Díaz, C.; Carreño, M. C.; Ribagorda, M., Light-Induced Tetrazole-Quinone 1,3-Dipolar Cycloadditions. *Chemistry – A European Journal* **2019**, *25* (66), 15050-15054.
211. Delafresnaye, L.; Schmitt, C. W.; Barner, L.; Barner-Kowollik, C., A Photochemical Ligation System Enabling Solid-Phase Chemiluminescence Read-Out. *Chemistry – A European Journal* **2019**, *25* (54), 12538-12544.

Ringraziamenti

Tre anni (e un poco più) sono ormai passati dall'inizio di questa avventura, intrapresa un po' per caso, ma con tanto entusiasmo, e, nonostante sembrasse il viaggio più lungo del mondo, ormai è terminato. Tuttavia, non posso chiudere quello che è stato uno dei periodi più importanti della mia vita, senza prima fermarmi a riflettere su quello che questa esperienza mi ha lasciato e, soprattutto, ringraziare chi ha condiviso con me, anche solo in parte, questo incredibile percorso.

La prima persona che vorrei ringraziare è Mauro, per essere stato la mia guida in questo percorso, per avermi trasmesso il tuo entusiasmo per la scienza, per essere sempre stato onesto, per aver contribuito non solo alla mia crescita scientifica, ma anche personale. Grazie per i preziosi consigli, sempre costruttivi, per le discussioni scientifiche, da cui ho sempre imparato qualcosa di nuovo, per avermi resa sempre un po' più curiosa e piena di domande, ma anche sempre un po' più indipendente, per avermi lasciato lo spazio di provare, sbagliare e imparare dai miei stessi errori. Grazie per avermi regalato una seconda possibilità: quando ci siamo incontrati, l'ultima cosa che credevo di volere era tornare a fare ricerca in università. Invece, anche se ero una perfetta sconosciuta, avete deciso di darmi una possibilità. Grazie per la fiducia che hai avuto in me in quel momento e quella che hai ancora adesso, nonostante tutto. Grazie, perchè mi avete dato l'opportunità di ricominciare, mi avete insegnato tanto e mi avete fatto ritrovare la passione che avevo perso.

Ringrazio Filippo, il "cuore" del Lab G, perchè, anche se in fondo saranno passati al massimo 6 o 7 anni da quando avete avviato il laboratorio, è in buona parte merito tuo se abbiamo un posto in cui non solo lavoriamo, ma soprattutto ci divertiamo, impariamo a stare insieme, da cui è difficile andarsene e in cui è bello tornare. Grazie, per tutto quello che mi hai insegnato, per avermi supportata in questi anni ed essere stato sempre presente, anche nei momenti di difficoltà, per avermi fatta sempre sentire coinvolta. Grazie perchè, nonostante tutti i tuoi impegni, riesci sempre a trovare un po' di tempo per aiutare, per un caffè insieme o per una chiacchierata. Il tuo buonumore contagioso è stato fondamentale: riesce sempre a sollevarci, anche nelle giornate in cui siamo tutti un po' a terra.

Un grazie speciale va sicuramente a Vale, che ha condiviso con me quasi ogni giornata degli ultimi quattro anni. Grazie, perchè, quando sono arrivata (un po' spaesata) in questo nuovo ambiente, sei stata un riferimento importante e, dopo tanti anni, lo sei ancora. Grazie, per avermi insegnato tante cose, per essere collega e amica, che mi ha sempre su(o)portata e ascoltata, soprattutto nei momenti no, che sono stati piuttosto frequenti. Negli anni abbiamo formato una buona squadra e siamo diventate l'una la spalla dell'altra (spero), sostenendoci a vicenda, impegnandoci per fare sempre funzionare le cose (tu un po' di più, perchè sei più brava nel bricolage, io sto ancora imparando). Grazie, perchè sei riuscita a trasmettermi un po' della tua empatia, la capacità di apprezzare le diverse sfumature delle persone, ma anche per tutti i bei momenti trascorsi.

Ringrazio tutte le persone che sono state con me in Lab G, in particolare tutti i tesisti che ho avuto modo di seguire e aiutare: Axel, Giovanni, Ilse, Marco e Lorenzo. Spero davvero di avervi insegnato qualcosa, ma, di sicuro, io sono cresciuta un po' con ciascuno di voi, imparando a rapportarmi con persone e situazioni molto diverse, a essere un po' più paziente, a capire tanti punti di vista diversi, ad ascoltare di più, a impegnarmi per altri e non solo per me stessa. Lorenzo, grazie per questi ultimi mesi: sei un "fantasticotesista", non so come farebbe il Lab G senza il tuo talento e simpatia.

Un altro grazie speciale va sicuramente alle ragazze del laboratorio: Alice, Francesca, Martina, Elena e Chiara. Anche se vi conosco da meno tempo, vi ringrazio per il "tocco rosa" che avete portato in Lab G e che davvero mancava. Vi ringrazio per tutte le risate, per la vostra spontaneità, per il supporto continuo, per le chiacchiere e per i bei momenti che ci avete regalato negli ultimi mesi. Spero ce ne saranno molti altri. Ci dicono spesso che mettere tante ragazze a lavorare tutte insieme non sia mai una buona idea ma, con un po' di impegno, stiamo dimostrando che si sbagliano, creando una squadra davvero forte, che costruisce senza distruggere.

Negli ultimi anni, ho trascorso più tempo in laboratorio che in qualunque altro posto, quindi il Lab G è diventato praticamente una seconda casa e le persone che ne fanno parte, una seconda famiglia. Tuttavia, non posso non ringraziare la mia vera famiglia e tutte le altre persone che condividono con me il loro tempo, al di fuori del sotterraneo del dipartimento di chimica organica. Mi sono sentita spesso in colpa per tutto il tempo che ho trascorso lontano da casa, senza la mia famiglia e le amiche di sempre ma, fortunatamente, sono circondata da persone meravigliose, che hanno compreso e accettato tutte le mie scelte, senza mai farmele pesare. La distanza di questi anni mi ha portato a realizzare quanto sono stata fortunata e ad apprezzare maggiormente ogni singolo momento che trascorro con loro.

Ringrazio mia mamma che, nonostante tutto, mi ha sempre spinta a provare a inseguire le mie ambizioni, anche a costo di allontarmi, che mi ha insegnato a non lasciarmi frenare dalle mie paure, che la strada più facile non è necessariamente la migliore, a lavorare sodo per ottenere quello che desidero. Grazie, per avermi incoraggiata ad essere indipendente, con la mente aperta, mai superficiale, ma ad essere egoista quel tanto che basta da ricordarmi di non rinunciare a quello a cui tengo. Grazie, per essere stata mamma e papà insieme, per tutto quello che hai fatto per me, sempre col tuo confortante sorriso, che ha illuminato sempre i miei momenti più bui.

Ringrazio mia sorella, Francesca, per essermi sempre vicina, anche se le nostre scelte ci hanno portate in luoghi diversi (per ora). Nonostante tutto, tra un battibecco e l'altro, ci siamo sempre l'una per l'altra, perchè in fondo sappiamo bene quanto sia importante restare unite. Con tutta questa distanza, abbiamo persino imparato ad apprezzare davvero i momenti che passiamo insieme. Speriamo di poter recuperare presto un po' di tutto questo tempo perso, magari mangiando una bella slerfa di "fugassa", passeggiando in riva al mare o divorando una enorme vaschetta di gelato del "Gelatomatto". Ringrazio mia zia, per essere sempre stata presente, in ogni momento, e, soprattutto, per i suoi insuperabili caffè. Ringrazio il nonno, che è stato più che altro un papà, e perchè, qualunque cosa io facessi, dalla pallavolo alla chimica, è sempre stato il mio più grande sostenitore.

Ringrazio Michi, per essere stato il miglior compagno di laboratorio e amico che potessi chiedere. Grazie, perchè lavorare con te mi ha spinta a fare sempre meglio, senza mai sentirmi in competizione, perchè con te ho imparato un sacco di cose, perchè il tuo credere in me mi ha fatto diventare un po' più sicura. Per tutte le ore che abbiamo passato in quel laboratorio, per le Mitsunobu alle 8 di sera, per tutti i nostri discorsi senza senso, per i caffè, per qualche serata davanti ad un calice di vino e per avermi fatto scoprire Parigi (i miei piedi se lo ricordano ancora bene). Abbiamo cominciato questo percorso insieme, ma tra un "...giuri che tra un po' te ne andrai..." e "...cosa mi dirai, quando sarò lontano", alla fine, te ne sei andato davvero. Nonostante ciò, riusciamo ancora ad esserci, a sostenerci a vicenda, ogni giorno, in questo difficile viaggio.

Ringrazio le mie amiche di sempre, le mie "quasi sorelle", con cui ho condiviso gioie e dolori negli ultimi quindici anni. Jennifer, Giulia, Irene ed Eleonora e Irene, grazie, perchè ci siete sempre, anche quando siamo lontane. Negli anni, abbiamo preso strade diverse, abbiamo fatto scelte differenti, ma non abbiamo mai smesso di vederci ogni settimana, appena possibile, nè di esserci le une per le altre. Grazie, perchè insieme abbiamo condiviso l'adolescenza, i momenti felici e quelli tristi, le risate e i pianti, le pizze al sabato sera, le giornate al mare, estati e inverni, le chiacchiere infinite, l'università, il primo lavoro, gli amori. Mi mancate, non avete idea quanto, non vedo l'ora di poter tornare presto per una serata insieme, per un aperitivo, una camminata vista mare o una pizza in spiaggia, probabilmente al tramonto, grazie. Jenny, la mia "terza sorella", siamo cresciute insieme e ancora mi sopporti, tutti i giorni. Grazie semplicemente di esserci sempre e da sempre, in tutto e per tutto.

Ultimo, ma non meno importante, ringrazio Luca, per tutto quello che sei e che fai per me, per essermi stato sempre vicino in questi anni. Se questa avventura è iniziata bene, probabilmente è perchè, nello stesso periodo, è iniziata la nostra storia: mi hai fatta ridere un paio di volte e tutto è andato nella direzione giusta. Grazie, per avermi sempre sostenuta in questi anni, per aver creduto in me, più di quanto abbia mai fatto io.

Grazie, perchè riesci a bilanciare tutti i miei eccessi, a smussare tutti i miei spigoli. Grazie, perchè mi fai il verso quando mi arrabbio, per quando inizi a dire cose divertenti quando sto per piangere davanti ad un film, perchè mi ascolti sempre (anche quando ripeto sempre le stesse cose), per la carbonara, perchè, anche se ti lamenti, assecondi le mie idee a volte un po' folli, perchè mi hai aspettata, perchè ti prendi sempre cura di me, per avermi sempre lasciata essere un po' egoista. In questa difficile avventura, sei stato la mia ancora, la mia nuova, piccola, famiglia, un porto sicuro in cui poter sempre rifugiarsi. Sono sempre stata bene da sola, ma da quando ci sei tu, tutto è un po' più bello. Spero che il nostro, di viaggio, sia solo all'inizio.

Infine, vorrei semplicemente dire che sono grata per quello che ho vissuto nel corso di questi tre anni, per le esperienze che ho avuto la possibilità di fare, per le persone che ho avuto modo di conoscere, per i luoghi che ho visto. Ho avuto modo di crescere come scienziata, ma anche di rendermi conto quanto ancora posso imparare, di realizzare che da chiunque si può apprendere qualcosa di nuovo, che sbagliare è necessario per migliorare, che chiedere una mano non è sintomo di debolezza o incapacità, ma un primo passo per costruire un lavoro migliore, che i fallimenti non ti rendono un incompetente, che una serie di grandi successi non fa di te un grande scienziato, ma la passione per il tuo lavoro e la perseveranza sì.

Questo percorso mi ha dato la possibilità di crescere anche come persona, di guadagnare una fiducia in me stessa che non ho mai avuto, di mettermi alla prova, di superare molte delle mie paure, di viaggiare, di imparare a confrontarmi con tanti punti di vista e situazioni differenti. I momenti felici che ho vissuto in questi anni, mi hanno insegnato che accettare le casualità della vita può portarti avventure inaspettate, che abbandonare la strada conosciuta per una nuova può portarti a scoprire posti meravigliosi.

Nonostante tutto, sono stati anni impegnativi, fatti di alti e bassi, che sembrava non sarebbero mai finiti e, invece, sono volati in un attimo. Sembrava la storia infinita, ma forse era solo felicità.